UNIVERSITY OF CALIFORNIA SAN DIEGO

Magnetoresistive Biosensor Circuits and Systems for Ultrasensitive Point-of-Care Diagnostics

A dissertation submitted in partial satisfaction of the
requirements for the degree Doctor of Philosophy

in

Electrical Engineering (Electronic Circuits and Systems)

by

Xiahan Zhou

Committee in charge:

Professor Drew A. Hall, Chair
Professor Gert Cauwenberghs
Professor Yu-Hwa Lo
Professor Patrick Mercier
Professor Dan Sievenpiper

2020

The Dissertation of Xiahan Zhou is approved, and it is acceptable in quality and form for publication on microfilm and electronically.

_____

_____

_____

_____

_____
Chair

University of California San Diego

2020

TABLE OF CONTENTS

LIST OF FIGURES

LIST OF TABLES

ACKNOWLEDGEMENTS

Over my six years at UCSD, I have received support and encouragement from a great number of individuals. I would like to first acknowledge my advisor, Professor Drew Hall, for providing me the opportunity to join his research lab. Before my decision of attending UCSD, Prof. Hall interviewed me twice, once over Skype and once in-person. Throughout our interactions, I came to learn about the project he was proposing for me – to extend research his Ph.D. work. This impressed me and excited to me. In my toughest first 2-3 years, his technical guide and passion for the project helped and encouraged me to overcome technical difficulties and broke the bottleneck. In recent years, his trust and support inspired me to be more confident and strengthened my abilities in time and project management. In addition to the technical guidance, his humor amused the group in such a highly stressful research environment. I am grateful to have had the opportunity to work with Prof. Hall on my PhD career and sincerely appreciate all the guidance he gave me, academically and mentally.

I also owe many thanks to my project partners, Dr. Chih-Cheng Huang who provided knowledge on magnetic sensors, biology, and fabrication; Michael Sveiven who ran lots of magnetic assays for my biological experiments; and Enhan Mai who helped design the ADC and test my last chip. I would like to thank my fellow colleagues in the BioEE Group for their help, advice, and friendship, especially Dr. Haowei Jiang for the technical discussion and off-work entertainment, and Da Ying for his optimistic attitude and healthy lifestyle. I would also like to express my gratitude to group alumni and members, Dr. Somok Mondal, Corentin Pochet, Omid Ghadami, Aditi Jain, Joshua Rosenberg, Tyler Hack, Matthew Chan, Dr. Saeromi Chung, Dr. Naveen Kumar Singh,

Dr. Venkatesh Alagarswamy Govindaraj, Dr. Rajesh Seenivasan, Dr. Chung-Lun Hsu, Dr. Alex Sun, Saurabh Kulkarni, Sandeep Adem, Sonal Jain, Tianlei Sun, Chengyang Yao, and Tom Phelps for their help and support. I appreciate all my friends who work in other groups at UCSD, namely Dr. Hui Wang, Dr. Li Gao, Xiaoyang Wang, Jiannan Huang, and Dr. Po-han Wang, for releasing my stress over the hard time.

Last, but definitely not the least, I would like to thank my family and extended family, especially my father, Liping, and mother, Yuanying, for their never-ending support and encouragement. I would also like to thank my parents-in-law, grandparents, uncle, aunt, cousin, and little nephew for keeping me happy even they are over 7,000 miles away. Most importantly, I owe many thanks my wife, Xiao, for her selfless love and endless support. As the most caring person with me, her mental support is my motivation during the most stressful moments. Not to mention, as an electrical engineer, her professional advice and understanding of long-hours working over the tape-out season are great gifts to me. Moreover, I would like to thank my son Bear, a 1-year-old golden retriever, for providing me the most enjoyable and memorable time this last year. This dissertation is dedicated to my family, a minor token of my immense gratitude.

Since portions of this dissertation have been published previously as a result of several collaborations, I must again acknowledge each of the authors for their tremendous contributions.

Chapter 1, 2 and 3, in part, are based on materials from Xiahan Zhou, Chih-Cheng Huang, and Drew A. Hall, “Magnetoresistive Biosensors for Quantitative Proteomics,” *Proceedings of SPIE Optics + Photonics*, San Diego, CA, Aug. 6-10, 2017, Xiahan Zhou, Michael Sveiven, and Drew A. Hall, “A Fast-Readout, Mismatch-Insensitive

Magnetoresistive Biosensor Front-End Achieving Sub-ppm Sensitivity," *IEEE International Solid-State Circuits Conference (ISSCC),* San Francisco, CA Feb. 17-21, 2019, and Xiahan Zhou, Michael Sveiven, and Drew A. Hall, "A CMOS Magnetoresistive Sensor Front-End with Mismatch-Tolerance and Sub-ppm Sensitivity for Magnetic Immunoassays," *IEEE Transactions on Biomedical Circuits (TBioCAS)*, Dec 2019. The dissertation author was the primary investigator and author of these papers.

Chapter 4, in part, is based on materials from Xiahan Zhou, Chih-Cheng Huang, and Drew A. Hall, "Giant Magnetoresistive Biosensor Array for Detecting Magnetorelaxation," *IEEE Transactions on Biomedical Circuits and Systems (TBioCAS)*, Aug. 2017, and Chih-Cheng Huang, Xiahan Zhou, and Drew A. Hall, "Giant Magnetoresistive Biosensors for Time-Domain Magnetorelaxometry: A Theoretical Investigation and Progress Toward an Immunoassay," *Scientific Reports*, Apr. 2017. The dissertation author was the primary investigator and author of these papers.

Chapter 5, in part, is currently being prepared for submission for publication of the material from Xiahan Zhou, Enhan Mai, Michael Sveiven, Corentin Pochet, Haowei Jiang, Chih-Cheng Huang, and Drew A. Hall. The dissertation author was the primary investigator and author of this paper.

Xiahan Zhou

La Jolla, CA

July 2020

VITA

EDUCATION

2012	Bachelor of Engineering in Microelectronics Technology, University of Electronic and Science Technology of China, Chengdu, China
2014	Master of Science in Electrical Engineering, University of Southern California, Los Angeles, USA
2020	Doctor of Philosophy in Electrical Engineering (Electronic Circuits and Systems), University of California San Diego, La Jolla, USA

PUBLICATIONS

C-C. Huang, P. Ray, M. Chan, **X. Zhou**, and D.A. Hall, "An aptamer-based magnetic flow cytometer using matched filtering," *Biosensors and Bioelectronics*, In Press.

S. Adem, S. Jain, M. Sveiven, **X. Zhou**, A.J. O'Donoghue, and D.A. Hall, "Giant magnetoresistive biosensors for real-time quantitative detection of protease activity," *Nature Scientific Reports*, vol. 10, no. 1, Art. no. 1, May 2020.

X. Zhou, M. Sveiven, and D.A. Hall, "A CMOS Magnetoresistive Sensor Front-End with Mismatch-Tolerance and Sub-ppm Sensitivity for Magnetic Immunoassays," *IEEE Transactions on Biomedical Circuits (TBioCAS)*, vol. 13, no. 6, pp. 1254-1263, Dec 2019. **(Invited Paper)**

X. Zhou, M. Sveiven, and D.A. Hall, "A Fast-Readout, Mismatch-Insensitive Magnetoresistive Biosensor Front-End Achieving Sub-ppm Sensitivity," *IEEE International Solid-State Circuits Conference (ISSCC),* San Francisco, CA Feb. 17-21, 2019.

H. Jiang,* **X. Zhou**,* S. Kulkarni, M. Uranian, R. Seenivasan, and D.A. Hall, “A Sub-1 µW Multiparameter Injectable BioMote for Continuous Alcohol Monitoring,” *IEEE Custom Integrated Circuits Conference (CICC),* San Diego, CA, Apr. 9-11, 2018.

C-C. Huang, **X. Zhou**, D. Ying, and D.A. Hall, “A GMR-Based Magnetic Flow Cytometer Using Matched Filtering,” *Proceedings of IEEE Sensors*, Glasgow, Scotland, Oct. 30 - Nov. 1, 2017.

X. Zhou, C-C. Huang, and D.A. Hall, “Magnetoresistive Biosensors for Quantitative Proteomics,” *Proceedings of SPIE Optics + Photonics*, San Diego, CA, Aug. 6-10, 2017.

X. Zhou, C-C. Huang, and D.A. Hall, “Giant Magnetoresistive Biosensor Array for Detecting Magnetorelaxation,” *IEEE Transactions on Biomedical Circuits and Systems (TBioCAS)*, vol. 11, no. 4, pp. 755-764, Aug. 2017.

C-C. Huang,* **X. Zhou**,* and D.A. Hall, “Giant Magnetoresistive Biosensors for Time-Domain Magnetorelaxometry: A Theoretical Investigation and Progress Toward an Immunoassay,” *Scientific Reports* **7**, 45493 (2017).

* These authors contributed equally.

FIELD OF STUDY

Major Field: Electrical Engineering

Studies in Electronic Circuits and Systems

Professor Drew A. Hall

ABSTRACT OF THE DISSERTATION

Magnetoresistive Biosensor Circuits and Systems for Ultrasensitive Point-of-Care Diagnostics

by

Xiahan Zhou

Doctor of Philosophy in Electrical Engineering (Electronic Circuits and Systems)

University of California San Diego, 2020

Professor Drew A. Hall, Chair

Over the past several decades, early diagnoses and disease monitoring that rely upon biomolecular testing are the primary factors that have led to the substantial increase in average life expectancy. Molecular tests, which analyze patient samples for disease-

specific biomarkers, are becoming the basis of the majority of diagnoses and therapy monitoring. Point-of-care (PoC) diagnostics uses a portable analytical device for accurate and fast tests to avoid frequent clinic visits and long turn-around time. Among biosensing techniques, magnetic sensors take advantage of the intrinsic lack of magnetic background in biological samples to achieve high sensitivity and are compatible with semiconductor-based fabrication processes to enable low-cost and small-size devices for PoC applications.

In this dissertation, magnetic sensor analog front-ends (AFEs) are designed to measure the signal from magnetoresistive (MR) sensors and overcome challenges such as small signal to baseline ratio, 1/*f* noise, and temperature drift. Two sensing techniques, magnetometry and magneto-relaxometry (MRX), are discussed and compared. Printed circuit boards (PCBs) and CMOS chips are designed to implement both techniques.

First, a CMOS chip based on magnetometry is presented, which reduces the baseline using a double modulation scheme and a reference sensor. The residual baseline from the sensor mismatch is further reduced using a high frequency interference rejection (HFIR) sampling technique embedded in the ADC. A fast settling duty-cycled resistor (DCR) is used to reduce the AFE settling time, thus enabling a readout time that is 22.7× faster than the state-of-the-art. This work results in sub-ppm sensitivity and a sensor mismatch tolerance of up to 10%.

While promising, the sensor mismatch still limits the baseline cancellation. MRX measures the relaxation signal after removing the excitation magnetic field, thus enabling baseline-free detection. PCBs, including an AFE and an electromagnet driver that can collapse the magnetic field within 10 μs, were designed to validate the time-domain MRX.

The signal dependency on the sensor coverage, applied field strength, and magnetization time was investigated.

Lastly, a CMOS chip based on MRX was designed that uses magnetic or magnetoresistive correlated double sampling to reject the systematic 1/*f* noise. Moreover, a fast settling Miller compensation (FSMC) technique was presented to save the power, while maintaining the amplifier's linearity and stability. As a result, this work achieves the best-reported magnetic sensor figure-of-merit (FoM).

These works enable ultrasensitive, broad dynamic range, and fast response magnetic sensing systems towards PoC diagnostics.

Chapter 1. INTRODUCTION

1.1 Research Motivation

Dramatic improvements in medicine and the healthcare system over the past century have increased average life expectancy in the United States from 50 years to over 75 years [1]. Unquestionably, one of the largest factors is the earlier diagnoses of life-threatening diseases. Medical decision-making, which used to be based solely on patient symptoms, is increasingly relying upon molecular testing for more accurate diagnostics. Therefore, the development of an analytical device to interrogate a variety of complex biological samples (*i.e.* saliva, urine, blood, sweat, etc.) would enable breakthroughs in all areas of medicine and life science related fields. Traditionally *in-vitro* diagnostic techniques rely on bulky and expensive medical instrumentation located in centralized facilities. This requires frequent clinic visits with a long turn-around time that may affect the treatment outcomes.

Point-of-care (PoC) biomolecular testing has drawn considerable attention worldwide due to its convenience, portability, and potential for long-term disease surveillance [2], [3]. The push towards PoC devices has focused on moving these devices

out of the lab and into the field (*e.g.*, clinics, bedside, at-home, etc.). Such a device would, for example, facilitate development of new targeted therapies for cancer (and other diseases) and set the stage for unprecedented diagnostic capabilities resulting in earlier disease diagnoses and better treatment outcomes. Furthermore, diseases could be routinely tracked using smartphones to enable data collection, computation, storage, and secure transmission to a medical facility. Thus, there has been significant interest in miniaturization and reducing turn-around time, ideally without compromising assay performance (*i.e*. sensitivity and specificity) [4]. Such advances could lead to broader access and a democratization of healthcare, particularly in developing parts of the world where such biomolecular testing infrastructure currently does not exist. Figure 1.1 shows a steady market increasing over years and expects $46.7 billion in 2024 [5].

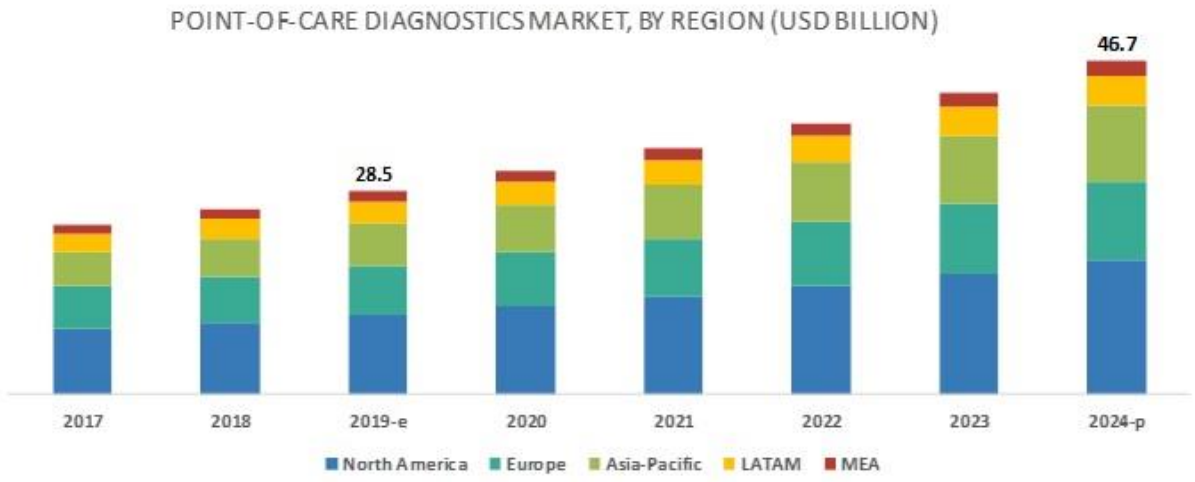

Figure 1.1 Point-of-care diagnostics market

1.2 Immunoassay and Biosensing

In-vitro diagnostics can be broadly categorized depending on if a label is used in the detection process (*i.e.* label-free and labeled). Although label-free biosensing

techniques (*e.g.*, ChemFET [6]–[9], microcantilever [10]–[12]) can be very sensitive via direct measurement of an intrinsic property of the analyte (*i.e.* charge, mass, etc.) [13], labeled detection is more specific and often preferred given the large heterogeneity of analytes in clinical samples [14]–[16]. Most labeled detection schemes use a variant of the sandwich immunoassay, as shown in Figure 1.2, where the analyte is flanked on both sides by a recognition molecule, the second of which is attached to a label. A sandwich assay first immobilizes analyte specific receptors (*e.g.*, antibodies, aptamers, etc.) on the surface of the sensor that selectively bind to the target analytes (antigens). This is followed with a second binding event using analyte specific receptors conjugated to a label (*e.g.*, an enzyme, fluorophore, or magnetic nanoparticle) that is detected by a corresponding sensor. As such, these affinity biosensors indirectly measure the analyte concentration via the number of labeled complexes tethered to the surface.

Biosensors work as transducers to convert biological signals to electrical signals, which can be measured by electrical circuits. Based on the label types, different types of biosensors (*e.g.*, optical, electrochemical, or magnetic) are used. Optical biosensors are highly sensitive and specific, easy to parallelize for multiplex detection, and low-cost [17]. While some optical biosensors, such as surface plasmon resonance (SPR) are label-free

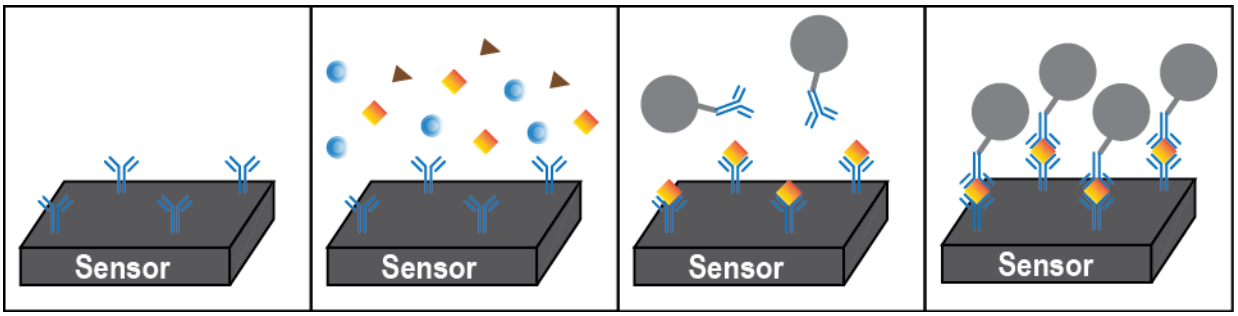

Figure 1.2 Sandwich immunoassay

(1) Capture receptors are immobilized on sensor surface, (2) target analytes in samples bind to the capture receptors, and (3) labeled detection receptors bind to the analytes to form a sandwich.

[18], [19], most are enzyme-based [20], [21], fluorescence-based [22], [23], or chemiluminescence-based [24]–[26] labeled immunoassays. The enzyme-linked immunosorbent assay (ELISA), which uses an enzyme label that reacts with a substrate solution to generate a colorimetric signal (Figure 1.3(a)), is currently the gold standard in immunology. Whereas many other biosensing techniques have yet to make it out of research laboratories, this technique is one of the most widely used techniques today [27]. Alternative formats using fluorophores [22] and quantum dots [28], [29], where a laser excites the label and the fluorescent signature is measured (Figure 1.3(b)), have shown better sensitivity and quantification as there is a one-to-one relationship between the analyte and the label compared to the enzymatic assay where a single enzyme can repeatedly convert substrate. As such, traditional ELISAs require tight control over timing and routine calibration, often with every assay. These are not issues with fluorescent assays; however, fluorescent readout requires much more complex optical setups with narrow-band optical filters tuned to the excitation and emission frequencies. Chemiluminescence-based biosensors detect light emission due to a chemical reaction and therefore forego the excitation source reducing the instrumentation complexity. They

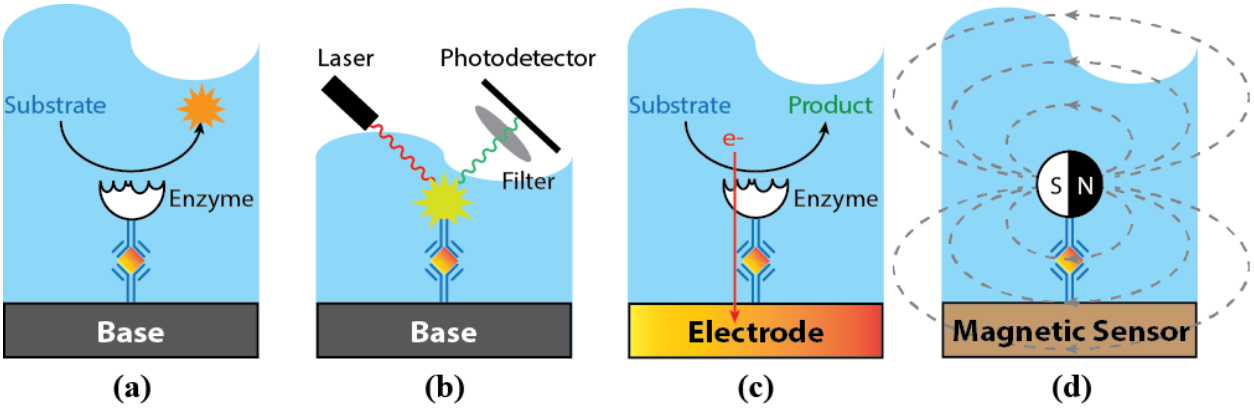

Figure 1.3 Types of biosensors

(a) Enzyme-labeled optical sensor, (b) fluorophore-labeled optical sensor, (c) enzyme-labeled electrochemical sensor, and (d) MNP-labeled magnetic sensor.

also have very large dynamic range, up to 6 decades, and high sensitivity due to the low background signal [24], [25]. However, tradeoffs between different types of chemiluminescence-based sensors result in none of them achieving high sensitivity, low cost, rapid assay time, and high quantum yield simultaneously [25], [26].

Electrochemical biosensors have been by far the most successful commercial biosensor to date, largely due to the glucometer, a critical device in managing healthcare for millions of diabetics worldwide [30]. Figure 1.3(c) illustrates an assay with an enzyme that catalyzes the substrate resulting in an oxidation-reduction reaction [31]–[33]. Common electrochemistry techniques include potentiometry [34]–[37], amperometry [38]–[42], and impedance spectroscopy [43]–[46]. A glucometer is an amperometry-based biosensor where the concentration of a byproduct (*e.g.*, hydrogen peroxide) generated by an enzyme (*e.g.*, glucose oxidase) reacting with glucose is detected and quantified. Although electrochemical biosensors are very low-cost, easy to operate and miniaturize, they often suffer from high background, low specificity, dependence on pH and ionic strength of the solution, and may require highly specific enzymes [31], [47].

Despite the success of optical and electrochemical biosensors, there remains an unmet need for *in-vitro* diagnostics platforms that are low-cost, highly sensitive with wide dynamic range, miniaturizable, little to no sample pretreatment required, and scalable for PoC diagnostics. Magnetic biosensors are introduced accordingly to address this need.

1.3 Magnetic Biosensors

Compared with its optical counterpart, magnetic biosensors do not require optical lasers, filters, and detectors and thus can be more compact while maintaining the benefit

of low-cost, high volume production. They use superparamagnetic nanoparticles (MNPs) as the label, which is polarized by an external magnetic field and generates a stray field that can be detected (Figure 1.3(d)). Due to the compatibility with semiconductor-based fabrication processing, it also allows tight integration of the sensors, readout circuits, and electromagnet, enabling a miniaturized sensing platform [48]–[53]. Another benefit of magnetic sensing is that biological samples are intrinsically non-magnetic, so the detection environment has very low background and does not require any sample pretreatment (*i.e.* the measurement is matrix-insensitive) [54]. As a result, magnetic sensors have very high sensitivity (down to femtomolar concentrations) [54]–[57] with wide dynamic range (6 decades) [54], [55] and compact size, making them ideal for PoC applications [58]–[60]. Recently, several types of magnetic detectors have been demonstrated including nuclear magnetic resonance (NMR) [61]–[63], oscillator-based sensors [48], [49], [64], [65], Hall-effect sensors [50], [51], [66]–[70], and magnetoresistive sensors [52]–[57], [71]–[80]. Although these sensors all use MNPs to quantitatively detect analytes, their operation mechanisms are quite different.

NMR is an indirect method to detect analytes by measuring the spin-spin relaxation time (T_2) of water molecules [81]. The setup requires at least one permanent magnet to provide a dc bias field, B_0, and one electromagnet to provide an RF excitation field, B_1 [61]. By setting the frequency of B_1 to the Larmor frequency of the protons in water, which is proportional to B_0, the protons periodically absorb the energy from B_1 perturbing their alignment from B_0. Due to the proton-proton interaction, some protons will be out-of-phase and the total magnetic moment decays over time as the protons precess after B_1 is removed. The rate of the decay is characterized by the spin-spin relaxation time, T_2. By

adding antibody-coated MNPs to the sample, the T_2 signal decreases as antibody-antigen complexes are formed, as shown in Figure 1.4(a). These binding events produce large aggregates, further intensifying the perturbation and shortening the T_2 signal thus allowing the concentration to be quantified. Biological experiments have shown avidin detection with a dynamic range of 80 dB [62].

Miniaturization is the key challenge for this technique. Since it requires a large permanent magnet and an electromagnet, the system is usually bulky [82]. A miniaturized NMR system, which can be held in the palm of a hand, was recently demonstrated [63]. However, since the signal amplitude is quadratically proportional to B_0, reducing the magnet size reduces the sensitivity significantly. As a result, this NMR system only achieved a sensitivity of 3 nM [62] (Figure 1.4(b)) compared to benchtop equivalents which have a sensitivity of 140 fM [83]. Further improving the sensitivity and size is difficult due to the fundamental tradeoff between the signal amplitude and the magnet size.

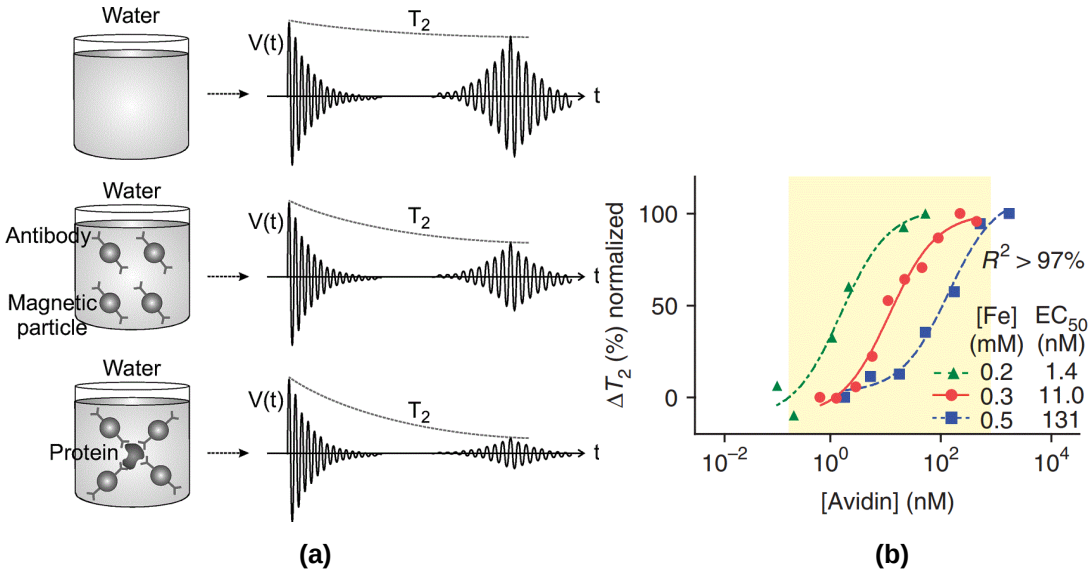

Figure 1.4 Nuclear magnetic resonance

(a) Spin-spin relaxation time T_2 for pure water, antibody-coated magnetic particles, and antibody-protein complexes [61], and (b) measured NMR calibration curve [62].

Oscillator-based biosensors are usually tuned LC resonators where the resonant frequency is dependent on the number of tethered MNPs. Figure 1.5(a) shows one such example where a sandwich immunoassay labeled with MNPs is assembled on the surface of an inductor. The magnetic field generated by current passing through the inductor magnetizes the MNPs, which alters the inductance, and thus changes the resonant frequency [48], [64]. These sensors are very attractive as they do not need an external magnetic field and are fully CMOS compatible allowing them to be compact and low-cost. Techniques such as correlated double counting (CDC) have been employed to reduce correlated noise and environmental conditions such as temperature drift allowing detection of a single 1 μm MNP (Figure 1.5(b)) [64]. However, these sensors often have reproducibility issues due to the non-uniform magnetic field resulting in spatial dependency and non-linearities. This issue can be remedied using a bowl-shaped inductor, but this requires more exotic fabrication and is not always CMOS compatible [49]. Although this technique was not used for detecting proteins, it has successfully detected DNA [48] and cells [65].

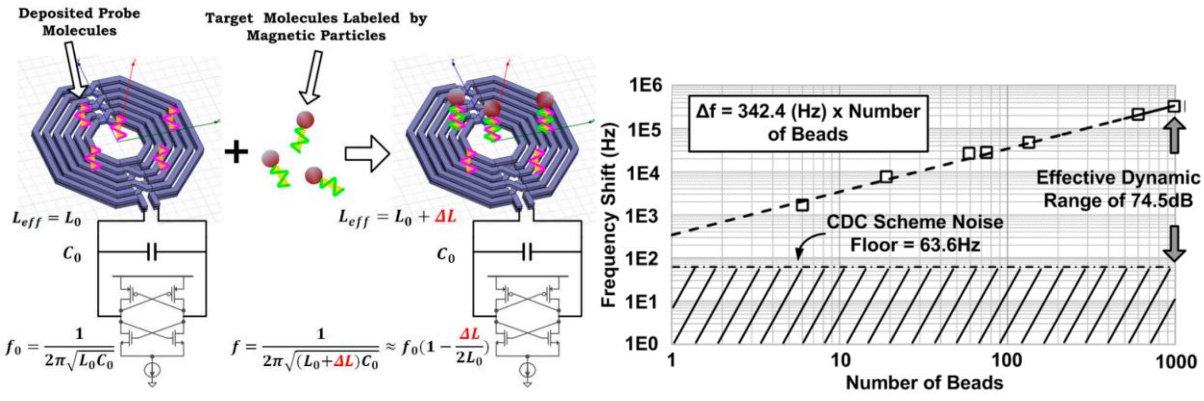

Figure 1.5 Oscillator-based sensor

(a) Illustration showing how tethered MNPs cause a resonance frequency shift in an LC oscillator [48] and (b) measured calibration curve [64].

Hall-effect sensors measure an induced voltage caused by the force a perpendicular magnetic field exerts on a charge carrying ion. These sensors can be realized using the diffusion layer (n-well) of a transistor and thus are compatible with standard semiconductor fabrication processes. However, the diffusion layer is the bottom layer in a CMOS process so post-processing is required to remove all (or most) metal and interlayer dielectric material above the sensor to minimize the distance between the sensors and MNPs [66]. Figure 1.6(a) shows a sandwich immunoassay on top of a Hall sensor with an integrated electromagnet to magnetize the MNPs. The presence of the MNPs induces a voltage on the underlying sensor that is readout by the nearby circuitry.

Researchers have demonstrated both magnetometry-based biosensing [66]–[68] and relaxometry-based biosensing [50], [51], [69] where instead of leaving the magnetic field on constantly and measuring the perturbation, the magnetic field is pulsed and the temporal dynamic response is measured as the MNPs relax back to equilibrium. The detail of these mechanisms will be discussed further in Section 2.4, but it should be noted that the relaxation of the MNPs is different from NMR sensors, which are based on the proton-proton interaction of water molecules. To maximize the signal, the sensor was sized comparable to a single 4 μm MNP and thus each sensor can detect only one MNP [70]. To have a reasonable dynamic range, a large array containing 10k pixels was built with single MNP sensitivity and a dynamic range of 80 dB by combining all of the small sensors into one effective sensor [51]. This sensor array was used to detect Human Serum Albumin (HSA) with a sensitivity of 15 pM (Figure 1.6(b)). By limiting the design to one MNP per sensor and using relaxometry-based biosensing technique, Hall-effect sensors resolve the MNP location dependency and field non-uniformity issue that impede

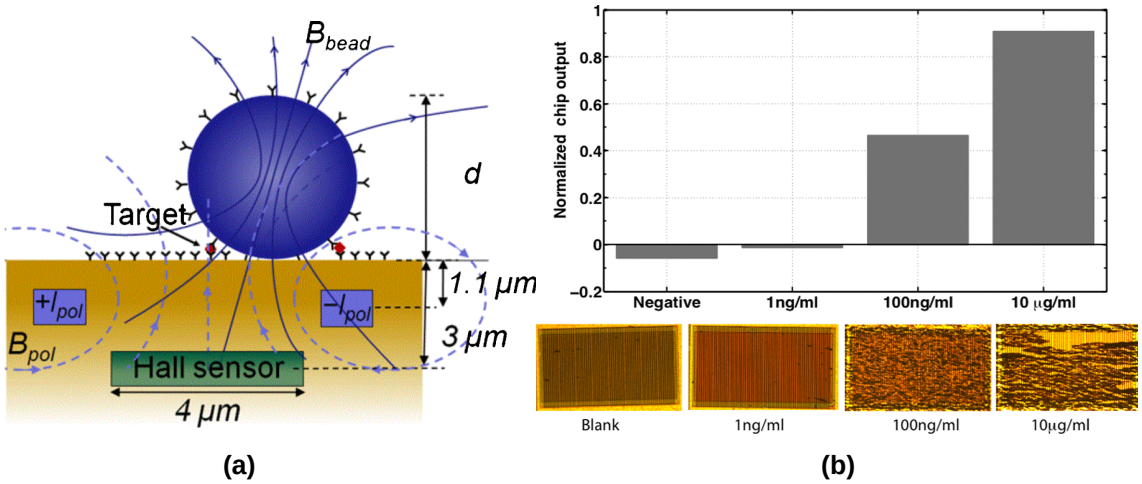

Figure 1.6 Hall-effect sensor

(a) Illustration of a Hall-effect sensor detecting a single captured MNP [70] and (b) measured signals with optical images for various HSA concentrations as low as 1ng/mL (15 pM) [51].

oscillator-based sensors. However, one MNP per sensor requires a very large array to achieve sufficient dynamic range, which becomes a bottleneck for Hall-effect sensors.

Oscillator-based sensors and Hall-effect sensors can both detect a single 1 μm MNP; however, micrometer-sized MNPs diffuse very slowly in solution and are much, much larger than the target analytes, thus they require washing steps to remove unbound MNPs and have longer assay time [14]. Magnetoresistive (MR) sensors are used extensively in commercial applications as the read-head in a hard disk drive. These sensors are elaborately engineered stacks of magnetic and non-magnetic thin films and have much higher transduction efficiency, allowing them to detect nanometer-sized MNPs. The detail of MR biosensing will be discussed on the next chapter.

1.4 Scope of Dissertation

This dissertation presents front-ends of the MR biosensors for PoC diagnostics. In Chapter 2, the MR sensors, sensing techniques, and prior magnetic sensor front-ends

are discussed and compared. A PCB implementation is presented to validate the system. Chapter 3 presents a CMOS front-end based on magnetometry that achieves sub-ppm sensitivity and sub-pM biological limit-of-detection (LOD). In Chapter 4, MRX is introduced for baseline-free detection and a discrete MR sensor system is presented. Chapter 5 presents a CMOS front-end based on MRX that achieves the best reported magnetic sensor figure-of-merit (FoM). Finally, Chapter 6 summarizes this dissertation and discusses areas of future work.

Chapter 1, in part, is based on materials from Xiahan Zhou, Chih-Cheng Huang, and Drew A. Hall, “Magnetoresistive Biosensors for Quantitative Proteomics,” *Proceedings of SPIE Optics + Photonics*, San Diego, CA, Aug. 6-10, 2017 [16]. The dissertation author was the primary investigator and author of this paper.

Chapter 2. MAGNETORESISTIVE BIOSENSING

2.1 Introduction

Magnetoresistance is the property of a material to change its electrical resistance in response to a magnetic field [84]. Anisotropic magnetoresistance (AMR), giant magnetoresistance (GMR), and tunnel magnetoresistance (TMR) are different types of magnetoresistance. AMR, the first discovered magnetoresistance by William Thomson (Lord Kelvin) in 1856, depends on the relative angle between the direction of the sense current and the local magnetization [85]. GMR is a quantum mechanical MR effect observed in multilayer filmstacks composed of alternating ferromagnetic and non-magnetic conductive layers. The resistance depends on whether the magnetization of adjacent ferromagnetic layers is in parallel or an antiparallel alignment. With to the discovery of GMR, Albert Fert and Peter Grünberg were awarded the 2007 Nobel Prize in Physics [86]. TMR, like GMR, is also a multilayer structure based on a quantum mechanical phenomenon. Instead of using a conductive layer between ferromagnetic

layers in GMR, TMR uses an insulating barrier layer that is thin enough for electrons to tunnel from one ferromagnetic layer to the other.

In this dissertation, GMR sensors purchased from MagArray, Inc. were used. The rest of this chapter introduces and characterizes the GMR sensors, as well as discusses the sensing techniques and prior sensor front-ends.

2.2 GMR Sensors

2.2.1 Principle of Operation

While GMR sensor has a complex multi-layer stack, its operation can be understood by three key components: the free layer, the pinned layer, and a non-magnetic spacer layer in-between, as shown in Figure 2.1(a). Both the free layer and the pinned layer are ferromagnetic. The magnetic moment of the pinned layer is fixed (to the right in this example) after fabrication, but the free layer rotates freely in-plane following the applied field, H_A. The sensor resistance depends on the angle of the magnetic moments between the free layer and the pinned layer, as shown in Figure 2.1(b).

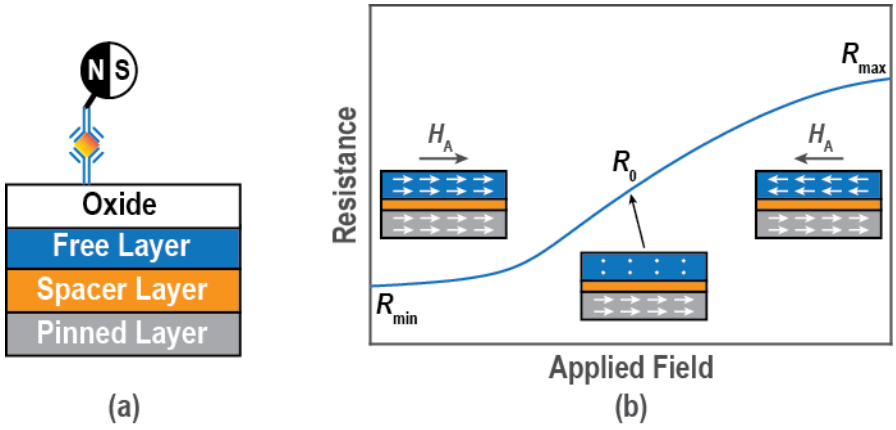

Figure 2.1 GMR sensor principle of operation

(a) Simplified layer stack and (b) sensor resistance vs. applied field.

Qualitatively, the sensor remains at its nominal resistance, R_0, when no field applied. When H_A biases the free layer to be in parallel with the pinned layer, the majority carriers in the free layer (electrons that have spin moment to the right) are in the same orientation as in the pinned layer. Therefore, electrons travel through both layers without additional electron scattering, resulting in low resistance. Conversely, when the free layer is anti-parallel with the pinned layer, carriers in the free layer (electrons that have spin moment to the left) are different from the majority carriers in the pinned layer. This results in more electron scattering, and thus a higher resistance. The magnetoresistance ratio is defined as

$$\text{MR Ratio} = \frac{R_{\max} - R_{\min}}{R_{\min}} \tag{2.1}$$

where R_{max} and R_{min} are the maximum and minimum resistance of the sensor, respectively. The MR ratio of AMR, GMR, and TMR are 1-3%, 5-20%, and 40-350%, respectively [87], [88]. Although TMR exhibits the highest MR ratio, it has not been widely

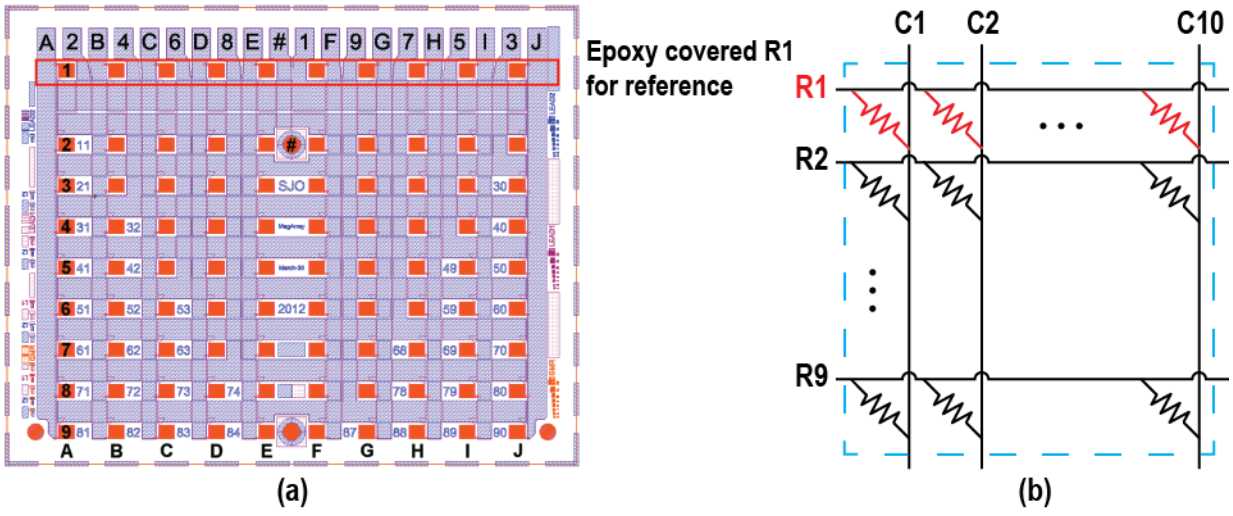

Figure 2.2 Sensor array

(a) Photograph and (b) equivalent schematic of the sensor array.

used in biosensing due to its much worse 1/*f* noise (1/*f* noise corner frequency of ~1 MHz vs. ~1 kHz in GMR) and they are harder to fabricate [89], [90].

2.2.2 Array

The MagArray sensor array consists of 90 sensors that are split into 9 rows and 10 columns, as shown in Figure 2.2. Sensors have shared rows and columns to reduce number of pads but suffer from increased noise that will be discussed in later. The first row is covered by epoxy to prevent MNP binding, so these sensors are considered reference sensors.

2.2.3 Transfer Curve

The sensors must be characterized first to understand the resistance, operating range, sensitivity, etc. A custom PCB and a graphic user interface (GUI) written by MATLAB were designed accordingly. Figure 2.3 shows the analog front-end (AFE) used for sensor characterization. The sensor under test, R_S, is biased by a dc voltage, $V_{in} = V_{cm} + V_B$, and the resulting current is amplified by a transimpedance amplifier (TIA). A bleed resistor, R_B, that is set close to R_S, is biased by a negative dc voltage, $V_{inb} = V_{cm} - V_B$, to cancel most of the R_0 baseline. Therefore, the output voltage V_{out} is

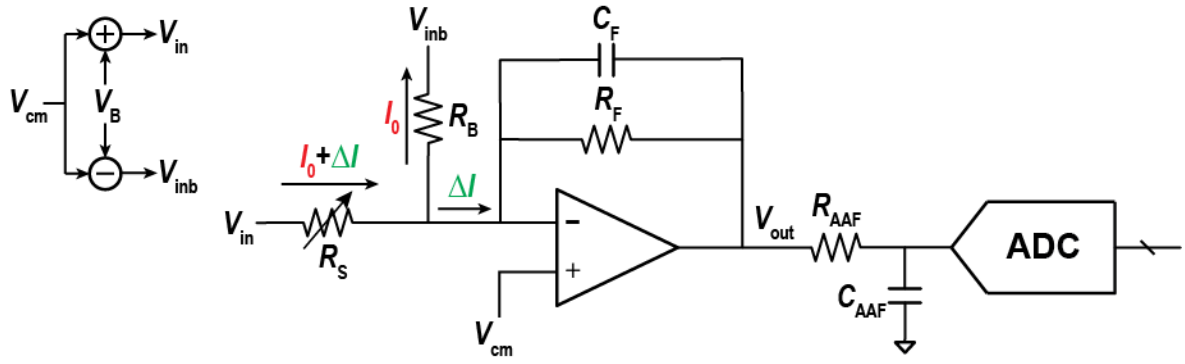

Figure 2.3 Schematic of the sensor AFE

$$V_{\text{out}} = \left(\frac{R_{\text{F}}}{R_{\text{S}}} - \frac{R_{\text{F}}}{R_{\text{B}}}\right) V_{\text{B}} + V_{\text{cm}}. \quad 2.2$$

It is often useful to split R_S into R_0 and the magnetoresistance, ΔR, so that $R_S = R_0 + \Delta R$. Assuming $R_B = R_0$ and $\Delta R << R_0$, it can be shown that

$$V_{\text{out}} = V_{\text{cm}} - \frac{R_{\text{F}}}{R_0}\frac{\Delta R}{R_0} V_{\text{B}} \quad 2.3$$

where V_{cm} is set to $V_{DD}/2$ for the maximum dynamic range. A data acquisition (DAQ, NI-6361) quantizes V_{out} after an anti-aliasing filter that is composed of R_{AAF} (100 Ω) and C_{AAF} (33 nF). Equation 2.3 indicates that larger R_F and V_B improve the signal gain but contradict the dynamic range, which is highly dependent on the matching between R_0 and R_B. Assuming a rail-to-rail output amplifier, the usable sensor resistance range is derived as

$$R_{\text{S,max}} = \frac{V_{\text{B}}}{\frac{V_{\text{B}}}{R_{\text{B}}} - \frac{V_{\text{DD}}}{2R_{\text{F}}}} \quad 2.4$$

$$R_{\text{S,min}} = \frac{V_{\text{B}}}{\frac{V_{\text{B}}}{R_{\text{B}}} + \frac{V_{\text{DD}}}{2R_{\text{F}}}}. \quad 2.5$$

R_S that is not in the range between $R_{S,min}$ and $R_{S,max}$ will saturate the AFE and thus is not usable. The sensor characterization setup does not need high resolution, so V_B is set to 100 mV for a large range. With R_F = 42.2 kΩ, R_B = 1.34 kΩ, and V_{DD} = 3.3 V, the usable range is 0.88 kΩ — 2.81 kΩ, which is wide enough to cover the process variation in the sensor array.

Figure 2.4(a) shows the applied magnetic field over time for characterizing the sensor MR. A sinusoidal field with an amplitude of 50 Oe and a frequency of 100 Hz is

applied first for 1 min to condition the sensors (remove magnetic domains). Then a dc field is swept from 0 Oe to +50 Oe to -50 Oe and finally back to 0 Oe, with a step size of 1 Oe/s. The AFE measures the sensor resistance simultaneously, as shown in Figure 2.4(b). This sensor has an R_0 of ~1.3 kΩ and a MR ratio of 7 – 9%. As a biosensor, the linear transfer curve around 0 Oe is of interest. The slope at H_A = 0 Oe represents the sensor sensitivity, which is measured to be ~0.9 Ω/Oe. The standard deviation of the transfer curve is ~1.6% that represents the sensor mismatch in single chip.

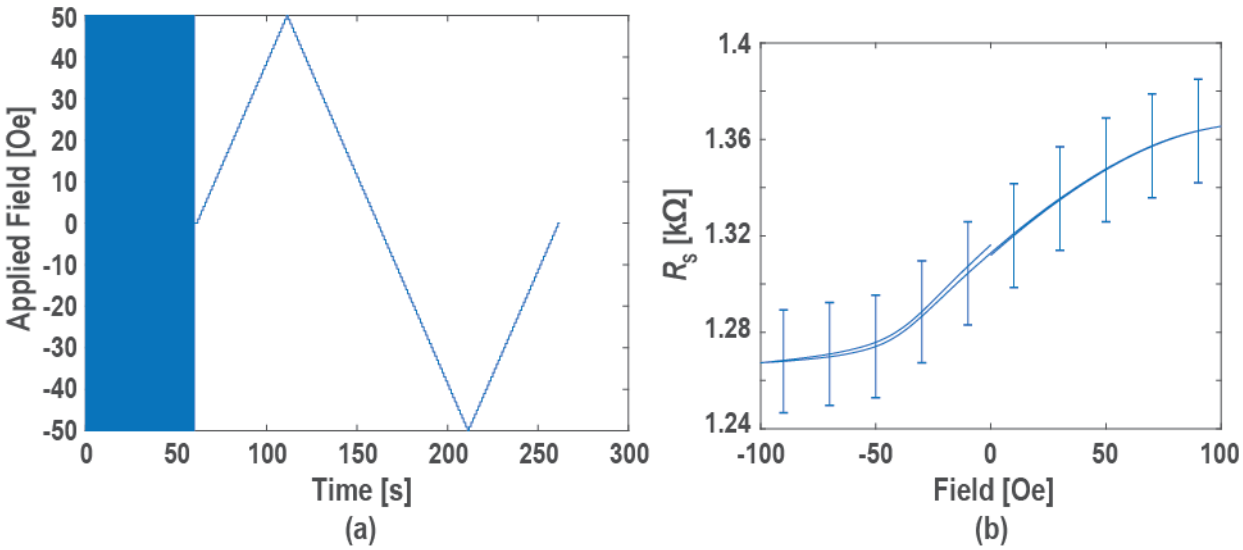

Figure 2.4 GMR sensor characterization

(a) Applied magnetic field over time and (b) measured sensor transfer curve.

The GUI shown in Figure 2.5 creates a user-friendly interface for people that are not familiar with electronics and programming. It can adjust the magnetic field sweep range, number of sweep cycles, etc. and show the real-time applied field and resulting MR transfer curve on the left figures. Test information that includes the error message is shown on the right bottom.

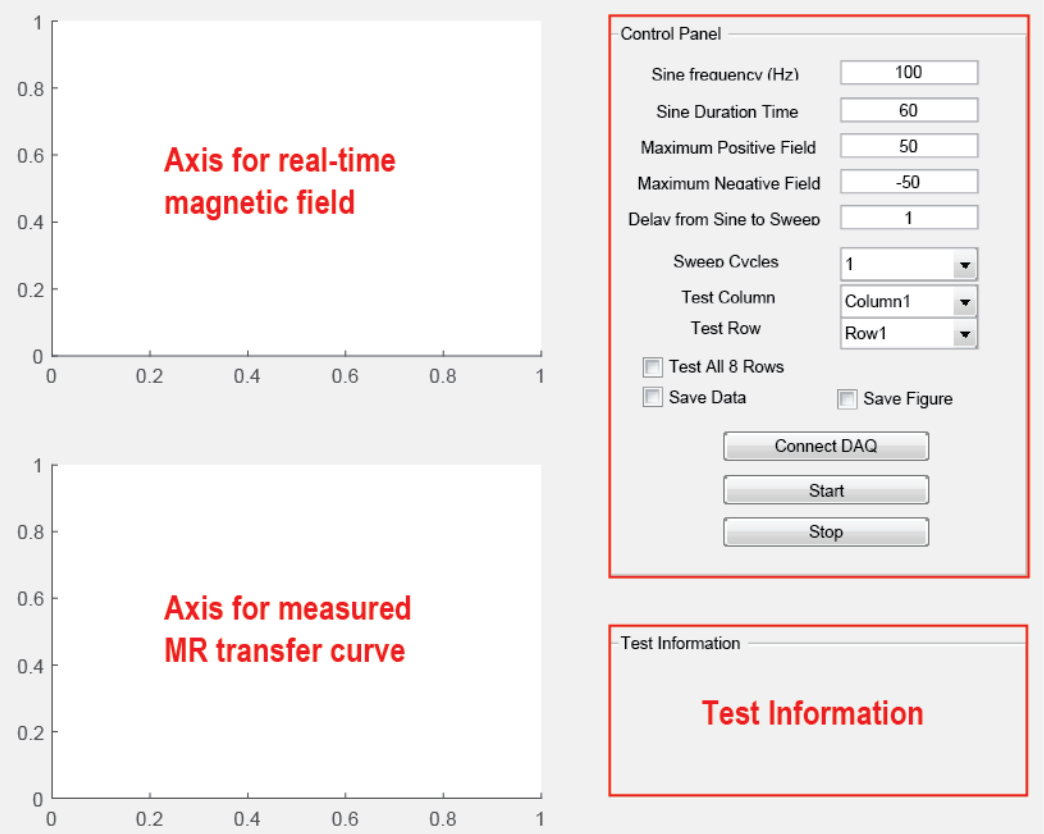

Figure 2.5 Graphical user interface for MR characterization

2.2.4 Noise

Another PCB was designed for measuring the sensor noise, as shown in Figure 2.6. For low noise readout, 9 sensors in a row are connected in parallel, which thus has 9× lower resistance than R_S. It is biased by a nickel-cadmium (Ni-Cd) battery, which provides negligible noise (~0.2 nV/√Hz) [91]. A current limiting resistor, R_B, which determines the bias current, I_B, is set larger than R_S to contribute a noise less than R_S. The resulting voltage, V_{in+}, and its low-pass filtered voltage, V_{in-}, are amplified by an instrumentation amplifier (IA, AD8429) and then measured by an ADC. The purpose of using a low-pass filter (LPF) here is to remove the dc bias, thus eliminating the offset between V_{in+} and V_{in-}, which can limit the IA gain. However, the LPF increases the settling

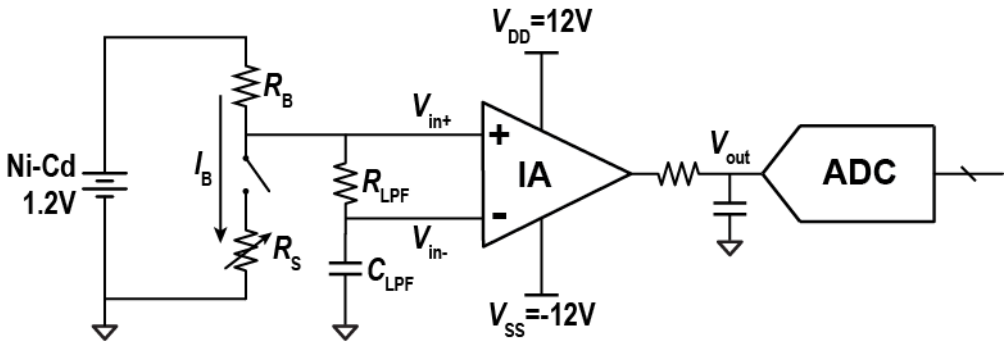

Figure 2.6 Schematic of the sensor AFE for noise measurement

time during sensor switching, and thus leads to a long readout time. The input-referred noise can be written as

$$v_{\mathrm{n,in}}^2 = \frac{v_{\mathrm{n,ADC}}^2}{G^2} + \left(\frac{R_\mathrm{B}}{R_\mathrm{S}+R_\mathrm{B}}\right)^2 v_{\mathrm{n,Rs}}^2 + \left(\frac{R_\mathrm{S}}{R_\mathrm{S}+R_\mathrm{B}}\right)^2 4k_\mathrm{B}TR_\mathrm{B} + \left(\frac{1+sR_\mathrm{S}C_\mathrm{LPF}}{1+s(R_\mathrm{S}+R_\mathrm{LPF})C_\mathrm{LPF}}\right)^2 4k_\mathrm{B}TR_\mathrm{LPF} + \left(\frac{(1+sR_\mathrm{S}C_\mathrm{LPF})R_\mathrm{LPF}}{1+s(R_\mathrm{S}+R_\mathrm{LPF})C_\mathrm{LPF}}\right)^2 i_{\mathrm{n,IA}}^2 \quad (2.6)$$

where k_B is Boltzmann's constant, T is the absolute temperature in Kelvin, $v_{n,ADC}$ is the noise contributed by the ADC, G is the IA gain, $v_{n,Rs}$ is the noise contributed by the sensor, and $i_{n,IA}$ is the current noise contributed from the IA. Equation 2.6 indicates that both the R_{LPF} noise and the IA noise are shaped by a very low frequency pole at $1/R_{LPF}C_{LPF}$ and a relatively higher frequency zero at $1/R_SC_{LPF}$, assuming that $R_{LPF} >> R_S$. Since the noise contributed by R_{LPF} and the IA is the lowest after the zero, C_{LPF} needs to be maximized. When the frequency is higher than the zero, Equation 2.6 can be simplified to

$$v_{\mathrm{n,in}}^2 = \frac{v_{\mathrm{n,ADC}}^2}{G^2} + \left(\frac{R_\mathrm{B}}{R_\mathrm{S}+R_\mathrm{B}}\right)^2 v_{\mathrm{n,Rs}}^2 + \left(\frac{R_\mathrm{S}}{R_\mathrm{S}+R_\mathrm{B}}\right)^2 4k_\mathrm{B}TR_\mathrm{B} + \frac{4k_\mathrm{B}TR_\mathrm{S}^2}{R_\mathrm{LPF}} + R_\mathrm{S}^2 i_{\mathrm{n,IA}}^2. \quad (2.7)$$

Assuming R_B = 1 kΩ, R_{LPF} = 50 kΩ, and C_{LPF} = 92 μF, the bias current I_B is ~1 mA and the zero is at ~10 Hz. G is set to 274 to reduce the ADC quantization noise and the IA is

selected so that both noises are lower than $4k_BTR_S$. Since R_B is 7× larger than R_S, this system is dominated by $v_{n,Rs}$. Therefore, the sensor 1/*f* noise can be observed if the 1/*f* corner frequency is >10 Hz.

The test setup was placed inside a Faraday cage to reduce electromagnetic interference (EMI). A resistor that has a similar resistance as the sensor was also measured for comparison, as shown in Figure 2.7. Although reduced by the Faraday cage, interference from the ac powerline and other instruments can still be observed. The slight difference between the resistor and the GMR sensor at 10 – 50 Hz indicates that the sensor 1/*f* noise corner frequency is <50 Hz.

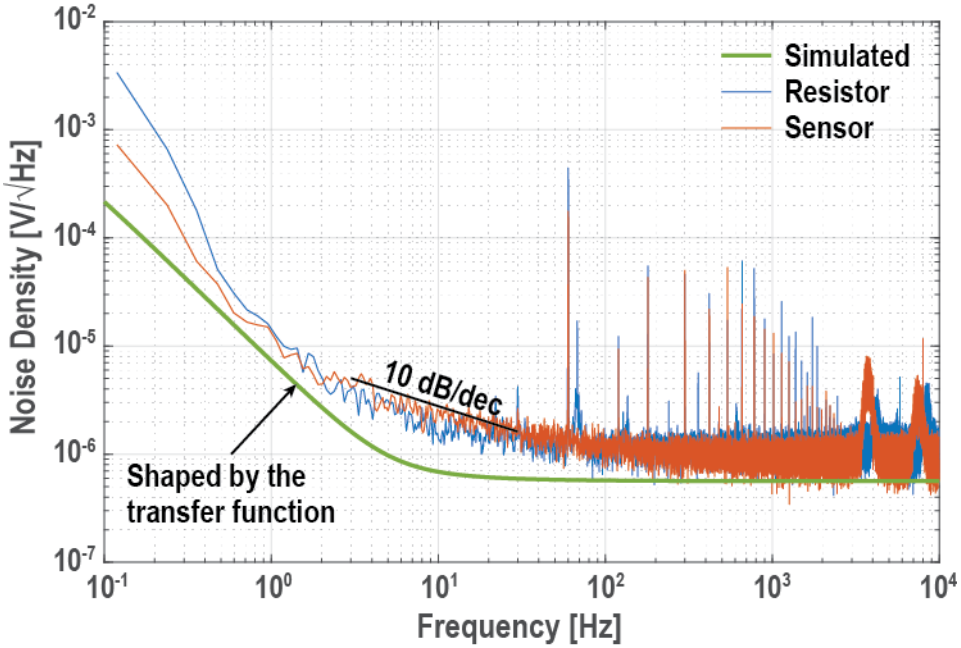

Figure 2.7 Simulated and measured noise spectra of a resistor and a GMR sensor

2.3 Magnetic Immunoassay

The GMR sensors measure the concentration of target biomarkers using a magnetic immunoassay (MIA). Figure 2.8 illustrates the steps in a MIA: 1) capture

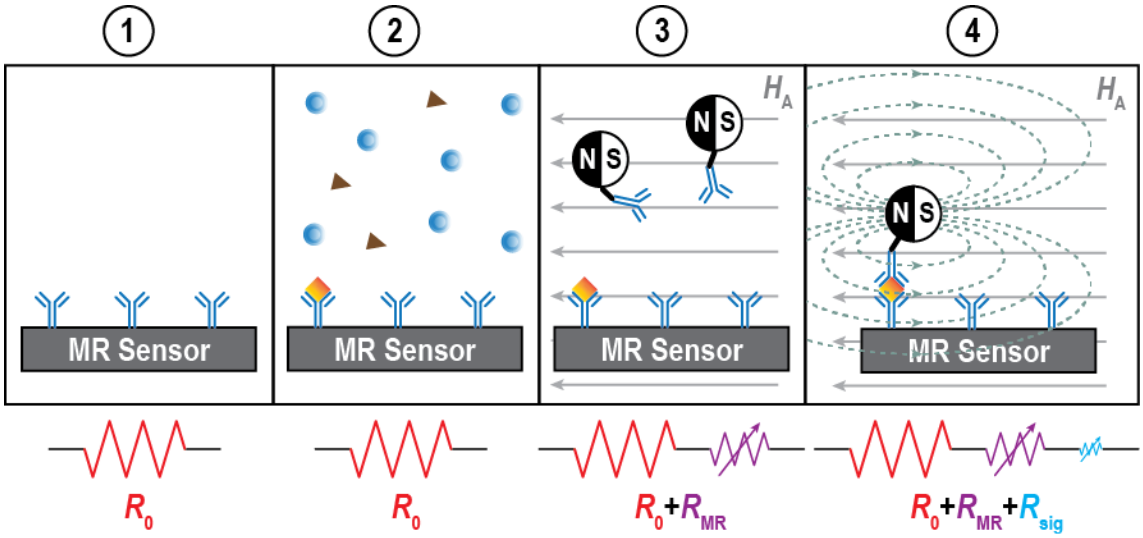

Figure 2.8 Magnetic immunoassay

antibodies are first immobilized on the sensor surface; 2) the sample is added and the target biomarkers bind to the immobilized capture antibodies; 3) MNP labeled detection antibodies are added and bind to the target biomarkers, thus generating a sandwich-like complex; 4) an external magnetic field is applied to polarize the tethered MNPs, which generate a stray field that is in the opposite direction of the applied field, H_A. The sensor resistance is $R_0 + R_{MR} + R_{sig}$, where R_{MR} and R_{sig} are the magnetoresistance from H_A and from the MNPs, respectively. Since R_{sig} is proportional to the number of tethered MNPs, it represents the concentration of the target biomarkers.

As shown in Figure 2.9, by assuming a single tethered MNP as a magnetic dipole, the signal induced by a MNP can be written as [55], [92]

$$\frac{R_{\mathrm{sig}}}{\mathrm{MNP}} = \frac{\partial R_S(H_A)}{\partial H} \cdot \frac{r_b^3}{3} \chi H_A \cdot \frac{1}{lwt} \int_{-\frac{l}{2}}^{\frac{l}{2}} \int_{-\frac{w}{2}}^{\frac{w}{2}} \int_{-\frac{t}{2}}^{\frac{t}{2}} \left(\frac{3(y-y_0)^2}{r^5} - \frac{1}{r^3} \right) dxdydz \qquad 2.8$$

where r_b is the MNP radius, χ is the volume susceptibility, H_A is the applied field, w is the sensor width, l is the sensor length, and t is the free layer thickness. r is the distance

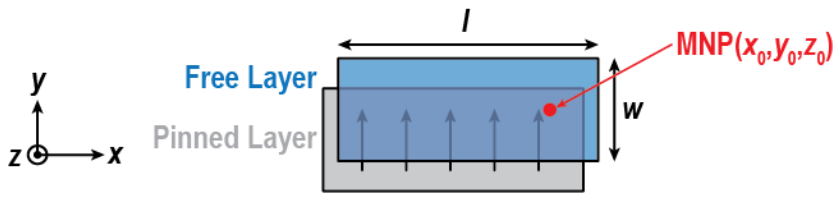

Figure 2.9 Sensor top view for MNP signal analysis

between the MNP (x_0,y_0,z_0) and a point of free layer (x,y,z) and can be written as $\sqrt{(x-x_0)^2+(y-y_0)^2+(z-z_0)^2}$, where z - z_0 = d that is the distance between the MNP and the sensor free layer. Equation 2.8 indicates that larger MNPs and smaller sensor gives larger signal. However, large-sized MNPs (micrometers) diffuse slowly in solution and are much larger than the target biomarkers, thus requiring washing steps to remove unbound MNPs and have a longer assay time [14]. Smaller sensors reduces the biological dynamic range, unless increasing the number of sensors in an array which complicates the design and increases the assay time [16]. Larger H_A increases the MNP magnetic moment but reduces the sensor sensitivity when it enters the nonlinear range. An optimal H_A can be found by measuring the signal amplitudes at different H_A [73]. The signal is inversely proportional to d^3, thus the unbound MNPs are too far away to be detected, which improves the specificity of the magnetic sensing and enables wash-free detection.

The MNPs used primarily in this work (Streptavidin microbeads, catalog # 130-048-101, Miltenyi Biotec and catalog # SHS-30-01, Ocean Nano-Technologies) have a core size of 30 – 50 nm and each sensor size is 125 × 125 μm^2. The optimal H_A is calibrated to be ~30 Oe. The distance is ~50 nm, which includes the oxide thickness of the sensor and the height of the sandwich complex. This results in a signal per MNP of 1 – 10 μΩ. Compared with an R_0 of 1.3 kΩ and an R_{MR} of 27 Ω, R_{sig} is very small, which becomes a major challenge in magnetic sensing.

2.4 Magnetic Sensing Techniques

There are two common detection techniques that can be used with the surface-based affinity assays: magnetometry and magneto-relaxometry (MRX), both of which are illustrated in Figure 2.10. In the absence of a magnetic field, the magnetic moments of the MNPs are randomly distributed resulting in zero net field for the underlying sensors. When an external magnetic field (dc or ac) is applied, the magnetic moments all align with the field generating a stray magnetic field that opposes the applied field at the sensor. Magnetometry measures the field difference with and without MNPs to quantify the number of tethered MNPs. For MRX, the applied magnetic field is rapidly removed, and the sensors temporally monitor the change in magnetic field as the MNPs slowly randomize capturing the dynamics.

2.4.1 Magnetometry

As the most straightforward method to detect MNPs, magnetometry-based biosensing was widely used by oscillator-based sensors [48], [49], [64], [65], Hall-effect sensors [66]–[68], and GMR sensors [52]–[57], [71]–[74]. However, this technique suffers from several drawbacks. First, the minute signal from the MNPs (μΩs) is superimposed on a large baseline signal (kΩs) from the applied field demanding very high dynamic range from the readout circuitry. This baseline can be rejected by a reference sensor, if one is able to achieve good matching between the sensors, which unfortunately is not always possible. Second, this technique requires a uniform external field to remove positional dependency, especially in low-concentration measurements. This is often accomplished using an off-chip electromagnet or a special structure for an on-chip coil

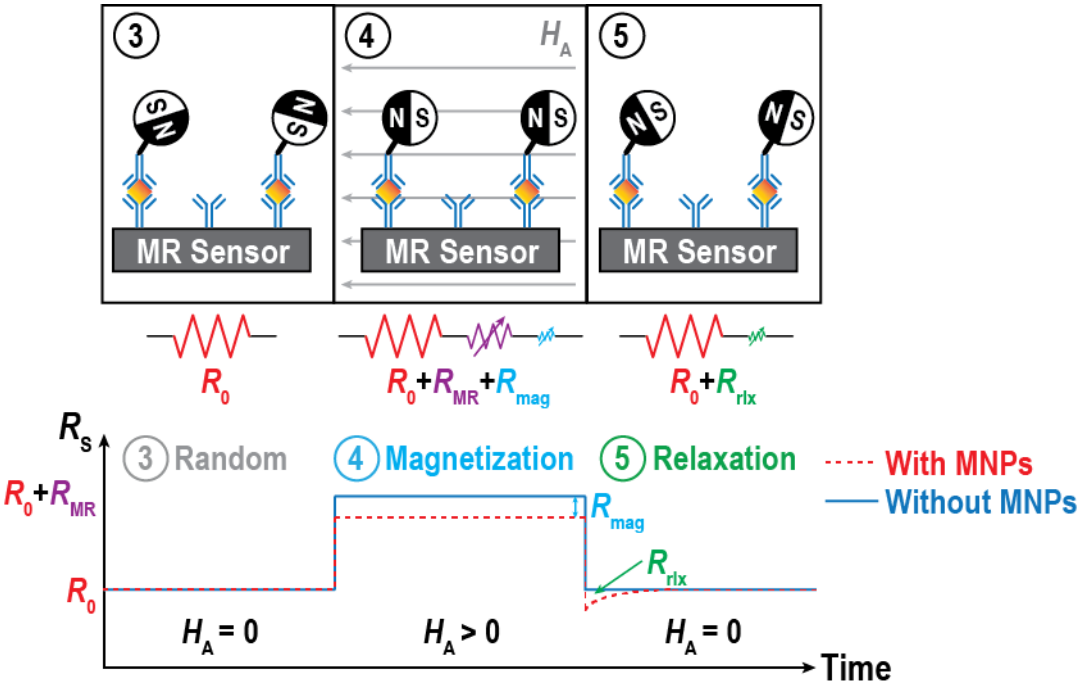

Figure 2.10 Magnetometry vs. MRX

Magnetometry measures R_{mag} at step 4 and MRX measures R_{rlx} at step 5.

[49]. Lastly, magnetometry is sensitive to temperature drift, process variation, and environmental perturbation that requires precise calibration and signal processing to overcome [73].

2.4.2 Magneto-Relaxometry

MRX-based biosensing technique resolves most of these issues. While there is no literature for oscillator-based sensors using relaxometry, Hall-effect sensors [50], [51], [69], [70] and GMR sensors [75]–[77] have been demonstrated. By detecting the relaxation of the MNPs temporally after turning off the applied field, this technique pushes the difficulty from accuracy in amplitude to accuracy in time. It accordingly overcomes the small signal-to-baseline ratio and eases the field uniformity requirement. Furthermore, techniques such as magnetic correlated double sampling (MCDS) that repeat the

relaxation and use the same sensor for correlated sampling remove the need for reference sensors and are immune to slowly changing environmental perturbations [51], [76]. Since different sized MNPs have different relaxation times and dynamics, MRX introduces another degree of freedom that enables multiplexed bioassays [69], [77].

However, MRX-based biosensing has drawbacks that still need to be investigated. First, the applied magnetic field cannot collapse instantaneously resulting in a deadzone that makes detection of MNPs with very fast relaxation times impossible. Off-chip electromagnets have been reported to have deadzone as low as 1.4 μs, which is still not fast enough to detect some MNPs [76], [77]. On-chip striplines can reduce the deadzone to just 16 ns [50], but suffer from area and device heating constraints [70]. From a signal to noise ratio (SNR) point-of-view, the relaxation signal decreases over time, thus covers a relatively wide bandwidth including the low frequency band that is vulnerable to 1/*f* noise. Moreover, high-speed readout circuitry is usually required to capture the fast-decaying signal. As a result, low noise and high speed are both required for the readout circuitry, but they are often at odds with each other.

2.4.3 Comparison between Magnetometry and Relaxometry

A comparison between these techniques is summarized in Table 2.1. MRX relaxes AFE DR requirement and applied field uniformity requirement by measuring the signal without the applied field, as well as rejects the environmental perturbation by sensor self-referencing. However, it suffers from more 1/*f* noise and requires longer readout time since it needs steps 3—5 while magnetometry only needs step 4. It also requires a high speed AFE and electromagnet to capture the fast relaxation signal from the MNPs.

Table 2.1 Comparison between magnetometry and magneto-relaxometry

	Magnetometry	Magneto-relaxometry
Baseline	High	Low
AFE DR	High	Low
H_A uniformity	High	Low
Sensor self-referencing	No	Yes
Temperature drift cancellation	No	Yes
Noise	Low	High
Readout speed	Fast	Slow
AFE speed	Low	High

2.5 Magnetic Sensor Front-End

2.5.1 Figure-of-Merit

To fairly compare the performance of different magnetic sensor AFEs, a figure-of-merit (FoM) is required. Since a magnetic sensor FoM was not presented in prior work, to the best of the author's knowledge, the FoM is adopted from temperature sensor prior art by changing the temperature resolution (in units of Kelvin) to the magnetic field resolution (in units of Tesla) [93]–[95]. Thus, the FoM is

$$FoM = Resolution^2 \cdot \frac{Energy}{Conversion} = Int.Noise^2 \cdot Readout\ Time \cdot Power, \quad (2.9)$$

in units of $nT^2 \cdot mJ$. According to Table 2.1, MRX tends to have a worse FoM than magnetometry due to longer readout time and higher integrated noise.

2.5.2 Prior Arts

Several architectures have been presented to measure the signal from magnetic sensors, either in magnetometry or in MRX. A Wheatstone bridge is the most commonly used technique in magnetometry, where two active sensors and two reference sensors or resistors form the bridge, as shown in Figure 2.11(a) [96]–[98]. An instrumentation amplifier followed by an ADC captures the differential signal. This technique ideally eliminates all common-mode baseline signals (R_0 and R_{MR}) and the output is proportional to R_{sig}. However, sensor mismatch, ΔR_0 and ΔR_{MR}, eat into the dynamic range. Therefore, the gain, G, must be reduced by $(\Delta R_0 + \Delta R_{MR})/R_{sig}$ to accommodate the mismatch and thus decreases the resolution by 10^2 – 10^5× for a 10% mismatch.

The double modulation scheme, shown in Figure 2.11(b), applies a sinusoidal excitation (either a voltage or current) at frequency f_C and a sinusoidal magnetic field at

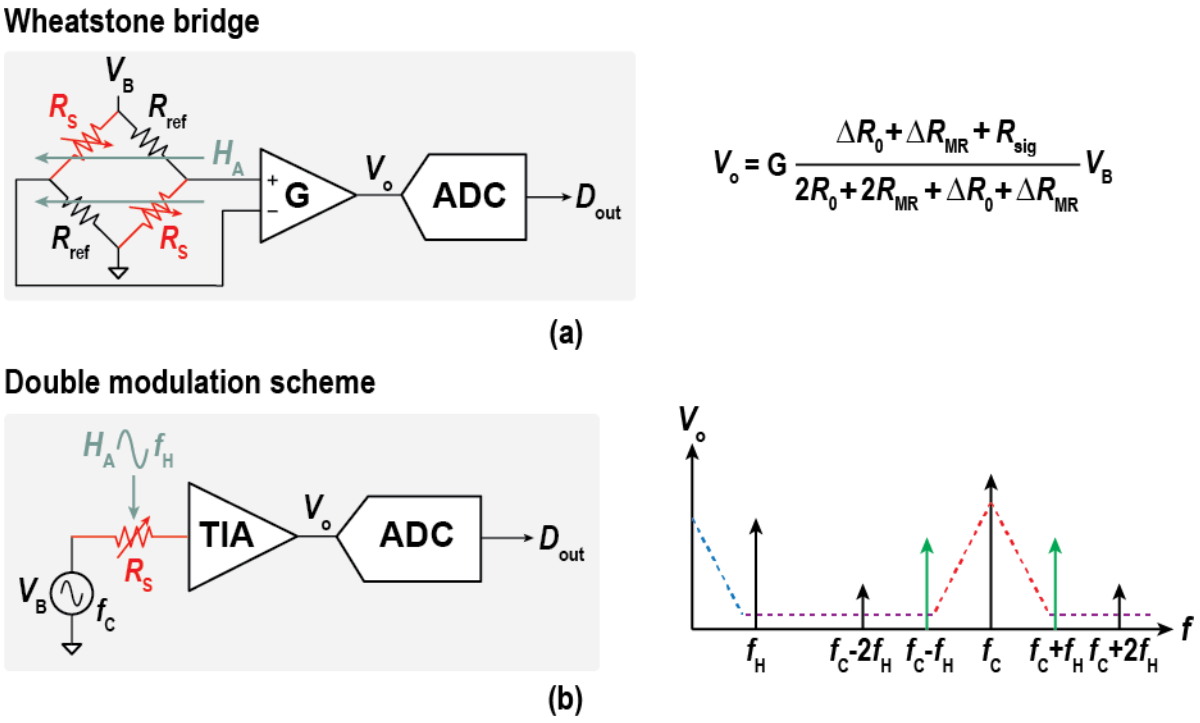

Figure 2.11 Prior magnetometry-based AFEs

frequency f_H to the sensor [52], [56]. This "*double modulation*" scheme spectrally separates the resistive (*i.e.* R_0 at f_C) and magnetoresistive components (*i.e.* R_{MR} and R_{sig} at $f_C \pm f_H$) of the signal. There are several benefits to this technique, namely the R_0 baseline can be reduced using excitation/carrier suppression, lock-in detection enables a very narrow noise bandwidth, and 1/*f* noise can be partially removed provided that f_H is at a higher frequency than the 1/*f* noise corner frequency [56]. (Note that some of the 1/*f* noise is of magnetic origin and thus not mitigated by this technique.) However, the signal at $f_C \pm f_H$ still contains the R_{MR} baseline, which can be 100× larger than R_{sig}. Moreover, the modulation scheme requires a higher bandwidth ADC and signal processing algorithms for demodulation.

MRX-based AFEs have only been reported for Hall-effect sensors, to the best of the author's knowledge. In Figure 2.12(a), a programmable gain amplifier (PGA) was used to amplify the signal [50]. To maximize the PGA gain, a 16b DAC was designed to continuously cancel the sensor offset, which is equivalent to the R_0 baseline for MR

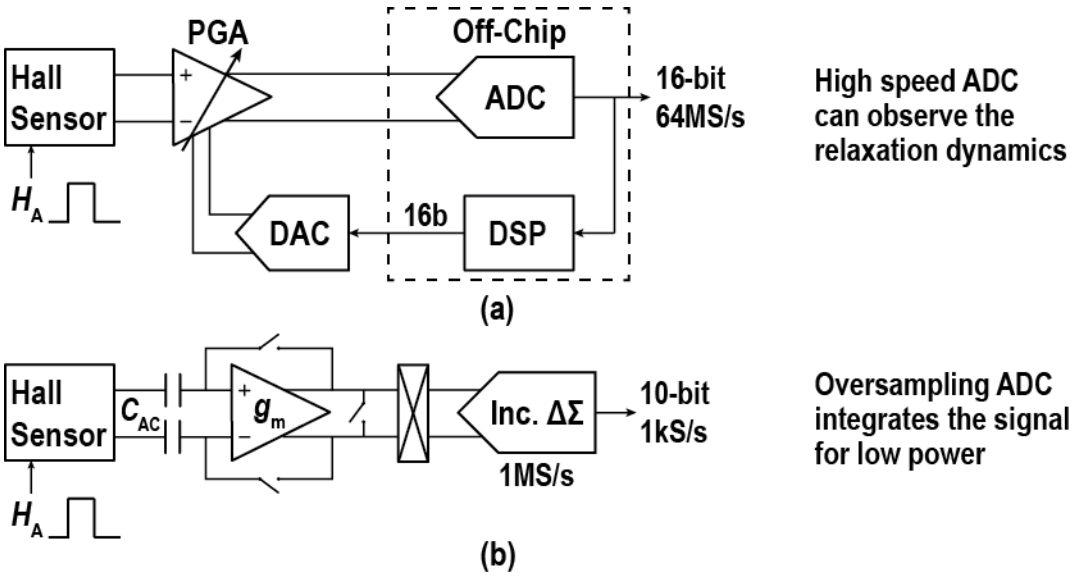

Figure 2.12 Prior MRX-based AFEs

sensors. An off-chip high-speed ADC measured and reproduced the fast relaxation curve of the MNPs. Instead of using a high-performance ADC, Figure 2.12(b) used an incremental ΔΣ ADC to integrate R_{rlx} during the relaxation phase, thus significantly reducing the power consumption but paid the penalty of losing the capability of observing the relaxation dynamics [51]. Ac coupling capacitors, C_{AC}, reject the sensor offset, thus simplify the design.

Table 2.2 Comparison table of magnetic sensor AFEs

	H. Wang ISSCC'09 [48]	D.A. Hall JSSC'13 [56]	T. Costa TBCAS'17 [53]	S.J. Han ISSCC'07 [52]	P. Liu JSSC'12 [50]	S. Gambini JSSC'13 [51]
Sensor Type	LC	GMR	GMR	GMR	Hall	Hall
Sensor R_0 (kΩ)	N/A	1.92	0.85	N/A	N/A	N/A
MR Ratio (%)	N/A	9.2	5.37	N/A	N/A	N/A
MNP Size (nm)	1,000	50	250	50	1,000	1,000
Sensing Method	Magneto	Magneto	Magneto	Magneto	MRX	MRX
AFE Architecture	LC oscillator	TIA	Amplifier	Mixer + PGA	PGA	V/I Converter
ADC Architecture	VCO-based	ΔΣ	No ADC	No ADC	No ADC	Inc. ΔΣ
Input-referred Integrated Noise (nT_{rms})	N/A	49	11.5Ψ	N/A	15Ψ	1207.5
Readout Time/Ch. (ms)	400	250	1,000	250	64,000	50
Power/Ch. (mW)*	N/A	3.15	4.9Ψ	N/A	6.2Ψ	0.825
Area/Ch. (mm^2)	N/A	0.219	3.17	N/A	N/A	0.012
Number of Ch	8	16	1	4	1	160
Input-referred Baseline (mT)	N/A	7.09	1.84	N/A	<0.001	0.007
Temperature Correction	Yes	Yes	No	Yes	Yes	Yes
Resolution FoM ($nT^2 \cdot mJ$)	N/A	1891	648Ψ	N/A	89280Ψ	60143

* Power/Ch does not include sensor bias and magnetic field generator. Ψ Does not include ADC.

2.5.3 Comparison and Discussion

The state-of-the-art CMOS AFEs for magnetic sensors is summarized in Table 2.2. It should be mentioned that the sensor bias current is highly dependent on the sensor (namely R_0) so it is excluded from the power consumption. It can be observed that although MRX-based AFEs provided >260× improvement in the input-referred baseline, they still have a 32× worse FoM compared to magnetometry-based AFEs. The state-of-the-art reported FoMs are from T. Costa and D. A. Hall, without and with ADCs, respectively [53], [56]. Therefore, the target of this dissertation is to design a CMOS AFE for GMR sensors that achieves the best FoM, while keeping the baseline small.

2.6 A Discrete 8 Channel GMR Biosensing System

2.6.1 System Overview

A custom PCB was designed to conduct MIA experiments using GMR sensors, as shown in Figure 2.13. The National Instruments DAQ (NI-6361) contains 8 ADCs and 2 DACs. One DAC provides a bias voltage, V_B, for the sensor and the other DAC generates the control signal, V_{coil}, for the power amplifier (PA, Kepco BOP 20-5), which supplies a current, I_{coil}, to the Helmholtz coil. The Helmholtz coil generates a homogeneous magnetic field for the sensor chip placed inside. A reference generator creates $V_{in} = V_{cm} + V_B$ and $V_{inb} = V_{cm} - V_B$ to bias the sensors. The resulting currents are amplified by 8 TIAs and quantized by the ADCs in the DAQ. A single channel AFE was discussed (Figure 2.3).

Figure 2.14 shows the sensor array connection to the multi-channel AFE. Each sensor row is directly connected to a TIA input. However, only 1 out of the 10 columns is

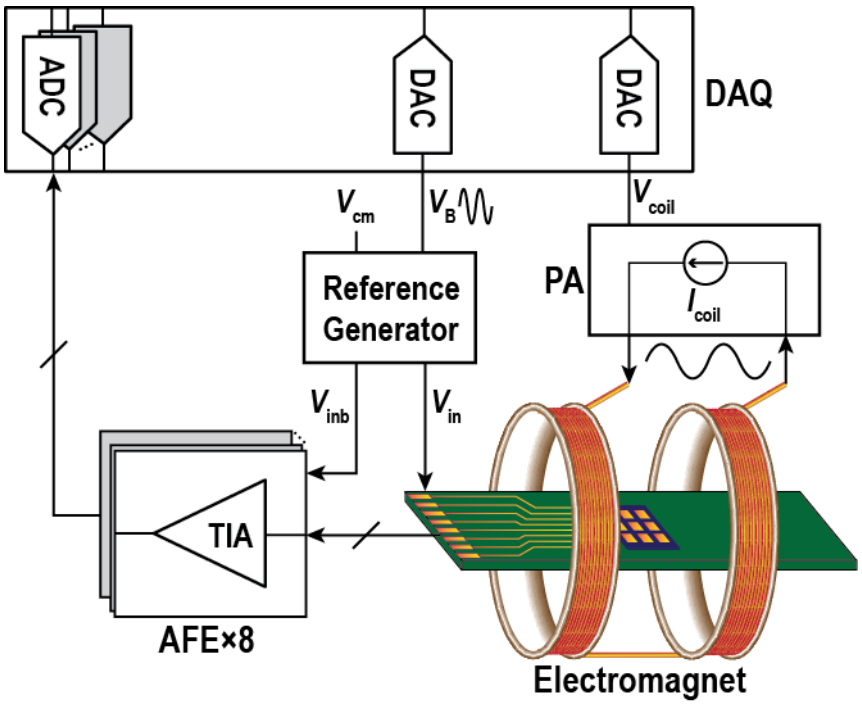

Figure 2.13 System architecture

connected to V_{in} at a time, while the others are connected to V_{cm} (and thus shorted). Time division multiplexing (TDM) is applied to read all sensors in a round robin fashion. The equivalent schematic of a single channel is illustrated in Figure 2.15. Assuming $R_{S1} = R_{S2} = \ldots = R_S$, the input-referred noise can be written as

$$v_{n,in}^2 = 10v_{n,Rs}^2 + \left(\frac{R_S}{R_B}\right)^2 4k_B T R_B + \left(\frac{R_S + 10R_B}{R_B}\right)^2 v_{n,op}^2 \qquad 2.10$$

where $v_{n,Rs}$ is the sensor noise and $v_{n,op}$ is the op-amp input-referred noise. Since R_B needs to be as close to R_S as possible to maximize the gain, by assuming $R_B = R_S$, the equation can be further simplified to

$$v_{n,in}^2 = 11v_{n,Rs}^2 + 11^2 v_{n,op}^2. \qquad 2.11$$

Therefore, it can be concluded that this sensor network increases the sensor noise by $\sqrt{11}\times$ and the op-amp noise by $11\times$.

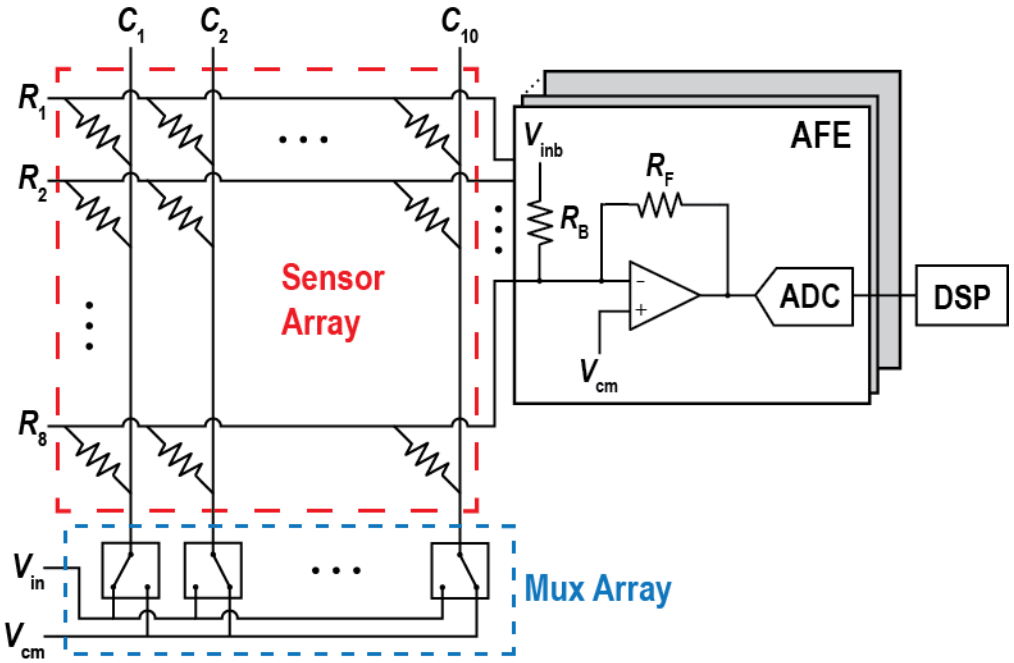

Figure 2.14 Sensor array network

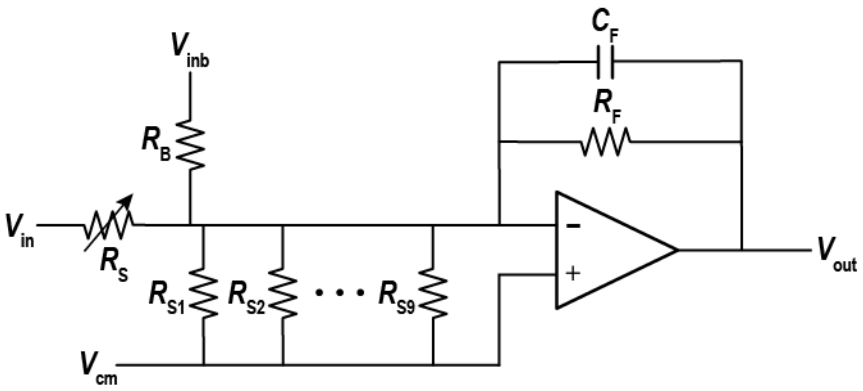

Figure 2.15 Equivalent schematic of a single channel

Figure 2.16 shows the schematic of the reference generator, which consists of a voltage adder and a voltage subtractor. The resistors used in both blocks are the same (1 kΩ). The common-mode voltage, V_{cm}, which is set to $V_{DD}/2$, is implemented by a resistor divider followed by a unity-gain buffer.

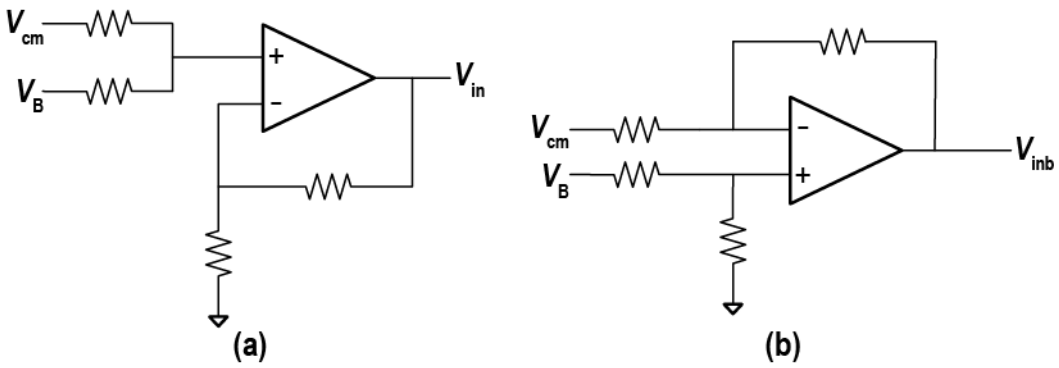

Figure 2.16 Schematic of the reference generator

(a) Voltage adder and (b) voltage subtractor.

2.6.2 Signal Processing

To measure the signal from tethered MNPs, the double modulation scheme is used to reject 1/*f* noise from both the sensor and the electronics. Specifically, a sinusoidal V_B is applied at frequency f_C and another sinusoidal I_{coil} is applied to the Helmholtz coil to generate an ac magnetic field at frequency f_H. The resulting current can be written as

$$I_B = \frac{V_B}{R_S} = \frac{V_0 \cos(2\pi f_C t)}{R_0 + \Delta R cos(2\pi f_H t)} \tag{2.12}$$

$$= \frac{V_0 \cos(2\pi f_C t)}{R_0}\left(1 - \left(-\frac{\Delta R}{R_0}\cos(2\pi f_H t)\right) + \left(-\frac{\Delta R}{R_0}\cos(2\pi f_H t)\right)^2 - \cdots\right)$$

where V_0 is the amplitude of V_B (400 mV in this work), f_C is the frequency of V_B (540 Hz), and f_H is the frequency of the applied field (210 Hz). The side tones that contain the MR signal are evenly distributed on both sides of f_C, as shown in Figure 2.17(a). Since the amplitudes of the side tone harmonics are decreasing, the first side tone at f_C - f_H is used for lock-in detection. Specifically, the amplified voltage V_{out} is quantized by the ADC at a sampling rate of 2 kS/s for 0.5 s. FFT demodulation is applied to the output data D_{out}, as shown in Figure 2.17(b). The 10,000 data points per window are digitally down modulated

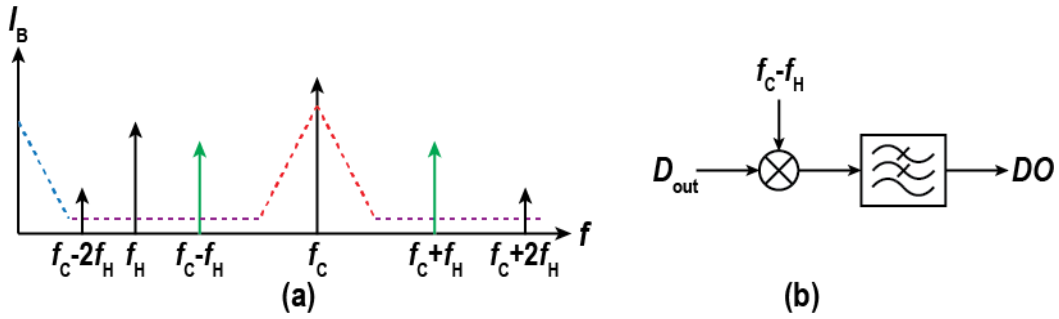

Figure 2.17 Illustration of the double modulation scheme

(a) Spectrum of the sensor current and (b) illustration of the DSP-based lock-in detection.

and low-pass filtered, resulting in one output, *DO*, that represents the amplitude of the side tone at f_C - f_H. Accordingly, the bandwidth is reduced to 2 Hz, which leads to a low noise readout.

2.6.3 Measurement Results

Figure 2.18 shows a photograph of the measurement setup. The sensor chip is placed in a 3D-printed chip holder that is connected to the AFE through a ribbon cable. A LabVIEW interface is programmed to configure the AFE and plot the real-time data.

The system noise is first characterized, as shown in Figure 2.19. An unfunctionalized (bare) sensor chip was used to collect a 40 min time series dataset and an FFT was applied to extract the noise spectrum. Figure 2.19(a) shows that there is no difference between the active sensors and reference sensors, and Figure 2.19(b) indicates that the noise is white. The total integrated noise was measured to be 134 nT_{rms}.

Biological experiments were then conducted to validate the system performance. The sensors were functionalized with biotinylated-bovine serum albumin (Biotin-BSA) as a positive control, a captured antibody towards human interleukin-6 (IL-6), a cancer biomarker, and bovine serum albumin (BSA) for use as a negative control to monitor non-

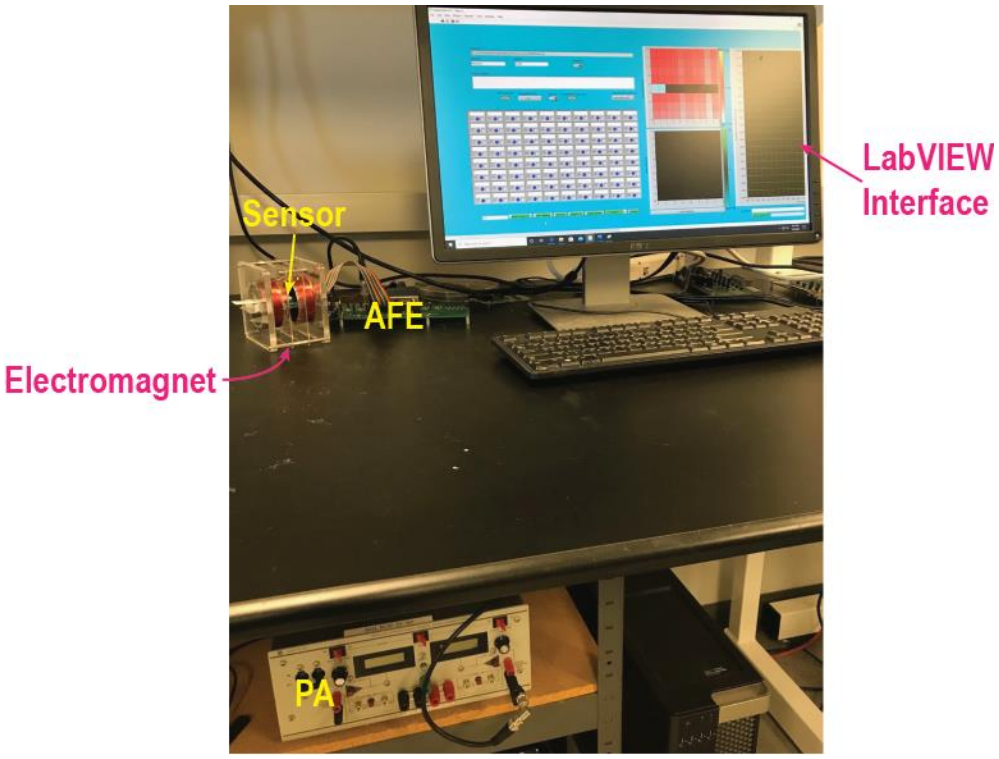

Figure 2.18 Photograph of the test bench

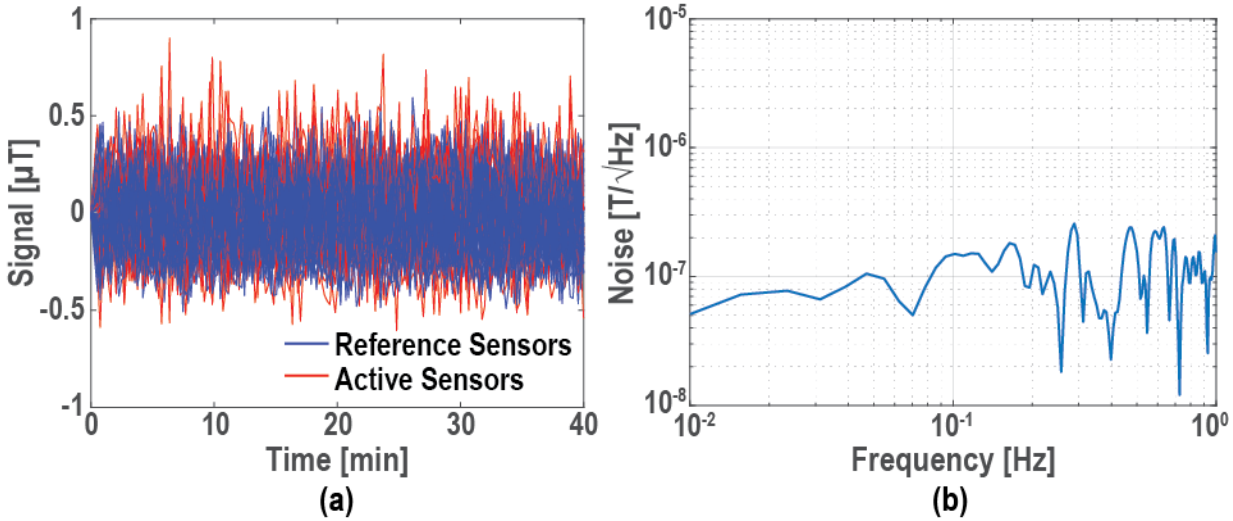

Figure 2.19 Measured noise of the system

(a) Transient results and (b) noise spectrum.

specific binding. The reference sensor was covered by epoxy, which prohibits MNP binding/interaction. To functionalize the sensor surface with the BSA or IL-6 antibodies, chips were washed with acetone, methanol, and isopropyl alcohol (IPA). After 5 minutes

of cleaning with oxygen plasma, 1% Poly(allylamine) in distilled water (DIW) was added for 5 minutes. After baking for 1 hour at 110 °C, 2% aqueous Poly(ethylene-alt-maleic anhydride) in DIW was added for 5 minutes. Finally, the chips were baked for 1 hour at 160 °C. Capture reagents were spotted on the sensors and incubated at 4 °C overnight.

Figure 2.20 shows overlaid measurement results for the negative control, positive control, and IL-6 sensors. The sensors were washed with phosphate buffered saline (PBS) before adding MNPs (Streptavidin microbeads, catalog number #130-048-101, Miltenyi Biotec). The system measured the real-time binding curves at a sampling rate of 0.1 S/s. Each readout takes 0.5 s for data capture and another 0.5 s for data processing. 10 readouts are required to complete the whole sensor array and thus the total acquisition time is 10 s. After the binding curves saturated, the chip was washed to remove any non-specific binding. The unchanged signal amplitudes indicate the binding is highly specific.

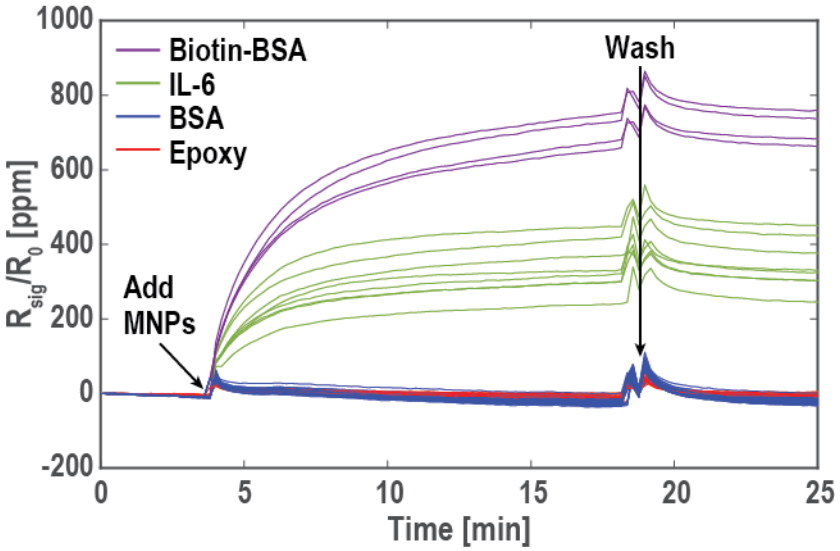

Figure 2.20 MIA experiment result

2.7 Summary

In this chapter, the GMR sensors that are used in the remainder of this dissertation were discussed and characterized. A MIA, which detects specific biomarkers for *in-vitro* diagnostics, was presented and the signal from a single magnetic tag was calculated. While a small signal to baseline ratio is a big challenge in MR biosensing, previously reported architectures and different sensing techniques were discussed and compared. A magnetic sensor FoM was described to evaluate and compare the performance of the sensor AFEs. Lastly, a discrete 8 channel sensor front-end and system was designed to conduct MIA experiments. A double modulation scheme and lock-in detection were applied to minimize the integrated noise. While this setup has been actively used for MIA experiments [99], it was also successfully expanded for other applications, such as sensor characterization and magnetic flow cytometry [100], [101].

Chapter 2, in part, is based on materials from Xiahan Zhou, Chih-Cheng Huang, and Drew A. Hall, “Magnetoresistive Biosensors for Quantitative Proteomics,” *Proceedings of SPIE Optics + Photonics*, San Diego, CA, Aug. 6-10, 2017 [16], and Xiahan Zhou, Michael Sveiven, and Drew A. Hall, “A CMOS Magnetoresistive Sensor Front-End with Mismatch-Tolerance and Sub-ppm Sensitivity for Magnetic Immunoassays,” *IEEE Transactions on Biomedical Circuits (TBioCAS)*, Dec 2019 [57]. The dissertation author was the primary investigator and author of this paper.

Chapter 3. A CMOS GMR SENSOR FRONT-END ACHIEVING SUB-PPM SENSITIVITY

3.1 Introduction

In the context of the MIA, as MNPs become tethered to the sensor surface through binding events [102], the resistance increases from R_0 (with $H_A = 0$) to $R_0 + R_{MR} + R_{sig}$ following Langmuir binding kinetics and thus is proportional to the number of captured antigen (Figure 3.1). As discussed in the last chapter, the tethered MNPs generate an incredibly small R_{sig} (μΩ – mΩ) that is on top of R_{MR} (1 – 100 Ω) and R_0 (0.1 – 5 kΩ). Thus, R_{sig} is often 10^3 – 10^6× smaller than R_0. This makes the readout circuit design challenging since it requires an AFE with more than 120 dB of DR. While the double modulation scheme and a bleed resistor were applied to reduce the R_0 baseline, R_{MR} baseline still limits the performance. A reference sensor can be used to reject the R_0 and R_{MR} baselines further, but is ultimately limited by the sensor mismatch, in both R_0 and R_{MR}. GMR sensor arrays usually have up to 10% mismatch, even intra-chip, due to fabrication challenges around the uniformity of the thin film stack [103].

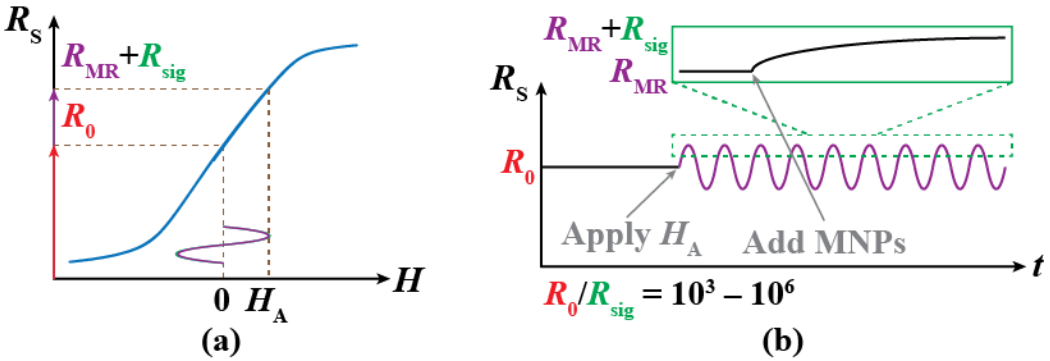

Figure 3.1 Illustration of sensor response in a MIA

(a) MR sensor transfer curve and (b) MR sensor response in a MIA with a sinusoidal H_A.

To address this, this chapter presents a CMOS architecture for GMR sensor arrays that is tolerant of up to 10% sensor mismatch. The resulting AFE and ADC achieves state-of-the-art performance with sub-ppm sensitivity, an input-referred noise power spectral density (PSD) of 46.4 nT/√Hz, an input-referred baseline less than 0.235 mT, and a readout time of 11 ms.

3.2 System Architecture

A new MR sensor front-end is reported, as shown in Figure 3.2, to improve tolerance of sensor mismatch and relax the DR requirement. The AFE contains three main blocks: sensor bias, a PGA with gain G, and an ADC with a decimation filter and high-frequency interference rejection (HFIR) sampling. The AFE works as follows: A sinusoidal bias current, I_{in}, is applied to the selected active sensor, R_S, and a reference sensor, R_R. Compared to using a voltage bias, current bias is spectrally purer and was thus chosen in this work [56]. Meanwhile, a sinusoidal magnetic field, H_A, generated from an off-chip Helmholtz coil is applied to both sensors. After buffering, the voltage at nodes V_S and V_R is

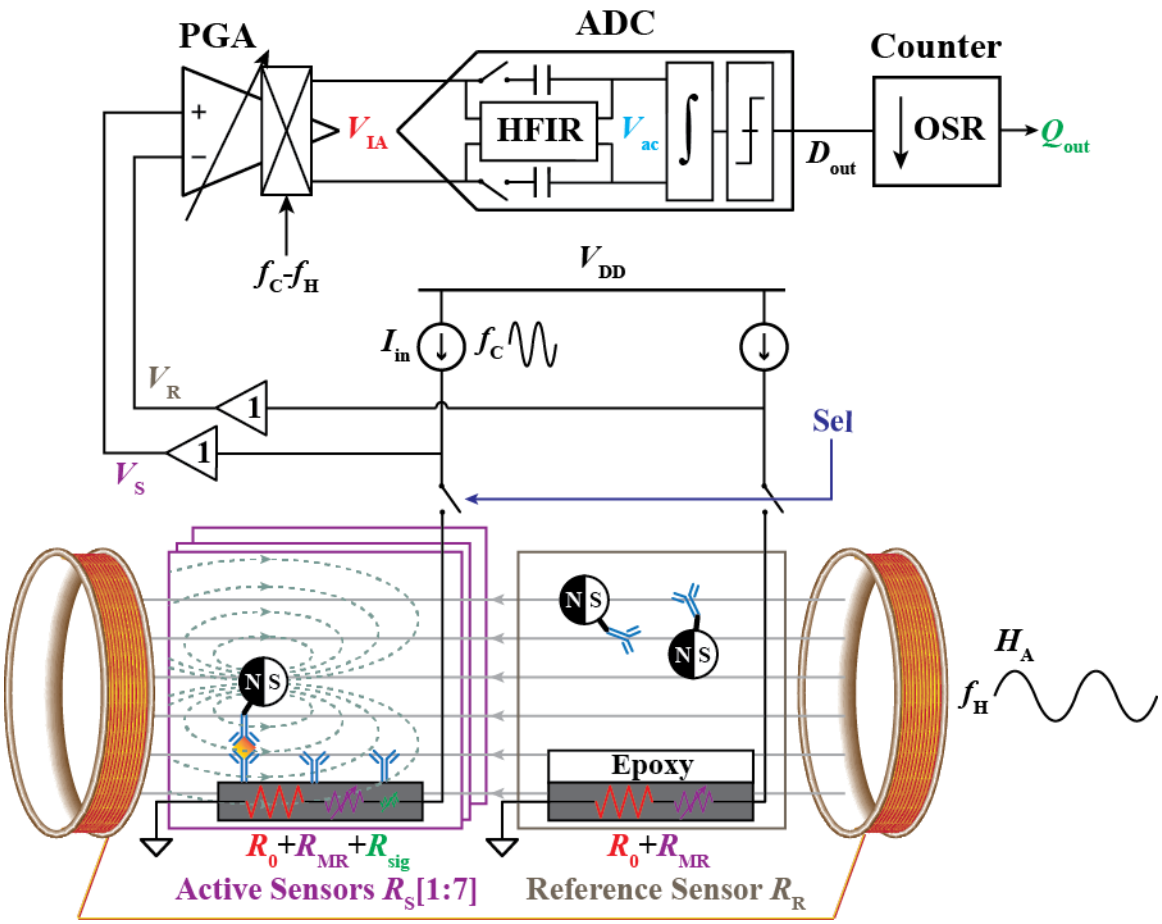

Figure 3.2 System architecture

$$V_{S,R} = I_0 R_0 + I_0 R_{MR} \sin(2\pi f_H t) + \Delta I R_0 \sin(2\pi f_C t) + \left[\frac{\Delta I (R_{MR} + R_{sig})}{2}\right] \sin(2\pi (f_C \pm f_H) t) \quad 3.1$$

where I_0 and ΔI are the dc and ac components of the bias current, respectively, R_0 and R_{MR} are the nominal resistance and magnetoresistance of the active and reference sensor, respectively. In this design, the carrier frequency, f_C, is 100 kHz and the magnetic field frequency, f_H, is 10 kHz, which is limited by the external power amplifier. The reference sensor is covered by epoxy that prevents MNP binding, thus there is no R_{sig} detected by R_R. Furthermore, since R_R is on the same die as the sensor array (R_S[1:7]),

it rejects common-mode environmental perturbations such as temperature drift removing the need for complicated temperature correction routines [73].

Spectra at nodes V_S and V_R are illustrated in Figure 3.3(a). Based on Equation 3.1, although R_{sig} has been modulated away from R_0 through the double modulation scheme, R_{MR} is still at the same frequency as R_{sig}. With perfect matching between R_S and R_R (*i.e.* $R_{MR,s} = R_{MR,r}$ and $R_{0,s} = R_{0,r}$), the PGA eliminates both common-mode baselines, amplifies R_{sig}, and downmodulates the signal from f_C - f_H to dc. Thus, the voltage at node V_{IA} is

$$V_{\mathrm{IA}} = \frac{G\Delta I R_{\mathrm{sig}}}{2} + \left(\frac{G\Delta I R_{\mathrm{sig}}}{2}\right)\sin(2\pi 2 f_{\mathrm{H}} t). \tag{3.2}$$

Although Equation 3.2 indicates that high gain should be used to amplify the small signal, sensor mismatch limits it. Consider that R_S and R_R have R_0 mismatch where $\Delta R_0 = R_{0,s} - R_{0,r}$ and MR mismatch where $\Delta R_{MR} = R_{MR,s} - R_{MR,r}$. The voltage at node V_{IA} is

$$\begin{aligned} V_{\mathrm{IA}} = G\Bigg[&\frac{\Delta I\left(\Delta R_{\mathrm{MR}} + R_{\mathrm{sig}}\right)}{2} + \Delta I \Delta R_0 \sin(2\pi f_{\mathrm{H}} t) \\ &+ \left[\frac{\Delta I\left(\Delta R_{\mathrm{MR}} + R_{\mathrm{sig}}\right)}{2}\right]\sin(2\pi 2 f_{\mathrm{H}} t) \\ &+ I_0 \Delta R_0 \sin(2\pi(f_{\mathrm{C}} - f_{\mathrm{H}})t) + I_0 \Delta R_{\mathrm{MR}} \sin(2\pi f_{\mathrm{C}} t)\Bigg]. \end{aligned} \tag{3.3}$$

The spectra with and without sensor mismatch are illustrated in Figure 3.3(b), indicated as red and green arrows, respectively. It should be noted that transistor mismatch in the bias block is much smaller than the sensor mismatch and manifests similarly at the output whereas mismatch in the PGA and ADC are eliminated by chopping and correlated double sampling, respectively. Equation 3.3 indicates that both ΔR_0 and ΔR_{MR} result in

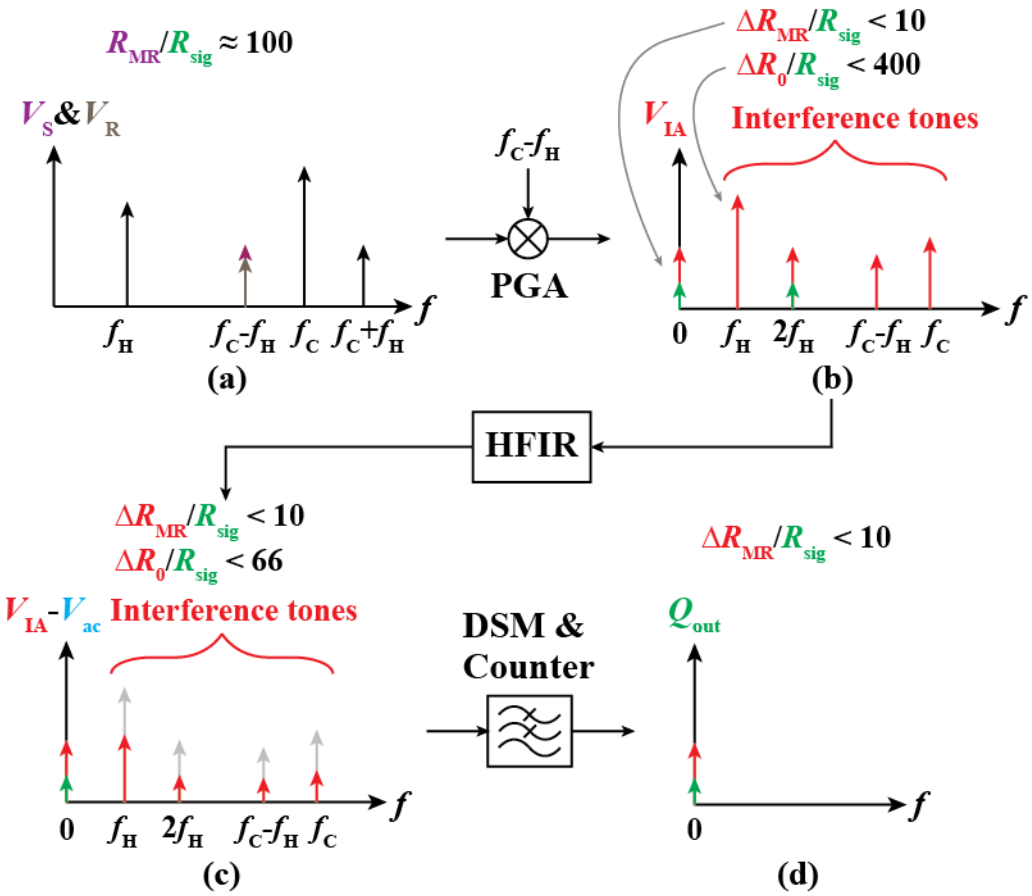

Figure 3.3 Illustration of spectra at critical nodes

residual baselines at their respective frequencies. Although ΔR_{MR} results in a signal at the same frequency as R_{sig}, a 10% MR mismatch only leads to a baseline that is ~10× larger than the signal, which can be accommodated by increasing the ADC DR. However, a 10% R_0 mismatch causes a tone at f_H that can be 400× larger than the signal, which would significantly increase the ADC DR requirement (Figure 3.4(a)). In theory, a LPF could be inserted between the PGA and ADC to filter out this interference (Figure 3.4(b)) but would increase the settling time and thus the readout time, particularly when switching active sensors. Instead, a HFIR sampling scheme is applied that reduces the ac interference without the settling penalty, as shown in Figure 3.4(c). The feedforward sampling scheme is comprised of two phases. In the first phase, the high-pass filter (HPF) passes all ac

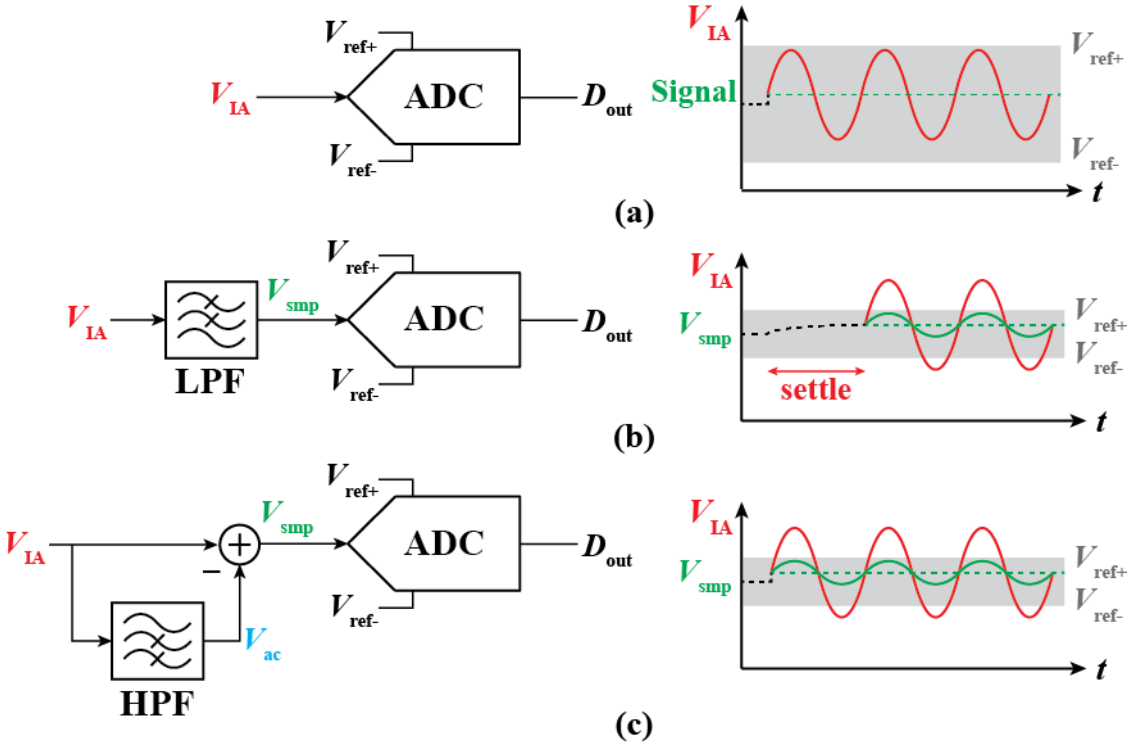

Figure 3.4 Solutions to improve the ADC DR by reducing high frequency interference tones

(a) The ADC DR is limited by high frequency interference that can be reduced by (b) low-pass filtering or (c) high-pass feedforward filtering.

signals through while blocking dc. In the second phase, the entire signal is sampled. After subtraction, V_{smp} contains only the signal at dc. The transfer function of this filter is

$$H(s) = 1 - \frac{s}{s + \omega_p} = \frac{1}{1 + \frac{s}{\omega_p}} \qquad 3.4$$

where ω_p is the high-pass corner frequency. Equation 3.4 shows that the HP feedforward technique has the same transfer function as an LPF but comes with a 1,400× reduction in the settling time.

This HFIR sampling technique embedded in the ADC sampler filters out these ac interference tones, and thus greatly relaxes the ADC DR requirement, as shown in Figure 3.3(c). A first-order, incremental ΔΣ modulator (DSM) oversamples V_{IA} with an

oversampling ratio (OSR) of 10,000. A subsequent counter decimates D_{out}, digitally filtering out all interference tones, leaving the desired signal at dc (Figure 3.3(d)).

3.3 Circuit Implementation

3.3.1 Bias Network

A constant g_m and wide-swing cascode network are designed to generate the bias current, I_{unit}, and the cascode node voltages, V_{cscp} and V_{cscn}, respectively (Figure 3.5). By sizing the W/L of M_{n2} 4× larger than M_{n1}, the constant g_m architecture ensures the transconductance of M_{n1} is $1/R_{CGm}$, where R_{CGm} is an off-chip precise resistor. R_{CGm} also sets the unit current I_{unit} to 10 μA. M_{n3}, M_{n4}, and C_{CGm} form the start-up circuit. When V_{DD} is powered on, V_x is pulled to V_{DD} due to C_{CGm}, thus turning on M_{n4}. The conducting path between V_p and V_n turns on M_{p1}, M_{p2}, M_{n1}, and M_{n2}, thus starting up the constant g_m. After V_p and V_n settle, M_{n3} discharges V_x to 0 so M_{n4} turns off. It should be mentioned that the constant g_m is ideally stable since the loop gain is ≤1, but the parasitic inductance and capacitance due to the wire-bonding and the PCB traces at node V_y can boost up the loop

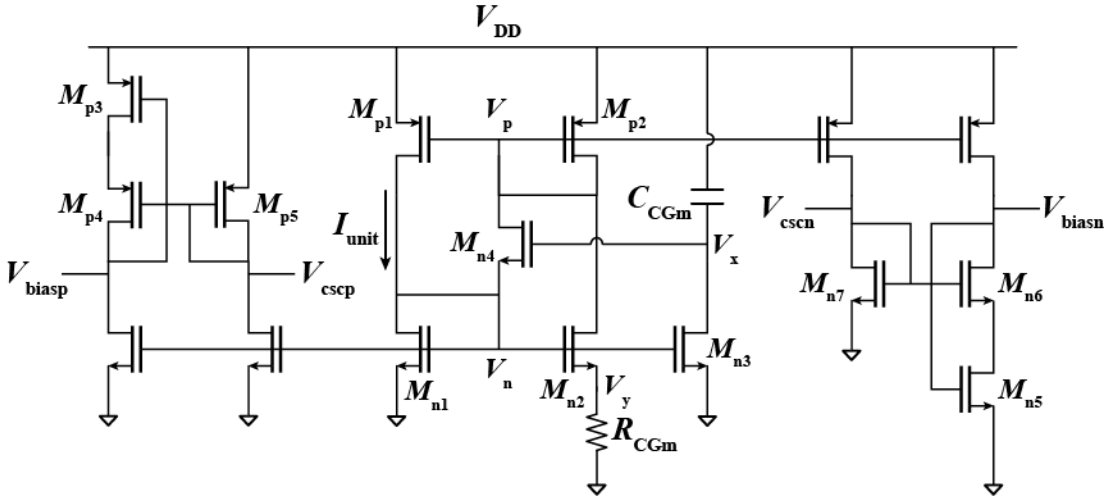

Figure 3.5 Schematic of the bias network

gain, causing stability issues. Minimizing the parasitics by placing R_{CGm} on the daughterboards and adding capacitors at V_n or V_p for compensation resolve this issue.

The wide-swing cascode bias network generates the cascode node voltages V_{cscn} and V_{cscp} for the OTAs. By sizing the W/L of M_{n7} and M_{p5} >4× smaller than the W/L of M_{n5} and M_{p3} respectively, the generated cascode voltages ensure the cascode transistors M_{n6} and M_{p4} are biased in the saturation region.

I_{unit} is mirrored into multiple branches that are connected to different OTAs in this chip. By connecting the current instead of the voltage through long paths, the leakage can be minimized to achieve accurate biasing.

3.3.2 Sensor Bias Block

The sensor bias block is composed of a bias current generator, sensor selection control logic, and two buffers (Figure 3.6). The bias current generator uses an external reference voltage, V_B, an off-chip resistor, R_B, and an on-chip feedback loop to generate a bias current, $I_{in} = V_B/R_B$. A compensation capacitor, C_C = 30 pF, is added for stability. I_{in} is mirrored into two channels to bias the selected active sensor and reference sensor. The sensor in this work has a breakdown voltage of ~500 mV, which limits I_{in} to be 2 mA_{pp}. Column-based readout is applied for the sensor array, which connects the rows together, thus sensors are placed in parallel to have a resistance of ~150 Ω (9× smaller). A 3-to-8 decoder generates control signals *Sel*[1:7] and a Rst_{RS} signal that opens all sensors during reset. Gated source followers that can also be disabled by Rst_{RS} buffer the voltages and drive the PGA. To reduce the noise mirrored from the bias current, I_{buf}, the bias voltage is low-pass filtered by a pseudo-resistor R_{buf} and a capacitor C_{buf}.

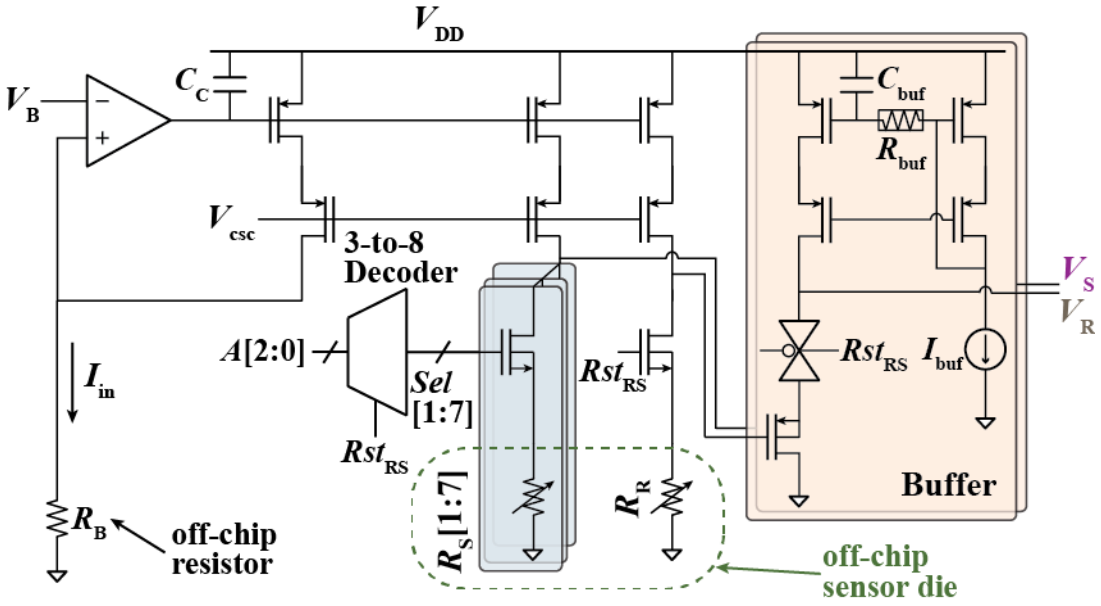

Figure 3.6 Schematic of the sensor bias

3.3.3 Programmable Gain Amplifier

A 2-bit PGA rejects the large common-mode component of V_S and V_R while amplifying the differential signal. It is implemented by a capacitively-coupled instrumentation amplifier with chopper switches in the OTA and the feedback loop (Figure 3.7(a)). The choppers inside the OTA downmodulate the signal from f_C - f_H to dc and upmodulate the offset and 1/*f* noise out-of-band where it is subsequently filtered. A 2-bit variable capacitor, C_3, is adjusted in tandem with the input capacitor, C_1, to maintain the same closed-loop 250 kHz bandwidth across different gain modes. The OTA is implemented by a folded-cascode differential amplifier, as shown in Figure 3.7(b). Figure 3.7(c) shows the transistor size and bias current for the OTA. The choppers are placed at the cascode nodes for better settling and $M_{3,5}$ are large devices to reduce 1/*f* noise as their noise is not chopped. To minimize the noise, M_1 is sized large to keep it in deep subthreshold region, which provides the best g_m/I_D. Most of the OTA power (71%) is spent on M_1 to maximize its g_m. Due to the large common-mode input swing (~300 mV_{pp}),

common-mode rejection ratio (CMRR) needs to be considered. Although CM-to-DM conversion only causes an offset at the output, it eats into the dynamic range of the system. For instance, a CM-to-DM gain of -20 dB can cause an offset of 15 mV, taking 15% of the ADC full range. A common-mode cancellation path was reported to reduce the swing, but it introduces more mismatch, thus leads to a worse CMRR [104]. Adding a

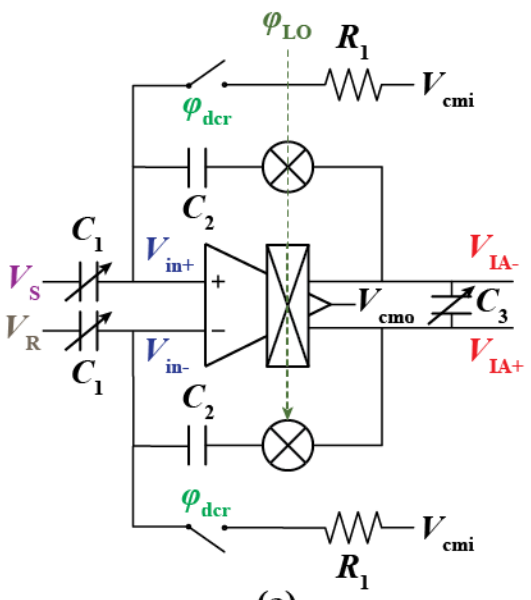

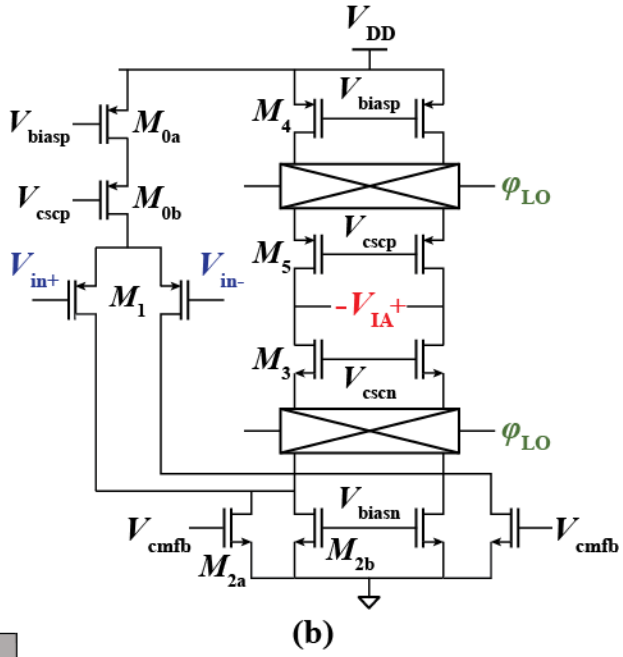

Transistor	W/L [μm]	Bias Current [μA]
M_{0a}	160/1	100
M_{0b}	160/1	100
M_1	100/0.2	50
M_{2a}	40/1	50
M_{2b}	16/1	20
M_3	80/1	20
M_4	32/1	20
M_5	80/1	20

(c)

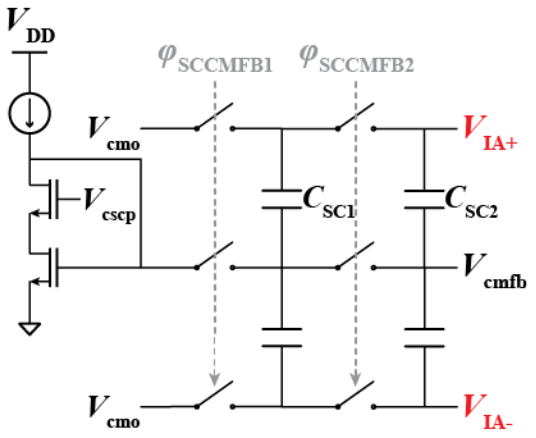

Figure 3.7 Schematic of the PGA

(a) The 2-bit PGA, (b) fully-differential folded-cascode OTA with built-in down modulator, (c) transistor size chart, and (d) switched capacitor common-mode feedback.

common-mode replica path to copy the common-mode signal to every node in the amplifier can boost the CMRR to 130 dB, but it requires additional design effort [105]. In this design, the tail current source in the OTA is cascoded to improve the CMRR to be >70 dB in simulation, which only leads to an offset of <0.5 mV. The output dc voltage is set to $V_{cmo} = V_{DD}/2$ by a switched-capacitor common-mode feedback (SC-CMFB) network for large swing (Figure 3.7(d)). Due to the cascoded tail current source and the large input swing, the input dc voltage is set to V_{cmi} = 300 mV. A pseudo-resistor is conventionally used for the dc bias but suffers from bad linearity and high process dependency (Figure 3.8(a)) [106], [107]. A duty-cycled resistor (DCR), implemented by a deep n-well switch controlled by φ_{dcr} and a poly-resistor R_1, is switched on for a short time of D over a period of T (Figure 3.8(b)) [108], [109]. Since it can only transfer the charge when the switch is on, the equivalent resistance, R_{DCR}, can be derived as

$$R_{\mathrm{DCR}} = R_1 \frac{T}{D}. \qquad 3.5$$

In this design, R_1 = 400 kΩ and T/D = 60, so R_{DCR} = 25 MΩ, which is large enough to provide low noise while not affecting the feedback factor in the band of interest.

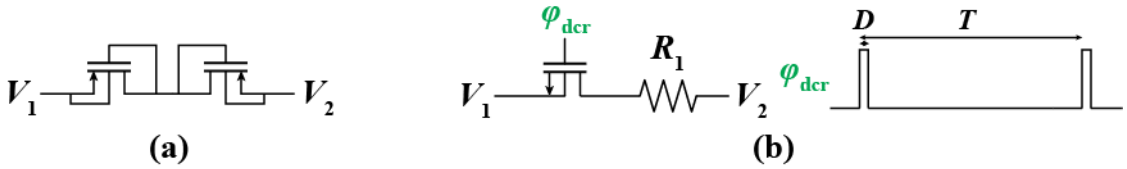

Figure 3.8 (a) Pseudo-resistor and (b) duty-cycled resistor

At the start of a measurement (*i.e.* when Rst_{RS} goes from 0→1), V_S and V_R are discharged from V_{DD} to V_{op}, resulting in a rapid transient at V_{in} that needs time to settle back to V_{cmi}. The settling time would be prohibitively long as DCRs have very large impedances. Worse, such settling happens every measurement when using TDM for

multi-sensor readout, thus significantly increasing the overall readout time. To reduce the settling time due to sensor switching, a modified DCR timing scheme is applied where the switches are briefly closed during and after sensor switching. Thus, V_{in} has a low-impedance path to V_{cmi} through R_1 enabling fast settling. Afterwards, the DCRs return to duty-cycled mode to operate as large bias resistors for low noise measurement. The timing diagram is shown in Figure 3.9. It should be mentioned that ac swings are not shown in the settling phase for convenience. Compared with a traditional DCR, the presented fast-settling DCR reduces the settling time by 40×.

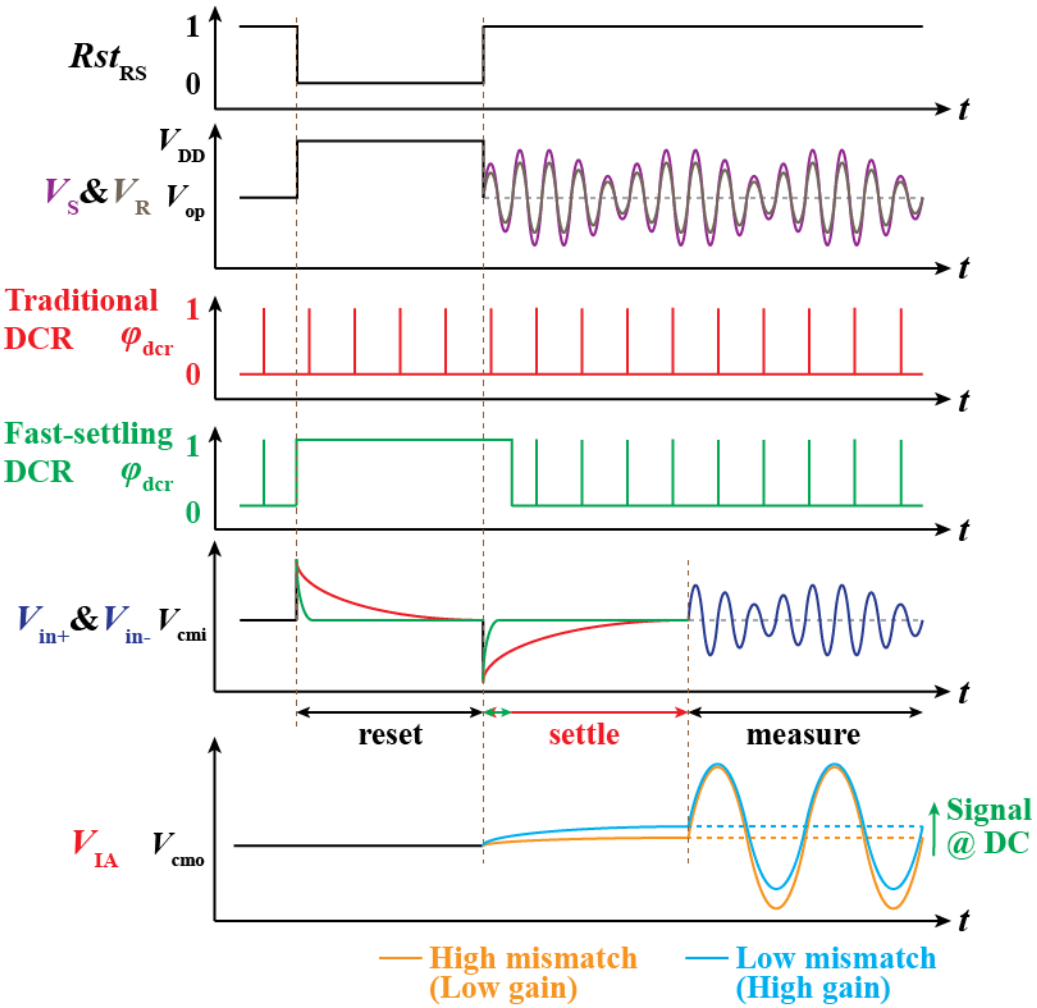

Figure 3.9 PGA timing diagram that includes clocks and analog waveforms

After settling, the PGA amplifies the signal with a programmable gain that depends on the sensor mismatch. Specifically, the PGA gain is set to amplify the dc signal as much as possible but ensure the ac swing is within the PGA linear range. The FPGA determines which gain mode is appropriate for each sensor during startup.

3.3.4 Incremental ΔΣ ADC

Figure 3.10 shows the block diagram of a first-order incremental DSM, which is suitable for low bandwidth TDM-based sensing applications [110]. Compared to conventional DSMs, it adds a switch to reset the ADC when switching between the sensors to eliminate the memory. This comes with a penalty that the quantization noise is only reduced by 2× when doubling the OSR, while conventional DSMs can reduce the quantization noise by $2^{1.5}$×. Therefore, to achieve the same resolution, incremental DSMs need a higher OSR that reduces the speed. Considering the total number of conversions is *N* and the number of '1s' is *m*, the input can be represented as

$$V_{\text{in}} = \frac{m}{N} V_{\text{ref}} \tag{3.6}$$

where V_{ref} is the ADC reference voltage. Therefore, the quantization noise is

$$e_{\text{q}} = \frac{LSB}{\sqrt{12}} = \frac{V_{\text{ref}}}{N\sqrt{12}}. \tag{3.7}$$

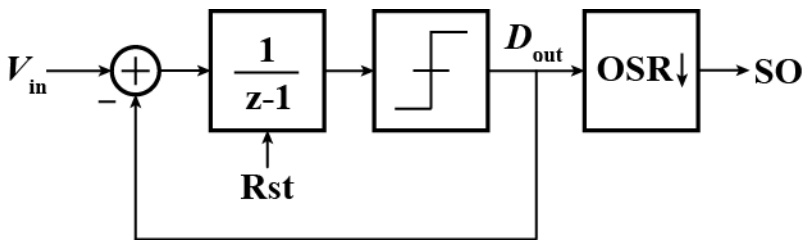

Figure 3.10 Block diagram of the incremental DSM

Since N = OSR, Equation 3.7 indicates that the quantization noise is inversely proportional to the OSR. In this design, the OSR = 10,000, so the resolution is $\log_2$(OSR) = 13.3 bit. The sampling frequency f_S is 1 MHz, so the bandwidth is f_S/OSR = 100 Hz.

The ADC implementation is shown in Figure 3.11. The HFIR block, which is embedded into the ADC sampling network, is implemented by a pseudo-differential, switched-capacitor HPF followed by a chopped buffer. When the HFIR sampler is enabled (EN_{HFIR} = 1), the sampling capacitor, C_4, samples the voltage difference (*i.e.* V_{IA} - V_{ac}) during the sampling phase ($\varphi_{1,1e}$ = 1). At the same time, C_6 samples the OTA offset and 1/*f* noise. It should be noted that the correlated double sampling (CDS) realized by C_6, S_1, and S_2 is different from conventional CDS, which does not need switches S_1 and S_2

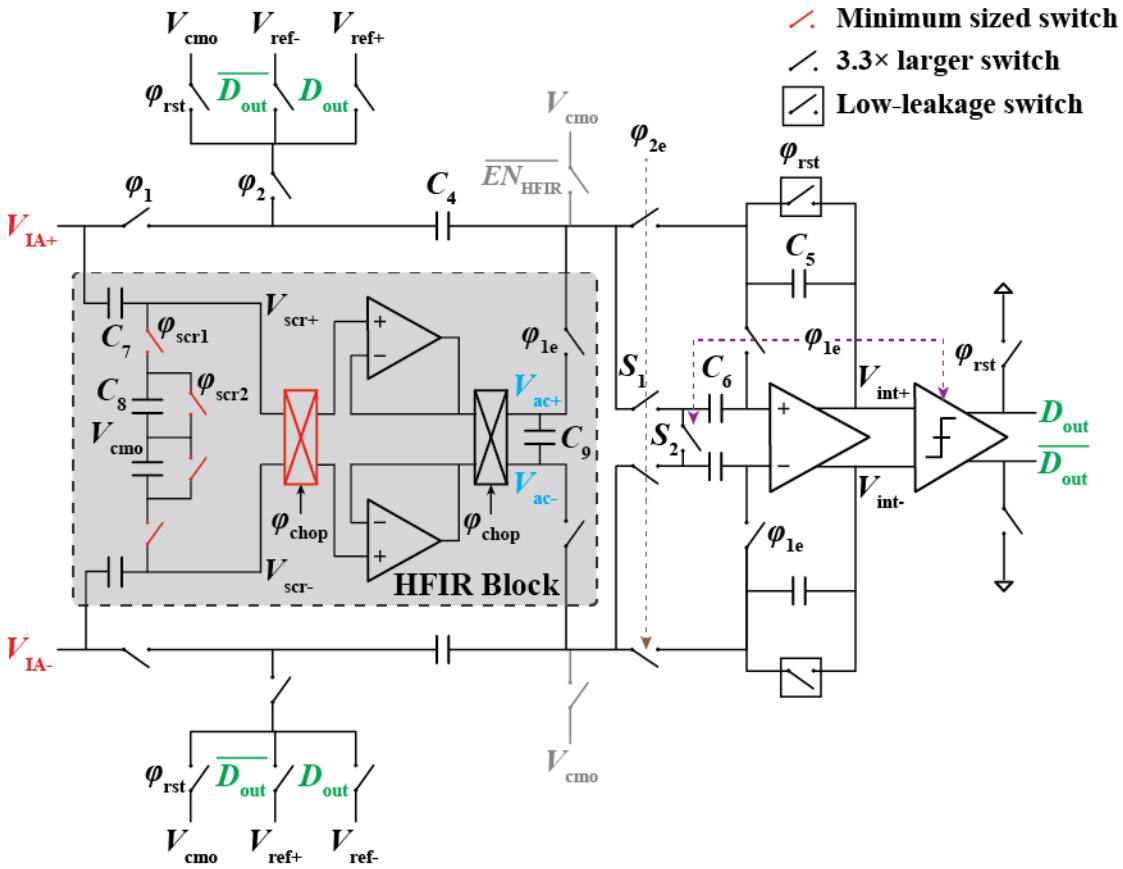

Figure 3.11 Schematic of the ADC with HFIR sampling

to isolate the top plate of C_6 and V_{ac}. During the integration phase ($\varphi_{2,2e}$ = 1), the charge stored on C_4 and C_6 is integrated on to C_5. A dynamic comparator compares V_{int} to generate the digital output, D_{out}.

The timing diagram of the ADC is illustrated in Figure 3.12(a). A non-overlapping clock generator creates φ_1 and φ_2 with early phases (φ_{1e} and φ_{2e}) to avoid signal-dependent charge injection (Figure 3.12(b)). The chopping frequency φ_{chop} and the switched capacitor resistor (SCR) switching frequency $\varphi_{scr1,2}$ are set to 1/4 and 1/8 of the sampling frequency, respectively. Both clocks change right after the sampling phase to ensure the maximum settling time on V_{ac}.

The reset switch used for the incremental DSM must have low leakage to ensure the charge stored in C_5 has negligible loss over the entire conversion. It is implemented

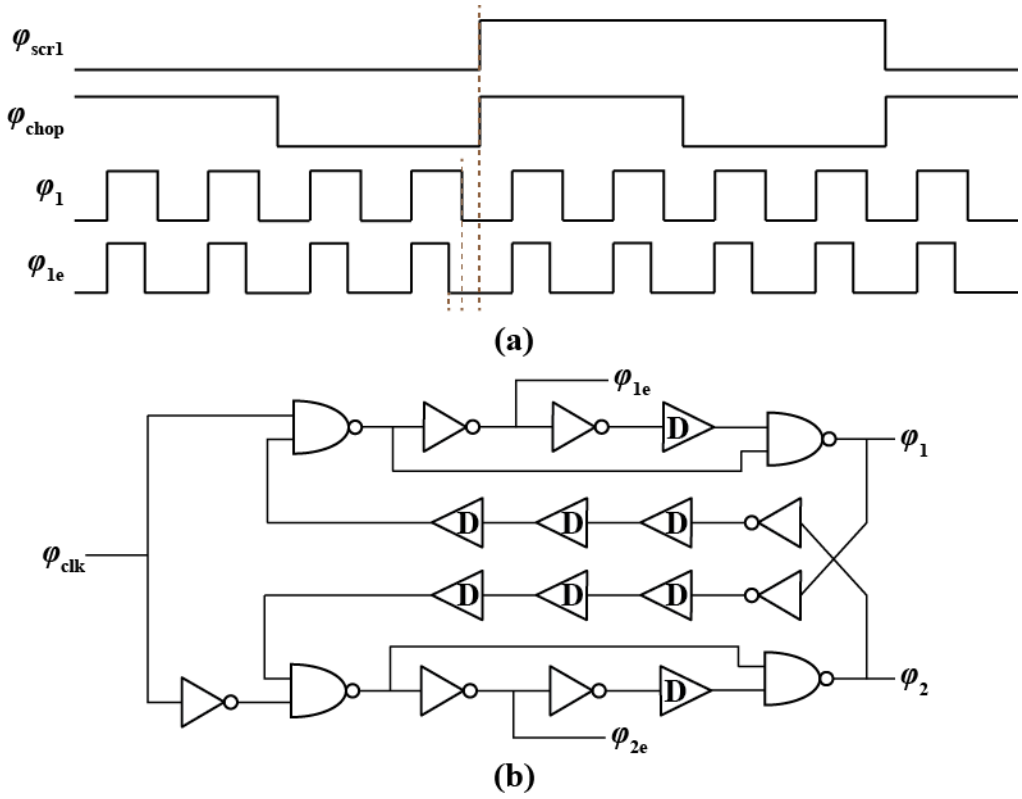

Figure 3.12 (a) ADC timing diagram and (b) clock generator

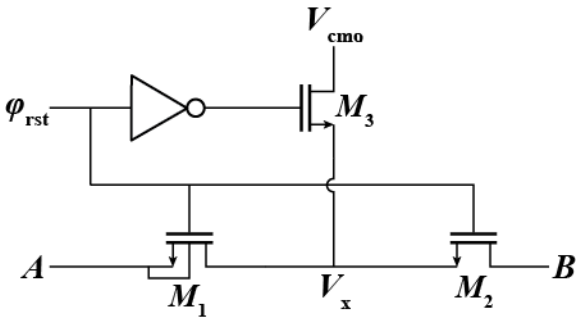

Figure 3.13 Schematic of the low leakage switch

by a low leakage switch, as shown in Figure 3.13 [111]. When $\varphi_{rst} = 0$, M_3 is turned on so that $V_x = V_{cmo}$, which is equal to the voltage at *A* since it is a virtual ground node in the ADC. Therefore, V_{DS} of M_1 is 0, thus reduces the leakage. Furthermore, M_1 is implemented by a deep n-well transistor, so the body leakage is minimized. As a result, the leakage current is <1 fA in simulation.

The switches must be sized properly to satisfy the ADC settling requirement. Specifically, the settling error within half clock cycle must be less than ½ LSB. Therefore,

$$\tau = 2R_{\text{on}}C_4 < \frac{1}{2(n+1)\ln(2)\,2f_S} \tag{3.8}$$

where R_{on} is the switch on-resistance, n is the ADC resolution, and f_S is the sampling frequency. With C_4 = 1 pF, n = 13.3 bit, and f_S = 1 MHz, R_{on} < 12.6 kΩ. In this design, the switches are sized 3.3× larger than the smallest size to have a simulated R_{on} of 0.8 kΩ.

The OTA in the switched capacitor integrator must also satisfy the required gain and speed requirement to achieve the desired performance. To ensure proper settling, the gain bandwidth product (GBW) of the OTA must satisfy

$$\text{GBW} > \frac{(n+1)\ln(2)}{\pi} 2f_S. \tag{3.9}$$

With n = 13.3 and f_S = 1 MHz, the GBW must be >6.3 MHz. To maintain the linearity and eliminate the deadzone, the dc gain of the OTA must be greater than the OSR (80 dB).

The OTA is implemented by a folded-cascode differential amplifier, as shown in Figure 3.14(a). Since the output swing is small (<100 mV_{pp}), continuous time CMFB is used to replace the SC-CMFB, which causes additional charge injection (Figure 3.14(b)). A Miller compensation capacitor, C_{cmfb}, of 0.4 pF is added for CMFB stability (simulated phase margin = 73°). Simulations show that the OTA can provide a dc gain of 81 dB and a GBW of 46 MHz, which are sufficient for the ADC.

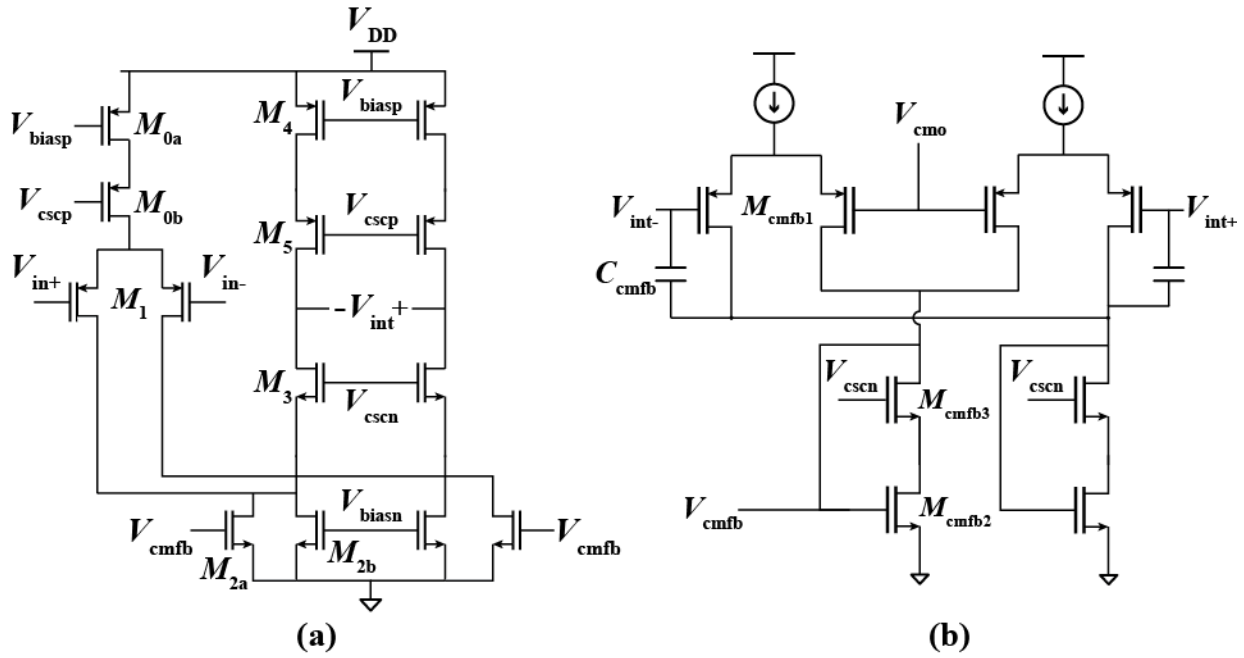

Figure 3.14 Schematic of the (a) OTA and (b) CMFB

The comparator is implemented by a dynamic latched comparator, as shown in Figure 3.15. When φ_{1e} changes from 0 to 1, the input pair in the pre-amp discharges the capacitance at this node decreasing $V_{preamp+,-}$ at different rates until it triggers one side of the latch and pulls V_{latch+} or V_{latch-} to 1. This sets (or resets) the SR latch until the next rising edge of φ_{1e}. When φ_{1e} is 0, $V_{preamp+,-}$ are pulled to V_{DD} and $V_{latch+,-}$ are pulled to

GND. The SR latch keeps the original value so D_{out} remains unchanged. Therefore, this comparator is edge triggered and consumes no static power. The load capacitors, C_L, is 0.4 pF to balance the speed and noise.

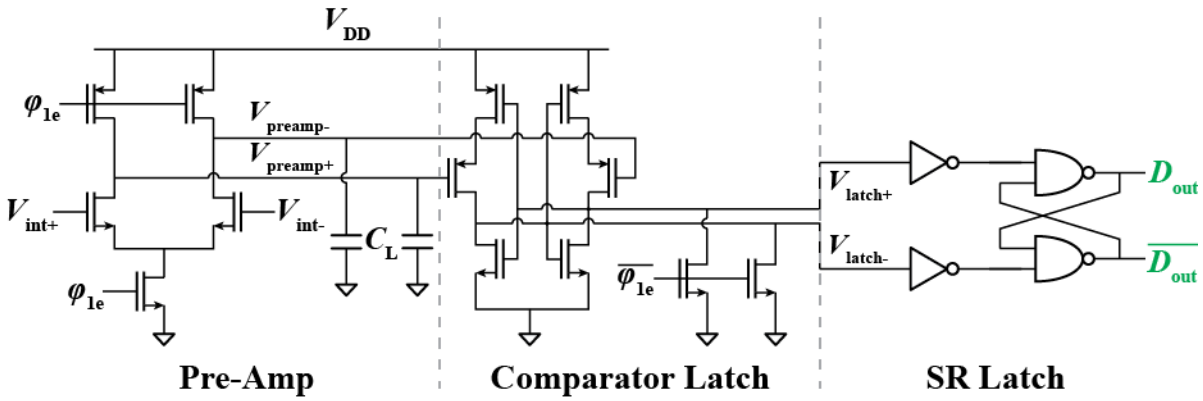

Figure 3.15 Schematic of the comparator

A 16-bit counter is used as a decimation filter, as shown in Figure 3.16. The transfer function of a counter can be derived as

$$H(z) = \frac{1}{N}(1 + z^{-1} + z^{-2} + \cdots + z^{1-N}) = \frac{1}{N}\frac{1 - z^{-N}}{1 - z^{-1}} \tag{3.10}$$

$$|H(f)| = \frac{1}{N}\frac{1 - e^{-jN2\pi\frac{f}{f_s}}}{1 - e^{-j2\pi\frac{f}{f_s}}} = \frac{sinc\left(N\pi\frac{f}{f_s}\right)}{sinc\left(\pi\frac{f}{f_s}\right)} \tag{3.11}$$

where N = OSR. Therefore, the counter acts as a *sinc* filter, which is sufficient for a first-order incremental DSM. Although a 14-bit counter is enough for an OSR of 10,000, the counter is expanded to 16-bit to be compatible with higher OSR up to 2^{16} = 65,536. The counter updates the outputs Q[0:15] at the negative edge of φ_{1e}, which triggers the comparator at its rising edge. $Rst_{counter}$ resets the counter after the ADC is reset. A shift register converts the data in parallel into series to save on the number of pads needed. When SH_LDb is 0, the shift register loads the data Q[0:15] at the rising edge of CLK_{SR}.

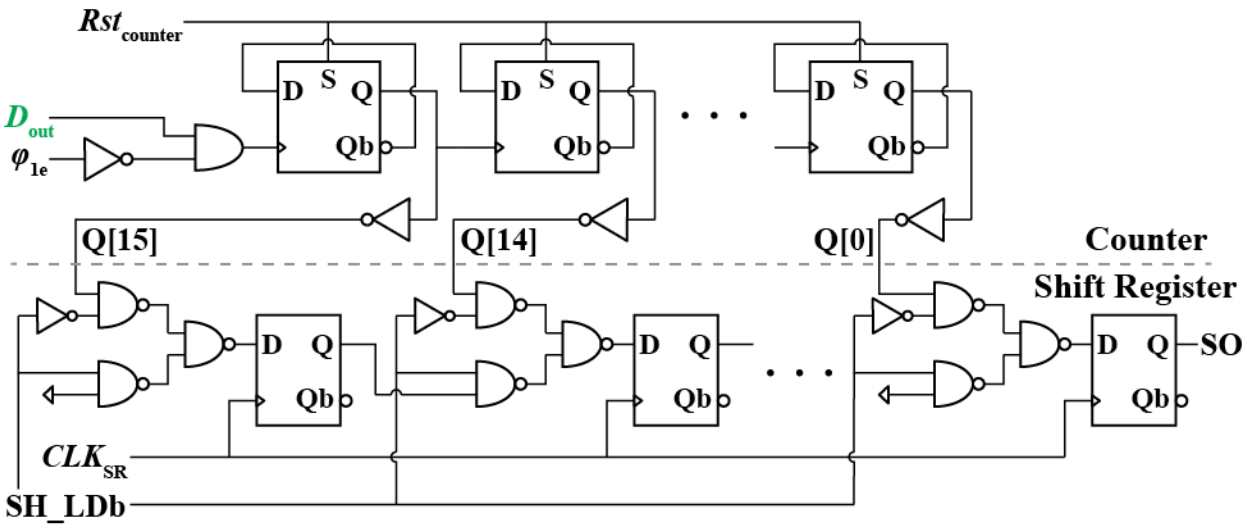

Figure 3.16 Counter and shift register

When SH_LDb is 1, it shifts the data to the right so SO transmits one data per CLK_{SR} cycle. It takes 16 cycles to complete the data transmission.

The HFIR block is re-addressed in Figure 3.17. It is implemented by a SC HPF followed by a chopped buffer. To reject the ΔR_0 interference, the HFIR block must provide a low enough high-pass corner frequency, f_{HP}, yet must have a high enough low-pass corner frequency, f_{LP}, to ensure that V_{ac} settles in time and does not integrate too much white noise. These two critical frequencies are

$$f_{\mathrm{HP}} = \frac{f_{\mathrm{scr}} C_8 + 2 f_{\mathrm{chop}} C_{\mathrm{in}}}{2\pi C_7} \tag{3.12}$$

$$f_{\mathrm{LP}} = \frac{1}{2\pi \left(\frac{1}{g_{\mathrm{m}}} + R_{\mathrm{on}} \right) 2C_9} \tag{3.13}$$

where f_{scr} is the SCR switching frequency, f_{chop} is the buffer chopping frequency, C_{in} is the capacitance at node V_{scr}, g_m is the buffer OTA transconductance, and R_{on} is the on-resistance of the output chopper. To have a low f_{HP} for better ac rejection, C_{in} must be minimized where C_{in} is mainly composed of the buffer input capacitance, switch parasitic

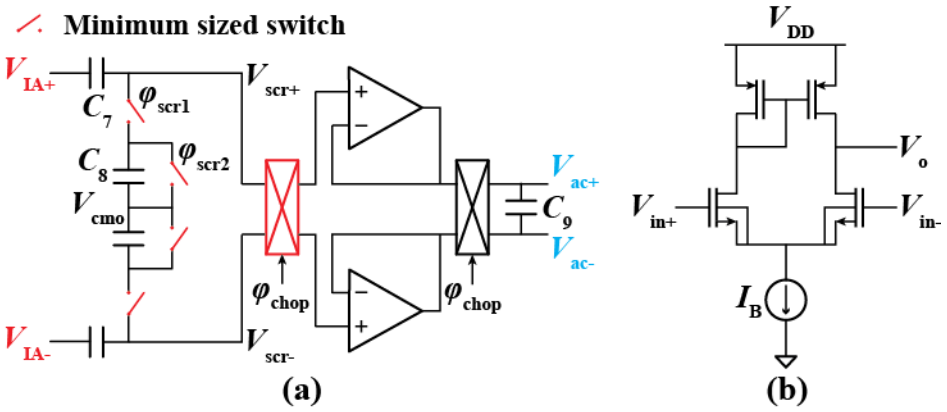

Figure 3.17 Schematic of the HFIR block

capacitance, and interconnect parasitic capacitance. Since the buffer input transistors must be large enough to provide g_m for settling, C_{in} can only be reduced by decreasing the parasitic capacitance. Therefore, minimum sized switches are used in the SCR and the buffer input chopper, indicated as red switches in Figure 3.17(a). The extracted layout simulation shows a pass-band between 1.1 kHz and 20 MHz (Figure 3.18(a)). The interference at 10 kHz passes through the HPF with -0.52 dB amplitude loss and 6.2° phase shift. Accordingly, after subtraction, the interference is reduced by 8.3×, thus relaxes the ADC DR requirement.

The HFIR noise at node V_{ac} is sampled into C_4, thus directly affects the input-referred noise of the ADC. The noise of a SC HPF is equivalent to a RC HPF, where $R_{HPF} = 1/f_{scr}C_8$. Therefore, the output noise of the HFIR can be derived as

$$v_{n,Vac}^2 = \frac{1}{1+\omega^2 R_{HPF}^2 C_7^2} 4k_B T R_{HPF} + v_{n,op}^2 \qquad 3.14$$

where $v_{n,op}$ is the op-amp noise that is designed much smaller than $4k_B T R_{HPF}$. Figure 3.18(b) shows the simulated noise. Although the 1/*f* noise from the op-amp has been chopped, the 1/*f* noise from the minimum sized switches dominates the low frequency

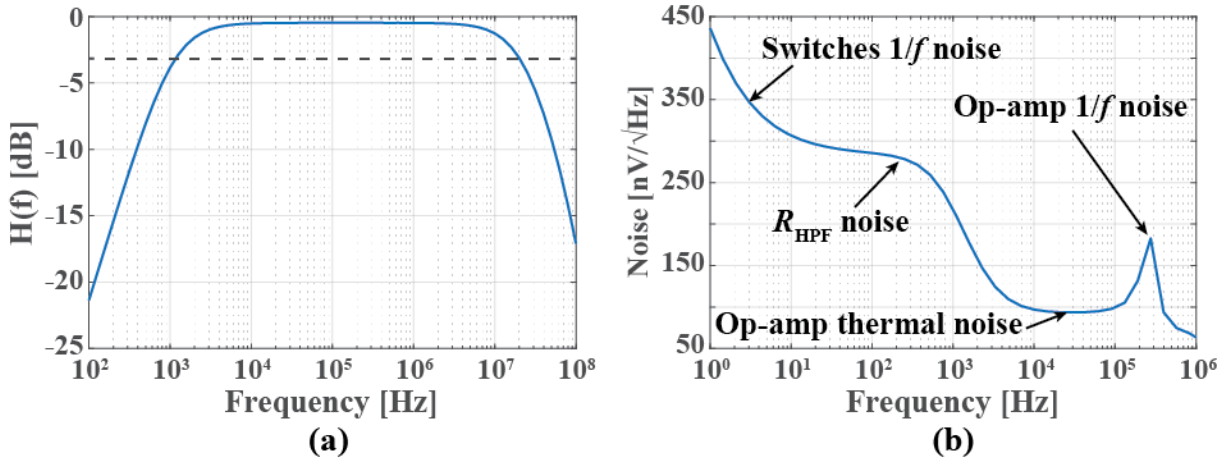

Figure 3.18 HFIR extracted layout simulation results

(a) Transfer curve and (b) noise spectrum.

band (<10 Hz). The integrated noise over the 100 Hz ADC bandwidth was simulated to be 2.93 μV_{rms}, which is comparable to the ADC quantization noise of 2.89 μV_{rms}.

3.4 Measurement Results

This chip was fabricated in a TSMC 180-nm CMOS process. An annotated die photo is shown in Figure 3.19. It operates from a single supply of 1.8 V and consumes 1.39 mW excluding the sensor bias, which is dependent on the sensor resistance and consumes 5.4 mW for the 150 Ω sensors used in this work. The power and noise contributions of each block are shown in Figure 3.20. When the PGA is configured to the low-gain mode (1×) for maximum sensor mismatch tolerance, the ADC dominates the noise; when the PGA is configured to the high-gain mode (4×) for the lowest noise, the ADC noise is reduced by 4× and thus the PGA dominates the noise.

3.4.1 Test Setup

Figure 3.21 shows the test setup for characterizing the chip. The reported AFE was connected to a GMR sensor chip placed inside of a custom designed Helmholtz coil.

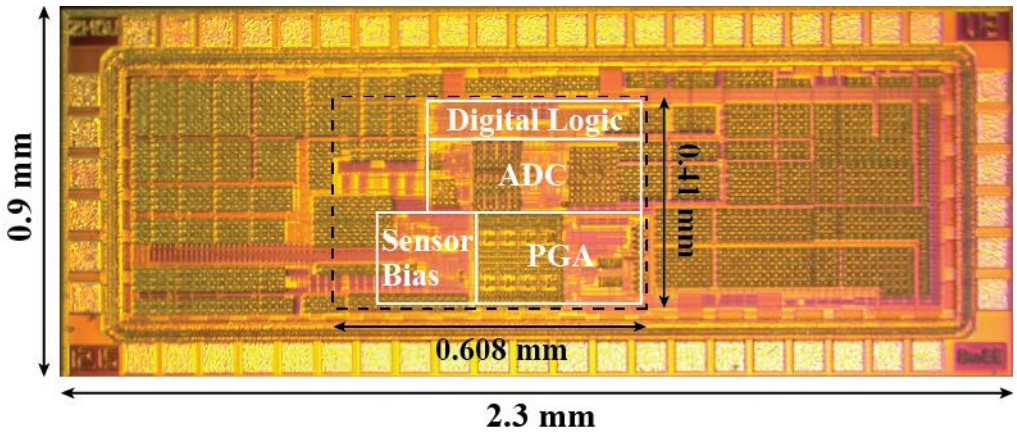

Figure 3.19 Annotated die photo

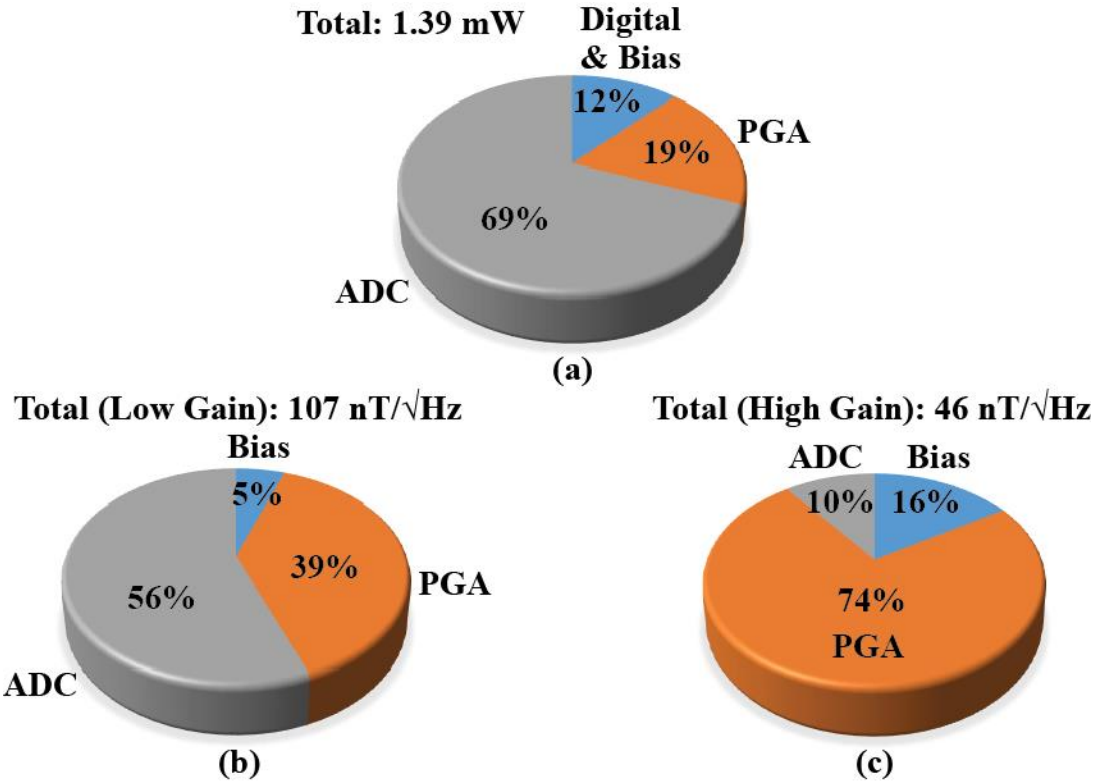

Figure 3.20 Distribution of power and noise

(a) Power distribution. Noise distribution when the PGA gain is (b) low (1×) and (c) high (4×).

A 100 µL well made by the Tygon plastic tube was attached over the sensing area. The sensors nominally have an R_0 of 150 Ω and a MR ratio of 9.04%. The synchronized excitation sources and clocks were generated externally by two function generators

(Keysight 33600A) with f_H = 9.9 kHz, f_C = 99 kHz, and f_C - f_H = 89.1 kHz. A power amplifier (Kepco BOP 36-12) provides an ac current at f_H to the Helmholtz coil to generate an ac magnetic field of 60 Oe_{pp} that was verified by a Gauss meter (LakeShore 475 DSP). It should be noted that the maximum f_H is 9.9 kHz, limited by the Helmholtz coil's large inductance (~80 μH). The DAQ (NI-6361) was used to measure the analog signals at critical nodes in the chip to characterize the internal blocks. The digital inputs and outputs were controlled by an FPGA (Opal Kelly XEM6310).

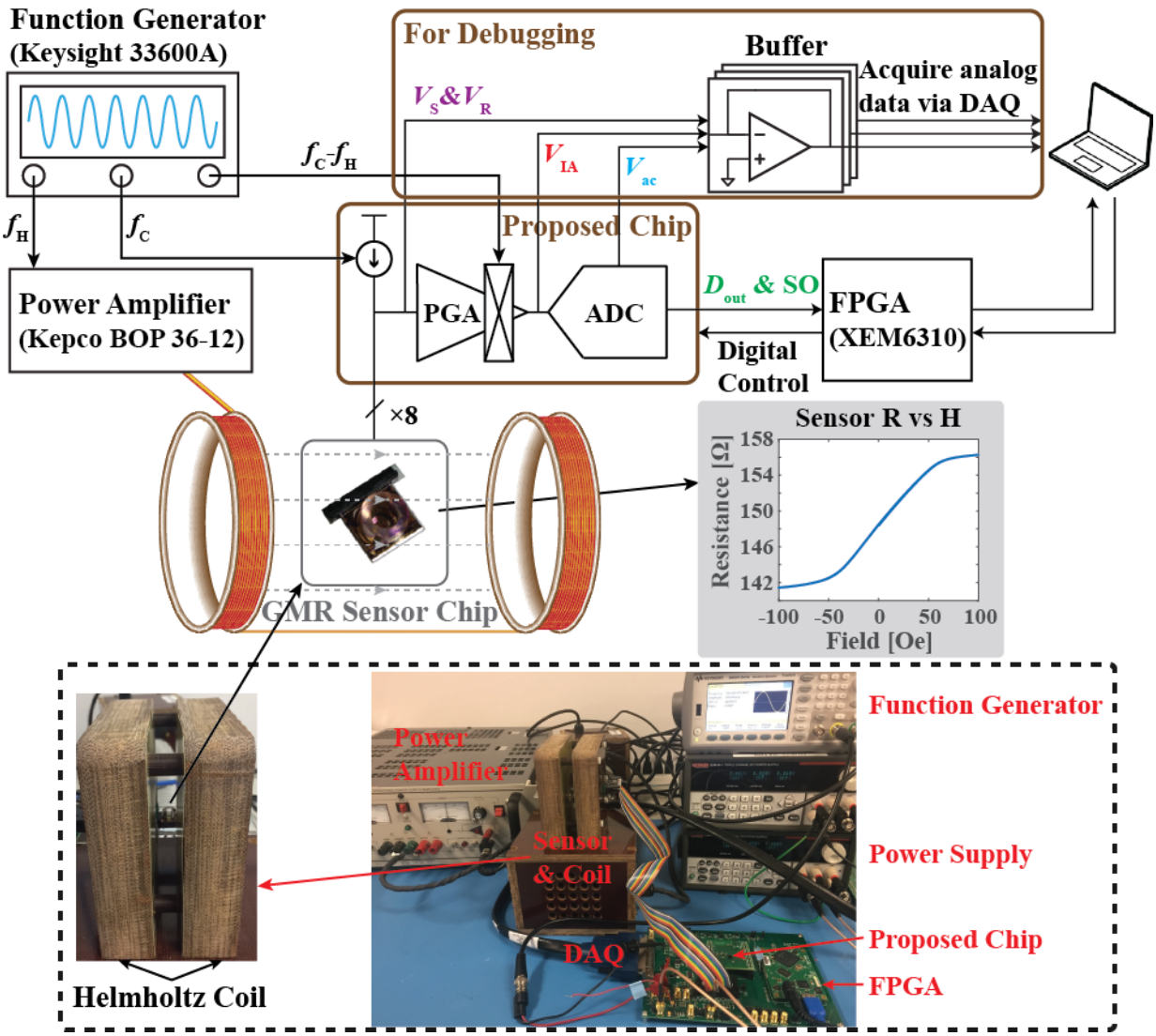

Figure 3.21 Test setup

To continuously capture the data (either D_{out} or SO) from the ADC, a ping-pong FIFO was built in the FPGA, as shown in Figure 3.22. Since the PC has an inaccurate internal clock, using one FIFO or not using FIFO result in losing data from the ADC. The ping-pong FIFO consists of two identical FIFOs that capture the data alternately. First, a serial peripheral interface (SPI) transfers the series SO from the chip to a 16-bit parallel data Q[0:15], which are fed into the FIFOs that have a 16-bit width and a 256-bit depth. At the beginning, both FIFOs are empty, and Q is written into the FIFO1 at a rate of 91 S/s since the ADC conversion time is 11 ms (1 ms for PGA settling and ADC reset + 10 ms for conversion). It takes 11 ms * 256 = 2.8 s to completely fill the FIFO1, which gives a full flag to the PC. The FIFO2 captures the subsequent data and the PC collects the stored data from the FIFO1 at the maximum speed and resets the FIFO1 after collecting all the data. The two FIFOs read the data alternately so the ADC data can be continuously readout without losing information.

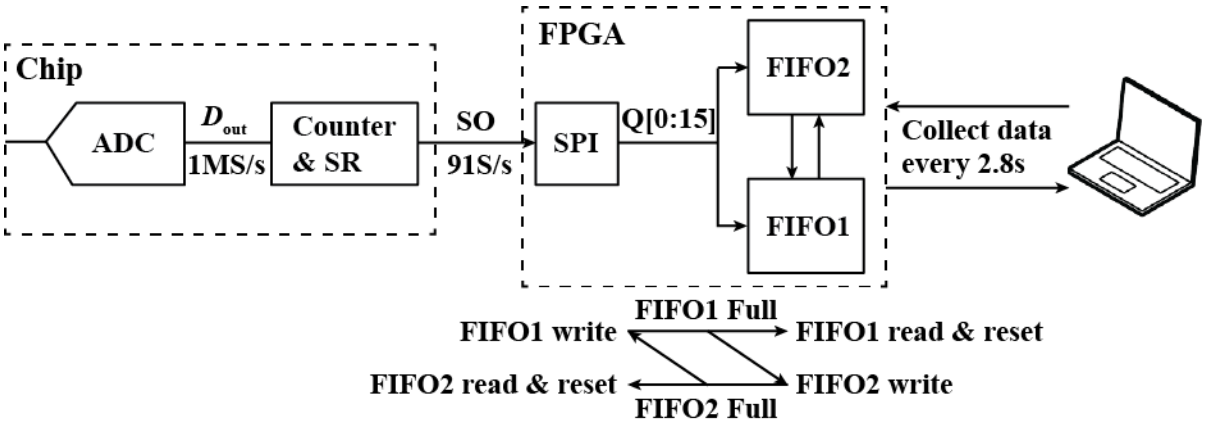

Figure 3.22 Ping-pong FIFO structure

3.4.2 Electrical Measurement Results

Figure 3.23 shows the measured spectra at critical nodes. In Figure 3.23(a), the sensor output (node V_S) contains large tones at f_H, f_C, and $f_C \pm f_H$. Most of the baselines

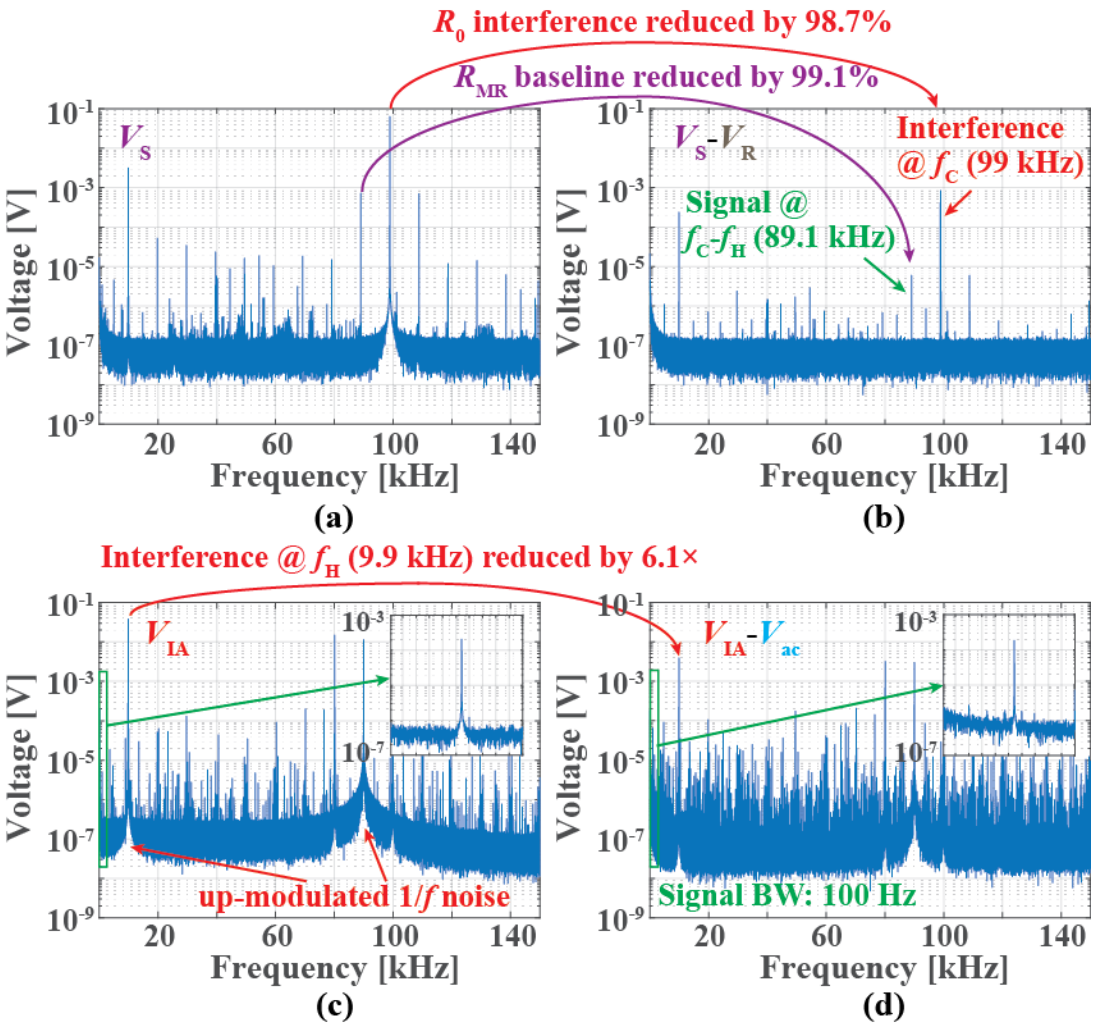

Figure 3.23 Measured spectra at critical nodes

are suppressed by the reference sensor, leaving only the residue tones due to mismatch (Figure 3.23(b)). The PGA downmodulates the signal to dc, and upmodulates 1/*f* noise (Figure 3.23(c)). The HFIR sampling technique reduces the interference tone at f_H by 6.1×, as shown in Figure 3.23(d). The suppression is slightly lower than in simulation due to larger parasitics at node V_{scr}. Although the spectrum looks crowded, the in-band spectrum is clean except for a small tone (<0.3 mV) from the instrument.

The sensor bias noise was characterized, as shown in Figure 3.24. The measured noise matches with simulation but is limited by the measurement circuit noise at high

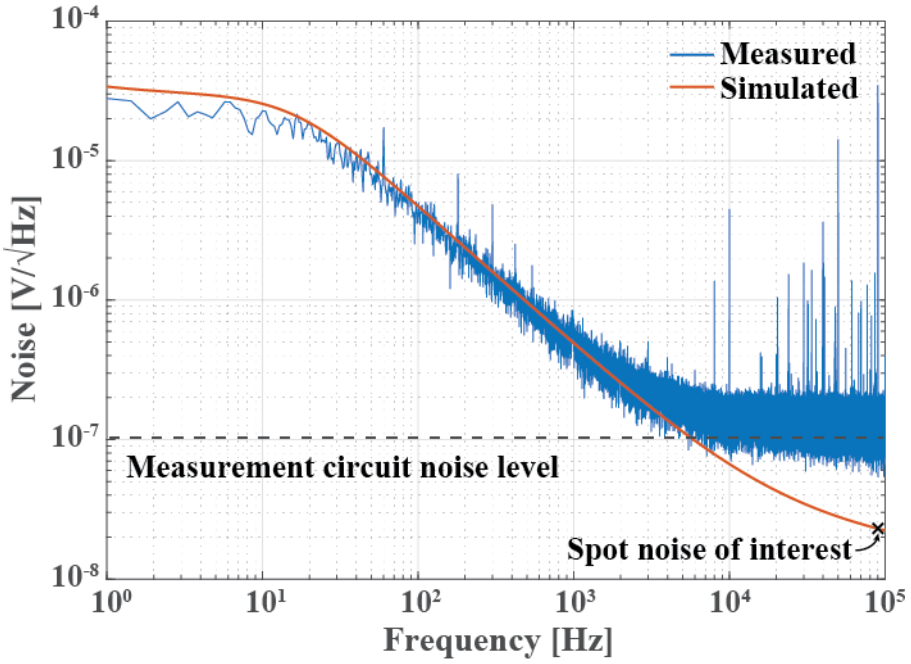

Figure 3.24 Measured and simulated noise spectra of the sensor bias

frequencies. Although the low frequency noise is high, the signal in the sensor bias block is at f_C - f_H = 90 kHz, thus only the spot noise at 90 kHz is of interest, which is simulated to be 23 nV/√Hz.

Figure 3.25 shows measured settling times of the PGA with a pseudo-resistor, a traditional DCR, and the reported fast-settling DCR, all implemented on-chip for comparison. After the row select switch closed, a sudden ~100 mV voltage drop at V_{in} was observed. The pseudo-resistor, traditional DCR, and fast-settling DCR had a recovery time of >14 ms, ~2 ms, and ~50 µs, respectively. Thus, the reported fast-settling DCR achieves 40× faster settling than a traditional DCR.

The PGA noise was characterized in the low-gain mode, as shown in Figure 3.26. The measured noise matches with simulation results, where the in-band input-referred thermal noise is ~30 nV/√Hz. While most 1/*f* noise has been modulated out-of-band, there is residual 1/*f* noise from the cascode transistors in the OTA.

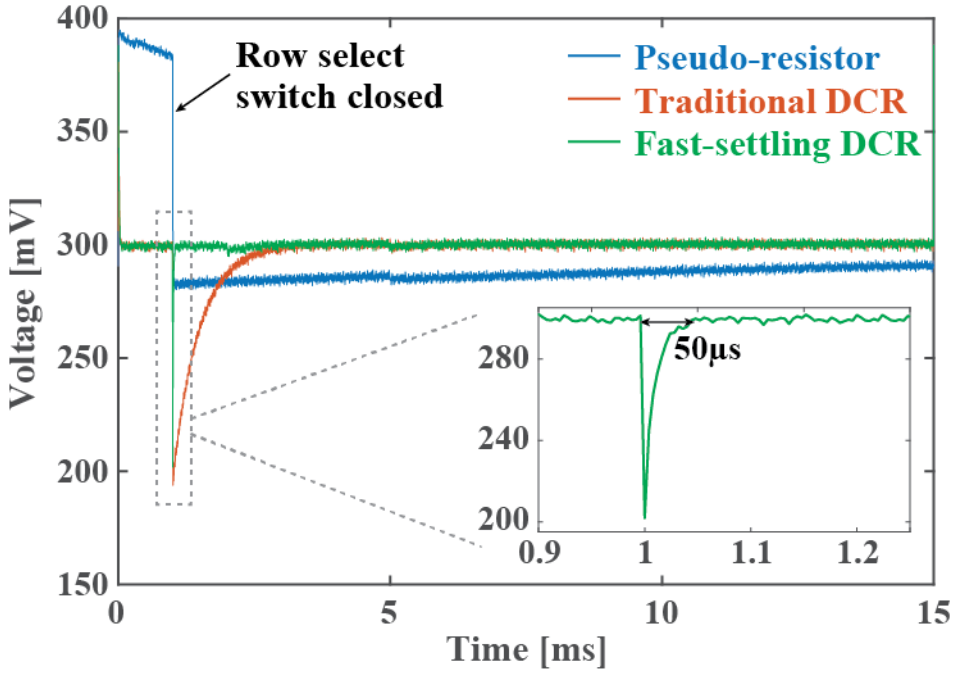

Figure 3.25 Measured settling time of pseudo-resistor, traditional DCR, and fast-settling DCR

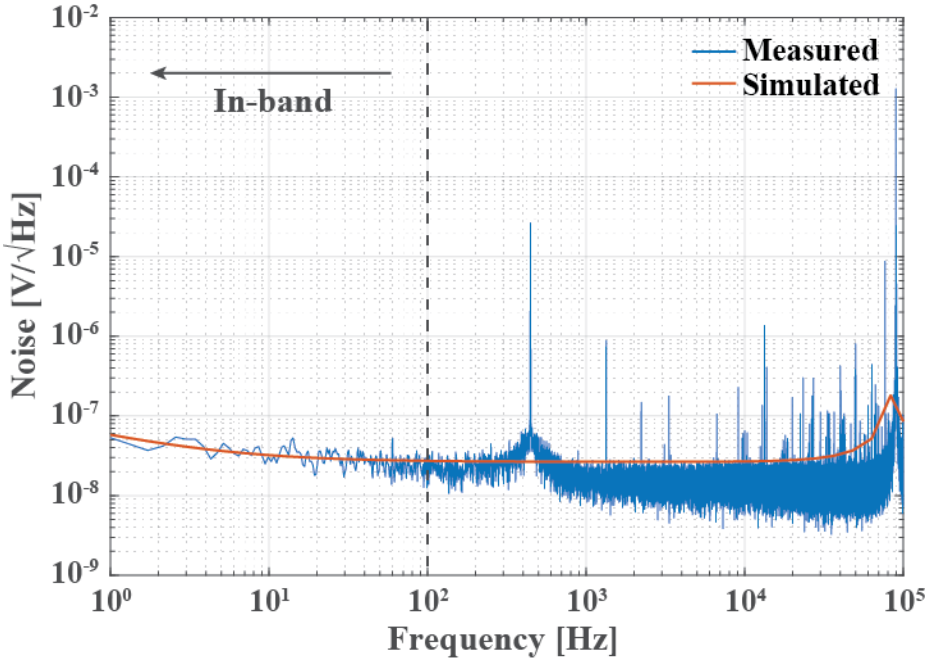

Figure 3.26 Measured and simulated noise spectra of the PGA

The HFIR was characterized by providing a sinusoidal input with an amplitude of 400 mV_{pp} and a frequency of 10 kHz. Figure 3.27 shows that the HFIR output, V_{ac}, follows

the input with an amplitude loss and a phase shift, resulting in a residual of 59 mV_{pp}. Therefore, the HFIR reduces the interference tone by 6.8×.

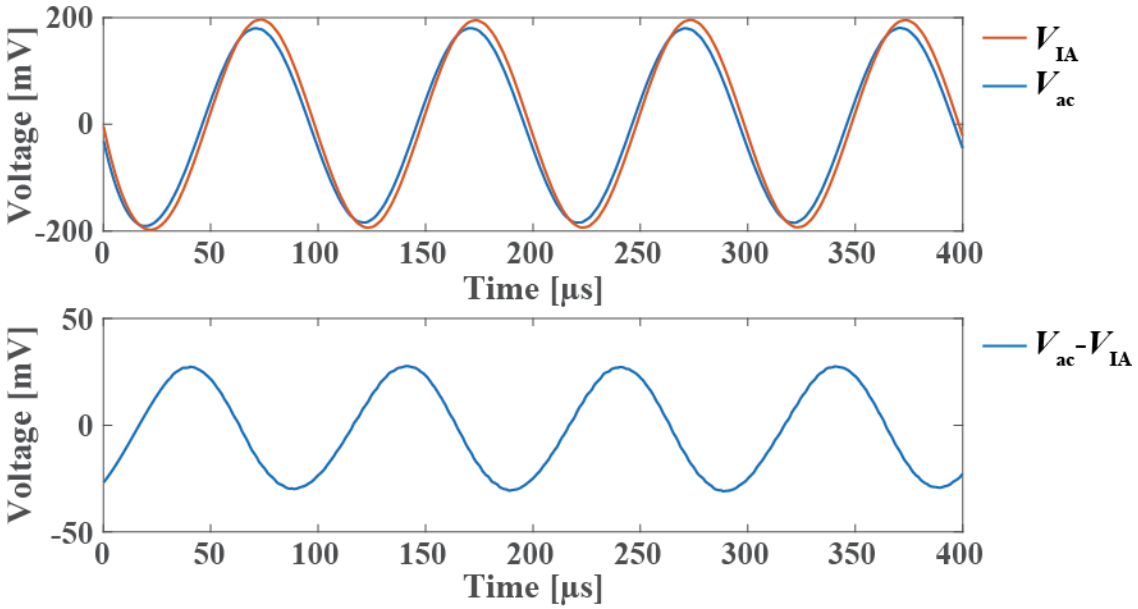

Figure 3.27 Measured HFIR transients

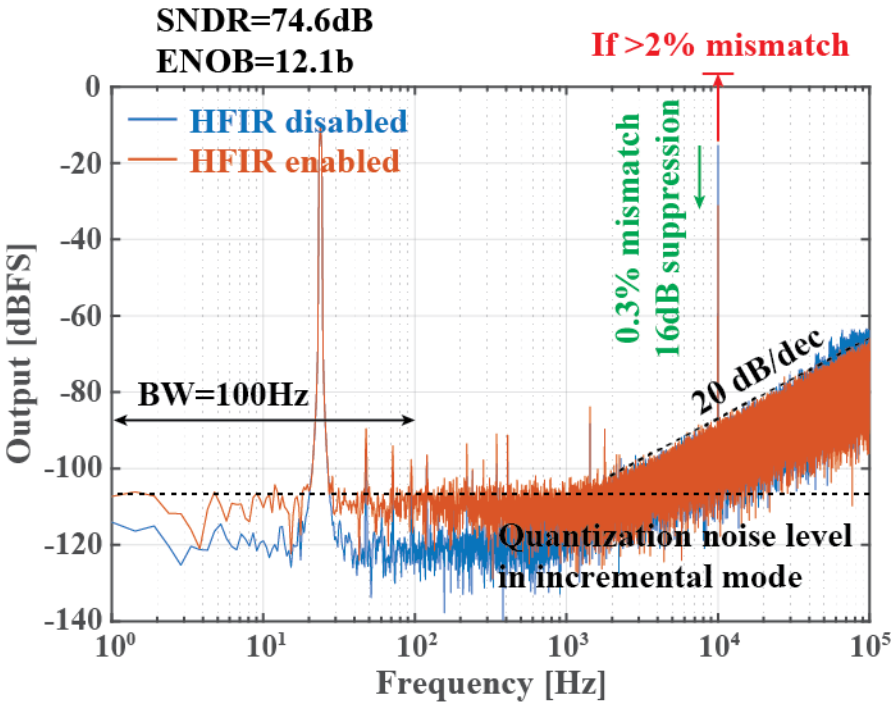

Figure 3.28 Measured ADC spectra with and without HFIR

The ADC achieves 74.6 dB SNDR and an ENOB of 12.1 bits within a 100 Hz bandwidth, as shown in Figure 3.28. Also evident from the spectra is the first-order noise shaping. The ADC was also measured with an in-band signal tone and an out-of-band interference tone at 10 kHz. The amplitude of the interference was calculated based on 0.3% R_0 mismatch to avoid saturating the ADC when the HFIR is disabled. The spectra demonstrate 16-dB suppression of the interference tone by the HFIR. Although the HFIR sampling increases the in-band noise, it is still comparable to the ADC quantization noise in incremental mode (-106 dBFS), which matches with the simulation results discussed in Section 3.3.4.

The HFIR sampling improves the ADC DR by reducing the ac swing from ΔR_0. In Figure 3.29(a), the ADC DR is improved by 10, 16, and >74 dB for 1.1%, 1.3%, and 2-10% mismatch, respectively. Figure 3.29(b) plots the ADC DR versus sensor mismatch. When the mismatch is <0.5%, the ADC DR is higher without the HFIR since the ac swing from mismatch is smaller than the added noise. However, when the mismatch is >0.5%, the HFIR sampling benefits the ADC by canceling the interference. When the mismatch is >2%, the ADC is saturated by the interference tone if the HFIR samping is disabled.

The readout time can be as fast as 11 ms, but it can also be traded off for higher sensitivity by averaging. Figure 3.30(a) shows the sensitivity versus readout time for different PGA gains. The spectra for the fastest readout and highest sensitivity are plotted in Figure 3.30(b) and (c), respectively. In the fastest readout mode, it takes 11 ms per acquisition and integrates 464 nT_{rms} noise in the high-gain mode, which corresponds to a 4.4 ppm sensitivity and a theoretical LOD of 9,280 MNPs (d = 50 nm). In contrast, the highest sensitivity mode takes 880 ms per acquisition but integrates only 111 nT_{rms} noise

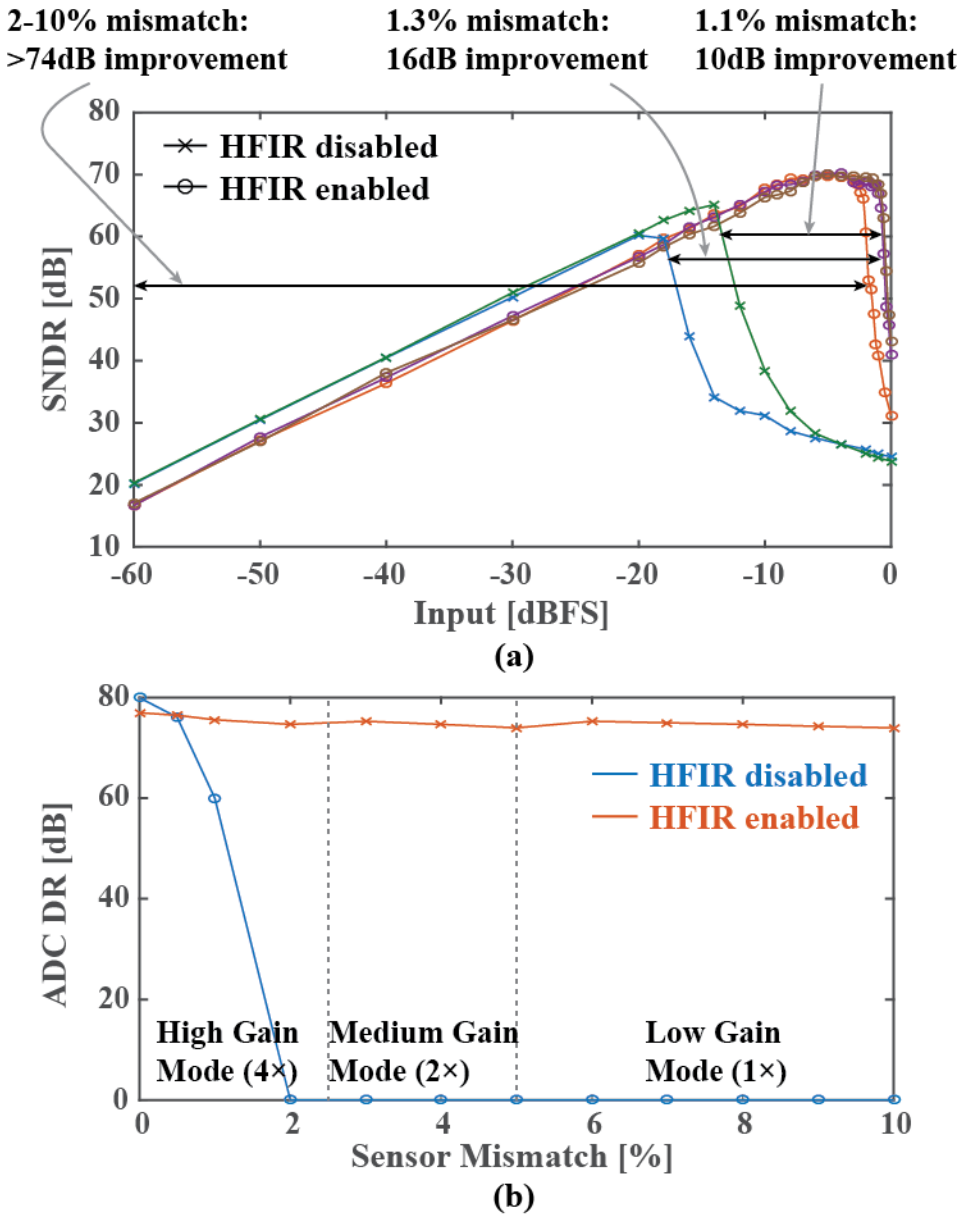

Figure 3.29 (a) Measured ADC SNDR under different sensor mismatch conditions and (b) ADC DR vs. sensor mismatch

corresponding to a sensitivity of 0.98 ppm and a theoretical LOD of 2,200 MNPs. Further increasing the acquisition time would not improve the sensitivity since the noise is limited by the 1/*f* noise and cannot be reduced by averaging.

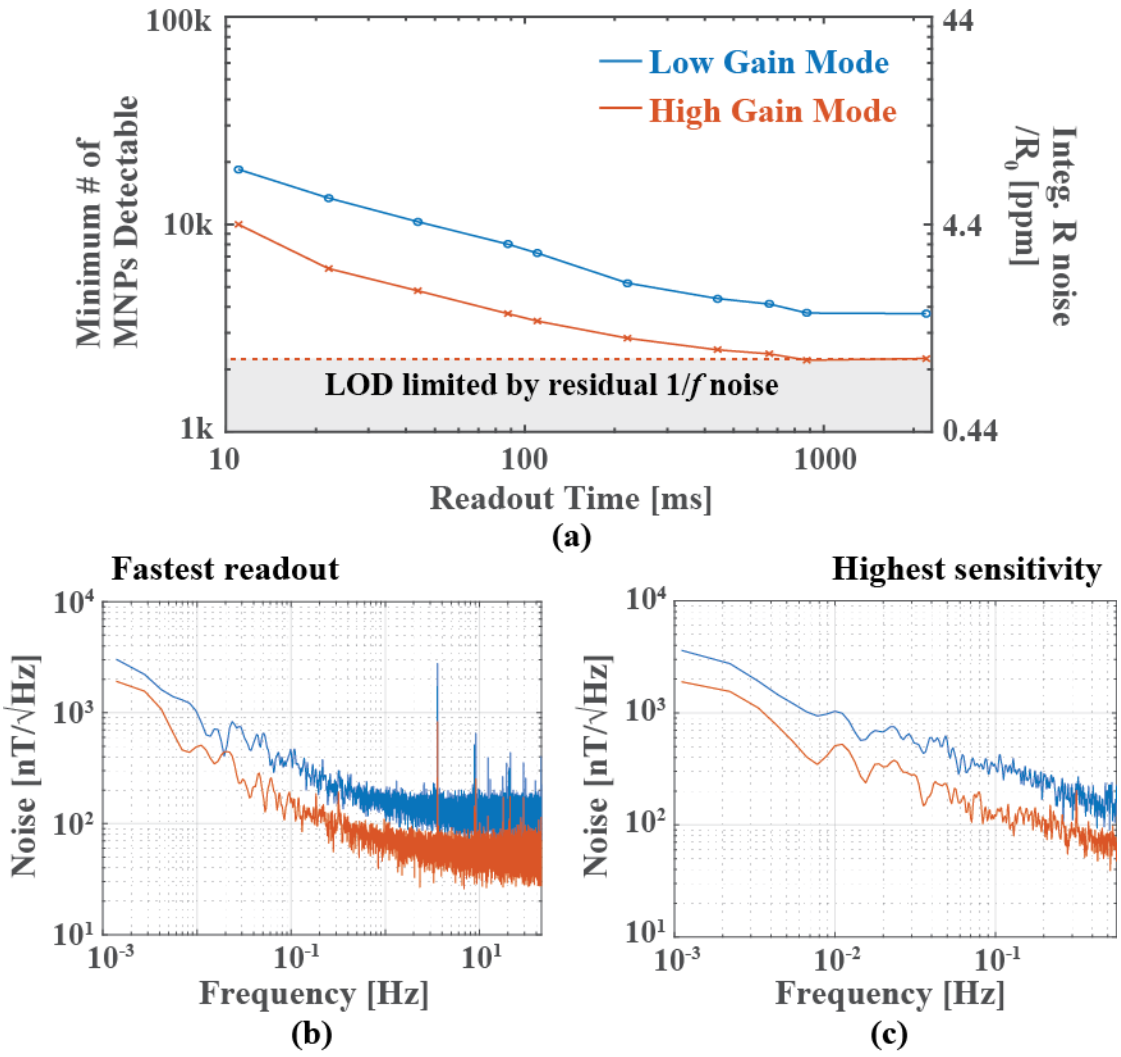

Figure 3.30 Measured system integrated noise

(a) Measured integrated noise vs. readout time for different gain modes. Measured input-referred noise spectra for (b) fastest readout (11 ms) and (c) highest sensitivity (880 ms).

Temperature sensitivity measurements are shown in Figure 3.31. Since a reference sensor is required in this AFE, to measure the temperature sensitivity of a standalone active sensor, a low temperature coefficient resistor with similar resistance as R_0 replaced the reference sensor. Cold IPA at 4 °C was dropped on sensor surface at t = 2 min, which caused a large temperature-induced signal (~240 ppm). The same experiment performed with the reference sensor caused only a negligible signal (10 ppm) demonstrating the ability to reject environmental common-mode interference.

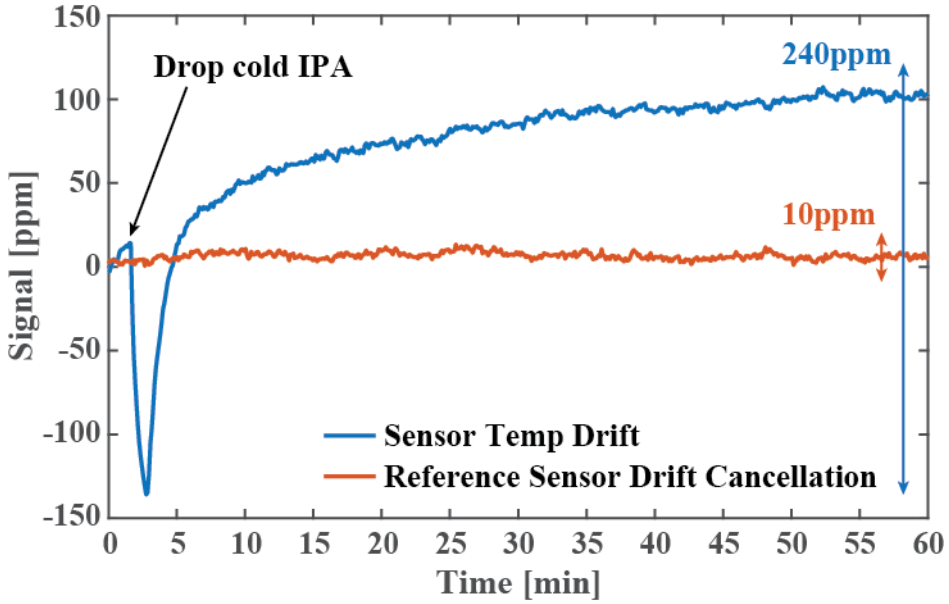

Figure 3.31 Measured temperature drift

3.4.3 Biological Measurement Results

Biological experiments were conducted to validate the system performance. Sensors were functionalized with Biotin-BSA as a positive control, a captured antibody for IL-6 as a sample under test, and BSA as a negative control. The reference sensor was covered by epoxy, preventing it from sensing signal from the MNPs. The sensor functionalization procedure is the same as the one discussed in Section 2.6.3.

Figure 3.32(a) shows overlaid transient measurement results for the negative control, positive control, and various concentrations of IL-6. In each assay, the sensors were washed with PBS 1 minute after starting and MNPs were added afterwards. The system continuously measured the real-time binding curves in the high-gain mode. After the binding curves saturated, a washing step (not shown in Figure 3.32(a)) was performed to remove any non-specific binding. Multiple experiments showed that the signal after washing did not drop indicating that the binding was highly specific. The averages of each

measurement (n = 6 sensors) are compiled to obtain the calibration curve shown in Figure 3.32(b). The resulting data is fit with a 4-parameter logistical (4-PL) regression with an R^2 value of 0.986. The LOD, calculated based on [112], is 0.96 pM.

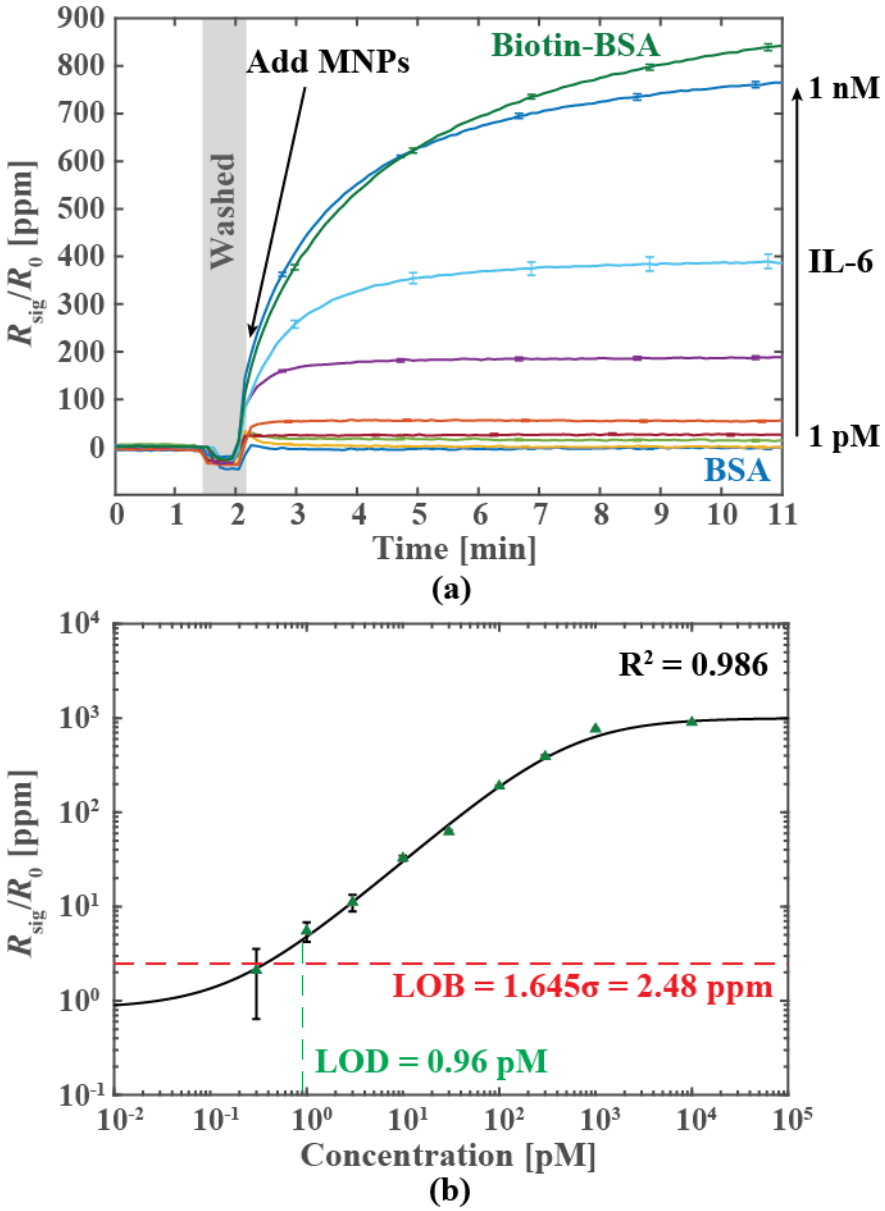

Figure 3.32 Biological experiment results

(a) Measured binding curves for negative control (BSA), positive control (Biotin-BSA), and IL-6 at different concentrations; (b) IL-6 calibration curve.

3.5 Conclusion

This chapter presented a GMR sensor AFE for MIA based on magnetometry. The design used a reference sensor to cancel most of the baseline and reject common-mode perturbation, such as temperature drift. A fast-settling DCR was presented to improve the system settling time by 40× comparing to a traditional DCR enabling fast readout. A HFIR sampling technique was embedded into the ADC to reject ac interference from sensor mismatch, thus improving the ADC equivalent DR to tolerate high sensor mismatch.

This work is summarized in Table 3.1 and compared to state-of-the-art magnetic sensor AFEs. Compared with other magnetometry-based designs such as Wheatstone bridge [96]–[98] and conventional double modulation architectures [52], [56], this work reported the HFIR sampling technique and the fast settling DCR to break the baseline rejection limit from sensor mismatch and reduce system settling time, respectively. As a result, this work achieves a 22.7× faster readout time, >7.8× lower input-referred baseline, and 2.3× lower power than other magnetometry-based AFEs. Although MRX-based designs inherently eliminate the baseline, their lower signal amplitude and higher input-referred noise confound high sensitivity measurements. Most importantly, this design can tolerate up to 10% sensor mismatch making it compatible with commercial tolerances for MR sensor fabrication. Finally, the achieved sub-ppm sensitivity and three order biological DR make this work ideal for multichannel, high sensitivity, PoC diagnostic systems.

Chapter 3, in part, is based on materials from Xiahan Zhou, Michael Sveiven, and Drew A. Hall, “A Fast-Readout, Mismatch-Insensitive Magnetoresistive Biosensor Front-End Achieving Sub-ppm Sensitivity,” *IEEE International Solid-State Circuits Conference*

Table 3.1 Comparison of the current state-of-the-art magnetic sensor AFEs

	H. Wang ISSCC'09 [48]	S. Gambini JSSC'13 [51]	T. Costa TBCAS'17 [53]	S.J. Han ISSCC'07 [52]	D.A. Hall JSSC'13 [56]	**This work**
Sensor Type	LC	Hall	GMR	GMR	GMR	**GMR**
Sensor R_0 (kΩ)	N/A	N/A	0.85	N/A	1.92	**0.15**
MR Ratio (%)	N/A	N/A	5.37	N/A	9.2	**9.04**
MNP Size (nm)	1,000	1,000	250	50	50	**50**
Technology Node (μm)	0.13	0.18	0.35	0.25	0.18	**0.18**
Sensing Method	Magneto	MRX	Magneto	Magneto	Magneto	**Magneto**
AFE Architecture	LC oscillator	V/I Converter	Amplifier	Mixer + PGA	TIA	**PGA with Mixer**
ADC Architecture	VCO-based	Inc. ΔΣ	No ADC	No ADC	ΔΣ	**Inc. ΔΣ with HFIR**
Input-referred Noise (nT/√Hz)	N/A	270	11.5Ψ	N/A	49	**107.1 (low gain) 46.4 (high gain)**
Readout Time/Ch. (ms)	400	50	1,000	250	250	**11**
Power/Ch. (mW)*	N/A	0.825	4.9Ψ	N/A	3.15	**1.39**
Area/Ch. (mm^2)	N/A	0.012	3.17	N/A	0.219	**0.249**
Sensor Mismatch Tolerance	N/A	N/A	N/A	N/A	N/A	**10% (low gain) 2.5% (high gain)**
Input-referred Baseline (mT)	N/A	0.007	1.84	N/A	7.09	**<0.235**
Temperature Correction	Yes	Yes	No	Yes	Yes	**Yes**

* Power/Ch does not include sensor bias and magnetic field generator. Ψ Does not include ADC.

(ISSCC), San Francisco, CA Feb. 17-21, 2019 [80], and Xiahan Zhou, Michael Sveiven, and Drew A. Hall, "A CMOS Magnetoresistive Sensor Front-End with Mismatch-Tolerance and Sub-ppm Sensitivity for Magnetic Immunoassays," *IEEE Transactions on Biomedical Circuits (TBioCAS)*, Dec 2019 [57]. The dissertation author was the primary investigator and author of these papers.

Chapter 4. A DISCRETE GMR BIOSENSING SYSTEM FOR DETECTING MAGNETO-RELAXATION

4.1 Introduction

In this chapter, a time-domain magneto-relaxometry (MRX) biosensing scheme is presented using GMR sensors to measure the relaxation response of MNPs in a pulsed magnetic field. The biosensor system consists of an 8×10 GMR sensor array, a Helmholtz coil, an electromagnet driver, and an integrator-based AFE needed to capture the fast relaxation dynamics of MNPs. A custom designed electromagnet driver and Helmholtz coil improve the switch-off speed to >5 Oe/μs, limiting the deadzone time to <10 μs, and thus enables the system to monitor the fast relaxation processes of 30 nm MNPs. A magnetic correlated double sampling (MCDS) technique is presented to reduce sensor-to-sensor variation by 99.98% while also reducing temperature drift, circuit offset, non-linearity below the noise level. An optimum integration time is calculated and

experimentally verified to maximize the SNR. Experiments with dried MNPs have shown successful relaxation detection, and MIA experiments have demonstrated their binding kinetics. To the best of the author's knowledge, this is the first time that GMR sensors have been reported for an MRX bioassay.

4.2 Relaxation Signal Analysis

While the basic theory of operation for MRX was introduced in Section 2.4, it is re-addressed here for deeper understanding, as shown in Figure 4.1. In the absence of an external magnetic field, the magnetic moment of the superparamagnetic nanoparticles tethered to the surface of the sensor are randomly oriented resulting in zero net field. Then, a magnetic field, H_{A}, is applied that magnetizes and aligns all the MNPs. The stray field from the MNP opposes the applied field resulting in a small change in resistance in the underlying MR sensor (Figure 4.1(a)). Note, this is the region of operation for magnetometry. However, in MRX, the applied magnetic field is then switched off and the sensors monitored as the MNPs gradually relax to their equilibrium state (Figure 4.1(b)). This relaxation occurs due to Néel and Brownian relaxation. For Brownian relaxation, the magnetization vectors undergo rigid rotation of the whole particle due to Brownian motion [113]. However, the MNPs here are tethered to the surface and thus have limited movement [114]. Instead, the MNPs must undergo Néel relaxation, where internal domain movement results in gradual randomization of the moment [115]. Note that the GMR sensor also exhibits Néel relaxation, but is orders of magnitude faster than the MNPs, allowing one to use the relaxation signature to detect the number of tethered MNPs. This relaxation signal can be either measured in the frequency- or time-domain. Frequency-domain MRX measures the complex magnetic susceptibility as function of frequency in

an alternating magnetic field [116], whereas time-domain MRX directly measures the relaxation signal in response to a pulsed magnetic field [50], [51]. One of the significant challenges in time-domain relaxation is the need to collapse the applied magnetic field faster than the relaxation of the MNPs, which can be in the nanosecond to millisecond range depending on the size and material composition of the MNPs [117]–[119]. In a PoC setting, the time-domain technique generally leads to a simpler implementation, thus is used in this work.

Once the MNP is magnetized and the field is removed, there is insufficient energy to keep the MNP moment fixed. There are two mechanisms by which this loss of energy, or relaxation process, can occur. With two competing processes, the relaxation time will

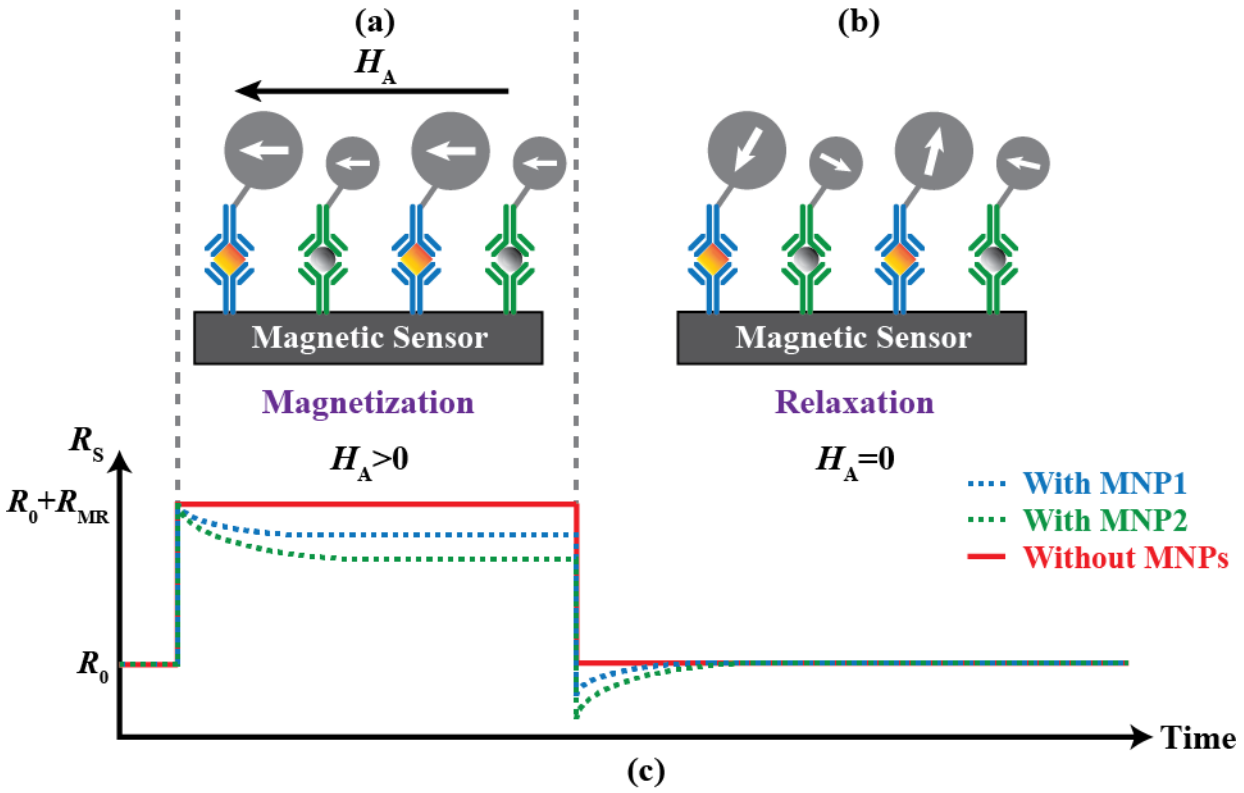

Figure 4.1 Illustration of time-domain MRX

(a) Magnetization phase (H_A > 0) where the MNP magnetic moments are aligned to the applied field. (b) Relaxation phase (H_A = 0) where the MNP magnetic moments gradually randomize. (c) The corresponding resistance of an MR sensor in response to H_A with and without MNPs.

depend on the faster of the two mechanisms. Néel relaxation follows an exponential decay relationship when the MNPs are monodisperse [120]–[123], and depends on the core volume and anisotropy of the MNP that is described as

$$\tau_{\mathrm{N}} = \tau_0 \exp\left(\frac{KV}{k_{\mathrm{B}}T}\right) \quad 4.1$$

where τ_0 is the attempt time (usually approximated as 10^{-9} sec), K is the anisotropy constant of the MNP, V is the core volume of the MNP, k_{B} is Boltzmann's constant, and T is the absolute temperature. This relationship becomes natural log-like when considering particle-particle interactions and the size/shape distributions of the MNPs [120]–[126]. The time course magnetization during relaxation can be empirically described by

$$M_{\mathrm{N}}(t) = \kappa a M_0 \ln\left(1 + \frac{t_{\mathrm{c}}}{t}\right) \quad 4.2$$

where κ is the coverage, a is a constant related to the magnetic viscosity, M_0 is the initial MNP magnetization before the applied magnetic field is removed, t is the time after turning off the field, and t_{c} is the characteristic time that has a strong dependence on the applied magnetic field (H_{A}) and magnetization time (t_{mag}). It has been reported that $t_{\mathrm{c}} \approx t_{\mathrm{mag}}$ when the applied field is relatively small (H_{A} = 0.1 Oe) [114]. However, this has not been measured for more moderate magnetic fields that are appropriate for MR biosensing (20-100 Oe).

4.3 System Overview

4.3.1 System Architecture

A block diagram of the reported MRX detector is shown in Figure 4.2. A PC provides a user-defined magnetization time and magnetic field amplitude to the PC-FPGA interface. The FPGA controls the timing of the electromagnet and readout circuitry. The power amplifier (PA) provides a dc current, I_0, to the electromagnet driver that delivers a pulsed current, I_{COIL}, to the Helmholtz coil, generating a pulsed magnetic field for the sensor chip located in the center. The AFE captures the resulting sensor response and transfers the data to the PC for post-processing.

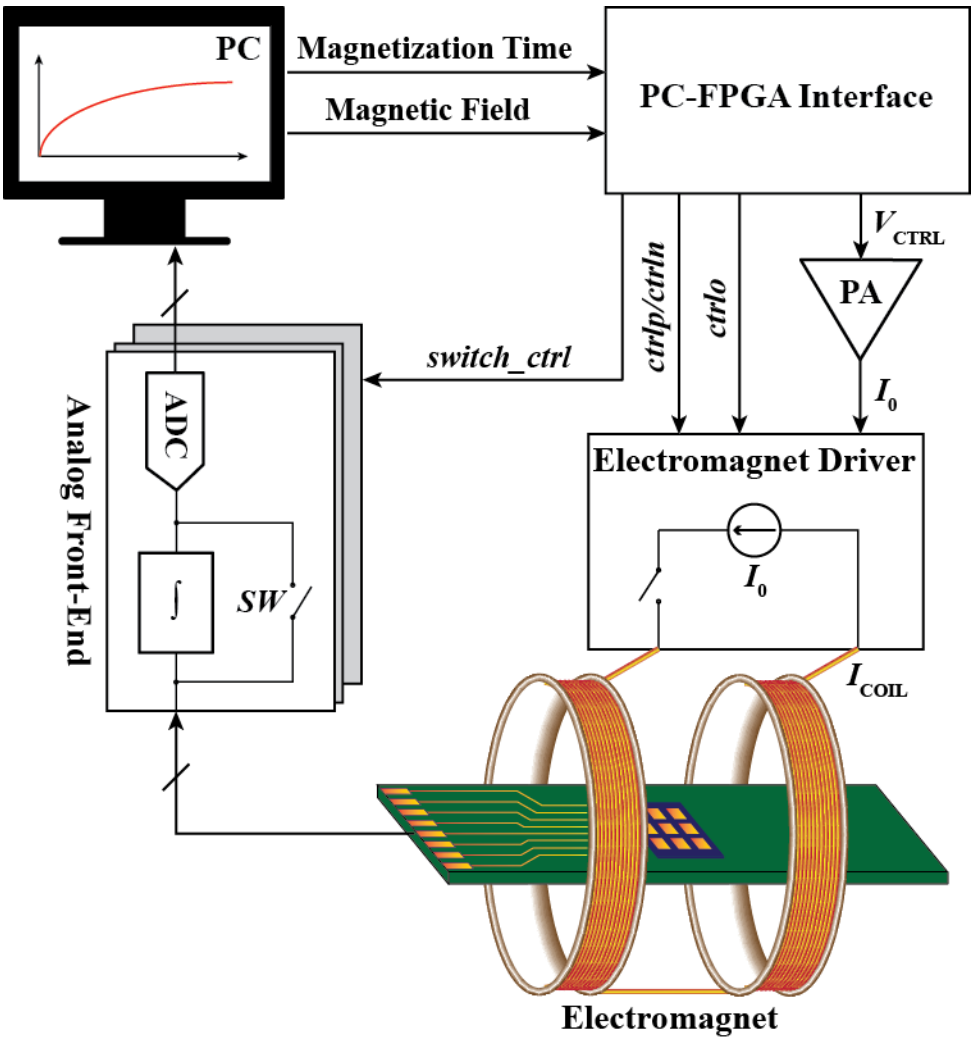

Figure 4.2 Block diagram of the relaxation detection system

The architecture of the readout circuitry is illustrated in Figure 4.3. All the columns of the 8×10 sensor array are connected to a column switching matrix that connects one column to V_{IN} and all others to a common-mode voltage, V_{CM}. Each of the rows is connected to an AFE consisting of a switched integrator and an ADC. The reference generator, the same as the one discussed in Section 2.6.1, produces voltages $V_{IN} = V_{CM} + V_B$ and $V_{INB} = V_{CM} - V_B$, for the switched integrators.

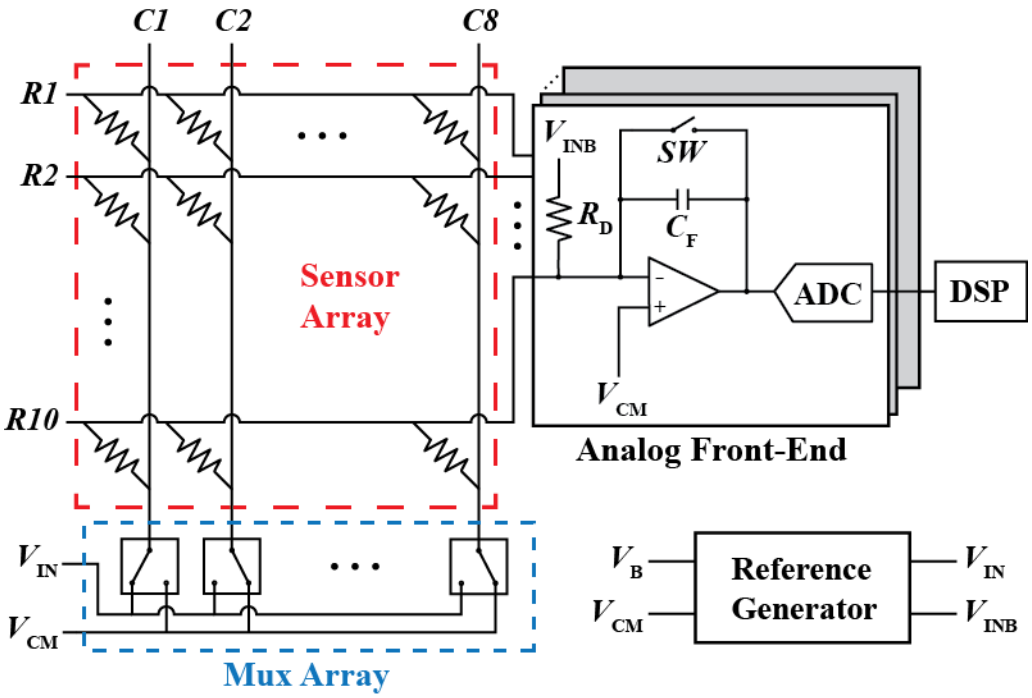

Figure 4.3 Sensor array and readout architecture

4.3.2 Magnetic Correlated Double Sampling

Despite eliminating the MR baseline, detecting the minute relaxation signal in the presence of a large R_0 baseline is still challenging. Traditional techniques, such as a Wheatstone bridge [127]–[129], require a matched reference sensor, which is challenging to control for GMR sensors [73]. Moreover, circuit imperfections, such as amplifier offset and non-linearity, can further limit the sensitivity of the whole system. To extract the

relaxation signal from these error sources, a MCDS technique is applied, as shown in Figure 4.4. The magnetic field is initially off and the integrator reset switch *SW* is closed. Then the magnetic field is turned on for a duration of t_{mag}, while *SW* remains closed (leaving the op-amp in unity gain configuration), therefore $V_{OUT} = V_{CM}$. Next, the magnetic field is turned off and the reset switch is opened simultaneously, resulting in V_{OUT} decaying. The integration time, t_{int}, is determined by the sensor resistance, R_0, and thus can be different due to sensor-to-sensor variation. This process is repeated in the subsequent cycle, except that the magnetic field remains off. Thus, the first cycle has the magnetic relaxation signal whereas the second does not.

The sensor response and V_{OUT} in both cycles are shown in Figure 4.4(b) and (c), respectively. When the magnetic field is turned off, the sensor resistance returns to R_0 slowly due to the relaxation of the MNPs. Therefore, instead of a linear decay of V_{OUT} in the case without field, V_{OUT} is distorted at the beginning of integration and returns to linear decay when the relaxation of the MNPs is completed. By subtracting V_{OUT} with and without the field, the integrated relaxation signal can be extracted.

This technique removes the sensor-to-sensor variation since each sensor is self-referenced. While temperature may cause sensor resistance drift with time, the change is very slow compared to the period of cycle, T_{CYC}. Therefore, MCDS is able to reduce the effect of temperature drift dramatically without the need for other temperature compensation techniques [73]. By selecting T_{CYC} as a multiple of the power line frequency, the 60 Hz interference in the two adjacent cycles will be in phase and thus rejected as well. This technique is also effective at eliminating errors such as the circuit offset and non-linearity since these errors are consistent in every cycle.

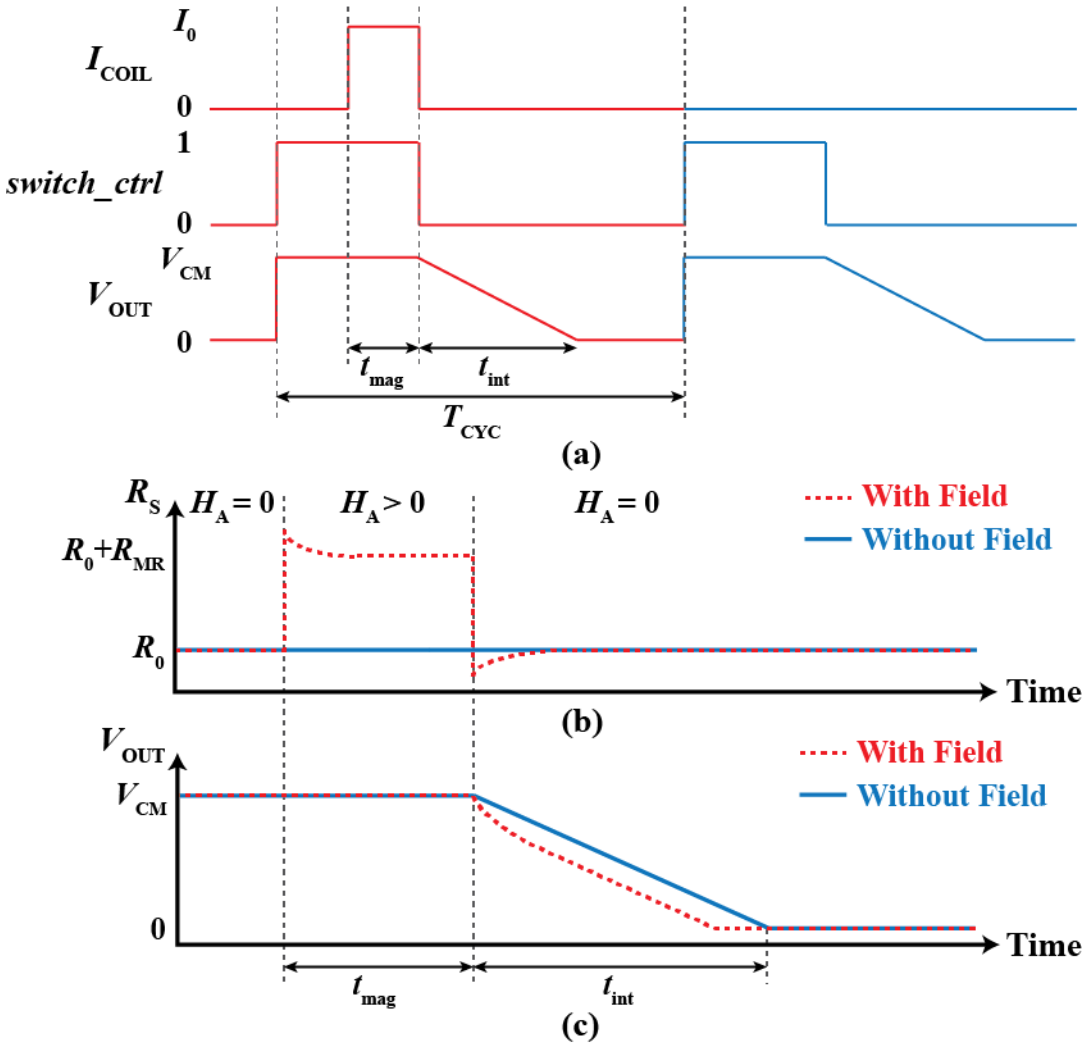

Figure 4.4 Illustration of MCDS

(a) Timing diagram of coil current, integrator switch control, and integrator output voltage; (b) sensor response to MCDS; and (c) integrator output voltage with and without a field applied.

4.4 Analog Front-End Implementation

4.4.1 Circuit Implementation

In prior work, time-domain relaxation measurement techniques used amplifiers to detect the relaxation signal with Hall-effect sensors [50], [51]. However, since the relaxation signal is largest at the time when external field is turned off and gradually decreases with time, traditional amplifier-based MRX requires a high sampling-rate ADC

to capture the dynamics. Since a high-resolution ADC is often needed to reduce the quantization error, integrators are applied to relax the bandwidth requirement of the ADC by integrating the relaxation signal with time. Figure 4.5 shows the switched integrator which consists of an op-amp with capacitive feedback, a reset switch, and a bleed resistor, R_D. Since the GMR sensors typically have an MR ratio of ~9%, there will be a substantial portion of the current flowing into the integrator that does not respond to the magnetic field and would limit the DR. To remedy this issue, a cancellation network that consists of R_D that bleeds off part of the baseline current has been added, so that a smaller feedback capacitor, C_F, can be used for the same integration time, t_{int}. R_D is selected ~10% lower than R_0 to account for process variation, and $V_{IN} = V_{CM} + V_B$ and $V_{INB} = V_{CM} - V_B$ where V_{CM} is a fixed common-mode voltage and V_B is an adjustable bias voltage. Consequently, in the integration phase, the output voltage V_{OUT} is

$$V_{\mathrm{OUT}} = V_{\mathrm{CM}} - \frac{1}{C_{\mathrm{F}}} \int \frac{V_{\mathrm{B}}}{R_0 + \Delta R(t)} - \frac{V_{\mathrm{B}}}{R_{\mathrm{D}}} dt \qquad 4.3$$

where $\Delta R(t)$ represents the sensor response due to the MNP relaxation. An ADC measures V_{OUT} after an anti-aliasing filter that is composed of R_{AAF} and C_{AAF}. Assuming $R_0 >> \Delta R(t)$, the relaxation signal after MCDS, ΔV_{OUT}, can be derived as

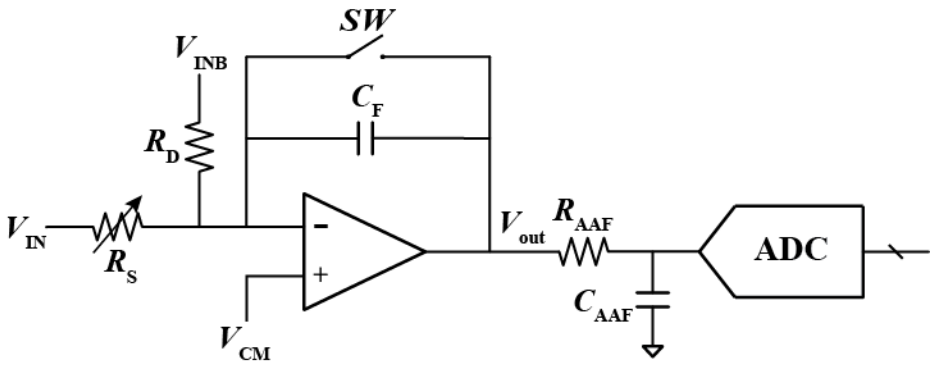

Figure 4.5 Schematic of the switched integrator

$$\Delta V_{\mathrm{OUT}} = V_{\mathrm{OUT|without\ field}} - V_{\mathrm{OUT|with\ field}}$$
$$= \frac{V_{\mathrm{B}}}{C_{\mathrm{F}}} \int \frac{1}{R_0 + \Delta R(t)} - \frac{1}{R_0} dt \cong -\frac{V_{\mathrm{B}}}{R_0^2 \cdot C_{\mathrm{F}}} \int \Delta R(t) dt. \quad 4.4$$

Therefore, increasing V_B and decreasing C_F improves the signal, but is limited by the sensor breakdown voltage and the integration time.

4.4.2 Noise Analysis

The equivalent schematic for noise analysis is shown in Figure 4.6. Since the parasitic capacitance at the inverting node of the op-amp is much smaller than C_F, the reset noise of the integrator is negligible [130]. In addition to the sensor under test, R_S, all other sensors, R_{S1}-R_{S7}, in the same row contribute to the noise due to the matrix configuration. The noises contributed by V_{CM}, V_{IN}, and V_{INB} are experimentally verified to be negligible due to the low bandwidth. Thus, the output-referred noise can be derived as

$$v_{\mathrm{n,out}}^2 = \left(\frac{1}{2\pi f C_{\mathrm{F}}}\right)^2 \left(8{i_{\mathrm{n,Rs}}}^2 + \frac{4k_{\mathrm{B}}T}{R_{\mathrm{D}}}\right) + \left(\frac{9}{2\pi f R_{\mathrm{S}} C_{\mathrm{F}}} + 1\right)^2 {v_{\mathrm{n,op}}}^2 \quad 4.5$$

where $i_{n,Rs}$ represents the current noise contributed by each sensor and $v_{n,op}$ represents the voltage noise contributed by the op-amp. Both $i_{n,Rs}$ and $v_{n,op}$ include white noise and 1/f noise. Therefore, decreasing C_F increases the noise, which contradicts with the signal gain analysis shown in Equation 4.4.

However, both C_F and V_B affect the integration time, t_{int}. While increasing t_{int} increases the signal amplitude because there is more time to integrate relaxation signal, it also increases the integrated noise by reducing the lower limit of integration f_{min}, where $f_{min} = 1/t_{int}$. Moreover, since 1/f noise dominates the low frequency band and the relaxation

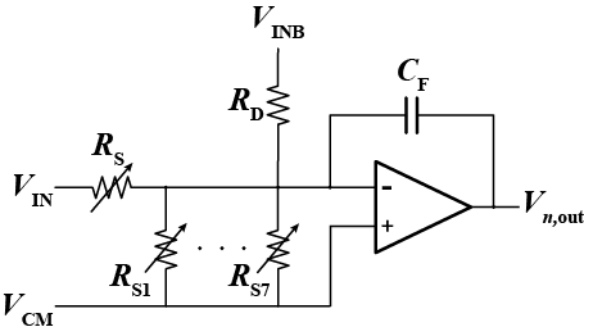

Figure 4.6 Equivalent schematic for noise analysis

signal decays with time, increasing t_{int} would improve the SNR when t_{int} is short but reduce the SNR when t_{int} is long. Hence, for a given sensor and relaxation time of MNPs, there exists an optimum t_{int} that needs to be determined.

4.5 Electromagnet Driver Implementation

4.5.1 Circuit Implementation

The finite switching time of the magnetic field results in a deadzone where measurements cannot be taken. To minimize the deadzone time to detect MNPs with fast relaxation, the switch-off response of the magnetic field needs to be as fast as possible. However, this requirement is at odds with typical methods of generating magnetic fields that result in large inductances. Both stripelines [131] and miniaturized coils [132], [133] have been used for achieving a fast switch-off response due to their low inductance. However, stripelines are incapable of generating large magnetic fields (3.2 Oe in [131]) and miniaturized coils require complex micromachining techniques. Helmholtz coils, on the other hand, can generate in-plane fields up to 100 Oe, are easy to fabricate, and facilitate proper sensor alignment due to their geometry [134]–[136]. However, the large inductance of a Helmholtz coil limits the bandwidth, making the fast switching difficult.

There are two methods to discharge the stored energy in an electromagnet: passively and actively. To passively discharge the electromagnet, both sides of the electromagnet are placed at the same potential and the current in the electromagnet can be written as: $I(t) = I_0 \exp(-t/\tau)$, where I_0 is the initial current and $\tau = L/R$ is the time constant. Given that Helmholtz coils usually have large L and small R by design, this results in a large τ and slow decay of the current. Alternatively, the energy can be actively removed by connecting a negative voltage source V, accordingly $I(t) = I_0 - (V/L)t$. With a large enough V, this technique can rapidly remove the energy stored in the electromagnet within 0.01τ, ~1,000× faster (Figure 4.7).

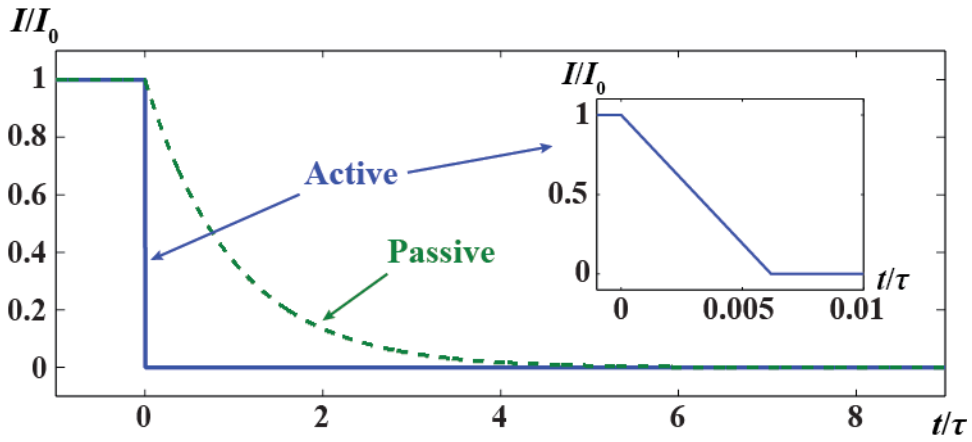

Figure 4.7 Comparison of energy dissipation methods

Based on the active discharge technique, a novel electromagnet driver was designed, as shown in Figure 4.8(a). To the first order, the electromagnet can be modeled as an inductor in series with a resistor. The driver is operated in two phases and controlled by pulse width modulation (PWM) signals *ctrln* and *ctrlp* through power MOSFET switches M_N and M_P. The reverse current elimination (RCE) path, which consists of M_O, *ctrlo*, and D_4, will be discussed later.

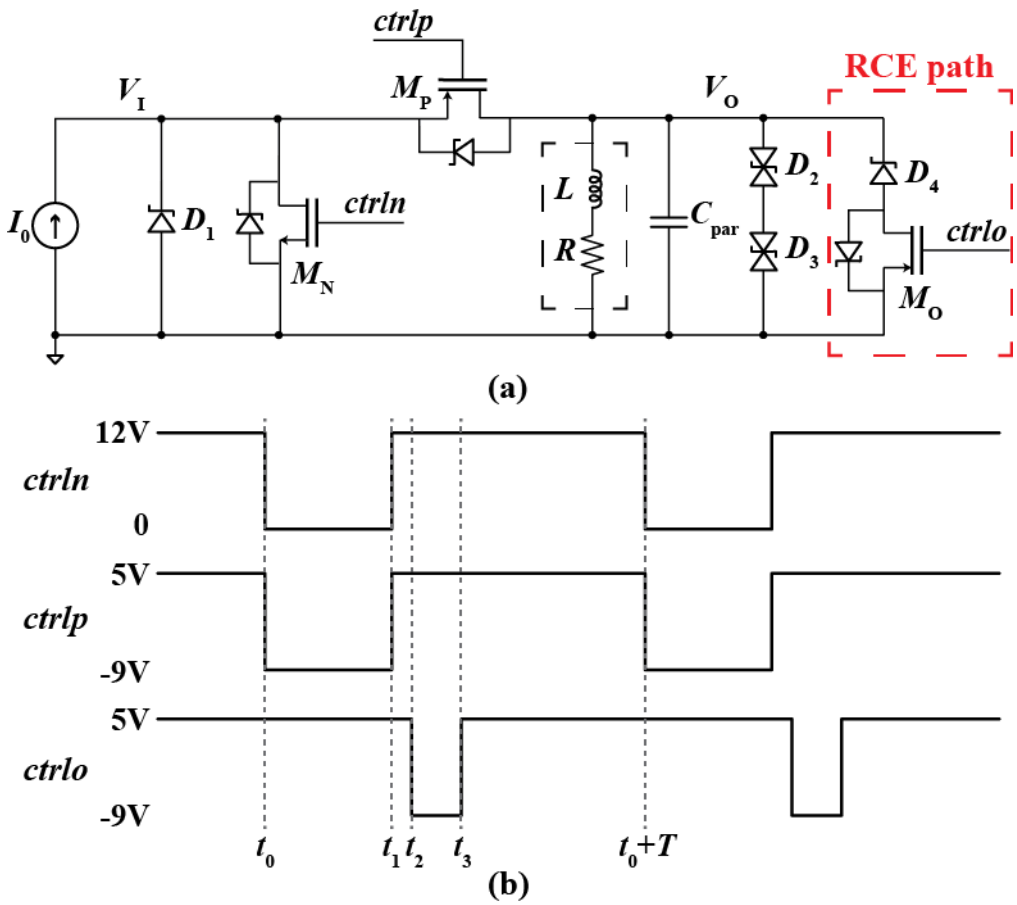

Figure 4.8 Electromagnet driver

(a) Schematic of electromagnet driver implementing active discharge and (b) timing diagram of control signals.

As shown in Figure 4.8(b), during the charge phase ($t_0 – t_1$), *ctrln* and *ctrlp* are both low, therefore M_N is off and M_P is on. A dc current I_0 flows into the electromagnet through M_P. To discharge the electromagnet ($t_1 – t_0 + T$), *ctrln* and *ctrlp* are both high, therefore M_N is on and M_P is off. Transient voltage suppression (TVS) diodes D_2 and D_3 clamp V_O at a negative voltage of -500 V, which generates a low impedance path to rapidly remove the stored energy. While the negative voltage should be as large as possible to achieve a fast switch-off response, it is limited by both the electromagnet breakdown voltage and the drain-source breakdown voltage of M_P. Meanwhile, I_0 flows to ground through M_N, and diode D_1 protects M_N and the current source from large transient voltage spikes.

The reported topology can speed up the switch-off response significantly, but comes with a reverse current, as shown in Figure 4.9(a). After the energy stored in the coil has been fully dissipated, V_O is expected to rise back to 0 V. However, the parasitic capacitance, C_{par}, from the electromagnet, TVS diodes, MOSFET M_P, and PCB prevents V_O from instantly returning to 0 V. Since there is no external source to charge C_{par}, current is pulled out of the coil during T_{REV}. Therefore, after I_{COIL} drops down to 0 A, the negative V_O continues "discharging" the electromagnet, resulting in a reverse current whose magnitude keeps increasing until V_O reaches 0 V. Making this issue worse, as $|V_O|$ decreases from 500 V to 0 V, the low-impedance path generated by D_2 and D_3 is broken. The reverse current must be dissipated as heat by the electromagnet resistance and thus lingers for a comparatively long time. This phenomenon was observed experimentally and was also discussed in [137]. In this application, this reverse current and the associated magnetic field is not acceptable as it magnetizes the MNPs, instead of allowing them to relax to equilibrium.

The solution is to reduce T_{REV} by forcing V_O to 0 V. To facilitate this, an RCE path is added at the output node in parallel with the electromagnet and TVS diodes (red dotted box in Figure 4.8(a)). The RCE path operates as follows: as soon as the energy in the electromagnet is fully dissipated, M_O is turned on, providing an alternative low-impedance path to charge C_{par}. This pulls V_O back to 0 V quickly, eliminating the reverse current. D_4 is needed to prevent unwanted current flow during the charge phase. The signal timing is illustrated in Figure 4.9(b). It should be noted that the turn-on time ($t_1 – t_2$) is nearly equal to the coil switch-off time, given that the rise and fall time of these signals are similar as confirmed through simulation and verified experimentally.

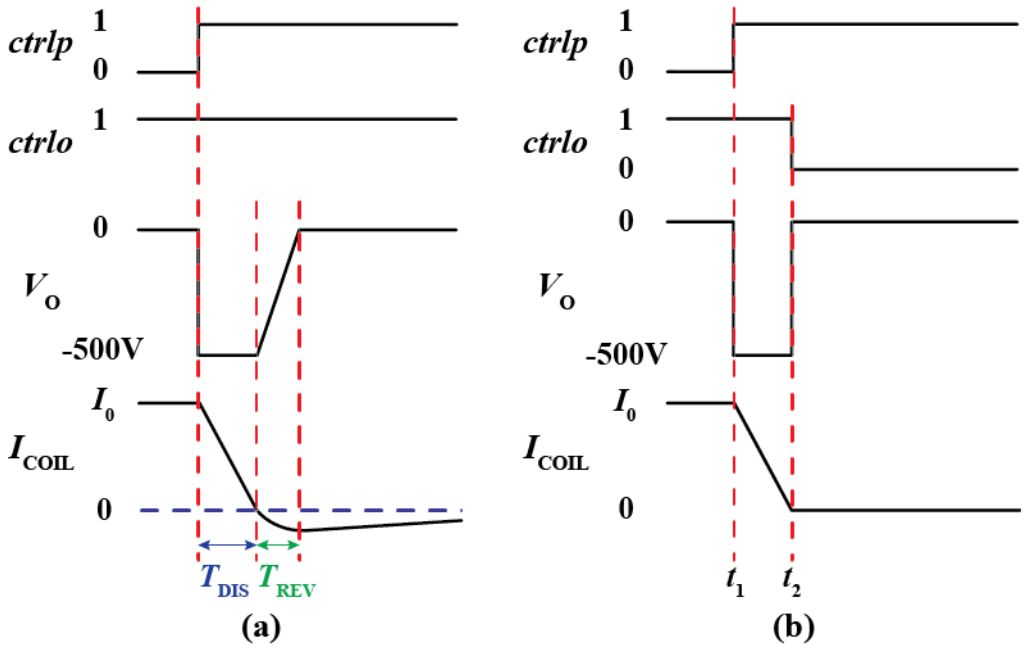

Figure 4.9 Reverse current elimination method

(a) Reverse current due to parasitic capacitance; (b) RCE path eliminates the reverse current.

The timing of *ctrlo* is critical and requires a sub-microsecond resolution for microsecond field switching times. Early turn-on causes V_O to start returning to 0 V too early when the energy stored in the electromagnet has not been fully dissipated. Without a large negative V_O, the residual current will decay exponentially with time constant of L/R, resulting in a long switch-off time. On the other hand, if *ctrlo* arrives late, the reverse current cannot be fully removed.

4.5.2 Timing Calibration

While inductor-current zero-crossing detection methods have been demonstrated to achieve high-accuracy timing control [138], [139], they all require additional detection circuits. In this case, the zero-crossing detector is not needed since the correct timing can be derived as

$$t = t_{\mathrm{os}} + \frac{I_0 L}{|V_{\mathrm{m}}|} \tag{4.6}$$

where t_{os} is the offset time that is determined by the circuit delay and V_m is the output voltage during switching-off, which is -500 V in this design.

For a given electromagnet, L and V_m are fixed. To use Equation 4.6 to calculate the turn-on delay, t, based on a given current, I_0, the offset time, t_{os}, which is highly dependent on C_{par}, must be measured. The measurement procedure is as follows:

1) Choose a current I_0, turn M_O off, and measure how long it takes I_{COIL} to drop to 0.
2) With this time as M_O turn-on time, verify that the reverse current can be eliminated.
3) Calculate t_{os} using the known parameters.

This calibration procedure only needs to be done once per electromagnet to determine t_{os}, after which the timing can be calculated for different current values.

In addition to the electromagnet driver, optimizing the Helmholtz coil is critical to further improve the switch-off speed. The magnetic field intensity generated by a Helmholtz coil, H, and the inductance of the Helmholtz coil, L, can be derived as

$$H = 10^4 (0.8)^{2/3} \frac{\mu_0 n I}{R} \tag{4.7}$$

$$L = \frac{2R^2 n^2}{9R + 10W} \tag{4.8}$$

where R is the radius of each coil, n is the number of turns, μ_0 is the permeability of free space, and W is the distance between the two coils. By combining Equations 4.6 – 4.8, the switch-off time can be derived as

$$t = t_{os} + \frac{2R^3Hn}{10^4(0.8)^{2/3}\mu_0 V_m(9R + 10W)}. \quad 4.9$$

Therefore, for a fixed magnetic field, fewer turns, and/or a smaller radius result in faster switching time. However, the minimum radius is dictated by the sensor size. Fewer turns results in lower inductance and larger current with the maximum current usually limited by the heat dissipation.

4.6 Measurement Results

4.6.1 System Implementation

This system was implemented using an FPGA (Opal Kelly XEM6310), a Data Acquisition Card (DAQ, NI PCIe-6351), a PA (Kepco BOP 36-12ML), a custom designed Helmholtz coil, and two PCBs, as shown in Figure 4.10. The DAQ has 8 analog input channels with 16-bit ADCs and 2 analog output channels with 16-bit DACs. The input channels were used to acquire the outputs of the integrators and the output channels

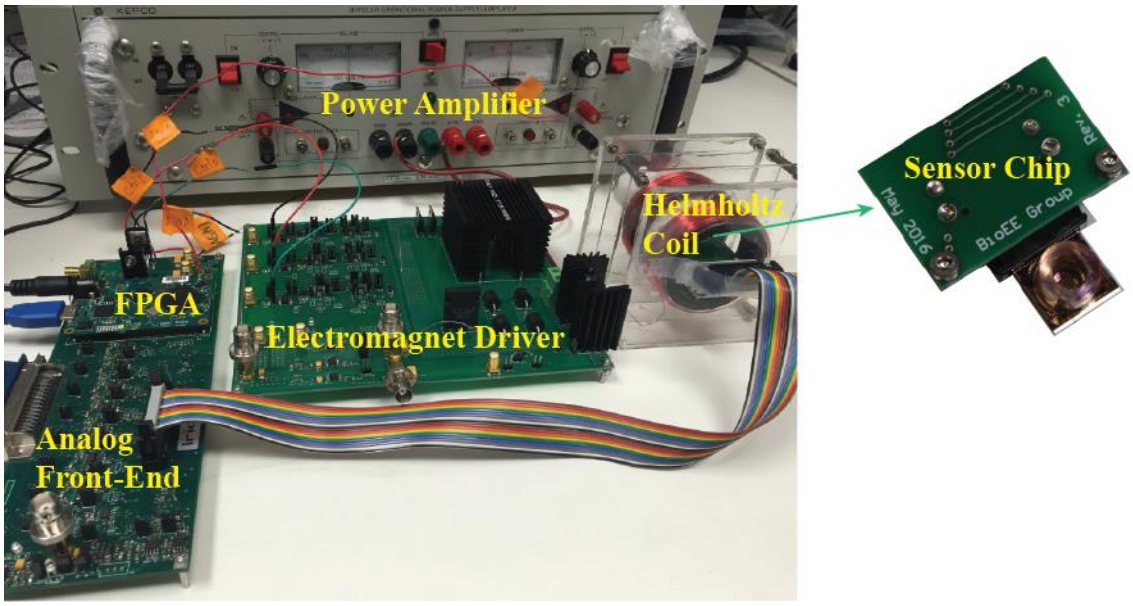

Figure 4.10 Photograph of the measurement setup

were used to generate V_B for the integrator bias voltage and V_{CTRL} for the PA control voltage. The PA was set to constant current mode and can provide a dc current of up to 12 A. The FPGA was controlled through USB by MATLAB.

The electromagnet driver and the AFE were implemented on separate PCBs to isolate ground currents. On the electromagnet driver, the critical P-Channel MOSFET, M_P, is a PolarP Power MOSFET (IXYS IXTK32P60P), which can handle 32 A and has a breakdown voltage, V_{DSS}, of 600 V. The N-Channel MOSFET, M_N, is an infrared sensing MOSFET (IRFB7434PBF) that can handle 195 A but has a relaxed breakdown voltage requirement (V_{DSS} = 40 V). Each FET requires a driver to control, as shown in Figure 4.11. Since 3 control signals *ctrlp0*, *ctrln0*, and *ctrlo0* are from the FPGA on the AFE board, optocouplers (Broadcom ACPL-077L) are used for isolation. Compound gate drivers (TI LM5110) shift the digital inputs to proper levels to drive different FETs. Since this FET driver cannot stand a voltage difference between IN_REF and VSS larger than 5 V, two

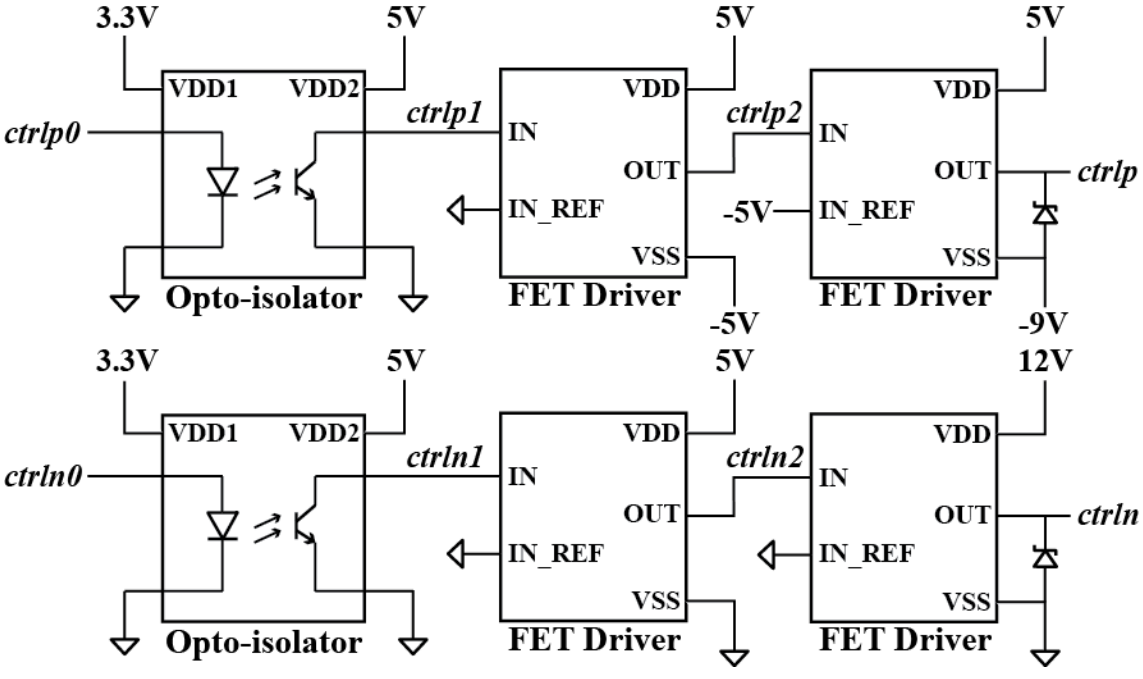

Figure 4.11 Schematic of the FET drivers on the electromagnet driver

drivers are cascaded for driving the PFETs. This is not required for the NFET driver but two cascaded drivers are still used to match the delay. It should be mentioned that the driver for *ctrlo* is the same as the driver for *ctrlp* so it is not drawn in the figure. On the layout floorplan, the low voltage control circuitry is placed on the left side and high-power driving circuitry are placed on the right side, separated by a thick and wide ground layer.

The sensor chip was positioned in the center of the electromagnet and connected to the AFE through a ribbon cable. The op-amps (AD8655) for the switched integrators have rail-to-rail input/output. The feedback capacitors C_F are 0.68 μF film capacitors, which have a lower voltage coefficient than ceramic capacitors.

4.6.2 Electrical Measurement Results

The AFE noise performance was first characterized, as shown in Figure 4.12. The white noise contributed by a sensor and op-amp were measured to be $i_{\mathrm{n,Rs}} = 3.2\ \mathrm{pA}/\sqrt{\mathrm{Hz}}$ and $v_{\mathrm{n,op}} = 2.7\ \mathrm{nV}/\sqrt{\mathrm{Hz}}$, respectively. Both noise sources have a 1/*f* corner frequency of ~1 kHz. Using Equation 4.5 with these values, it turns out that 1/*f* noise is dominant below 10 kHz. Through subtracting integration curves in adjacent cycles, the noise in the integration phase can be extracted. To observe the low frequency band, t_{int} was extended to 2.6 s by decreasing V_B. In Figure 4.12(a), although the high frequency band was limited by the ADC quantization noise, the low frequency band has a slope of -30 dB/dec, which matches with the theoretical analysis.

Due to the limitation on C_F, the relaxation signal under large t_{int} but the same V_B cannot be measured. To analyze the SNR for different t_{int} to find the optimum, simulated relaxation signals were calculated based on Equation 4.2. Since parameters $\kappa a M_0$ and t_C

are unknown, the simulated signal was first fitted to the measured signal for t_{int} = 100 ms to extract the parameters. Then, the signal was estimated for different t_{int} up to 5 s.

Since multiple cycles were used for signal averaging and t_{int} would affect the number of cycles to average, a fixed measurement time of 60 s was applied for noise and SNR tests. It should be noted that MCDS requires two measurement cycles (one with field and one without field) to extract one processed cycle, and there is a gap of 0.6 s

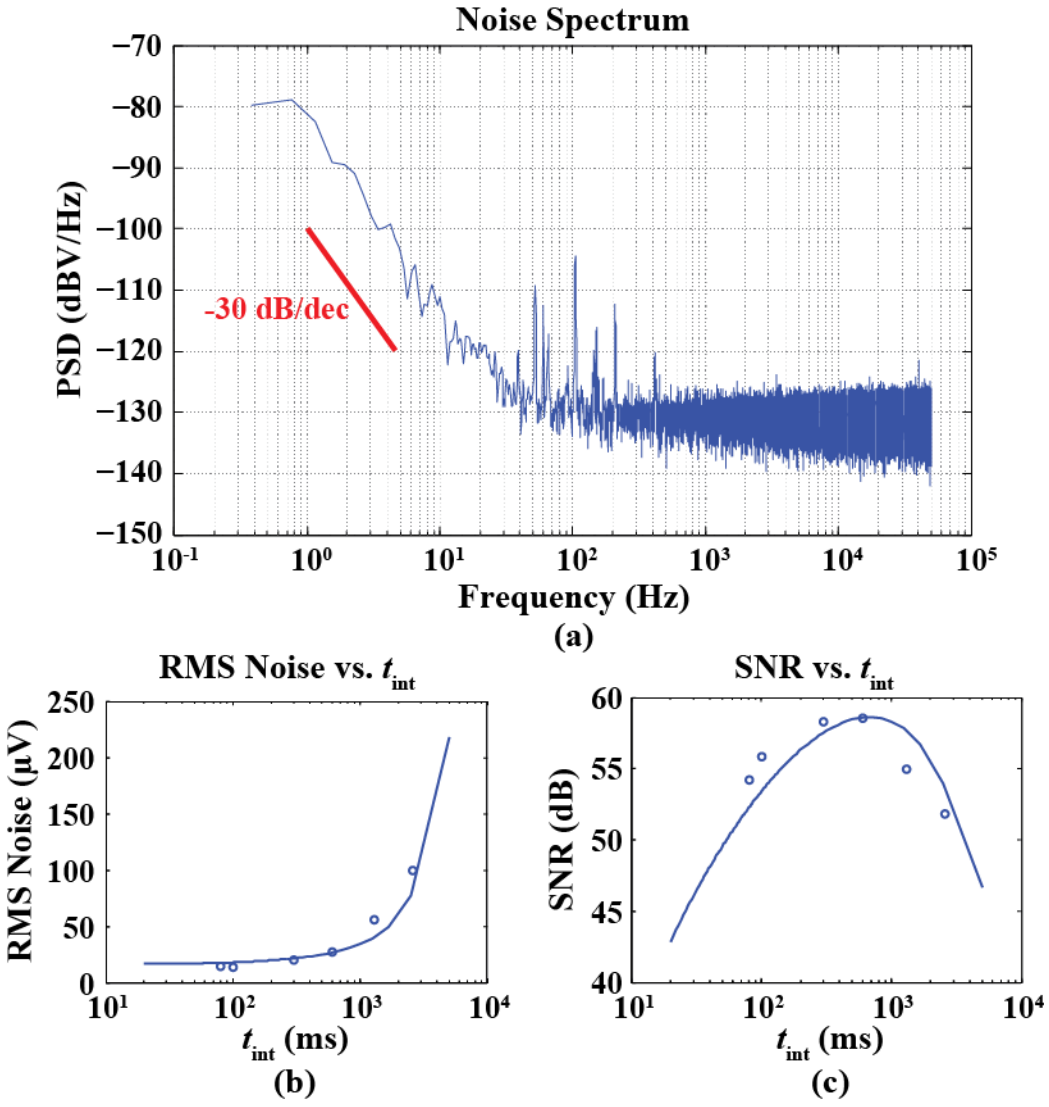

Figure 4.12 Measured noise performance of the AFE

(a) Noise spectrum for t_{int} = 2.6 s, (b) simulated and measured RMS noise vs. t_{int}, and (c) simulated and measured SNR vs. t_{int}.

between integration curves in adjacent measurement cycles. Therefore, the sampled data in adjacent processed cycles were separated by the time of $2T_{CYC} = 2 \times (t_{int} + 0.6)$ s. This time was long enough to neglect the correlation of the 1/*f* noise, therefore both white noise and 1/*f* noise could be reduced through signal averaging. The simulated (solid line) and measured (dots) noise and SNR vs. t_{int} are shown in Figure 4.12(b) and (c), respectively. The optimum t_{int} was found to be 600 ms. Since the data with MCDS enabled is uncorrelated, signal averaging can be used to reduce the noise variance.

The performance of the electromagnet driver switch-off response was measured using both a GMR sensor and an oscilloscope (Tektronics TDS2014C). By biasing the sensor with a dc current, the transient response of sensor was captured to monitor the

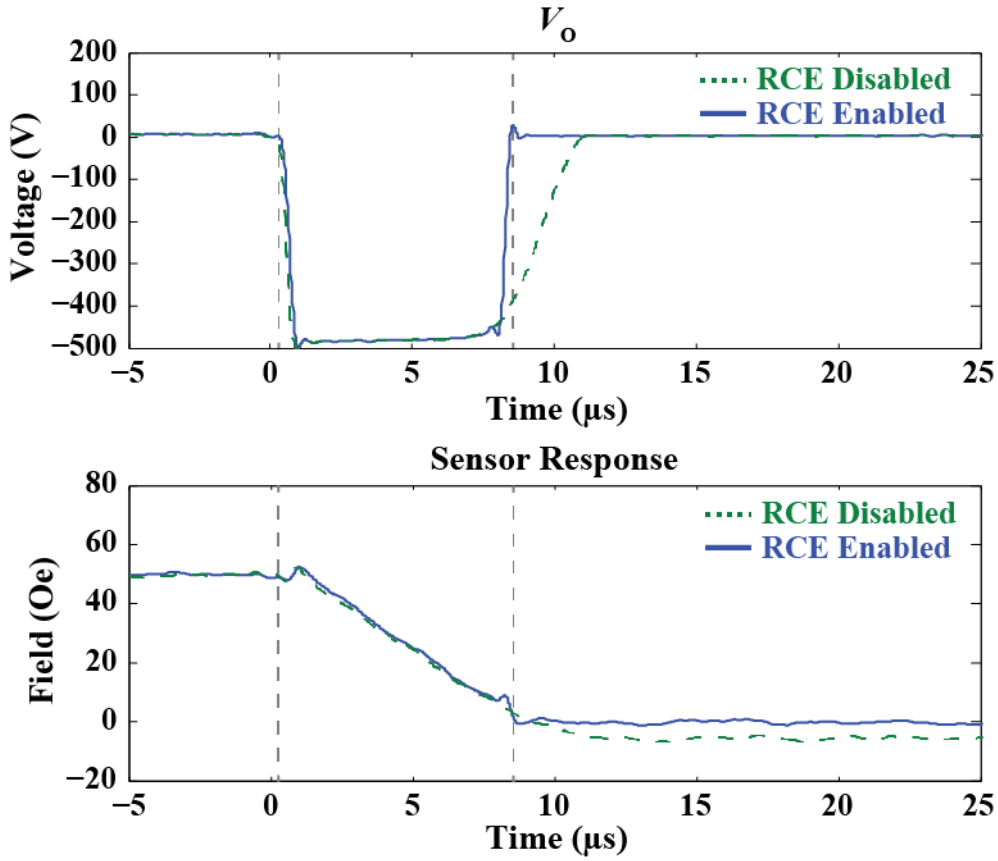

Figure 4.13 Measurement results showing the RCE technique

magnetic field. The bandwidth of the GMR sensor, bias circuit, and oscilloscope was measured to be much higher than the switch-off response of the magnetic field.

Figure 4.13 shows the measured transients with the RCE enabled and disabled. It can be observed that the RCE forced V_O back to 0 V rapidly when enabled. Thus, the reverse current, which caused a reverse magnetic field of up to -10 Oe and took 500 μs to dissipate, was fully removed. To verify the electromagnet optimization, two Helmholtz coils were custom designed, as summarized in Table 4.1. The currents in both were set to achieve a magnetic field of 50 Oe. Figure 4.14 shows the measurement results obtained from each of the electromagnets. The switch-off speed of Coil 2 (35.7 Oe/μs), which had lower inductance and higher current, was faster than Coil 1 (5.9 Oe/μs), supporting the electromagnet design principle stated in Section 4.5.2. However, Coil 2 requires 4× higher current and a cooling fan for proper heat dissipation resulting in a larger physical size. Compared with the natural exponential decay time constant τ, the switch-off speeds for both coils were improved significantly enabling MNPs with relaxation times of only a few microseconds to be detected.

Table 4.1 Comparison of different electromagnets

	Coil1	**Coil2**
Inductance L	1.5 mH	80 μH
Current I_0	2 A	8 A
Physical Size (W×L×H)	10×8×10 cm^3	15×59×23 cm^3
Time Constant τ	600 μs	1600 μs
Switch-off Time	8.5 μs	1.4 μs
Switch-off Speed	5.9 Oe/μs	35.7 Oe/μs
Improvement	71×	1,142×

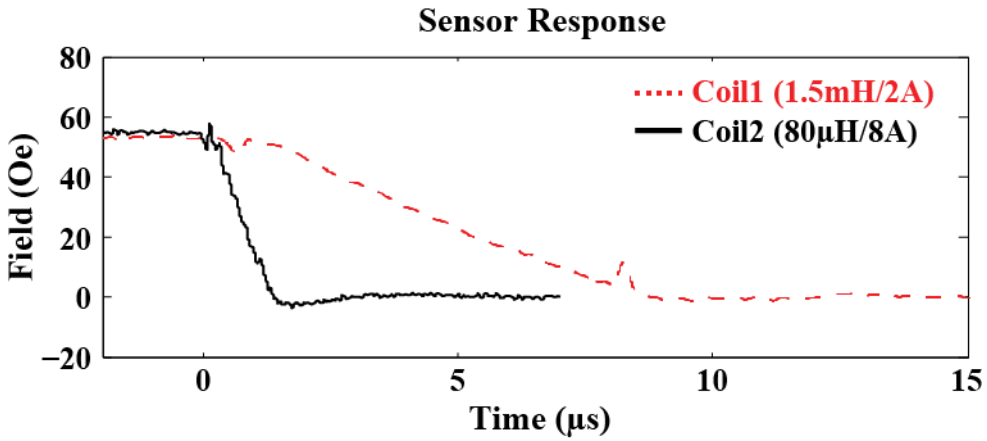

Figure 4.14 Measurement results for comparison between two coils

The large voltage swing at V_{OUT} from V_{CM} to 0 V during the integration phase causes non-linearity from both the op-amp and the feedback capacitor, C_F. To illustrate this, a measurement was taken using a bare GMR sensor, as shown in Figure 4.15(a). The non-linearity was extracted by subtracting the measured data from a linear fit of the curve. Without MCDS, the non-linearity is ~10 mV, which is comparable to the relaxation signal amplitude and similar in shape. After applying MCDS, the non-linearity is eliminated below the noise level. Similarly, the standard deviation of the sensor resistance on the same chip was measured to be 5.9 Ω and reduced to 0.86 mΩ (99.98%) with MCDS.

While the non-linearity is constant, environmental variation such as temperature drift is not. This is illustrated in Figure 4.15(b) where the temperature and amplitude of 7 sensors are plotted over time. 20 μL DIW stored in the refrigerator (4˚C) was added at t = 40 s, and the temperature was indirectly monitored from R_0. The signals without MCDS show a strong correlation with the temperature whereas MCDS significantly reduces the temperature dependence. It should be noted that there is a single-point spike when the DIW was added since it occurred in the middle of an MCDS cycle.

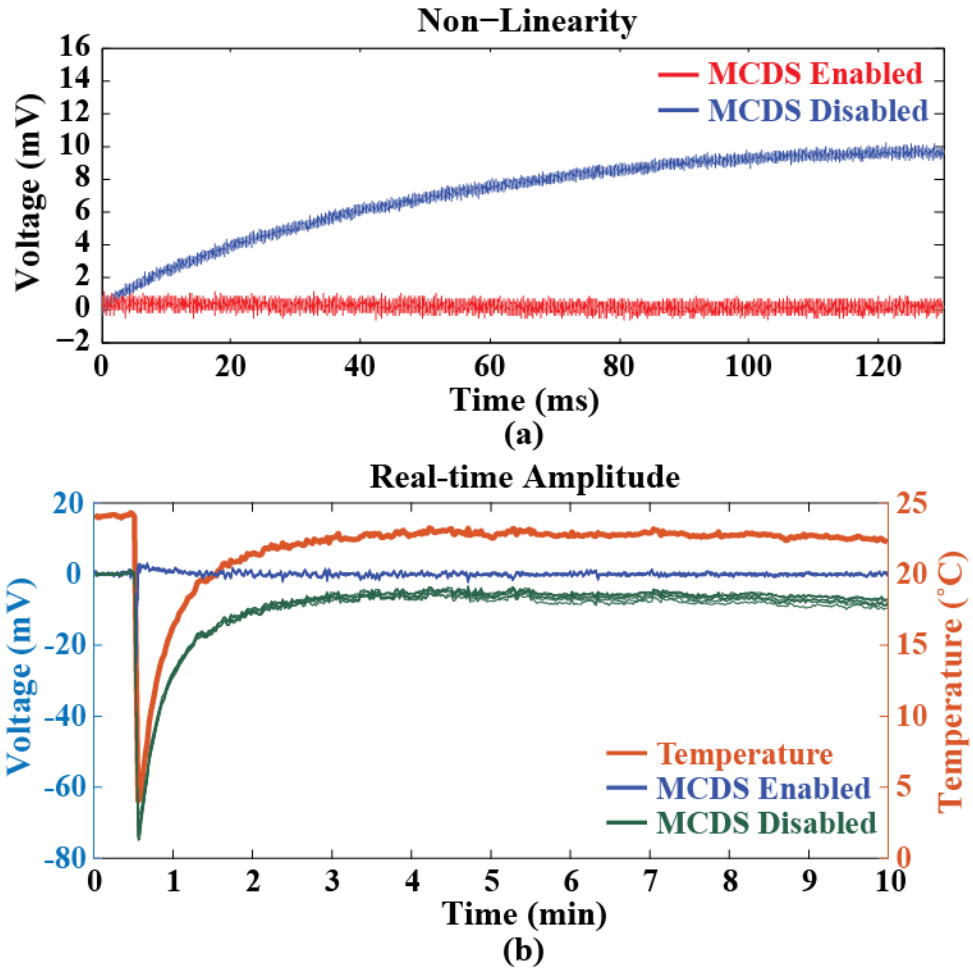

Figure 4.15 MCDS improvement on (a) linearity and (b) temperature drift

4.6.3 Biological Measurement Results

The MNPs used in all experiments were coated with streptavidin and purchased from Ocean NanoTech (SHS-30). To measure the relaxation response, the MNPs are restricted to Néel relaxation by drop-casting a fixed volume of MNPs on the surface of the sensors and allowed them to dry while applying an ac magnetic field (100 Oe_{pp} at 200 Hz). In such a configuration, the MNPs are rigidly attached and cannot undergo Brownian relaxation serving as a model system for the MIA. Moreover, the MNPs preferentially migrate into the trenches in the presence of an ac external field during the drying process, which significantly enhances the sensor response when MNPs are located close to the

edge of trenches [140], [141]. In these experiments, the applied magnetic field, H_A, was set to 50 Oe and pulsed for a duration, t_{mag}, of 100 ms. The field was subsequently collapsed, and the resulting resistance of the MR sensors was measured. The integrators were synchronized to start integrating after the electromagnet was turned off. The sensor array contained both active sensors (n = 29) and reference sensors (n = 20) that were coated with epoxy to prevent the MNPs from being in close proximity to the MR sensor.

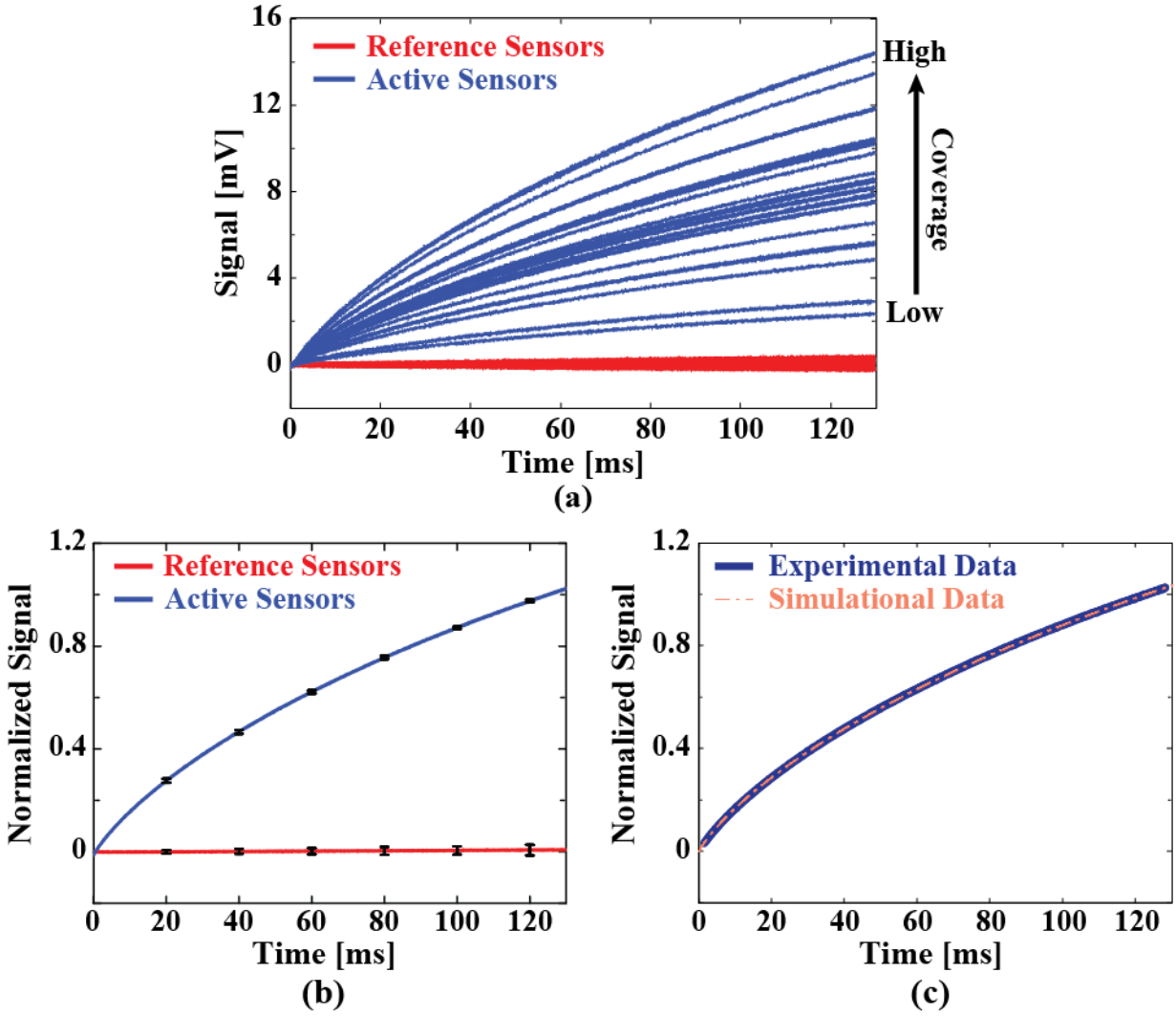

Figure 4.16 Measured relaxation signal from dried MNPs

(a) Measured MRX signals from active sensors (blue, n = 29) and reference sensors (red, n = 20); (b) normalized relaxation signals demonstrating the homogeneous relaxation behavior (error bars = $\pm 1\sigma$); and (c) comparison between experimental data and simulation.

The reference sensors all showed near zero signal, as expected, whereas the active sensors all exhibited a characteristic MRX signal with an amplitude ranging from 2 to 15 mV due to the uncontrolled coverage on each sensor (Figure 4.16(a)). When normalized, it is readily apparent that each sensor is measuring the same process, just scaled by the surface coverage (Figure 4.16(b)). Curve fitting shows that $t_{\mathrm{c}} = 3.3t_{\mathrm{mag}}$ = 330 ms at H_{A} = 50 Oe and t_{mag} = 100 ms. Using magnetic modeling to simulate the response of this system with the same t_{c}, the simulation result was in good agreement with the measured data (Figure 4.16(c)).

After verifying the natural log behavior of the relaxation signal and measuring the corresponding characteristic time, the signal dependency on the MNP coverage needs to be investigated. For the detection of biomolecules labeled by MNPs, extraction of the MNP coverage is required to quantitatively retrieve the concentration of analytes and further deduce the ligand-receptor interaction such as binding affinity and kinetics. The proof-of-principle experiments were conducted to extract the coverage of MNPs in the absence of probe molecules (*i.e.* surface immobilization). For a single MNP, the signal would be highly dependent on the location within the sensor [141], however with moderate surface coverage, the signal per MNP is roughly constant and independent of location other than if it is on top of the sensor or in the trench next to it [142], [143]. Previously only the relative MNP coverage can be calculated based on the signal amplitude. To precisely extract the absolute coverage κ in Equation 4.2, different MNP concentrations were applied and the sensors were imaged using a SEM after MRX measurements (Figure 4.17). The number of MNPs on the sensor was calculated from the SEM images and compared with the corresponding measured MRX curve. The signal is dependent on

the concentration of MNPs as shown in Figure 4.17(a), and the average signal at t = 150 ms is 0.86, 5.34, and 10.51 mV for 0.02×, 0.1×, and 2× concentration of SHS-30 MNPs, respectively. It is important to note that the ratio of average signals between 0.02× and 0.1× ($Signal_{0.02\times}/Signal_{0.1\times}$ = 0.16) is similar to the ratio of their concentrations ($Conc_{0.02\times}/Conc_{0.1\times}$ = 0.2); however, this linear concentration dependency didn't adequately represent the signal with higher MNP concentration (2×) since multi-layer MNP structures were formed at this high of concentration. Furthermore, high MNP concentration is not a realistic scenario for bioassays where a monolayer is the theoretical

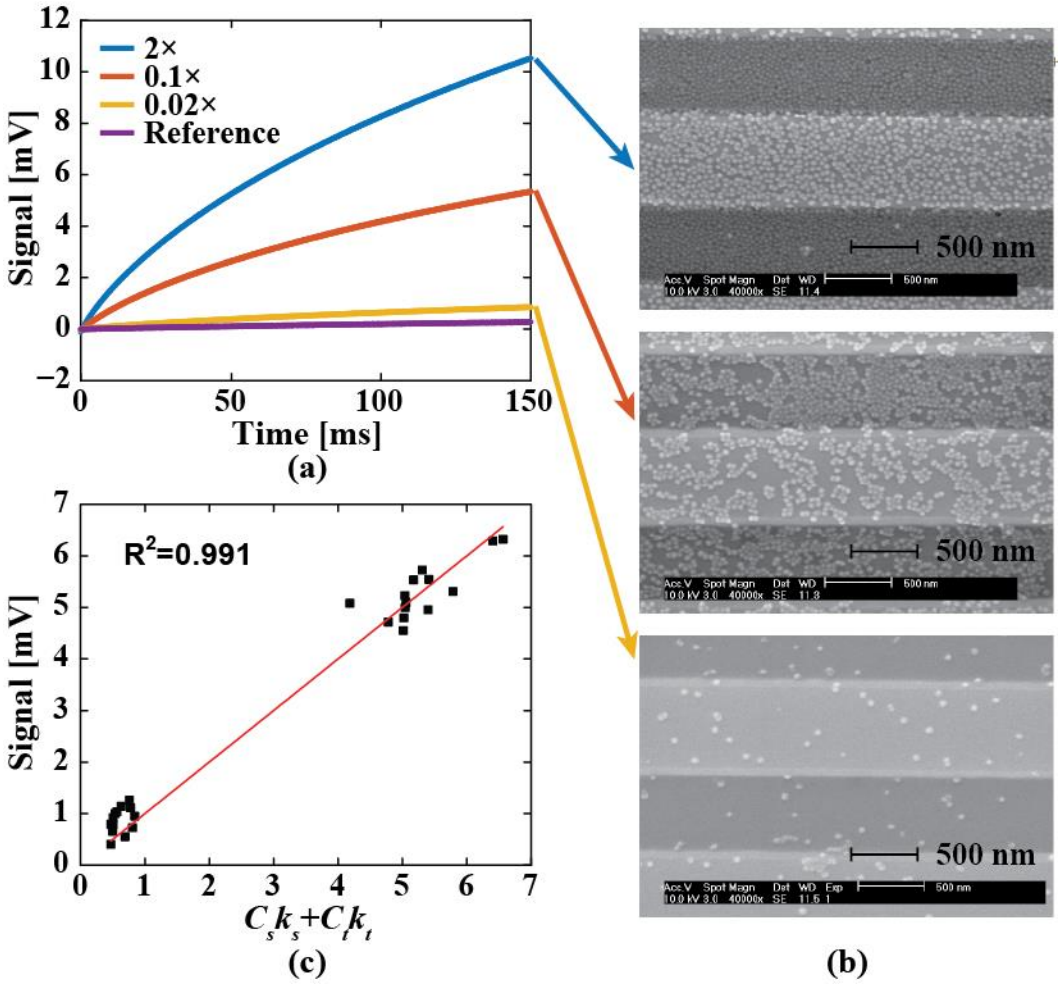

Figure 4.17 Relaxation signal dependency over coverage

(a) Average signal under different MNP concentrations; (b) the corresponding SEM images; and (c) extraction of coverage showing the signal dependency on stripe coverage and trench coverage.

limit. Consequently, the 0.02× and 0.1× MNP concentrations were focused to extract the coverage where the signal per particle is linear and the coverage is still monolayer. Since the specific design of the sensor geometry created the different signal dependency on the position of beads [138], the total coverage over sensor area is not sufficient to address and extract the information of MNP coverage. Instead, the coverage should be evaluated with covered area over the GMR stripes and trenches (area between adjacent stripes), respectively. Equation 4.2 is modified accordingly to account for this dependency

$$Signal(t) = (C_s k_s + C_t k_t) \int \ln\left(1 + \frac{t_c}{t}\right) dt \qquad 4.10$$

where C_s and C_t are coefficients containing the magnetic viscosity and signal per particle on the sensor and trench, respectively, and k_s and k_t are the stripe and trench coverage. From the measured data, C_s = 4.01 and C_t = 9.54 were found for the MRX system (Figure 4.17(c)). The inequality of C_s and C_t proves the different signal dependency over the stripes and trenches and also reaffirms the previously reported result that the MNPs in the trenches contributed to signal more than the MNPs on the stripes did. Interestingly, the ratio between C_t and C_s (C_t/C_s = 2.38) is not as high as the signal difference described in the literature [141], this phenomenon can be regarded as the compensation effect from the total MNPs that diminish the high yield of stray field from the MNPs at the stripe edges. The correlation between signal and extracted coverage coefficients exhibited strong consistency (R^2 = 0.991).

Subsequently, the experiment was extended to measure the signal dependency on H_A and t_{mag} to optimize the time-domain MRX response. As expected, t_c has strong dependency on H_A and t_{mag}, varying from 85 to 450 ms (Figure 4.18(a)). Based on these

results, t_c has quasi-linear relationship with t_{mag}, while it is exponentially dependent on H_A (Figure 4.18(b),(c)). The underlying theory still needs to be investigated to validate this observation. It should be noted that the extracted t_c = 380 ms at H_A = 50 Oe and t_{mag} = 100 ms is not the same as previously measured (t_c = 330 ms). It is likely that this discrepancy is a result of different measurement temperatures (particularly here where the electromagnet was running for an extended duration resulting in an elevated temperature). Nevertheless, the signal amplitude followed the trend of t_c, as expected, when sweeping H_A and t_{mag}. The normalized data, which were processed to remove the coverage, showed a positive correlation with the H_A and t_{mag}. In terms of signal

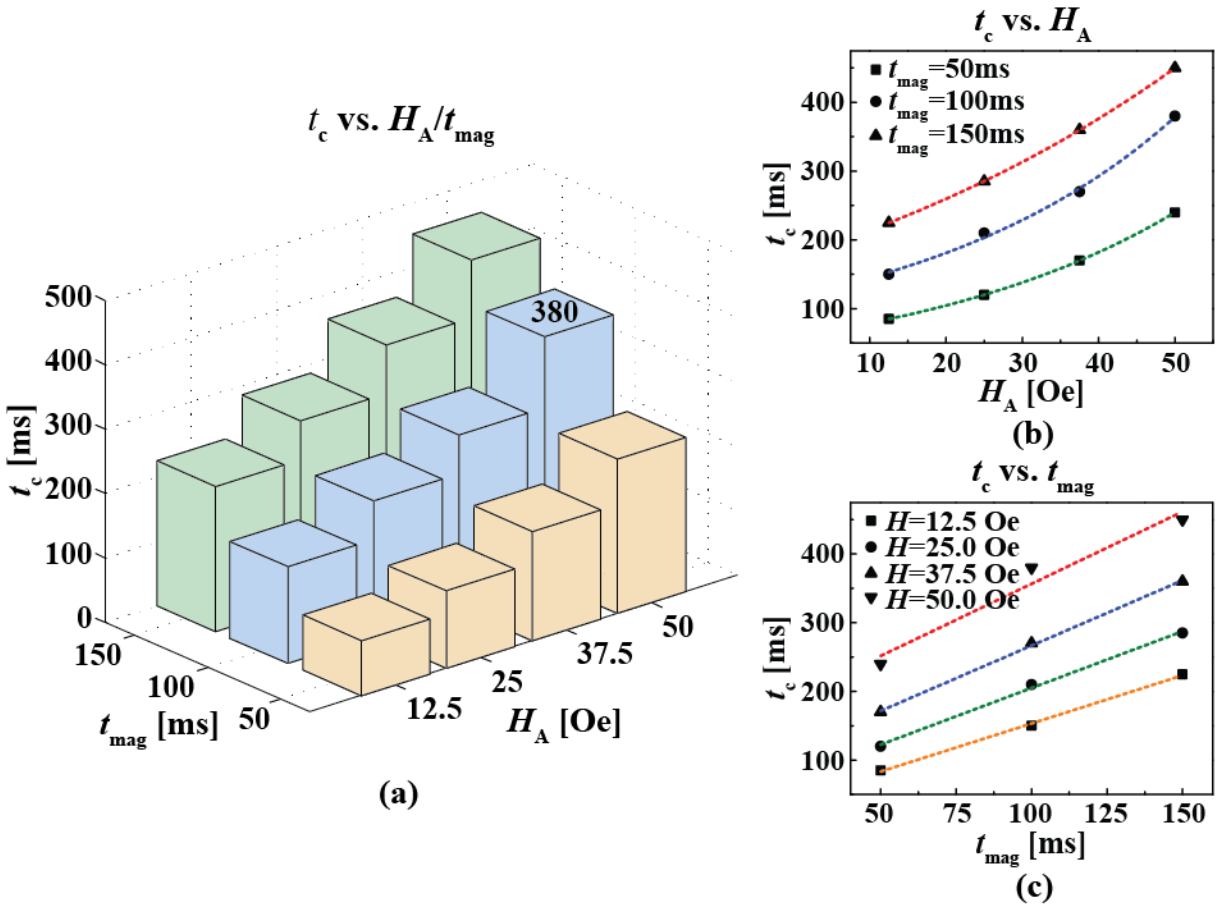

Figure 4.18 Measured t_c dependency on H_A and t_{mag}

(a) t_c dependency on H_A and t_{mag}, (b) the dependence of H_A on t_c, and (c) the dependence of t_{mag} on t_c.

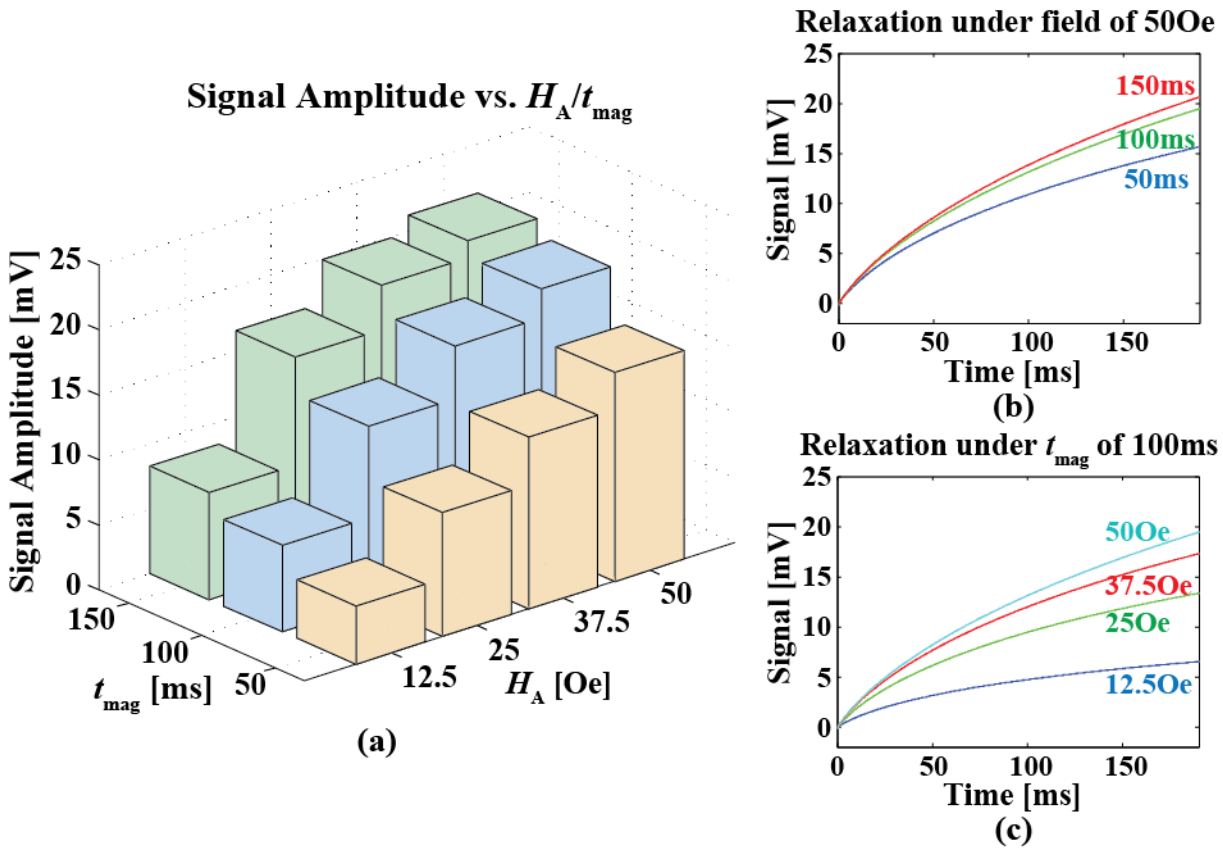

Figure 4.19 Measured signal amplitude dependency on H_A and t_{mag}

(a) the signal amplitude dependency on H_A and t_{mag}, (b) relaxation signal under H_A = 50 Oe with increasing t_{mag}, and (c) relaxation signal under t_{mag} = 100 ms with increasing H_A.

amplitude, it shows diminishing returns when increasing H_A and t_{mag}, *i.e.* the increasing trend of signal is not as obvious as t_c with increasing H_A and t_{mag} (Figure 4.19).

To demonstrate MRX as a biosensing technique, an immunoassay was performed and the results were compared to the conventional magnetometry approach that was discussed in Section 2.6. In this experiment, the active sensors were functionalized with 99% (3-Aminopropyl) triethoxysilane (APTES, Sigma Aldrich) for 1 hour at 37 °C, followed by Biotin (EZ-Link™ NHS-PEG12-Biotin, ThermoFisher Scientific) incubated for 1 hour at 37 °C, and then coated with 2% BSA (Blocker™ BSA (10×) in PBS, ThermoFisher Scientific) for 30 min at room temperature. The reference sensors were covered with

epoxy and part of sensors had only BSA without biotin as negative controls. It should be noted that this protocol was designed specifically for the SHS-30 MNPs that have a zeta potential between -40 to -20 mV [144], [145]. To compare both techniques, the measurements were conducted with magnetometry to ensure the efficacy of MNPs binding via biotin-streptavidin interaction, followed by 1× PBS washing 3× to remove unbound MNPs, and then performed MRX to detect the MNPs' relaxation signal via specific binding. The assay was monitored in real-time using conventional magnetometry (Figure 4.20(a)). As expected, the streptavidin-conjugated MNPs bound to the biotin on

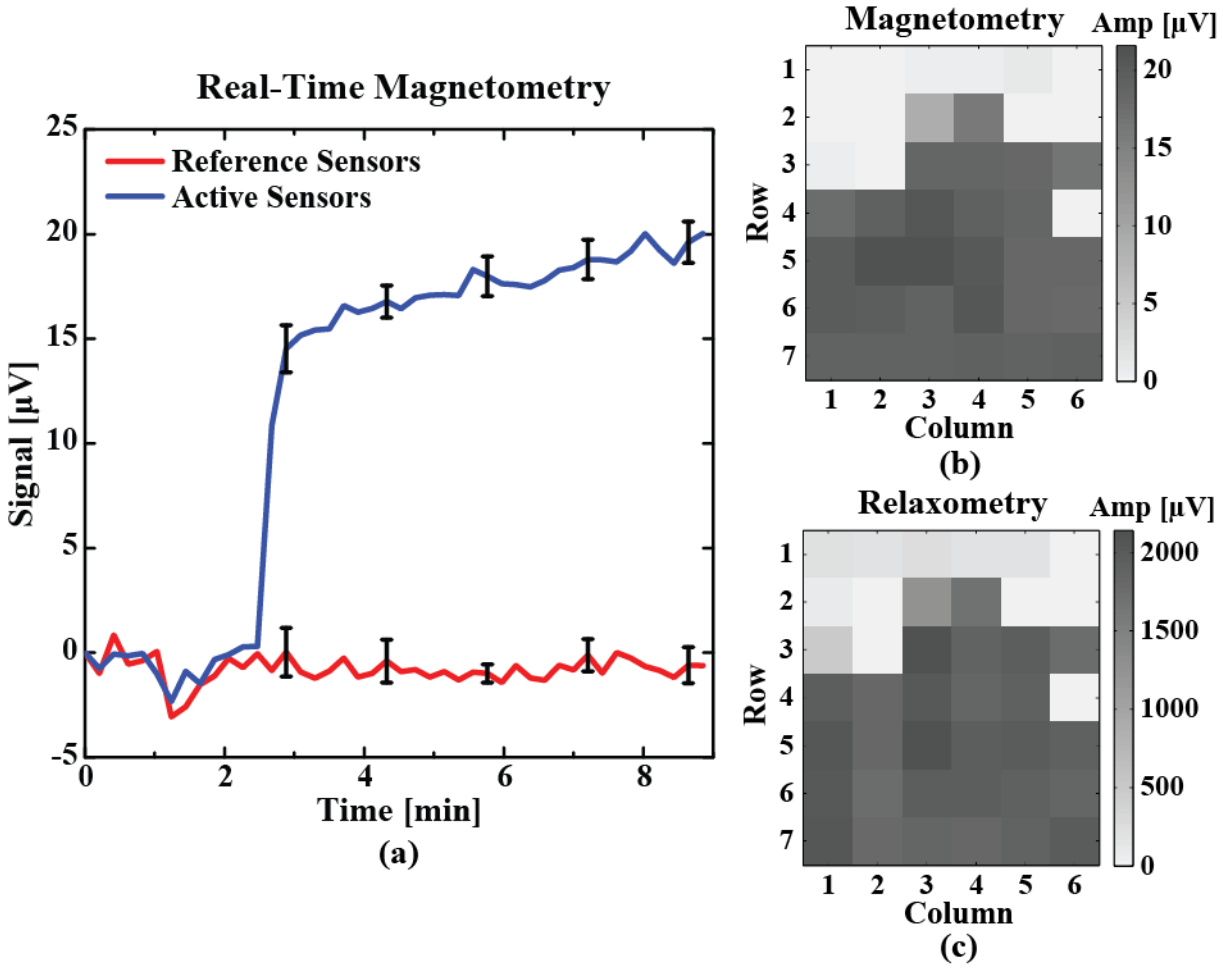

Figure 4.20 Measured real-time immunoassay based on magnetometry

(a) Measured binding kinetics based on magnetometry (error bars = $\pm 1\sigma$), and corresponding coverage map for (b) magnetometry and (c) magneto-relaxometry.

the surface of the active sensors. The reference sensors showed no signal, indicating no specific binding. The corresponding coverage maps are shown in Figure 4.20(b) and (c) for magnetometry and MRX, respectively. Both coverage maps show a high degree of similarity, confirming the validity of the reported technique.

Lastly, this experiment was performed with real-time relaxation measurement to validate the MIA based on MRX, as shown in Figure 4.21(a). The MNPs were added at *t* = 80 s and the experiment lasted until the binding plateaued. The sensors were then washed with PBS 3× to remove unbound MNPs, which showed no change in signal amplitude indicating minimal non-specific binding. The full chip results are shown in Figure 4.21(b) with the active sensors denoted by a + and the reference sensors by a -. The red and blue dotted squares indicate the reference sensor and the active sensor in the real-time plot, respectively. The variation in amplitude for the active sensors was the result of the MNP surface coverage, which could be improved using individual spot functionalization versus the blanket functionalization procedure used here.

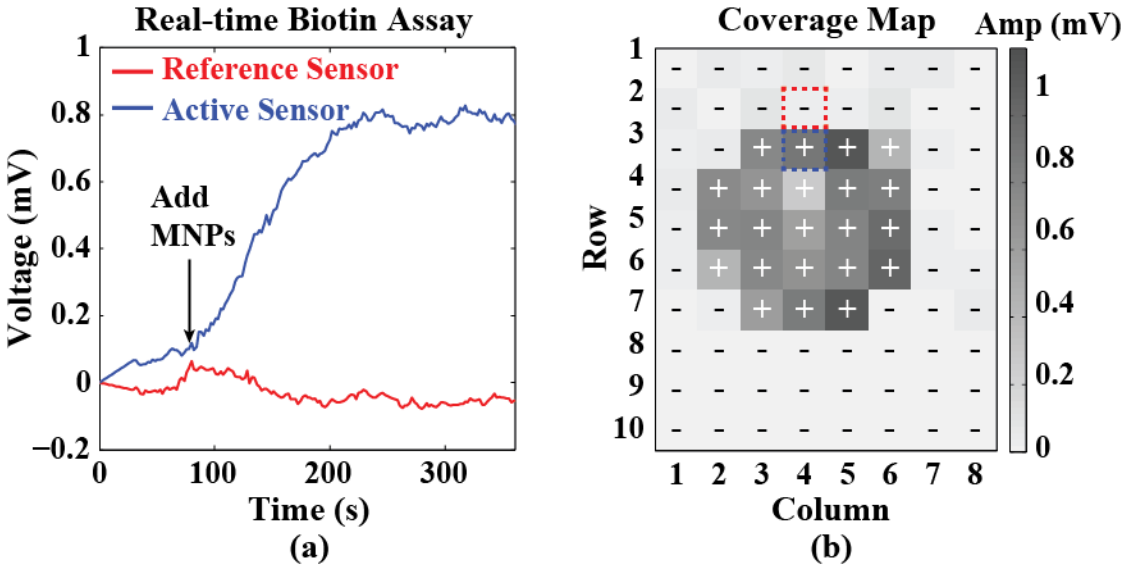

Figure 4.21 Measured immunoassay based on MRX

(a) Measured binding kinetics based on MRX and (b) the corresponding coverage map.

4.7 Conclusion

In this chapter, an MRX biosensor system was demonstrated to detect relaxation of MNPs. A switched integrator was designed to integrate the relaxation signal with time, relaxing the bandwidth requirement of the ADC. An ultrafast electromagnet driver that actively dissipated the stored energy in the Helmholtz coil was designed to reduce the deadzone time. A MCDS technique effectively eliminated the sensor-to-sensor variation, temperature drift, circuit offset and non-linearity. Measurement results for the electromagnet driver showed a fast switch-off response of >5 Oe/μs. The experimental results of dried MNPs showed that the relaxation of MNPs can be successfully detected and the biotin-BSA immunoassay demonstrated the capability of monitoring the binding kinetics in real-time. Furthermore, the time-domain MRX was systematically investigated by measuring the signal dependency on the applied field intensity and magnetization time, as well as the signal contribution based on the MNP location. This work lays the foundation for a fast and sensitive biosensing for PoC diagnostics platform.

Chapter 4, in part, is based on materials from Xiahan Zhou, Chih-Cheng Huang, and Drew A. Hall, “Giant Magnetoresistive Biosensor Array for Detecting Magnetorelaxation,” *IEEE Transactions on Biomedical Circuits and Systems (TBioCAS)*, Aug. 2017 [76], and Chih-Cheng Huang, Xiahan Zhou, and Drew A. Hall, “Giant Magnetoresistive Biosensors for Time-Domain Magnetorelaxometry: A Theoretical Investigation and Progress Toward an Immunoassay,” *Scientific Reports*, Apr. 2017 [77]. The dissertation author was the primary investigator and author of these papers.

Chapter 5. A CMOS GMR SENSOR FRONT-END FOR DETECTING MAGNETO-RELAXATION

5.1 Introduction

The last chapter validates the MRX sensing approach using discrete components. Although successfully eliminating the baseline, the MRX-based system does not show better SNR than a magnetometry-based system. In this chapter, a CMOS chip that consists of a low-noise GMR sensor AFE and an 18b Zoom ADC is reported to detect MNP relaxation with better resolution. As discussed in Section 2.4, the challenges of MRX based AFEs are: 1) MRX requires two more steps than magnetometry, leading to a 3× readout time. 2) The relaxation signal has a relatively wide low-frequency band that overlaps with the 1/*f* noise. Although MCDS can reject part of the 1/*f* noise, the magnetization phase reduces the 1/*f* noise correlation. 3) MCDS can only cancel the R_0 baseline digitally, so the AFE still needs a large DR.

To address this, a CMOS architecture and a signal extraction technique is presented to improve the magnetic sensor FoM. Specifically, a magnetoresistive correlated double sampling (MR-CDS) technique is used to reduce the readout time and system 1/*f* noise. A rotating dynamic element matching (DEM) technique in the sensor bias block reduces the 1/*f* noise from the transistors. A fast settling miller compensation (FSMC) in the capacitively coupled chopper instrumentation amplifier (CCIA) reduces the power consumption. These result in an input-referred noise of 9.7 nT_{rms}, a power consumption of 4.32 mW, a readout time of 704 ms, and a FoM of 286 $nT^2 \cdot mJ$ that is 4.9× and 210× better than previously reported magnetic sensor and MRX-based AFEs, respectively.

5.2 Signal and System

5.2.1 Magnetoresistive Correlated Double Sampling

Figure 5.1(a) shows the timing diagram that includes 3 steps with a same duration time, T_{cycle}. Conventional MCDS subtracts the signal at step 5 from the signal at step 3 to eliminate the baseline but suffers from long readout time and poor 1/*f* noise rejection. A MR-CDS technique is reported to subtract the signal at step 5 from the signal at step 4. Step 3 is no longer needed and thus the readout time is reduced. The 1/*f* noise rejection is illustrated in Figure 5.1(b). Due to higher correlation, the 1/*f* noise that is < $1/2T_{cycle}$ can be eliminated for MR-CDS while MCDS can only eliminate the 1/*f* noise that is < $1/3T_{cycle}$. It should be noted that both techniques completely remove 1/*f* noise at low frequencies, thus enabling an unlimited tradeoff between resolution and readout time. This is in contrast to most analog techniques that have residual 1/*f* noise that limits this tradeoff.

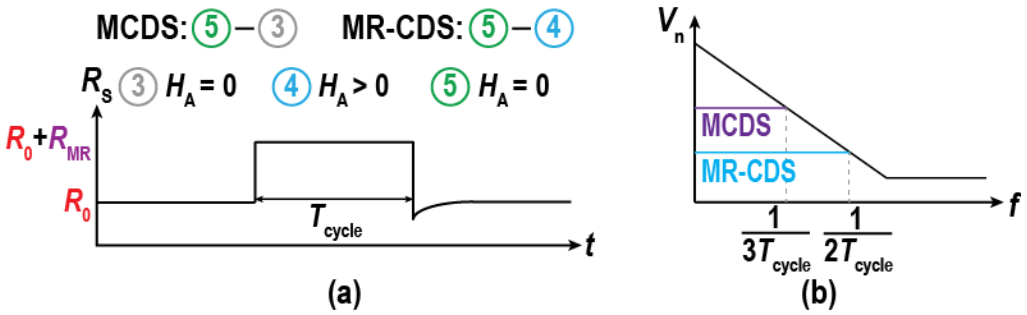

Figure 5.1 MR-CDS vs. MCDS

(a) Signal extraction timing diagram for MCDS and MR-CDS, and (b) 1/*f* noise rejection comparison between MCDS and MR-CDS.

Table 5.1 Comparison of MR-CDS and MCDS

	MCDS	MR-CDS
1/*f* Noise Rejection	$f < 1/(3T_{cycle})$	$f < 1/(2T_{cycle})$
Readout Time	$3T_{cycle}$	$2T_{cycle}$
Total Noise in Same Time	√1.5 – 1.5×	1×
Baseline	0	R_{MR}
Temperature Drift Cancellation	Good	Fair
Need Reference Sensor?	No	No

Normalized to the same readout time, if only white noise is considered, the noise improvement from MR-CDS is √1.5× lower because of the 1.5× shorter time; if only 1/*f* noise is considered, the total noise improvement from MR-CDS is 1.5× because of another √1.5× in 1/*f* noise improvement. Therefore, the total noise improvement for the same readout time is √1.5 – 1.5×.

However, MR-CDS cannot remove the R_{MR} baseline, which must be accommodated by the AFE DR. Given $R_{MR}/R_{rlx} \leq 10^4$, the AFE DR requirement is 80 dB. Temperature dependent R_{MR} also limits the temperature drift rejection for MR-CDS [56], [146]. The comparison between MCDS and MR-CDS is summarized in Table 5.1.

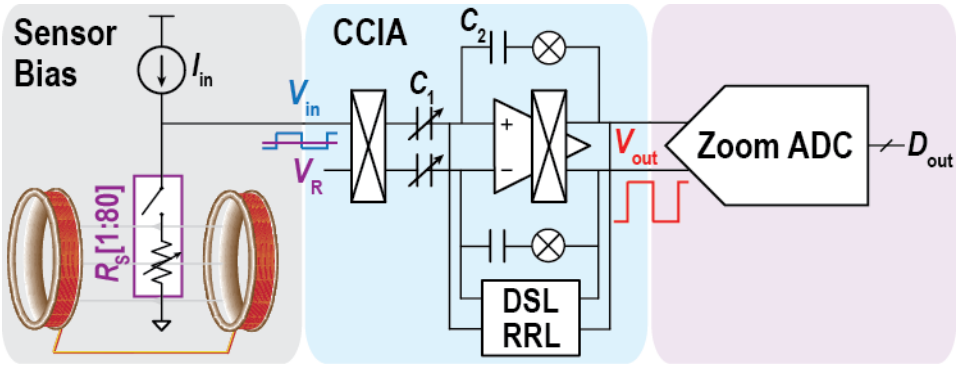

Figure 5.2 Block diagram of the AFE

5.2.2 System Architecture

Figure 5.2 shows the block diagram of the sensor AFE. It consists of a sensor bias block, a CCIA, and a Zoom ADC. A low noise dc current, I_{in}, flows into the selected sensor, R_S, which is magnetically biased by an external Helmholtz coil. The resulting voltage, V_{in}, is amplified by the CCIA, which contains a dc reference input, V_R, and a dc servo loop (DSL) to continuously cancel the R_0 baseline. A ripple rejection loop (RRL) rejects the ripple on V_{out}, which is quantized by the ADC. The Zoom ADC consists of a 6b SAR for coarse quantization and a 13b ΔΣ modulator (DSM) for fine quantization. It is configured to measure V_{out} twice, either at steps 3 and 5 for MCDS or at steps 4 and 5 for MR-CDS, respectively.

5.3 Circuit Implementation

5.3.1 Sensor Bias Block

Figure 5.3 shows the schematic of the sensor bias block. The chopped OTA and the bias transistor, M_0, form a negative feedback to provide a low output impedance. An off-chip precision resistor, R_{set}, and an externally provided dc voltage, V_{bias}, generate a

bias current, $3I_{in}$, that is attenuated by 3× to bias the selected sensor. An on-chip moscap, C_C, loads node V_x for stability and source degeneration resistors, R_D, are used for noise reduction. The total thermal noise power at V_{in} can be written as

$$v_{n,in}{}^2 = \left(\frac{v_{n,op}R_S}{3R_{set}}\right)^2 + \frac{4k_BTR_S^2}{9R_{set}} + \frac{4k_BT\gamma R_S}{g_{m0}R_D} + \frac{4k_BTR_S^2}{R_D} + 4k_BTR_S \qquad 5.1$$

where $v_{n,op}$ is the input-referred noise of the OTA and g_{m0} is the transconductance of M_0. The 5 noise contributors are the OTA, R_{set}, M_0, R_D, and R_S. Since $V_{bias}/R_{set} = 3V_{in}/R_S$, larger V_{bias} and R_{set} reduces the noise contributed by the OTA and R_{set}. Having $R_D > R_S$ helps reduce the noise from M_0 and R_D. Due to a constant R_S and sensor breakdown voltage limit on V_{in}, both R_{set} and R_D should be maximized for low noise readout but are limited by maximum V_{bias} headroom and minimum V_x headroom, respectively.

The 1/*f* noise from M_0 is a challenge since it flows a dc current. To reduce it, a rotating DEM technique is added at the cascode node. A 2-to-4 decoder selects one of

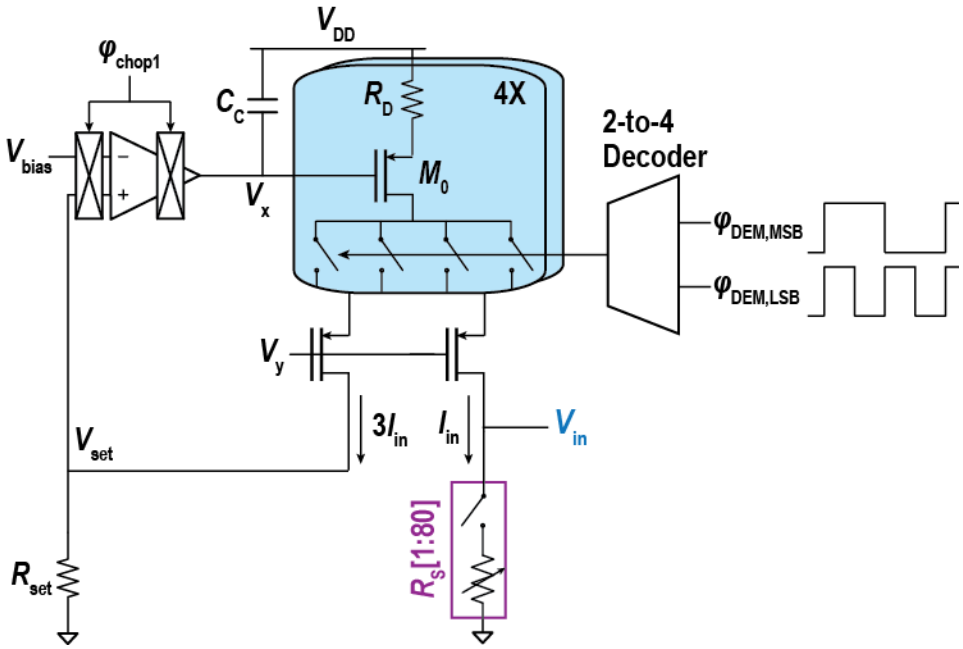

Figure 5.3 Schematic of the sensor bias block

the branches to the output path and the remaining 3 branches to the feedback path. It is configured to rotate the 4 branches so the 1/*f* noise from M_0 is upmodulated to the rotating frequency, f_{DEM}. The mismatch from M_0 causes ripple on V_{in} at f_{DEM} but are out of band and can be filtered by the ADC decimation filter.

5.3.2 Capacitively Coupled Chopper Instrumentation Amplifier

Figure 5.4 shows the CCIA schematic that includes a DSL and an RRL. The CCIA has a dc gain of C_1/C_2, where C_1 is a 2-bit programmable capacitor for a variable gain. The OTA is implemented by a 2-stage OTA, where g_{m1} is a differential difference folded cascode OTA for low noise and g_{m2} is a current mirror OTA for high output swing (Figure 5.5). The 2-stage OTA is simulated to have a dc gain of 120 dB. Although current reuse OTAs or stacked OTAs have been reported recently for better efficiency, their nonlinearity limits the performance [109], [147]–[149]. Both OTAs use SC-CMFB for large output swing. Dc bias resistors, R_B, are implemented by DCRs for high linearity and fast settling during sensor switching. A novel FSMC technique is used to reduce the g_{m1} power by 4×, while maintaining the linearity and the stability, as will be discussed later.

The voltage across the sensor, V_{in}, and an externally provided dc voltage, V_R, are fed into the CCIA to form a pseudo-differential input. V_R is chosen to be $\sim I_{in}R_0$ to reject the R_0 baseline in the analog domain. The offset between V_R and V_{in} can be further nulled up to $(C_3/C_1)V_{DD}$ by the DSL, which consists of an integrator and a 1-bit programmable capacitor C_3. The input-referred noise from the DSL is $(C_3/C_1)v_{n,DSL}$, where $v_{n,DSL}$ is the noise of the DSL that is a tradeoff between the maximum tolerable offset and the noise. Since $g_{m,DSL}$ cannot be chopped otherwise the low input impedance loads R_{DSL}, the 1/*f*

noise from this OTA dominates the CCIA noise at low frequencies. Although a mixed-mode DSL can reduce the noise from DSL, it requires complex digital configuration [150]. Fortunately, MR-CDS rejects the 1/*f* noise, thus resolving this issue. Both the sensor mismatch and dependence on the temperature set the maximum input offset, thus the ratio of C_3/C_1. In the literature, the sensor mismatch can be up to ±5% [151], which results in an offset up to 27 mV, leading to $C_3/C_1 > 0.015$. Since C_1 is programmable for a variable

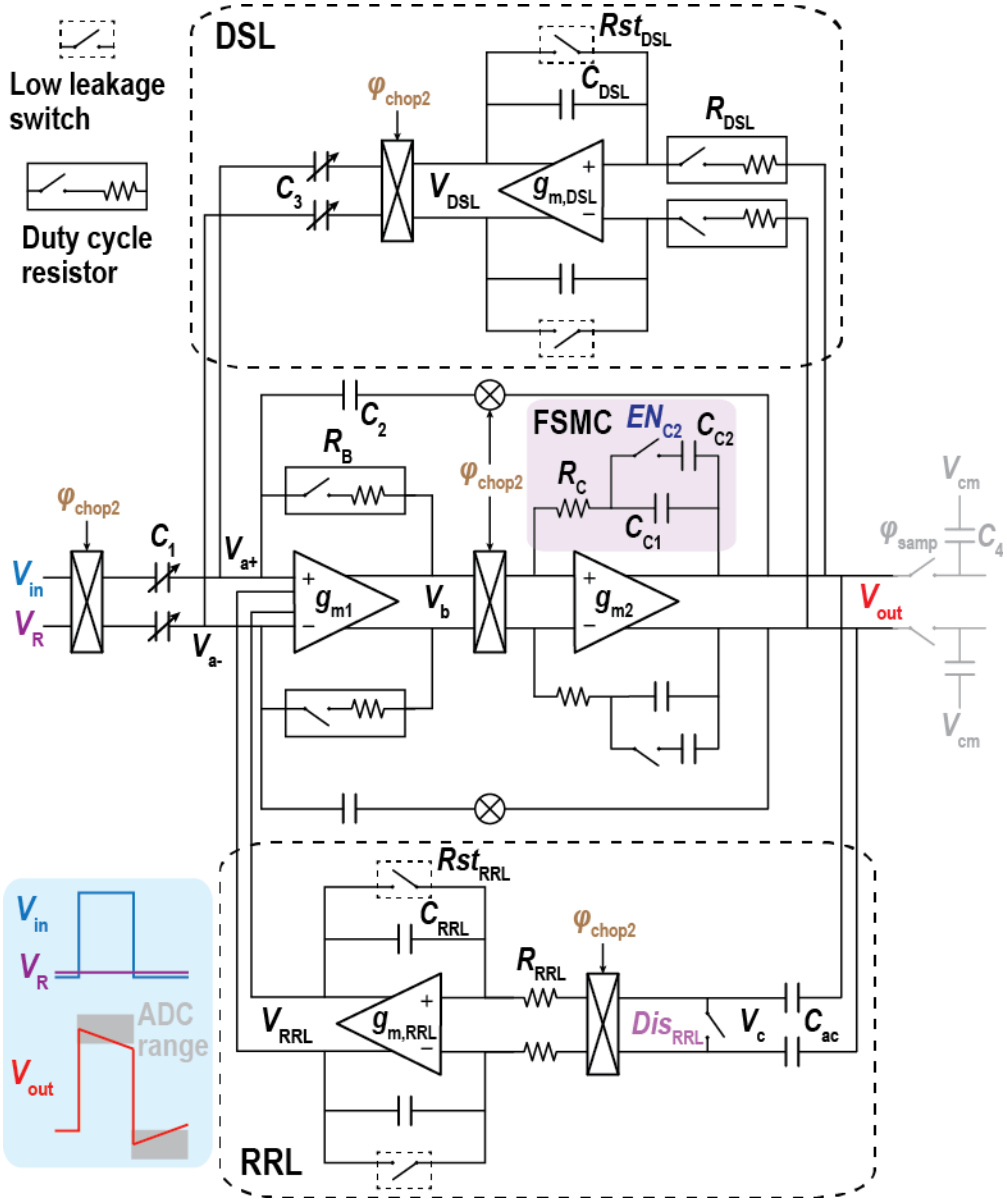

Figure 5.4 Schematic of the CCIA

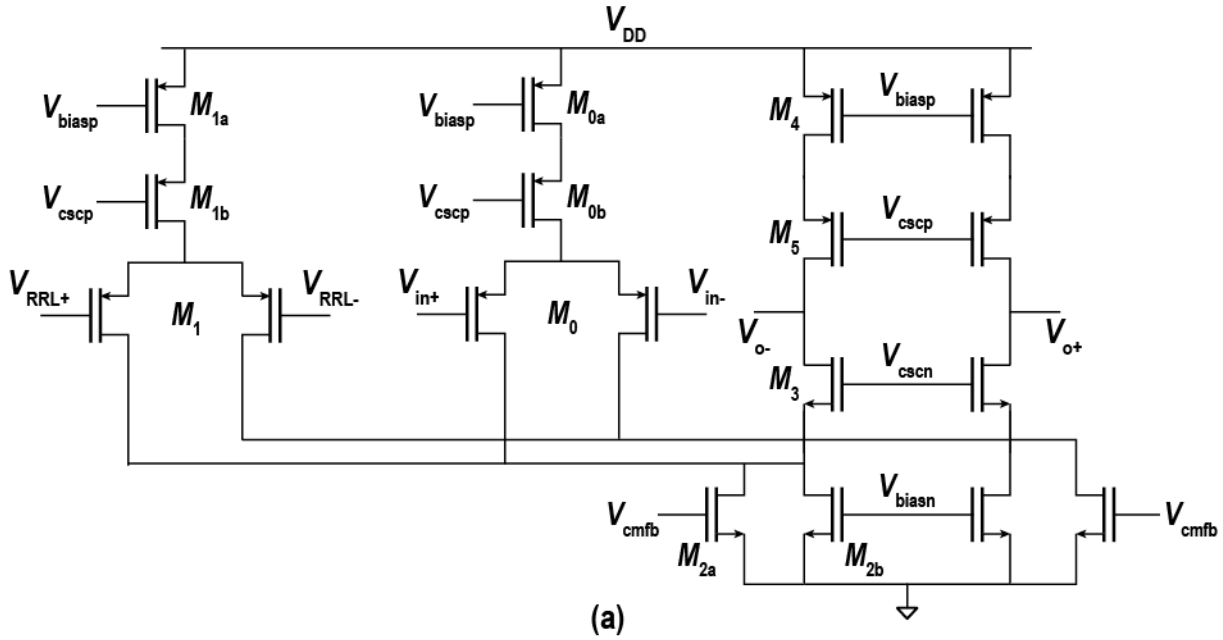

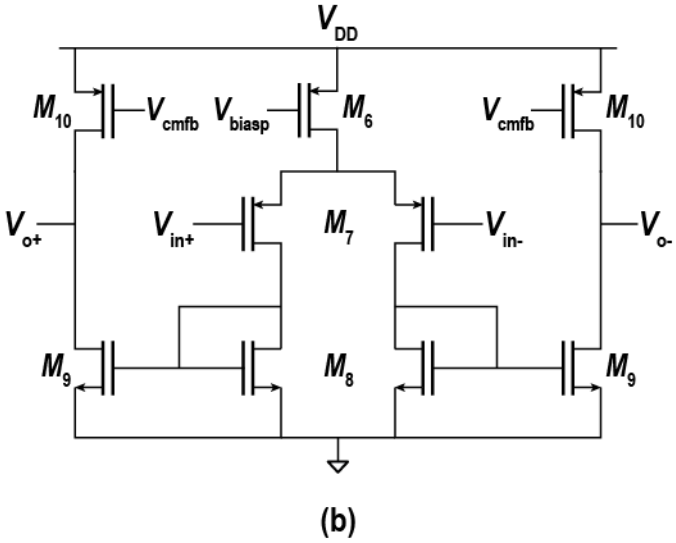

Transistor	W/L [μm]	I_{bias} [μA]
M_0	800/0.4	200
M_1	80/0.4	20
M_{2a}	320/2	200
M_{2b}	96/2	60
M_4	64/1	40
M_7	80/0.2	40
M_8	64/2	40
M_9	64/2	40
M_{10}	128/2	40

(c)

Figure 5.5 Schematics of the OTAs

(a) Schematic of OTA g_{m1}, (b) g_{m2}, and (c) size chart of the two OTAs.

gain, C_3 is also designed to be programmable to coarsely keep the ratio. To have some headroom for accommodating R_0 temperature drift, C_3/C_1 is designed to be 0.02–0.033 in all gain configurations. The DSL sets the high-pass corner frequency of the CCIA as

$$f_{\mathrm{HP}} = \frac{C_1}{C_3}\frac{1}{2\pi R_{\mathrm{DSL}} C_{\mathrm{DSL}}}. \quad (5.2)$$

Since V_{in} is a pulsed waveform, the CCIA distorts the waveform and f_{HP} determines the voltage drop on V_{out} at steps 4 and 5 (Figure 5.4 bottom left). The Zoom ADC is configured as a SAR to quantize V_{out} coarsely and then "Zoom" into ±1 SAR_{LSB} for fine quantization, thus the voltage drop in one ADC cycle cannot exceed 1 SAR_{LSB}. Simulation shows that f_{HP} must be <1 Hz to not saturate the ADC. Given C_1/C_3 = 30–50, C_{DSL} = 100 pF, R_{DSL} must >80 GΩ to satisfy this requirement. Therefore, R_{DSL} is implemented by a DCR with a poly-resistor of 32 MΩ and a duty cycle of <1/2500.

To achieve such a small duty cycle, an on-chip pulse generator was designed, as shown in Figure 5.6(a). 2-bit programmable capacitors, C_{delay}, adjust the pulse width to compensate for process variation [109]. Since the multiplexed sensor array is read in a time sequenced manner, the settling time when switching between sensors significantly increases the array readout time. Thus, fast settling DCRs are used to improve the settling [57], [80]. In Figure 5.6(b), the DSL and RRL are first reset when switching sensors. The switches for R_{B} are kept closed to generate a low impedance path from V_{b} to $V_{\mathrm{a+/-}}$, enabling fast settling at $V_{\mathrm{a+/-}}$. When the DSL starts to operate, the switches for R_{DSL} are closed so the DSL integrator can quickly find the input offset. In both reset and settling phases, EN_{DCR} = 0 so $\varphi_{\mathrm{out}} = \varphi_{\mathrm{in}}$ for both DCRs. After the CCIA is fully settled, EN_{DCR} changes to 1 to configure both DCRs into duty cycled mode. After a short idle period, the ADC sampling clock, φ_{samp}, starts quantizing V_{out}.

To ensure the CCIA stability, Miller compensation is commonly used. Conventional Miller compensation uses a large capacitor, C_{C}, to compensate the amplifier and create

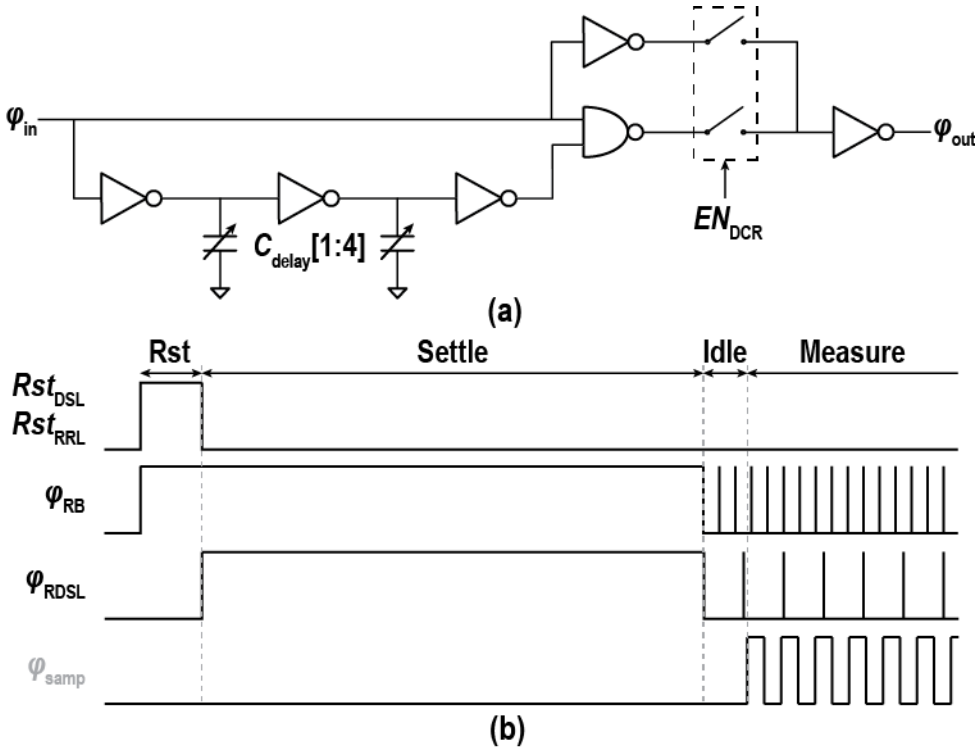

Figure 5.6 Implementation of a DCR

(a) Schematic of the pulse generator, and (b) DCR timing diagram.

a dominant pole whereas the non-dominant pole is at the output due to the ADC sampling capacitor, C_4. However, dc offset at the input and V_{DSL} cause input-dependent charge injection from the input choppers, which requires finite time to settle. Without proper settling, the CCIA linearity drops significantly. The settling time is inversely proportional to the CCIA bandwidth (g_{m1}/C_C). To ensure proper settling before the first ADC sampling instant, g_{m1} must be increased, resulting in an increased power consumption. FSMC is applied to resolve this issue, as shown in Figure 5.7(a). The timing of the CCIA and ADC is adjusted so that the sample switch is turned off right before every chopping edges to ensure that C_4 does not load V_{out} when spikes appear. EN_{C2} disconnects C_{C2} so that only C_{C1} compensates the CCIA, enabling fast spike settling. EN_{C2} closes the switches right before the next rising edge of φ_{samp} to ensure C_{C2} is included for compensating the CCIA

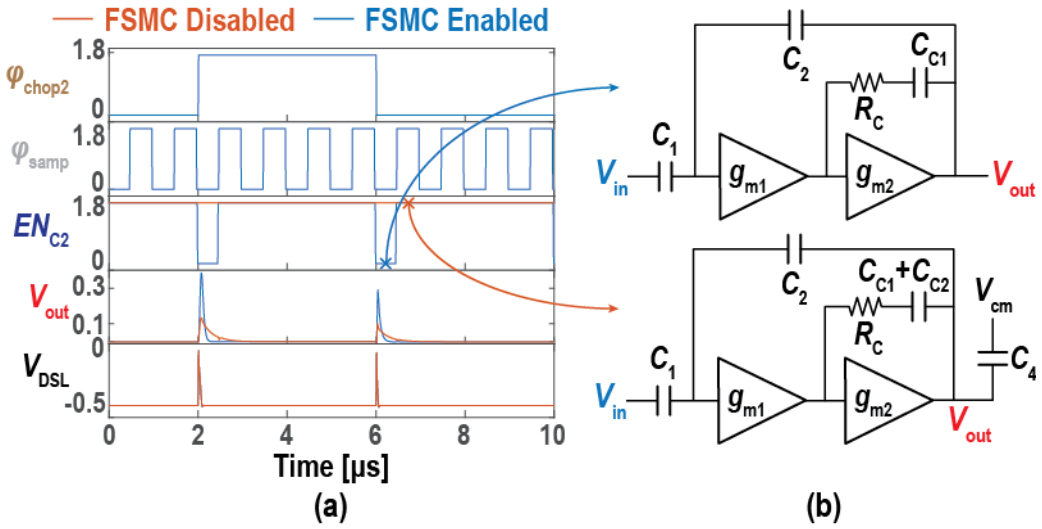

Figure 5.7 Illustration of FSMC

(a) FSMC timing diagram and simulated transient results, and (b) equivalent schematics.

when C_4 loads V_{out}. The equivalent schematics are illustrated in Figure 5.7(b). Simulation results show that although the FSMC results in larger spikes due to higher bandwidth, the spikes settle much faster than the case that always connects C_{C1} + C_{C2}. A nulling poly-resistor, R_C, is placed in series with C_{C1} + C_{C2} to generate a zero that cancels the non-dominant pole. The values of R_C for EN_{C2} = 0 and EN_{C2} = 1 can be calculated as

$$R_C = \frac{C_{C1} + C_2}{g_{m2} C_{C1}} \tag{5.3}$$

$$R_C = \frac{C_{C1} + C_{C2} + C_4}{g_{m2}(C_{C1} + C_{C2})}, \tag{5.4}$$

respectively. Therefore, by selecting the capacitances properly, R_C can be equal in both cases. Inaccurate R_C can cause mismatch between pole and zero but would not cause additional settling since the pole-zero doublet is placed close enough to the unity gain bandwidth (UGBW) [152]. C_{C2} is designed to be 3× larger than C_{C1} to have a worst-case phase margin of >75°. As a result, FSMC relaxes g_{m1} by 4× and thus reduces the CCIA power consumption by 2.5×.

A RRL eliminates the output ripple from the g_{m1} offset [153]. The ripple at f_{chop2} first passes ac coupling capacitors, C_{AC}, and then is downmodulated to dc. After the integrator, the RRL dynamically adjusts the g_{m1} offset through another diff pair, that consumes 10× less power than the main diff pair in the OTA (Figure 5.5(c)). Moreover, one more switch controlled by Dis_{RRL} is added after C_{AC} to disable the RRL during the voltage pulses at V_{out}. In Figure 5.8(a), without this switch (Dis_{RRL} = 0), the instantaneous voltage changes at V_{out} pass C_{AC} to change V_{RRL}, thus creating additional ripple. It is simulated to take >100 µs to settle, significantly increases the deadzone in the relaxation signal readout. To address it, the switch is turned on (Dis_{RRL} = 1) right before the voltage changes to short the inputs of the integrator, thus V_{RRL} remains unchanged. After V_{out} is settled, the switch is turned off (Dis_{RRL} = 0) so the RRL returns to operation and keeps track on the g_{m1} offset. It should also be mentioned that the RRL is required for FSMC, as shown in Figure 5.8(b). Without the RRL, the ripple leads to a different V_{out} before and after EN_{C2} = 0. When EN_{C2} changes from 0 to 1, g_{m1} needs to charge C_{C2}, leading to another settling issue. The RRL cancels the V_{out} ripple so the voltage remains unchanged before and after

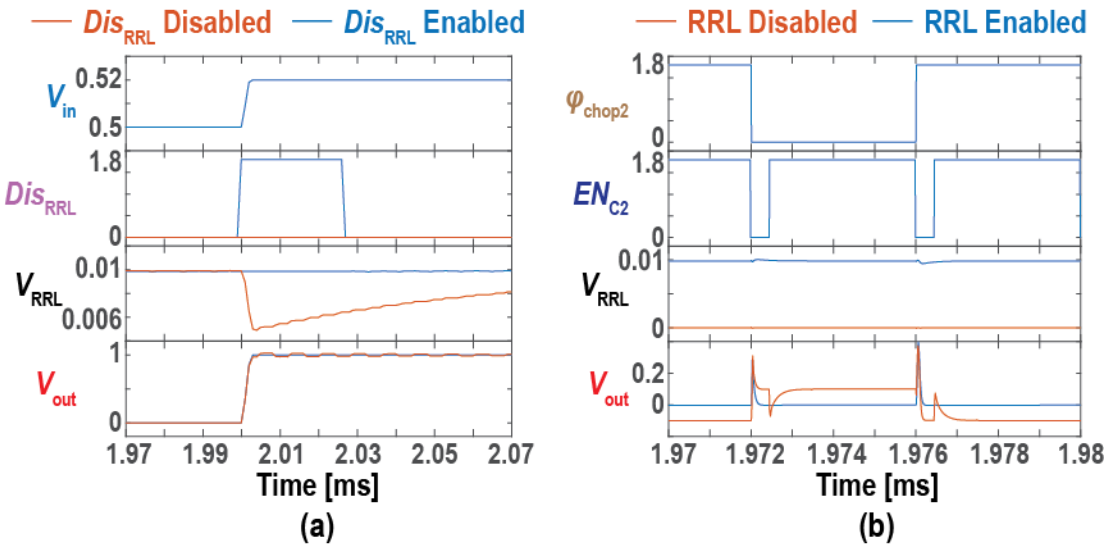

Figure 5.8 RRL timing diagram and simulated results for (a) MRX and (b) FSMC

EN_{C2} = 0. Accordingly, g_{m1} only needs to settle the charge injection from the EN_{C2} switches, which include half-sized dummy switches to absorb the charge injection [154].

While the CCIA has many variables to change, most of them are correlated and even contradict with each other. Table 5.2 summarizes the effect of these parameters. It can be observed that both the tolerable input offset and the high-pass corner frequency, f_{HP}, are contradicting with the input-referred noise. Although f_{HP} can be decreased by reducing the R_{DSL} switching frequency, it would fold noise from V_{out} and thus increase the input-referred noise. Reducing C_{delay} in the pulse generator can benefit the CCIA but is limited by the parasitic capacitance and thus is not a good design parameter. Increasing the chopping frequency, f_{chop2}, rejects more 1/*f* noise but reduces the linearity by making more chopping artifacts. The nominal configuration sets the closed-loop gain to 34 dB, C_1/C_3 to 50, R_{DSL} switching frequency to 10 kHz, and f_{chop2} to 125 kHz. With these values, the transfer function of the CCIA is simulated to have a pass band of 0.34 Hz – 520 kHz.

Table 5.2 Design variables of the CCIA

	Benefit	**Drawback**
Input cap C_1↑	Gain↑, stability↑, input-referred noise↓	Tolerable input offset↓, f_{HP}↑, DR↓
DSL cap C_3↓	Input-referred noise↓	Tolerable input offset↓, f_{HP}↑
DSL DCR R_{DSL}↑ by reducing DCR switching frequency	f_{HP}↓	Input-referred noise↑
DSL DCR R_{DSL}↑ by reducing pulse width (C_{delay}↓)*	f_{HP}↓	Timing mismatch↑
RRL DCR R_{RRL}↑ by reducing pulse width (C_{delay}↓)*	Notch BW↓	Settling time↑
Chopping frequency f_{chop2}↑	Input-referred noise↓	Linearity↓

* Not a significant source.

5.3.3 18b Zoom ADC

A Zoom ADC is an incremental hybrid ADC for dc-input, high resolution conversion [155]. Figure 5.9 illustrates the block diagram, where a 6b SAR first coarsely quantizes V_{out} and then adjusts the reference voltages of the following DSM through a 6b DAC. Pseudo random bit sequence (PRBS) non-segmented DEM is implemented off-chip by an FPGA to shape the mismatch of the DAC [156]. A first-order single-bit DSM quantizes the residue with an OSR of 9,956 and an on-chip counter decimates the bitstream, providing a 13b output. Since the SAR result SAR_{out} needs to be extended for ±1 SAR_{LSB} to avoid saturating the DSM, the Zoom ADC provides a resolution of 6 + 13 - 1 = 18b. The sampling frequency is 1 MHz and the noise bandwidth is 100 Hz. Since the voltage residue during DSM cannot exceed ±1 SAR_{LSB}, the maximum input signal frequency can be written as

$$f_{\text{sig}} < \frac{V_{\text{ref}}}{2\pi A_{\text{sig}} T_{\text{cycle}} 2^6} \tag{5.5}$$

where V_{ref} is the ADC reference voltage, A_{sig} is the input signal amplitude, and T_{cycle} is the ADC cycle time.

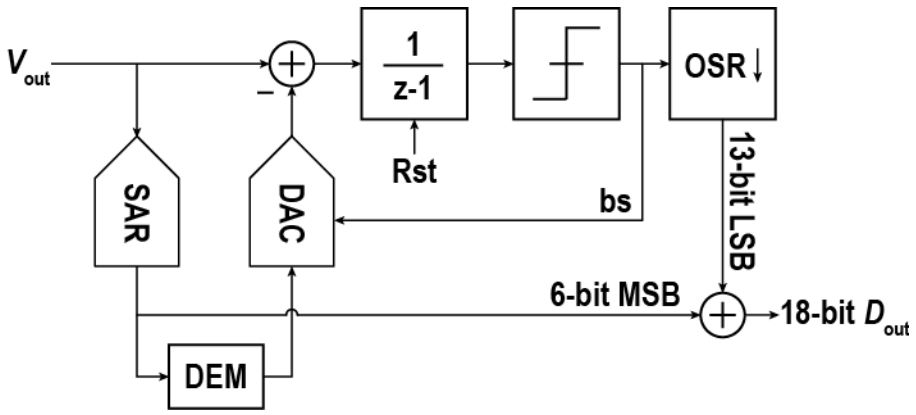

Figure 5.9 Block diagram of the Zoom ADC

Considering a fullscale sinusoidal input ($A_{sig} = V_{ref}/2$), T_{cycle} = 10 ms, f_{sig} must be <0.5 Hz to not saturate the ADC. Although a dynamic Zoom ADC was reported to improve the ADC speed by running the SAR and the DSM concurrently, the hardware cannot be shared [157]. Therefore, the Zoom ADC is for a high-resolution dc input, which is the right fit in this application.

The implementation of the Zoom ADC is shown in Figure 5.10. It consists of a switched capacitor integrator, a dynamic latched comparator, and digital logic that generates clocks. The SAR and DSM share most of the same hardware. The ADC timing diagram is illustrated in Figure 5.11(a). First, the ADC is configured as a SAR that samples V_{out}. Since it is the first sample in an ADC cycle, it takes 3× longer time for settling. Then, 6 SAR conversion cycles are conducted through charge redistribution between C_4 and C_5. Afterwards, the 6b SAR result, SAR_{out}, is stored in the FPGA and sets the DSM reference voltages to $SAR_{out} \pm 1 * SAR_{LSB}$. More specific operation of the DSM phase is

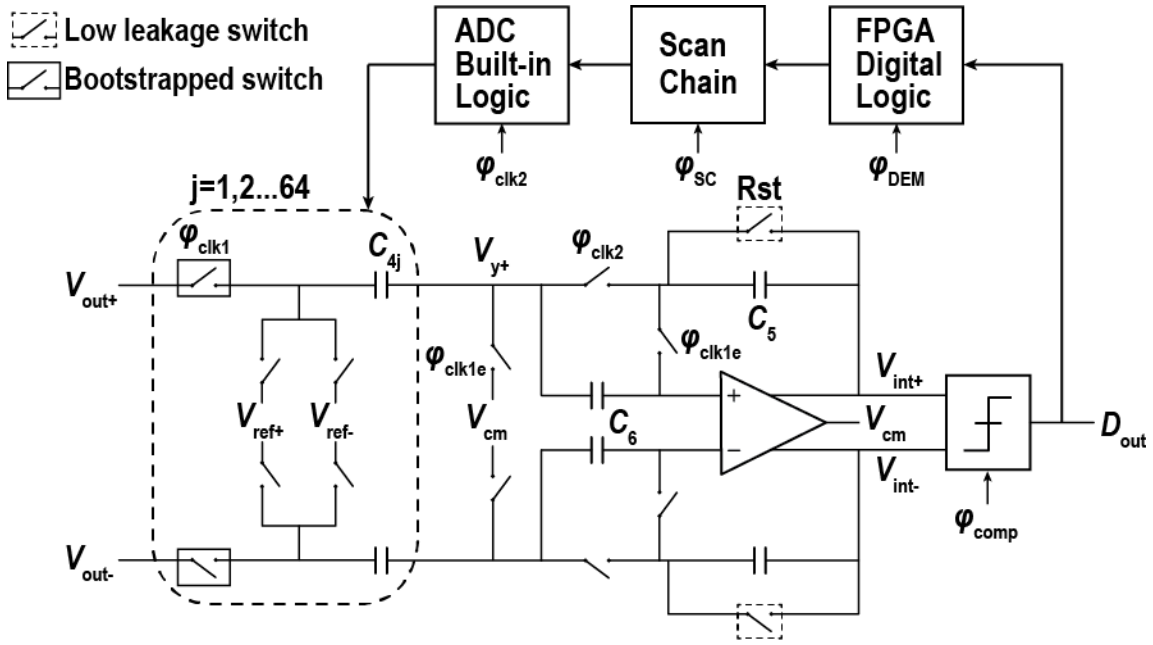

Figure 5.10 Schematic of the Zoom ADC

illustrated in Figure 5.11(b). During the sampling phase, C_4 samples the input, V_{out}, and the charge stored on C_4 and C_5 can be written as

$$Q_4 + Q_5 = C_4 V_{\text{out}}[n] + C_5 V_{\text{int}}[n-1]. \quad 5.6$$

The comparator clock, φ_{comp}, which is delayed from φ_{clk1} to settle any charge injection, compares the integrator output from the previous cycle, V_{int}[n-1]. The DEM clock, φ_{DEM}, is delayed to compensate for the comparator delay. The scan chain clock, φ_{SC}, transfers the 16b data from the FPGA to the chip, and 4 scan chains work in parallel for the 64 CDAC control signals. The rising edge of φ_{SC} converts the parallel data from the DEM block to series data, which is implemented in the FPGA, and the falling edge of φ_{SC} converts it back to parallel that is implemented on-chip. While these digital delays limit the ADC speed, synthesizing the digital logic on-chip can get rid of the scan chain and improves the speed. During the integration phase, the ADC built-in logic sets the 64 switches for the CDAC. Specifically, $SAR_{out} \pm 1$ C_{4j} connect to V_{ref+} and the others connect to V_{ref-}, where D_{out}[n-1] determines the sign. As a result, the charge stored on C_4 and C_5 can be written as

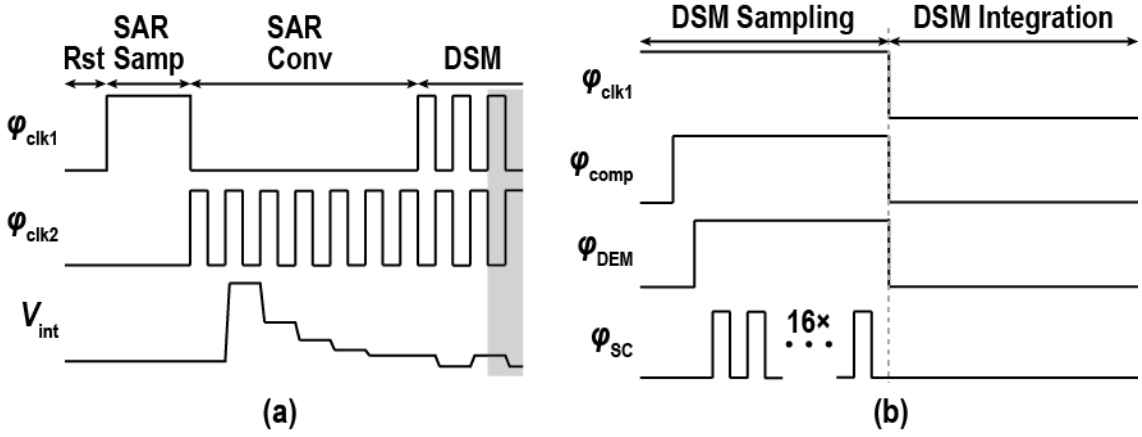

Figure 5.11 Timing diagram of the ADC

$$Q_4 + Q_5 = C_4(SAR_{\text{out}} \pm 1)\frac{V_{\text{ref}}}{2^6} + C_5 V_{\text{int}}[n]. \quad 5.7$$

Since the total charge is the same assuming negligible leakage, the integrator output can be derived by combining Equations 5.6 and 5.7 as

$$V_{\text{int}}[n] = V_{\text{int}}[n-1] + \frac{C_4}{C_5}V_{\text{out}}[n] - \frac{C_4}{C_5}(SAR_{\text{out}} \pm 1)\frac{V_{\text{ref}}}{2^6}. \quad 5.8$$

As $C_4 = C_5$, Equation 5.8 indicates that the DSM has been bounded within (SAR_{out} + 1) $V_{ref}/2^6$ and (SAR_{out} - 1) $V_{ref}/2^6$.

The reference voltages of the ADC, V_{ref+} and V_{ref-}, are set to V_{DD} and GND, respectively ($V_{ref} = V_{ref+} - V_{ref-} = V_{DD}$). Similar to a conventional DSM, bottom plate sampling and CDS are applied for high linearity and low 1/*f* noise, respectively. The comparator and OTA architecture are the same as the ones used in Section 3.3.4.

The CDAC mismatch limits the ADC linearity to be 12b. It can be improved by the PRBS DEM that is implemented off-chip for flexibility. The 6b CDAC consists of 64 identical capacitors (C_{4j} = 200 fF) that are independently controlled. The illustration of the non-segmented DEM is shown in Figure 5.12(a). The 6b CDAC requires 6 levels to convert the binary input code to a thermometer output code, and thus needs 6 uncorrelated random bit sequences $r_{1..6}$. At each clock cycle during the DSM phase, D_{out} determines the input of the DEM to be either SAR_{out} - 1 or SAR_{out} + 1. One additional LSB, a_0 = 0, is added to the input to contain two LSBs, which can avoid using adders. If the LSBs are 00, both output LSBs of the first switching block $S_{6,1}$ are 0; if the LSBs are 10, one output LSB is 0 and the other one is 1, depending on r_6[n]. The output MSBs are simply equal to the input MSBs. The remaining 5 levels follow the same process until all

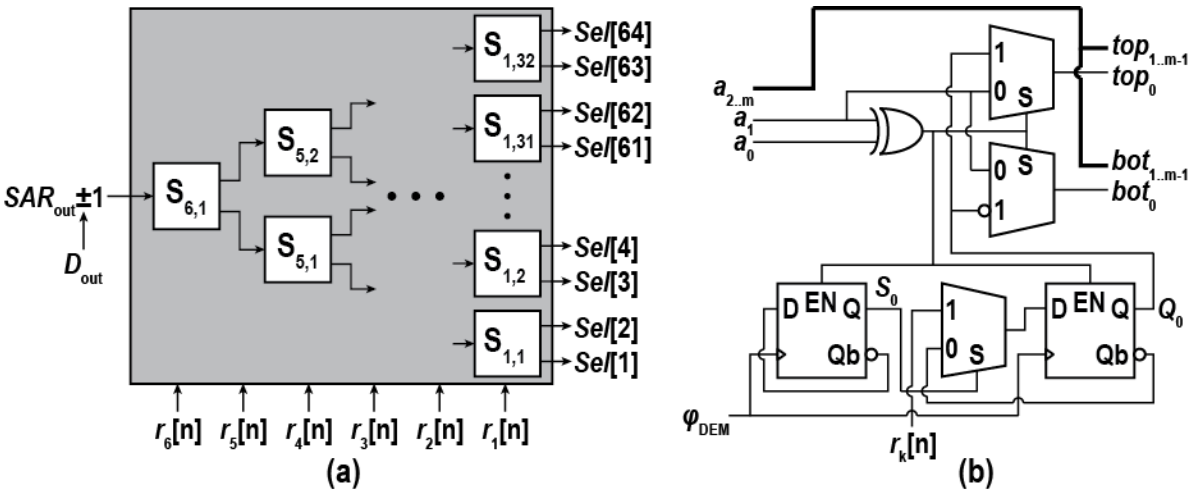

Figure 5.12 Illustration of the DEM

(a) Block diagram of the DEM, and (b) implementation of each switching block.

64 1b control signals come out. Figure 5.12(b) shows the implementation of each switching block. The XOR gate and two muxes on the top implement the previously described function. The mux and two DFFs on the bottom generate '0' and '1' doublets to bound the output. Assuming $r_k[n] = 1$ and $S_0 = 1$, at the rising edge of φ_{DEM}, the output, Q_0, is 1, which leads to $top_0 = 1$ and $bot_0 = 0$ if the input, $a_{0,1}$, is odd. Meanwhile, the left DFF changes S_0 from 1 to 0. Therefore, on the next clock cycle, Q_0 would change to $\sim r_k[n] = 0$, no matter what $r_k[n+1]$ is. Each level has one uncorrelated random bit sequence ($r_{1..6}$), which is generated by a 2^9-1 PRBS generator [158]. As a result, pseudo-random doublets are generated to have a PRBS, which first-order shapes the CDAC mismatch without generating spurious tones [159]. It should be noted that although φ_{DEM} is used for synchronization, the signal path only consists of combinational logic and thus the propagation delay is relatively short.

Bootstrapped sampling switches are used for high linearity, as shown in Figure 5.13(a). Instead of using 64 independent switches, the switches share the control transistors and the capacitor, C_{bs}. As shown in Figure 5.13(b), C_{bs} is pre-charged to V_{DD}

during the ADC integration phase (φ_{clk1b} = 1) and V_{bst} is tied to GND to turn off the sampling switches, M_{samp}[1:64]. During the sampling phase (φ_{clk1b} = 0), C_{bs} is connected to V_{out} and V_{bst}, leading to a charge sharing between C_{bs} and the parasitic capacitance, C_{par}. Thus, $V_{bst} = V_{out} + V_{DD} - \Delta V$, where ΔV is due to the charge sharing. Assuming $\Delta V << V_{DD}$, the bootstrapped switch provides a constant V_{GS} of V_{DD} to M_{samp}, thus achieving high linearity. Sharing the control transistors not only reduces the area, more importantly, it reduces C_{par} and thus ΔV. A sinusoidal input with an amplitude of $0.8V_{ref}$ and a frequency of 305.4 kHz was used to simulate a shared bootstrapped switch, an independent bootstrapped switch, and a CMOS switch with a sampling rate of 1 MS/s. Table 5.3 shows that the shared bootstrapped switch provides an ENOB of 17.7b, that is 0.6b and 7b higher than the independent bootstrapped switch and the CMOS switch, respectively.

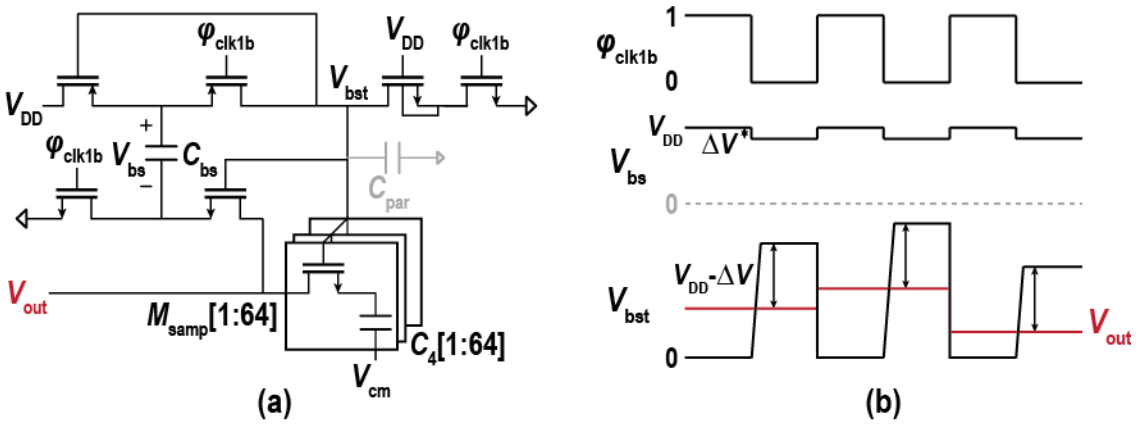

Figure 5.13 Illustration of the bootstrapped switch

(a) Schematic of the bootstrapped switch and (b) timing diagram.

Table 5.3 Comparison between different sampling switches

	CMOS	Independent Bootstrapped	Shared Bootstrapped
ΔV	N/A	300 mV	80 mV
THD	-66.3 dB	-104.9 dB	-108.3 dB
ENOB	10.7b	17.1b	17.7b

5.4 Measurement Results

5.4.1 Test Setup

This chip was fabricated in a TSMC 180-nm CMOS process. An annotated die photo is shown in Figure 5.14(a). It operates from a single supply of 1.8 V and consumes 4.32 mW excluding the sensor bias, which is dependent on the sensor resistance and consumes 3.9 mW for the 1.3 kΩ sensors used in this work. The power contributions of each block (CCIA: 52%, ADC: 22%, digital: 20%, bias: 6%) are shown in Figure 5.14(b).

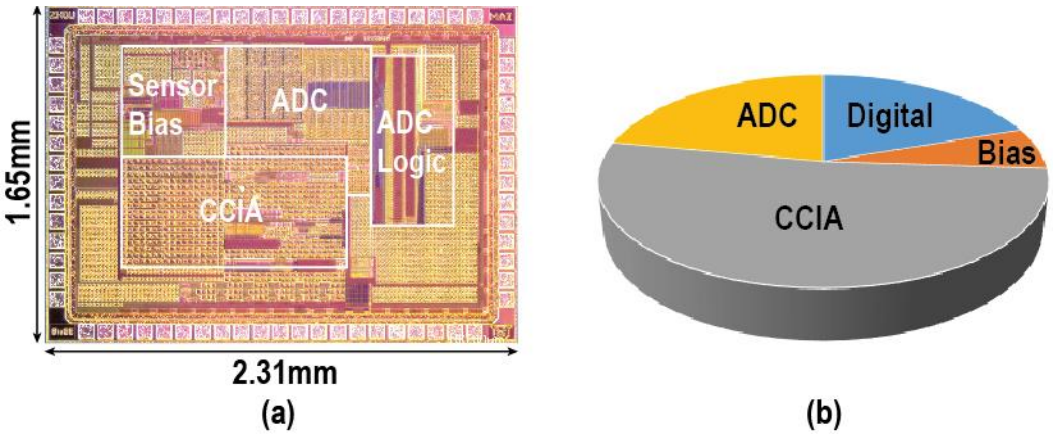

Figure 5.14 (a) Annotated die photo and (b) power distribution

The measurement setup is shown in Figure 5.15. A power amplifier (Kepco BOP 36-12ML) and a customized coil driver PCB (the same one discussed in Section 4.5) provides a pulsed current for the Helmholtz coil, which generates a pulsed magnetic field (30 Oe) for the sensor bias. The coil driver, which is controlled by the FPGA (Opal Kelly XEM6310), provides a fast decay (<2 μs) magnetic field for the sensor to minimize the measurement deadzone [76]. The same FPGA provides clocks and control signals for the chip, as well as captures the data from the ADC. The CM voltage generator, which consists of resistor dividers and low noise buffers, generates dc voltages V_{bias}, V_{cm}, and

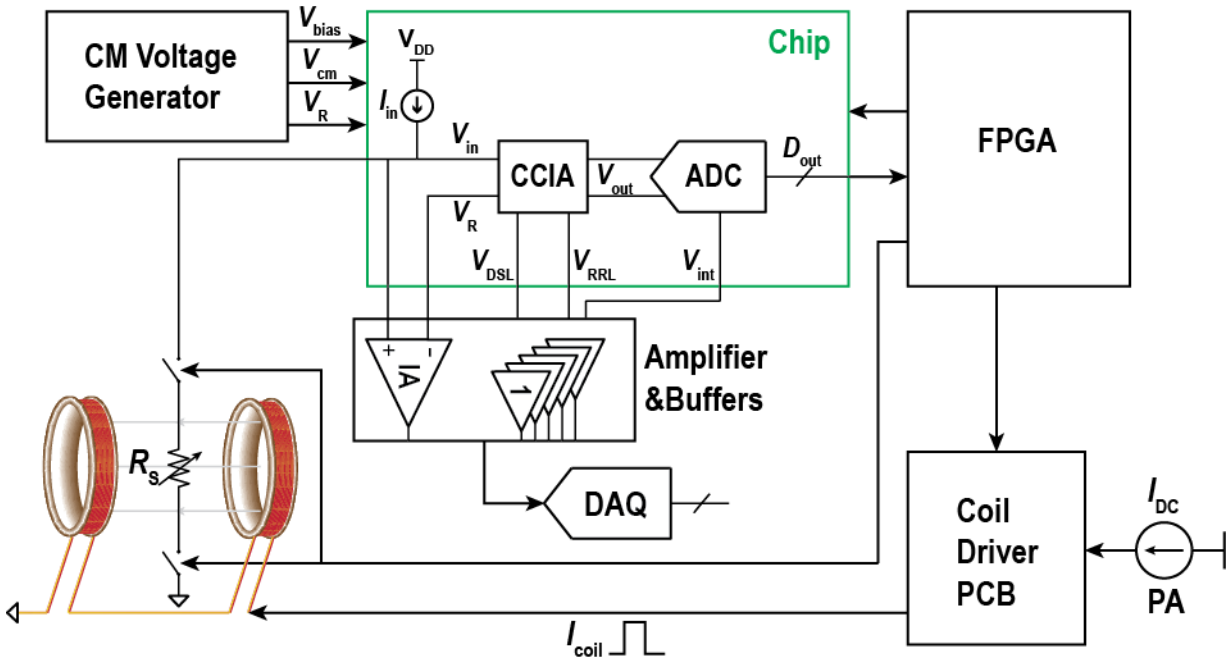

Figure 5.15 Illustration of the test setup

V_R for the chip. Each critical analog node in the chip can be measured by a DAQ (NI-6289) after off-chip buffering. It should be noted that an off-chip instrumentation amplifier (IA, Analog Devices AD8429) is used to amplify the input voltages V_{in} and V_R before the DAQ for low noise measurement.

To read each sensor independently from a 10×9 sensor array, a feedback configuration is required, as shown in Figure 5.16(a). A row mux connects one row at a time to the chip and other rows are open. A column mux connects one column at a time to GND, while other columns are connected to V_{in_buf}, which is a buffered version of V_{in}. As a result, the bias current only flows into one selected sensor. All other sensors in the same row are shorted and sensors in other rows are open. TDM is applied to measure all sensors, and thus takes $90T_{total}$, where $T_{total} = T_{settle} + 2T_{cycle}$ for MR-CDS and $T_{total} = T_{settle} + 3T_{cycle}$ for MCDS. The standard configuration has T_{settle} = 2 ms and T_{cycle} = 10 ms, therefore the total measurement time for reading all sensors is 1.98 s and 2.88 s for MR-

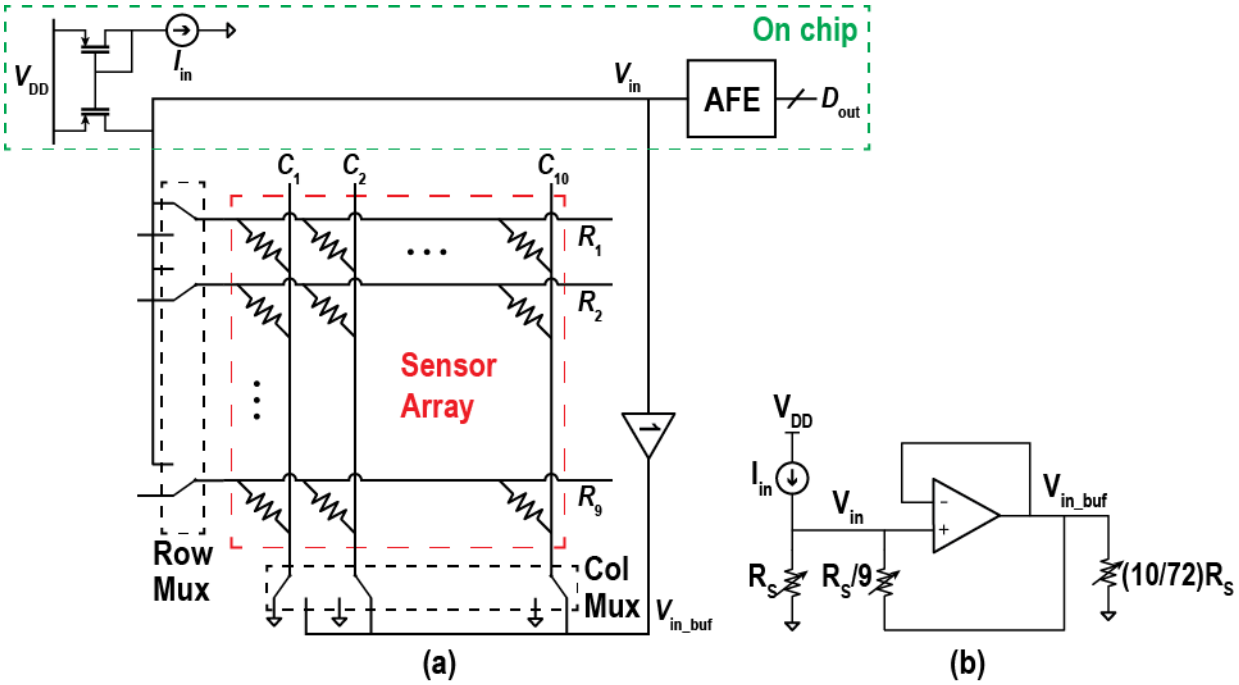

Figure 5.16 Sensor array network

(a) Configuration of the sensor array for individual pixel readout, and (b) equivalent schematic for noise analysis.

CDS and MCDS, respectively. The equivalent schematic of the sensor network is shown in Figure 5.16(b). The noise at node V_{in} can be derived as

$$v_{n,in}^2 = (10 \cdot 4k_B T R_S) + \left(9v_{n,op}\right)^2 \quad 5.9$$

where $v_{n,op}$ is the op-amp input-referred noise. Therefore, the sensor network generates √10× higher sensor noise and 9× higher op-amp noise. An ultra-low noise op-amp (Analog Devices ADA4897-1) was used to have a comparable noise contribution as the sensor array. Since this noise penalty can be eliminated by using an independently controlled sensor array, a resistor with the similar resistance as R_0 was used to characterize the AFE for the rest of this chapter, unless otherwise notified.

5.4.2 Electrical Measurement Results

Figure 5.17 shows the measured noise spectra of the sensor bias block. The rotating DEM reduces the spot noise at 50 Hz (16 nV/√Hz) by 2.2×. It should be noted that only the spot noise at 50 Hz is considered because MR-CDS can eliminate the 1/*f* noise that is <50 Hz, given T_{cycle} = 10 ms. Upmodulated 1/*f* noise and current mirror mismatch generate tones at f_{DEM} and f_{chop}, which are out of the signal band and will be filtered out by the ADC decimation filter.

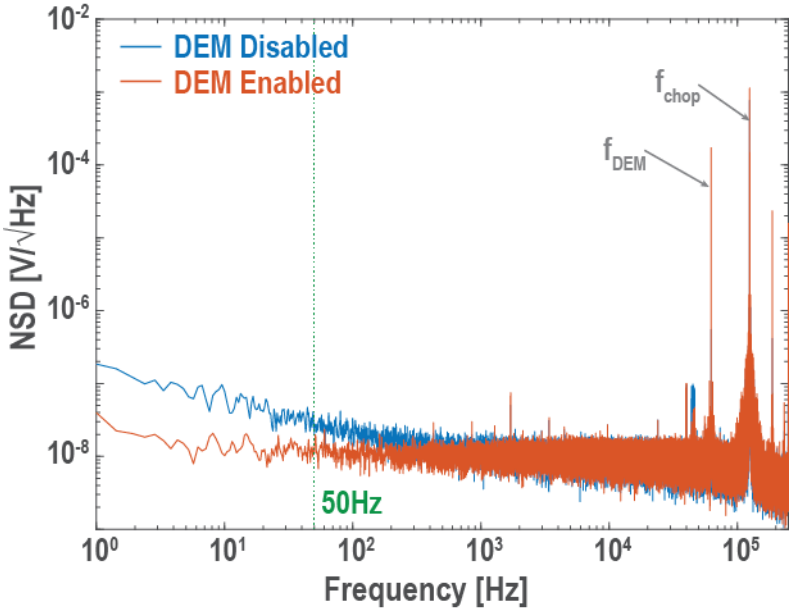

Figure 5.17 Measured sensor bias noise spectra

Figure 5.18 shows the measured noise spectra of the CCIA under different conditions. The highest DR configuration has the lowest gain and largest tolerable input offset, thus has the highest noise. On the contrary, the lowest noise configuration has the highest gain and lowest tolerable input offset. The standard configuration has been discussed in Section 5.3.2. The noise spectra show that most 1/*f* noise has been upmodulated out-of-band but there is some residual 1/*f* noise, which comes from the DSL.

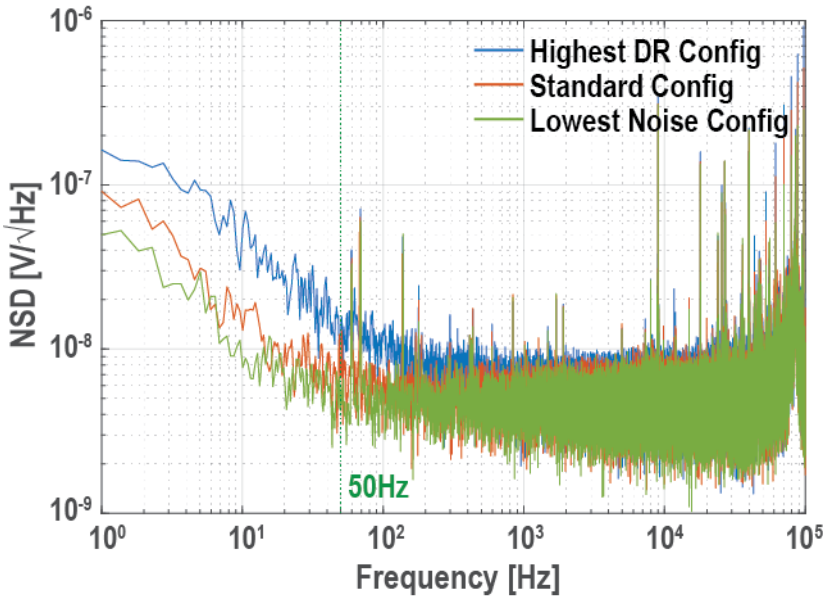

Figure 5.18 Measured CCIA noise spectra

Since the nominal and the lowest noise configuration only has a gain difference and no difference on C_3, the noise is similar, indicating that the DSL dominates the noise. The CCIA input-referred spot noise at 50 Hz was measured to be 7 nV/√Hz.

Figure 5.19 shows the measured CCIA THD versus the input offset using a sinusoidal input that has an output swing of 1.6 V_{pp}. This output swing can cover a magnetic field up to 43 Oe, which is high enough to polarize the MNPs. Larger input offset leads to larger V_{DSL}, thus causes higher spikes at V_{out}. Without FSMC, these spikes are not fully settled when the ADC samples, thus causing distortion. The FSMC settles the spikes faster and improves the CCIA linearity variation from 10 dB to 1.2 dB across the input offset range. The spectra at V_{os} = -17 mV show a HD2 improvement of 18 dB. It should be mentioned that the unbalanced input offset range is due to the offset from the DSL. The linearity across the input offset range was measured to be >85 dB, which is sufficient for the magnetic biosensing that requires a DR of >80 dB.

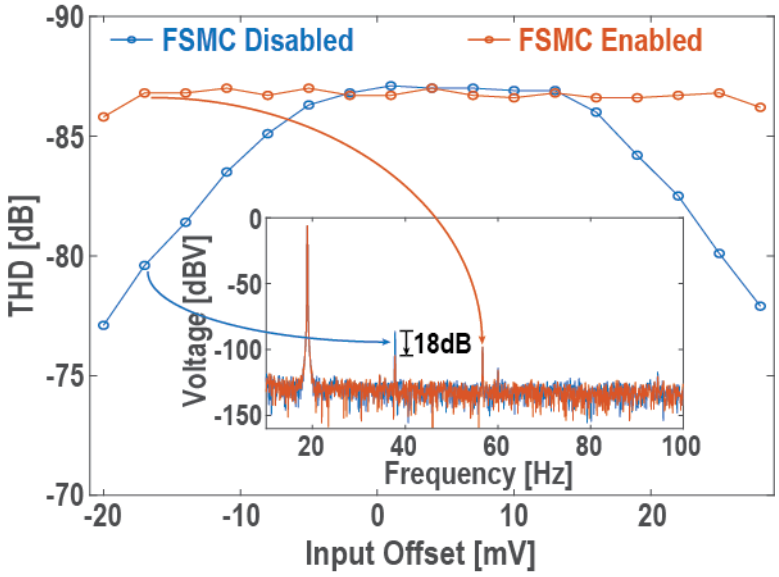

Figure 5.19 CCIA linearity vs. input offset

The ADC noise was measured, as shown in Figure 5.20. The spectrum shows pure white noise, that is 710 nV/√Hz. It can be input-referred based on the nominal CCIA configuration, resulting in 14.2 nV/√Hz that is comparable to the noise from the sensor bias block. Therefore, it necessitates the 18-bit resolution.

The ADC linearity was characterized using a dc sweep histogram by an audio analyzer (APx555B). Figure 5.21 shows the measured DNL and INL over the input range of -0.8 – 0.8 V, the same as the CCIA test range. The ADC has a DNL of -0.87/+1.19 LSB and an INL of -4.2/+4.5 LSB. The equivalent SFDR is 95 dB, 10 dB higher than the CCIA and thus sufficient for the application.

Figure 5.22 shows the system integrated noise vs. the readout time. MR-CDS has a readout time of 22 ms, which consists of 2 ms for reset and settling and 20 ms for measurement. MCDS needs 32 ms due to one additional cycle. The measured data can be averaged for lower noise with a longer readout time. With CDS, both MCDS and MR-CDS show a linear tradeoff between the readout time and integrated noise on a log scale

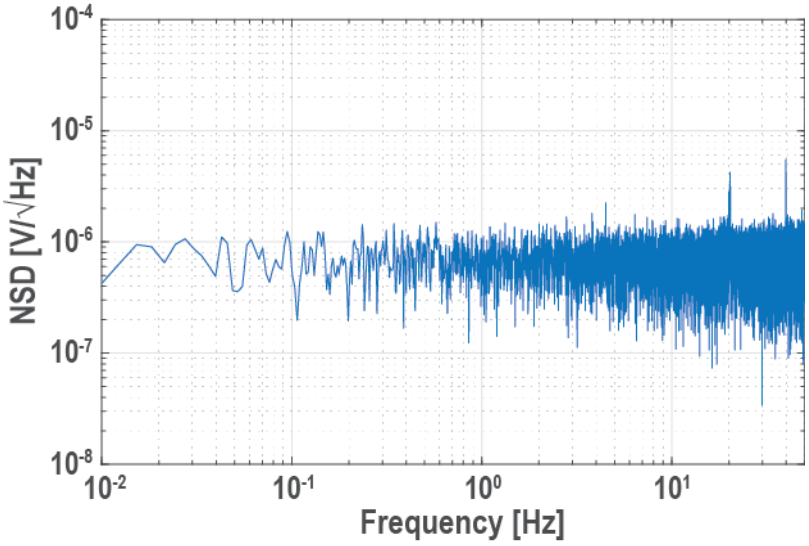

Figure 5.20 Measured noise spectrum of the ADC

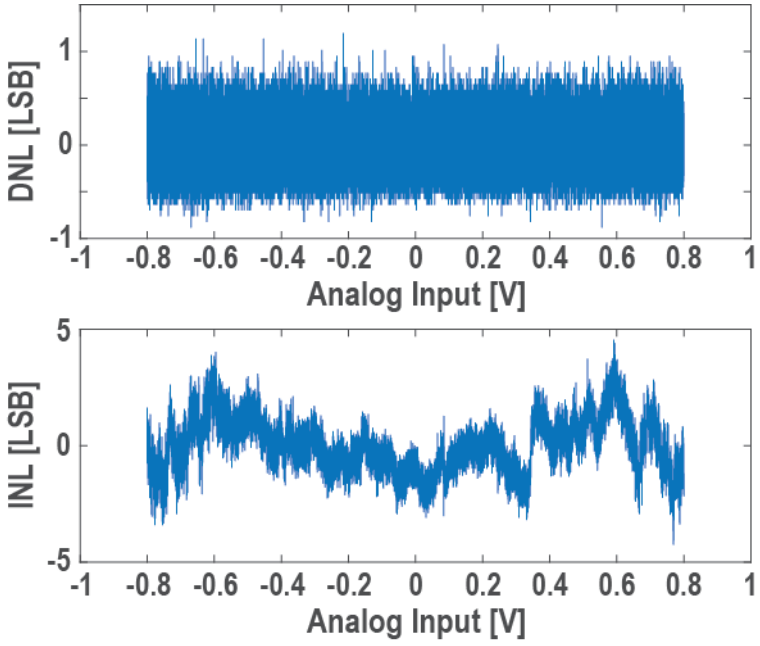

Figure 5.21 Measured DNL and INL of the ADC

because the 1/*f* noise is eliminated. Without CDS, the residue 1/*f* noise limits the resolution for long readout times. MR-CDS was measured to reduce the integrated noise by 1.34× compared to MCDS, which matches the theoretical result of √1.5 – 1.5×, as discussed in Section 5.2.1.

The system baseline was measured in both MCDS and MR-CDS, as shown in Figure 5.23. MR-CDS could not reject MR baseline, thus has higher baseline than MCDS. The residual baseline in MCDS comes from the DSL. Although f_{HP} in the CCIA is low enough to not saturate the ADC, it still distorts the waveform, leading to a residual baseline. Increasing R_{DSL} decreases f_{HP}, and thus reduces the baseline. The AFE has a measured residual baseline of 0.12 mT in the standard configuration of the CCIA, that is 25× smaller than MR-CDS.

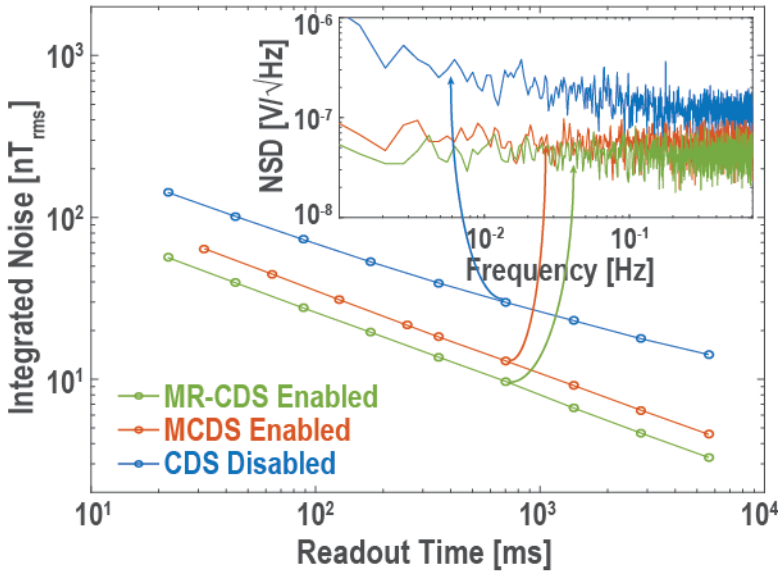

Figure 5.22 Measured system integrated noise vs. readout time

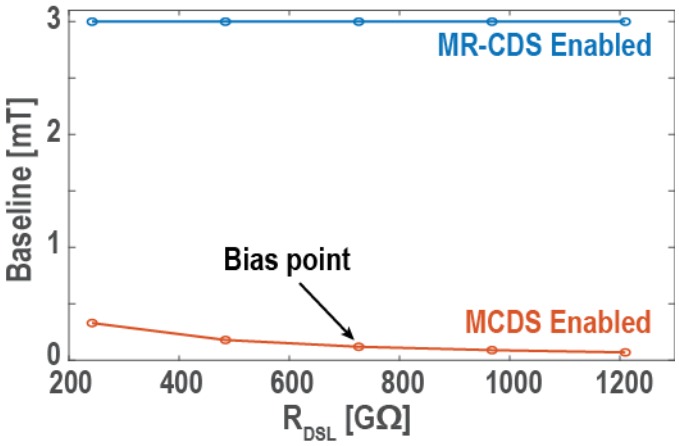

Figure 5.23 Measured system baseline vs. DSL integrator resistance

Figure 5.24 shows the system temperature drift. Cold IPA (-18 °C) was dropped on the sensor surface at t = 3 min while the system was continuously measuring for 33 min. As a result, MR-CDS shows large drift up to 46 ppm and MCDS only shows a drift of <3 ppm. Although both R_0 and R_{MR} are temperature sensitive, R_0 drift is rejected by both the DSL and the CDS techniques. R_{MR} drift, however, can only be rejected by MCDS because MR-CDS still contains the MR baseline.

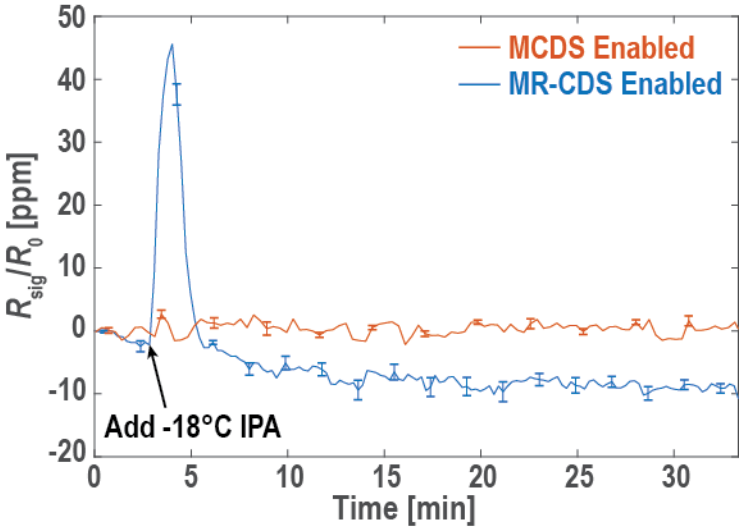

Figure 5.24 Measured temperature drift

5.4.3 Biological Measurement Results

Biological experiments were conducted for proof-of-principle demonstration. First, MNPs (Ocean Nano-Technologies SHS-30-01) were dried on the sensor surface. To measure the temporal relaxation signal, the DAQ was used to measure the CCIA outputs at a sampling rate of 500 kS/s with an 18b resolution. Figure 5.25(a) shows the measured relaxation curves of 70 sensors. With a relaxation time of 10 ms, the signal amplitude ranges from 1200 ppm to 1500 ppm, depending on the coverage of the MNPs. Normalizing the relaxation curves, all curves follow Equation 4.2, with a characteristic time (t_C) of 19.3 ms (Figure 5.25(b)). While t_C is highly dependent on the magnetization

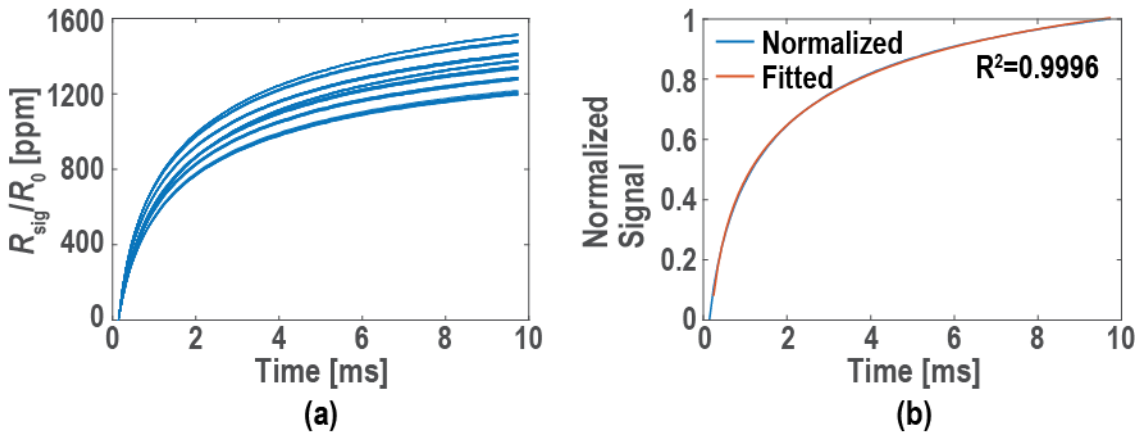

Figure 5.25 Measured temporal relaxation curves of the dried MNPs

(a) Measured relaxation curves from 70 sensors, and (b) normalized and fitted relaxation curves.

time and the magnetic field strength, the measured t_C fits with the analytical results discussed in Section 4.6.3.

A MIA was conducted afterwards to validate the system, as shown in Figure 5.26(a). The first row of the sensor array (10 sensors) was covered by epoxy, thus serving as reference sensors. The other 70 sensors were functionalized with NHS-Biotin through APTES chemistry. First the sensors were immersed in 100 µL of 1% KOH in DIW for 10 minutes at 37 °C. Once the KOH solution was removed, the sensors were washed with 300 µL of DIW and allowed to dry. Then 70 µL of 100% APTES was added to the sensors for 1 hour at 37 °C (paraffin was wrapped around the sensor well to prevent evaporation). After the APTES was removed, the sensors were washed 5× with 300 µL of PBS. Then, 50 µL of NHS-Biotin (1 mg/mL in DMSO) was added to the sensors for 1 hour at 37 °C before removal and 3 cycles of washing with 300 µL of PBS. Blocking was accomplished by adding 100 µL of 10% BSA in PBS for 15 minutes at 37 °C before removal and 3 cycles of washing with 300 µL of PBS. Lastly, 100 µL of PBS was added before the sensor array was moved to the test bench.

After removing the PBS and adding the MNPs (50 µL of MNPs), the active sensors show signals of ~140 ppm, while the reference sensors show no signal. The error bars represent one standard error in the plot. Figure 5.26(b) illustrates the signal map of the 8×10 sensor array at t = 800 s. Compared to the dried MNPs, the MIA shows ~10× smaller signal amplitude because of the farther distance between the MNPs and the sensor and the lower density due to the binding equilibrium.

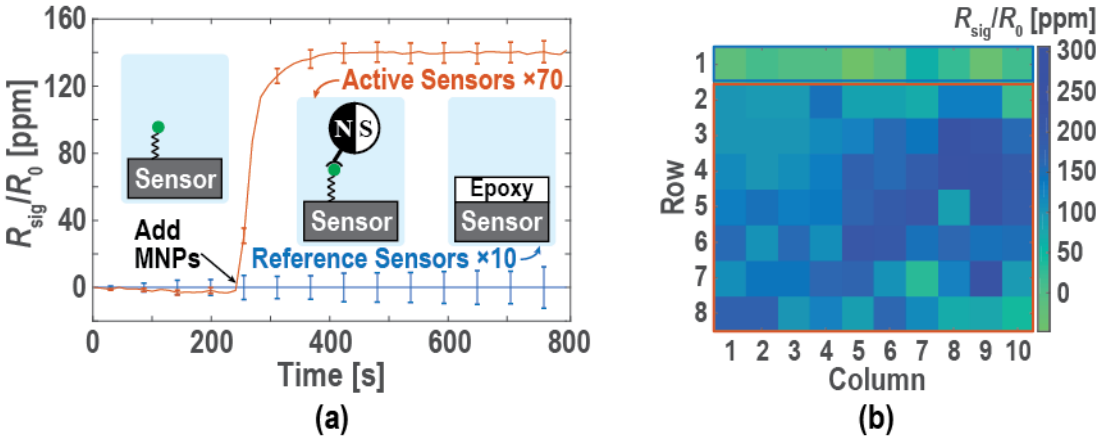

Figure 5.26 MIA experiment result

(a) MIA real-time binding curves for active and reference sensors; and (b) MIA coverage map.

5.5 Conclusion

This chapter presented a GMR sensor AFE with an 18b Zoom ADC to detect MNP relaxation. A sensor bias block with rotating DEM reduced 1/f noise from the bias transistors by 2.2×. A CCIA with FSMC reduced the CCIA power consumption by 2.5×, while maintaining the linearity and stability. An 18b Zoom ADC quantized the CCIA outputs with an INL of 4.5 LSB. The system could use either MR-CDS or MCDS to capture the signal, as well as rejecting R_0 baseline and removing the noise/time tradeoff limitation by eliminating 1/f noise. This work is summarized in Table 5.4. Compared to other magnetic sensor front-ends, this work provides lowest input-referred noise, along with

comparable power consumption and readout time. It results in a best-reported resolution FoM of 286 and 514 $nT^2 \cdot mJ$, respective to MR-CDS and MCDS, which is 4.9× better than other magnetic AFEs and 210× better than MRX-based AFEs. While MR-CDS shows the best FoM, MCDS has advantages on the baseline reduction and temperature drift cancellation. This work supports both techniques to enable different techniques in

Table 5.4 Comparison of the current state-of-the-art magnetic sensor AFEs

	Wang ISSCC'09 [48]	Hall JSSC'13 [56]	Costa Tbcas'17 [53]	Liu JSSC'12 [50]	Gambini JSSC'13 [51]	**This work (MR-CDS)**	**This work (MCDS)**
Sensor Type	LC	GMR	GMR	Hall	Hall	**GMR**	
Sensor R_0 (kΩ)	N/A	1.92	0.85	N/A	N/A	**1.3**	
MR Ratio (%)	N/A	9.2	5.37	N/A	N/A	**7.74**	
MNP Size (nm)	1,000	50	250	1,000	1,000	**40**	
Technology Node (μm)	0.13	0.18	0.35	0.18	0.18	**0.18**	
Sensing Method	Magneto	Magneto	Magneto	MRX	MRX	**MRX**	
AFE Architecture	LC oscillator	TIA	Amplifier	PGA	V/I Converter	**CCIA**	
ADC Architecture	VCO-based	ΔΣ	No ADC	No ADC	Inc. ΔΣ	**Zoom**	
Input-referred Int. Noise (nT_{rms})	N/A	49	11.5Ψ	15Ψ	1207.5	**8.6Ψ 9.7**	**13**
Readout Time/Ch. (ms)	400	250	1,000	64,000	50	**704**	
Power/Ch. (mW)*	N/A	3.15	4.9Ψ	6.2Ψ	0.825	**2.5Ψ 4.32**	
Area/Ch. (mm^2)	N/A	0.219	3.17	N/A	0.012	**1.92**	
Number of Ch.	8	16	1	1	160	**1**	
Input-referred Baseline (mT)	N/A	7.09	1.84	<0.001	0.007	**3**	**0.12**
Temperature Correction	Yes	Yes	No	Yes	Yes	**No**	**Yes**
Resolution FoM ($nT^2 \cdot mJ$)	N/A	1891	648Ψ	89280Ψ	60143	**133Ψ 286**	**514**

* Power/Ch does not include sensor bias and magnetic field generator. Ψ Does not include ADC.

different applications. Lastly, both dried MNP experiment and a MIA were conducted to validate the system performance, which enables high sensitivity magnetic biosensing for PoC diagnostics.

Chapter 5, in part, is currently being prepared for submission for publication of the material from Xiahan Zhou, Enhan Mai, Michael Sveiven, Corentin Pochet, Haowei Jiang, Chih-Cheng Huang, and Drew A. Hall. The dissertation author was the primary investigator and author of this paper.

Chapter 6. SUMMARY

6.1 Summary of Dissertation

This dissertation described the innovations made to the MR sensor circuit front-end, system, and signal processing. The following is a summary of the key contributions and results presented in the dissertation.

Chapter 2 discussed two magnetic sensing techniques, magnetometry and MRX. While magnetometry measures the signal superimposed on the baseline, MRX detectes the MNP relaxation after removing the applied field, and thus can overcome the small signal to baseline problem. However, MRX requires two more steps and the low frequency relaxation signal needs longer acquisition time and is more vulnerable to 1/*f* noise. Therefore, MRX had worse FoM in terms of resolution, power, and readout time than magnetometry in the literature. A discrete-time 8-channel sensor front-end and system was designed to perform experimental work with a double modulation scheme and lock-in detection for low noise measurement.

Chapter 3 presented a CMOS sensor front-end based on magnetometry. In addition to the double modulation scheme, a reference sensor that is covered by epoxy

further canceled the baseline but was limited by the sensor mismatch. A PGA rejected the common-mode signal and amplified the differential signal between the active sensor and the reference sensor. A fast settling DCR was reported to improve the settling speed by 40× during the sensor switching. Moreover, the PGA downmodulated the signal tone to dc, which relaxed the ADC bandwidth requirement. A first-order incremental ΔΣ ADC quantized the PGA output with an OSR of 10,000. A HFIR technique embedded in the ADC sampling network reduced the interference tone caused by the sensor mismatch by 6—7×, thus relaxed the ADC DR requirement. As a result, this work achieved 22.7× faster readout time, >7.8× lower input-referred baseline, and 2.3× lower power than other magnetometry-based AFEs. More importantly, this design achieved sub-ppm sensitivity and tolerated up to 10% sensor mismatch. Lastly, this work demonstrated a sub-pM biological LOD and 3 orders of biological DR.

Chapter 4 presented a discrete 8-channel sensor front-end and system for detecting MNP relaxation. A switched integrator integrated the decaying relaxation signal with time, thus relaxed the ADC speed requirement. While a longer integration time could integrate more signal, it also integrated more 1/*f* noise. An optimal integration time was found to achieve the best SNR. To reduce the common-mode interference such as the temperature drift and the system nonlinearity, MCDS that subtracted the active phase ($H_A > 0$) from the reference phase ($H_A = 0$) was used to take advantage of the sensor self-reference. To reduce the measurement deadzone, a customized coil driver discharged the highly-inductive electromagnet using a high voltage of -500 V, which reduced the deadzone to <10 μs. This system was used to characterize the relaxation effect using dried MNPs. The signal dependency on the sensor coverage, magnetization time, and

magnetic field strength were discussed. Lastly, an MRX-based MIA was performed to validate the system.

Chapter 5 presented a CMOS sensor front-end based on MRX. MR-CDS, which subtracted the signal phase from the magnetization phase, was presented to reduce the readout time and improve 1/*f* noise rejection. Although it provided a better FoM than MCDS, it contained residual MR baseline and had poor temperature drift rejection. A sensor bias scheme with rotating DEM reduced the 1/*f* noise from the bias transistors. A CCIA amplified the pseudo-differential input and canceled the input offset by adding a DSL. To settle the chopping artifacts before being sampled by the ADC, a FSMC technique was reported, which used smaller Miller capacitance for fast settling when chopping and switches to a larger Miller capacitance for stability when the ADC sampling capacitors loaded the output. This resulted in 2.5× lower CCIA power consumption while maintaining the linearity and stability. Lastly, an 18b Zoom ADC that contained a 6b SAR and 13b DSM quantized the CCIA output. As a result, this work provided lowest input-referred noise, along with comparable power consumption and readout time. It achieved the best-reported FoM that is 4.9× better than other magnetic AFEs and 210× better than MRX-based AFEs. Finally, both dried MNP and MIA experiments were conducted to validate the system performance.

6.2 Areas for Future Work

The MR sensor project presented in this dissertation can be further expanded upon in a few ways.

First, the GMR sensor array can be fabricated on-chip with the CMOS circuitry, which enables large sensor array [53], [74]. Based on Equation 2.8, the signal can be improved by using smaller sensors, but the biological DR is limited. Therefore, large arrays with small sensors can achieve both high sensitivity and broad DR. A multi-channel design is required to read the large array in a reasonable acquisition time.

Second, the electromagnet can be integrated into the chip. By placing the CMOS circuitry on the bottom layers, the sensor array on the top layers, and the electromagnet right below the sensors, a fully integrated biochip can be implemented. The electromagnet can be implemented by metal stripelines, which are driven by a voltage controlled current source [51]. While the field uniformity from stripelines is a challenge for magnetometry, MRX can be applied to relax this requirement. Furthermore, power can be saved by periodically turning on and off the system in MCDS [160], [161].

Third, TMR sensors can be used to replace GMR sensors. TMR sensors have been shown to have higher MR but are limited by larger 1/*f* noise. 1/*f* noise rejection techniques such as the double modulation scheme and MCDS can be applied to achieve higher SNR than GMR sensing, and thus higher sensitivity.

Lastly, PoC diagnoses also require short-range wireless data transmission to send the diagnostic results to a smartphone that can be reviewed by the patient or a doctor [162]–[166]. Moreover, a wake-up receiver can wake up the device when necessary for continuous monitoring [167]–[169]. By integrating the wireless transmission features into the analytical device, this device can be further expanded to be wearable, or even implantable, that can communicate with smart devices from patients.

References

[1] “Life expectancy at birth, total (years) | Data.” https://data.worldbank.org/indicator/SP.DYN.LE00.IN?most_recent_value_desc=true (accessed May 04, 2020).

[2] S. K. Vashist, “Point-of-Care Diagnostics: Recent Advances and Trends,” *Biosensors*, vol. 7, no. 4, Dec. 2017.

[3] S. Nayak, N. R. Blumenfeld, T. Laksanasopin, and S. K. Sia, “Point-of-Care Diagnostics: Recent Developments in a Connected Age,” *Anal. Chem.*, vol. 89, no. 1, pp. 102–123, Dec. 2016.

[4] S. K. Vashist, P. B. Luppa, L. Y. Yeo, A. Ozcan, and J. H. T. Luong, “Emerging Technologies for Next-Generation Point-of-Care Testing,” *Trends Biotechnol.*, vol. 33, no. 11, pp. 692–705, Nov. 2015.

[5] “Point-of-Care Diagnostics Market Analysis by Testing & Platform. Global Industry Forecast to 2022 : MarketsandMarkets.” https://www.marketsandmarkets.com/Market-Reports/point-of-care-diagnostic-market-106829185.html (accessed May 03, 2020).

[6] C.-C. Huang, G.-Y. Lee, J.-I. Chyi, H.-T. Cheng, C.-P. Hsu, Y.-R. Hsu, C.-H. Hsu, Y.-F. Huang, Y.-C. Sun, C.-C. Chen, S.-S. Li, J. Andrew Yeh, D.-J. Yao, F. Ren, and Y.-L. Wang, “AlGaN/GaN high electron mobility transistors for protein–peptide binding affinity study,” *Biosens. Bioelectron.*, vol. 41, pp. 717–722, Mar. 2013.

[7] X. P. A. Gao, G. Zheng, and C. M. Lieber, “Subthreshold Regime has the Optimal Sensitivity for Nanowire FET Biosensors,” *Nano Lett.*, vol. 10, no. 2, pp. 547–552, Feb. 2010.

[8] J. Kimura and T. Kuriyama, “FET biosensors,” *J. Biotechnol.*, vol. 15, no. 3, pp. 239–254, Aug. 1990.

[9] Y.-L. Wang, C.-C. Huang, and Y.-W. Kang, “Incorporation of ligand-receptor binding-site models and transistor-based sensors for resolving dissociation constants and number of binding sites,” *IET Nanobiotechnol.*, vol. 8, no. 1, pp. 10–17, Mar. 2014.

[10] K. W. Wee, G. Y. Kang, J. Park, J. Y. Kang, D. S. Yoon, J. H. Park, and T. S. Kim, “Novel electrical detection of label-free disease marker proteins using piezoresistive self-sensing micro-cantilevers,” *Biosens. Bioelectron.*, vol. 20, no. 10, pp. 1932–1938, Apr. 2005.

[11] Y. Arntz, J. D. Seelig, H. P. Lang, J. Zhang, P. Hunziker, J. P. Ramseyer, E. Meyer, M. Hegner, and C. Gerber, “Label-free protein assay based on a nanomechanical cantilever array,” *Nanotechnology*, vol. 14, no. 1, p. 86, 2003.

[12] R. McKendry, J. Zhang, Y. Arntz, T. Strunz, M. Hegner, H. P. Lang, M. K. Baller, U. Certa, E. Meyer, H.-J. Güntherodt, and C. Gerber, “Multiple label-free biodetection

and quantitative DNA-binding assays on a nanomechanical cantilever array," *Proc. Natl. Acad. Sci.*, vol. 99, no. 15, pp. 9783–9788, Jul. 2002.

[13] M. A. Cooper, "Label-free screening of bio-molecular interactions," *Anal. Bioanal. Chem.*, vol. 377, no. 5, pp. 834–842, Nov. 2003.

[14] J.-R. Lee, D. M. Magee, R. S. Gaster, J. LaBaer, and S. X. Wang, "Emerging Protein Array Technologies for Proteomics," *Expert Rev. Proteomics*, vol. 10, no. 1, pp. 65–75, Feb. 2013.

[15] X. Luo, A. Morrin, A. J. Killard, and M. R. Smyth, "Application of Nanoparticles in Electrochemical Sensors and Biosensors," *Electroanalysis*, vol. 18, no. 4, pp. 319–326, Feb. 2006.

[16] X. Zhou, C.-C. Huang, and D. A. Hall, "Magnetoresistive biosensors for quantitative proteomics," in *Biosensing and Nanomedicine X*, Aug. 2017, vol. 10352, p. 103520F.

[17] P. Damborský, J. Švitel, and J. Katrlík, "Optical biosensors," *Essays Biochem.*, vol. 60, no. 1, pp. 91–100, Jun. 2016.

[18] C. Boozer, G. Kim, S. Cong, H. Guan, and T. Londergan, "Looking towards label-free biomolecular interaction analysis in a high-throughput format: a review of new surface plasmon resonance technologies," *Curr. Opin. Biotechnol.*, vol. 17, no. 4, pp. 400–405, Aug. 2006.

[19] K. Pimková, M. Bocková, K. Hegnerová, J. Suttnar, J. Cermák, J. Homola, and J. E. Dyr, "Surface plasmon resonance biosensor for the detection of VEGFR-1--a protein marker of myelodysplastic syndromes," *Anal. Bioanal. Chem.*, vol. 402, no. 1, pp. 381–387, Jan. 2012.

[20] E. Engvall and P. Perlmann, "Enzyme-linked immunosorbent assay (ELISA) quantitative assay of immunoglobulin G," *Immunochemistry*, vol. 8, no. 9, pp. 871–874, Sep. 1971.

[21] B. k. Van Weemen and A. h. w. m. Schuurs, "Immunoassay using antigen—enzyme conjugates," *FEBS Lett.*, vol. 15, no. 3, pp. 232–236, Jun. 1971.

[22] A. P. de Silva, H. Q. N. Gunaratne, T. Gunnlaugsson, A. J. M. Huxley, C. P. McCoy, J. T. Rademacher, and T. E. Rice, "Signaling Recognition Events with Fluorescent Sensors and Switches," *Chem. Rev.*, vol. 97, no. 5, pp. 1515–1566, Aug. 1997.

[23] S. J. Dwight, B. S. Gaylord, J. W. Hong, and G. C. Bazan, "Perturbation of Fluorescence by Nonspecific Interactions between Anionic Poly(phenylenevinylene)s and Proteins: Implications for Biosensors," *J. Am. Chem. Soc.*, vol. 126, no. 51, pp. 16850–16859, Dec. 2004.

[24] Q.-Y. Zhang, H. Chen, Z. Lin, and J.-M. Lin, "Comparison of chemiluminescence enzyme immunoassay based on magnetic microparticles with traditional colorimetric ELISA for the detection of serum α-fetoprotein," *J. Pharm. Anal.*, vol. 2, no. 2, pp. 130–135, Apr. 2012.

[25] H. A. H. Rongen, R. M. W. Hoetelmans, A. Bult, and W. P. Van Bennekom, “Chemiluminescence and immunoassays,” *J. Pharm. Biomed. Anal.*, vol. 12, no. 4, pp. 433–462, Apr. 1994.

[26] C. Dodeigne, L. Thunus, and R. Lejeune, “Chemiluminescence as diagnostic tool. A review,” *Talanta*, vol. 51, no. 3, pp. 415–439, Mar. 2000.

[27] D. Dey and T. Goswami, “Optical Biosensors: A Revolution Towards Quantum Nanoscale Electronics Device Fabrication,” *J. Biomed. Biotechnol.*, vol. 2011, 2011.

[28] V. Pavlov, “Enzymatic Growth of Metal and Semiconductor Nanoparticles in Bioanalysis,” *Part. Part. Syst. Charact.*, vol. 31, no. 1, pp. 36–45, Jan. 2014.

[29] R. Grinyte, J. Barroso, M. Möller, L. Saa, and V. Pavlov, “Microbead QD-ELISA: Microbead ELISA Using Biocatalytic Formation of Quantum Dots for Ultra High Sensitive Optical and Electrochemical Detection,” *ACS Appl. Mater. Interfaces*, vol. 8, no. 43, pp. 29252–29260, Nov. 2016.

[30] J. D. Newman and A. P. F. Turner, “Home blood glucose biosensors: a commercial perspective,” *Biosens. Bioelectron.*, vol. 20, no. 12, pp. 2435–2453, Jun. 2005.

[31] D. Grieshaber, R. MacKenzie, J. Vörös, and E. Reimhult, “Electrochemical Biosensors - Sensor Principles and Architectures,” *Sensors*, vol. 8, no. 3, pp. 1400–1458, Mar. 2008.

[32] A. Chaubey and B. D. Malhotra, “Mediated biosensors,” *Biosens. Bioelectron.*, vol. 17, no. 6, pp. 441–456, Jun. 2002.

[33] A. L. Ghindilis, P. Atanasov, M. Wilkins, and E. Wilkins, “Immunosensors: electrochemical sensing and other engineering approaches,” *Biosens. Bioelectron.*, vol. 13, no. 1, pp. 113–131, Jan. 1998.

[34] T. Goda and Y. Miyahara, “Label-free and reagent-less protein biosensing using aptamer-modified extended-gate field-effect transistors,” *Biosens. Bioelectron.*, vol. 45, pp. 89–94, Jul. 2013.

[35] C.-S. Lee, S. K. Kim, and M. Kim, “Ion-Sensitive Field-Effect Transistor for Biological Sensing,” *Sensors*, vol. 9, no. 9, pp. 7111–7131, Sep. 2009.

[36] D. G. Hafeman, J. W. Parce, and H. M. McConnell, “Light-addressable potentiometric sensor for biochemical systems,” *Science*, vol. 240, no. 4856, pp. 1182–1185, May 1988.

[37] C. Ercole, M. D. Gallo, M. Pantalone, S. Santucci, L. Mosiello, C. Laconi, and A. Lepidi, “A biosensor for Escherichia coli based on a potentiometric alternating biosensing (PAB) transducer,” *Sens. Actuators B Chem.*, vol. 83, no. 1, pp. 48–52, Mar. 2002.

[38] N. J. Ronkainen-Matsuno, J. H. Thomas, H. B. Halsall, and W. R. Heineman, “Electrochemical immunoassay moving into the fast lane,” *TrAC Trends Anal. Chem.*, vol. 21, no. 4, pp. 213–225, Apr. 2002.

[39] J. Wang, A. Ibáñez, M. P. Chatrathi, and A. Escarpa, “Electrochemical Enzyme Immunoassays on Microchip Platforms,” *Anal. Chem.*, vol. 73, no. 21, pp. 5323–5327, Nov. 2001.

[40] Z. Dai, F. Yan, J. Chen, and H. Ju, “Reagentless Amperometric Immunosensors Based on Direct Electrochemistry of Horseradish Peroxidase for Determination of Carcinoma Antigen-125,” *Anal. Chem.*, vol. 75, no. 20, pp. 5429–5434, Oct. 2003.

[41] M. S. Wilson, “Electrochemical Immunosensors for the Simultaneous Detection of Two Tumor Markers,” *Anal. Chem.*, vol. 77, no. 5, pp. 1496–1502, Mar. 2005.

[42] H. Jiang, X. Zhou, S. Kulkarni, M. Uranian, R. Seenivasan, and D. A. Hall, “A Sub-1 µW multiparameter injectable BioMote for continuous alcohol monitoring,” in *2018 IEEE Custom Integrated Circuits Conference (CICC)*, Apr. 2018, pp. 1–4.

[43] E. Katz and I. Willner, “Probing Biomolecular Interactions at Conductive and Semiconductive Surfaces by Impedance Spectroscopy: Routes to Impedimetric Immunosensors, DNA-Sensors, and Enzyme Biosensors,” *Electroanalysis*, vol. 15, no. 11, pp. 913–947, Jul. 2003.

[44] O. Ouerghi, A. Touhami, N. Jaffrezic-Renault, C. Martelet, H. B. Ouada, and S. Cosnier, “Impedimetric immunosensor using avidin–biotin for antibody immobilization,” *Bioelectrochemistry*, vol. 56, no. 1, pp. 131–133, May 2002.

[45] A. Manickam, A. Chevalier, M. McDermott, A. D. Ellington, and A. Hassibi, “A CMOS Electrochemical Impedance Spectroscopy (EIS) Biosensor Array,” *IEEE Trans. Biomed. Circuits Syst.*, vol. 4, no. 6, pp. 379–390, Dec. 2010.

[46] H. Jiang, A. Sun, A. G. Venkatesh, and D. A. Hall, “An Audio Jack-Based Electrochemical Impedance Spectroscopy Sensor for Point-of-Care Diagnostics,” *IEEE Sens. J.*, vol. 17, no. 3, pp. 589–597, Feb. 2017.

[47] P. D’Orazio, “Biosensors in clinical chemistry,” *Clin. Chim. Acta*, vol. 334, no. 1, pp. 41–69, Aug. 2003.

[48] H. Wang, Y. Chen, A. Hassibi, A. Scherer, and A. Hajimiri, “A frequency-shift CMOS magnetic biosensor array with single-bead sensitivity and no external magnet,” in *2009 IEEE International Solid-State Circuits Conference - Digest of Technical Papers*, Feb. 2009, pp. 438-439,439a.

[49] H. Wang, C. Sideris, and A. Hajimiri, “A frequency-shift based CMOS magnetic biosensor with spatially uniform sensor transducer gain,” in *IEEE Custom Integrated Circuits Conference 2010*, Sep. 2010, pp. 1–4.

[50] P. P. Liu, K. Skucha, Y. Duan, M. Megens, J. Kim, I. I. Izyumin, S. Gambini, and B. Boser, “Magnetic Relaxation Detector for Microbead Labels,” *IEEE J. Solid-State Circuits*, vol. 47, no. 4, pp. 1056–1064, Apr. 2012.

[51] S. Gambini, K. Skucha, P. P. Liu, J. Kim, and R. Krigel, “A 10 kPixel CMOS Hall Sensor Array With Baseline Suppression and Parallel Readout for Immunoassays,” *IEEE J. Solid-State Circuits*, vol. 48, no. 1, pp. 302–317, Jan. 2013.

[52] S. J. Han, H. Yu, B. Murmann, N. Pourmand, and S. X. Wang, “A High-Density Magnetoresistive Biosensor Array with Drift-Compensation Mechanism,” in *2007*

IEEE International Solid-State Circuits Conference. Digest of Technical Papers, Feb. 2007, pp. 168–594.

[53] T. Costa, F. A. Cardoso, J. Germano, P. P. Freitas, and M. S. Piedade, “A CMOS Front-End With Integrated Magnetoresistive Sensors for Biomolecular Recognition Detection Applications,” *IEEE Trans. Biomed. Circuits Syst.*, vol. 11, no. 5, pp. 988–1000, Oct. 2017.

[54] R. S. Gaster, D. A. Hall, C. H. Nielsen, S. J. Osterfeld, H. Yu, K. E. Mach, R. J. Wilson, B. Murmann, J. C. Liao, S. S. Gambhir, and S. X. Wang, “Matrix-insensitive protein assays push the limits of biosensors in medicine,” *Nat. Med.*, vol. 15, no. 11, pp. 1327–1332, Nov. 2009.

[55] D. A. Hall, R. S. Gaster, T. Lin, S. J. Osterfeld, S. Han, B. Murmann, and S. X. Wang, “GMR biosensor arrays: a system perspective,” *Biosens. Bioelectron.*, vol. 25, no. 9, pp. 2051–2057, May 2010.

[56] D. A. Hall, R. S. Gaster, K. A. A. Makinwa, S. X. Wang, and B. Murmann, “A 256 Pixel Magnetoresistive Biosensor Microarray in 0.18 um CMOS,” *IEEE J. Solid-State Circuits*, vol. 48, no. 5, pp. 1290–1301, May 2013.

[57] X. Zhou, M. Sveiven, and D. A. Hall, “A CMOS Magnetoresistive Sensor Front-End With Mismatch-Tolerance and Sub-ppm Sensitivity for Magnetic Immunoassays,” *IEEE Trans. Biomed. Circuits Syst.*, vol. 13, no. 6, pp. 1254–1263, Dec. 2019.

[58] R. S. Gaster, D. A. Hall, and S. X. Wang, “nanoLAB: An ultraportable, handheld diagnostic laboratory for global health,” *Lab. Chip*, vol. 11, no. 5, pp. 950–956, Mar. 2011.

[59] H. Wang, “Magnetic Sensors for Diagnostic Medicine: CMOS-Based Magnetic Particle Detectors for Medical Diagnosis Applications,” *IEEE Microw. Mag.*, vol. 14, no. 5, pp. 110–130, Jul. 2013.

[60] I. Giouroudi and E. Hristoforou, “Perspective: Magnetoresistive sensors for biomedicine,” *J. Appl. Phys.*, vol. 124, no. 3, p. 030902, Jul. 2018.

[61] N. Sun, Y. Liu, H. Lee, R. Weissleder, and D. Ham, “CMOS RF Biosensor Utilizing Nuclear Magnetic Resonance,” *IEEE J. Solid-State Circuits*, vol. 44, no. 5, pp. 1629–1643, May 2009.

[62] H. Lee, E. Sun, D. Ham, and R. Weissleder, “Chip–NMR biosensor for detection and molecular analysis of cells,” *Nat. Med.*, vol. 14, no. 8, pp. 869–874, Aug. 2008.

[63] N. Sun, T. J. Yoon, H. Lee, W. Andress, R. Weissleder, and D. Ham, “Palm NMR and 1-Chip NMR,” *IEEE J. Solid-State Circuits*, vol. 46, no. 1, pp. 342–352, Jan. 2011.

[64] H. Wang, S. Kosai, C. Sideris, and A. Hajimiri, “An ultrasensitive CMOS magnetic biosensor array with correlated double counting noise suppression,” in *2010 IEEE MTT-S International Microwave Symposium*, May 2010, pp. 616–619.

[65] H. Wang, A. Mahdavi, D. A. Tirrell, and A. Hajimiri, “A magnetic cell-based sensor,” *Lab. Chip*, vol. 12, no. 21, pp. 4465–4471, Oct. 2012.

[66] K. Skucha, P. Liu, M. Megens, J. Kim, and B. Boser, “A compact Hall-effect sensor array for the detection and imaging of single magnetic beads in biomedical assays,” in *2011 16th International Solid-State Sensors, Actuators and Microsystems Conference*, Jun. 2011, pp. 1833–1836.

[67] T. Aytur, J. Foley, M. Anwar, B. Boser, E. Harris, and P. R. Beatty, “A novel magnetic bead bioassay platform using a microchip-based sensor for infectious disease diagnosis,” *J. Immunol. Methods*, vol. 314, no. 1, pp. 21–29, Jul. 2006.

[68] P.-A. Besse, G. Boero, M. Demierre, V. Pott, and R. Popovic, “Detection of a single magnetic microbead using a miniaturized silicon Hall sensor,” *Appl. Phys. Lett.*, vol. 80, no. 22, pp. 4199–4201, May 2002.

[69] P. Liu, K. Skucha, M. Megens, and B. Boser, “A CMOS Hall-Effect Sensor for the Characterization and Detection of Magnetic Nanoparticles for Biomedical Applications,” *IEEE Trans. Magn.*, vol. 47, no. 10, pp. 3449–3451, Oct. 2011.

[70] K. Skucha, S. Gambini, P. Liu, M. Megens, J. Kim, and B. E. Boser, “Design Considerations for CMOS-Integrated Hall-Effect Magnetic Bead Detectors for Biosensor Applications,” *J. Microelectromechanical Syst.*, vol. 22, no. 6, pp. 1327–1338, Dec. 2013.

[71] G. Li, S. Sun, R. J. Wilson, R. L. White, N. Pourmand, and S. X. Wang, “Spin valve sensors for ultrasensitive detection of superparamagnetic nanoparticles for biological applications,” *Sens. Actuators Phys.*, vol. 126, no. 1, pp. 98–106, Jan. 2006.

[72] S. X. Wang, S.-Y. Bae, G. Li, S. Sun, R. L. White, J. T. Kemp, and C. D. Webb, “Towards a magnetic microarray for sensitive diagnostics,” *J. Magn. Magn. Mater.*, vol. 293, no. 1, pp. 731–736, May 2005.

[73] D. A. Hall, R. S. Gaster, S. J. Osterfeld, B. Murmann, and S. X. Wang, “GMR biosensor arrays: correction techniques for reproducibility and enhanced sensitivity,” *Biosens. Bioelectron.*, vol. 25, no. 9, pp. 2177–2181, May 2010.

[74] S. J. Han, L. Xu, H. Yu, R. J. Wilson, R. L. White, N. Pourmand, and S. X. Wang, “CMOS Integrated DNA Microarray Based on GMR Sensors,” in *2006 International Electron Devices Meeting*, Dec. 2006, pp. 1–4.

[75] M. Denoual, S. Saez, F. Kauffman, and C. Dolabdjian, “Magnetorelaxometry using Improved Giant MagnetoResistance Magnetometer,” *Sens. Actuators Phys.*, vol. 159, no. 2, pp. 184–188, May 2010.

[76] X. Zhou, C.-C. Huang, and D. A. Hall, “Giant Magnetoresistive Biosensor Array for Detecting Magnetorelaxation,” *IEEE Trans. Biomed. Circuits Syst.*, vol. 11, no. 4, pp. 755–764, Aug. 2017.

[77] C.-C. Huang, X. Zhou, and D. A. Hall, “Giant Magnetoresistive Biosensors for Time-Domain Magnetorelaxometry: A Theoretical Investigation and Progress Toward an Immunoassay,” *Sci. Rep.*, vol. 7, p. srep45493, Apr. 2017.

[78] W. Shen, B. D. Schrag, M. J. Carter, and G. Xiao, “Quantitative detection of DNA labeled with magnetic nanoparticles using arrays of MgO-based magnetic tunnel junction sensors,” *Appl. Phys. Lett.*, vol. 93, no. 3, p. 033903, Jul. 2008.

[79] Z. Q. Lei, L. Li, G. J. Li, C. W. Leung, J. Shi, C. M. Wong, K. C. Lo, W. K. Chan, C. S. K. Mak, S. B. Chan, N. M. M. Chan, C. H. Leung, P. T. Lai, and P. W. T. Pong, “Liver cancer immunoassay with magnetic nanoparticles and MgO-based magnetic tunnel junction sensors,” *J. Appl. Phys.*, vol. 111, no. 7, p. 07E505, Mar. 2012.

[80] X. Zhou, M. Sveiven, and D. A. Hall, “11.4 A Fast-Readout Mismatch-Insensitive Magnetoresistive Biosensor Front-End Achieving Sub-ppm Sensitivity,” in *2019 IEEE International Solid- State Circuits Conference - (ISSCC)*, Feb. 2019, pp. 196–198.

[81] J. M. Perez, L. Josephson, T. O’Loughlin, D. Högemann, and R. Weissleder, “Magnetic relaxation switches capable of sensing molecular interactions,” *Nat. Biotechnol.*, vol. 20, no. 8, pp. 816–820, Aug. 2002.

[82] “Time Domain NMR | TD-NMR | Benchtop,” *Bruker.com*. https://www.bruker.com/products/mr/td-nmr.html (accessed Jul. 06, 2020).

[83] I. Koh, R. Hong, R. Weissleder, and L. Josephson, “Sensitive NMR Sensors Detect Antibodies To Influenza,” *Angew. Chem. Int. Ed Engl.*, vol. 47, no. 22, pp. 4119–4121, 2008.

[84] “Magnetoresistance,” *Wikipedia*. Apr. 13, 2020, Accessed: May 05, 2020. [Online]. Available: https://en.wikipedia.org/w/index.php?title=Magnetoresistance&oldid=950662923.

[85] W. Thomson, “XIX. On the electro-dynamic qualities of metals:—Effects of magnetization on the electric conductivity of nickel and of iron,” *Proc. R. Soc. Lond.*, vol. 8, pp. 546–550, Jan. 1857.

[86] “The Nobel Prize in Physics 2007,” *NobelPrize.org*. https://www.nobelprize.org/prizes/physics/2007/summary/ (accessed May 05, 2020).

[87] P. P. Freitas, R. Ferreira, S. Cardoso, and F. Cardoso, “Magnetoresistive sensors,” *J. Phys. Condens. Matter*, vol. 19, no. 16, p. 165221, Apr. 2007.

[88] L. Jogschies, D. Klaas, R. Kruppe, J. Rittinger, P. Taptimthong, A. Wienecke, L. Rissing, and M. C. Wurz, “Recent Developments of Magnetoresistive Sensors for Industrial Applications,” *Sensors*, vol. 15, no. 11, pp. 28665–28689, Nov. 2015.

[89] D. Mazumdar, X. Liu, B. D. Schrag, W. Shen, M. Carter, and G. Xiao, “Thermal stability, sensitivity, and noise characteristics of MgO-based magnetic tunnel junctions (invited),” *J. Appl. Phys.*, vol. 101, no. 9, p. 09B502, Apr. 2007.

[90] J. M. Teixeira, J. Ventura, F. Carpinteiro, J. P. Araujo, J. B. Sousa, P. Wisniowski, and P. P. Freitas, “The effect of pinhole formation/growth on the tunnel magnetoresistance of MgO-based magnetic tunnel junctions,” *J. Appl. Phys.*, vol. 106, no. 7, p. 073707, Oct. 2009.

[91] C. K. Boggs, A. D. Doak, and F. L. Walls, “Measurement of voltage noise in chemical batteries,” in *Proceedings of the 1995 IEEE International Frequency Control Symposium (49th Annual Symposium)*, San Francisco, CA, USA, 1995, pp. 367–373.

[92] G. Li and S. X. Wang, “Analytical and micromagnetic modeling for detection of a single magnetic microbead or nanobead by spin valve sensors,” *IEEE Trans. Magn.*, vol. 39, no. 5, pp. 3313–3315, Sep. 2003.

[93] K. A. A. Makinwa, “Smart temperature sensors in standard CMOS,” *Procedia Eng.*, vol. 5, pp. 930–939, Jan. 2010.

[94] H. Jiang, C.-C. Huang, M. R. Chan, and D. A. Hall, “A 2-in-1 Temperature and Humidity Sensor With a Single FLL Wheatstone-Bridge Front-End,” *IEEE J. Solid-State Circuits*, pp. 1–1, 2020.

[95] H. Jiang, C.-C. Huang, M. Chan, and D. A. Hall, “A 2-in-1 Temperature and Humidity Sensor Achieving 62 fJ·K2 and 0.83 pJ·(%RH)2,” in *2019 IEEE Custom Integrated Circuits Conference (CICC)*, Apr. 2019, pp. 1–4.

[96] J. C. Rife, M. M. Miller, P. E. Sheehan, C. R. Tamanaha, M. Tondra, and L. J. Whitman, “Design and performance of GMR sensors for the detection of magnetic microbeads in biosensors,” *Sens. Actuators Phys.*, vol. 107, no. 3, pp. 209–218, Nov. 2003.

[97] C.-P. Lee, M.-F. Lai, H.-T. Huang, C.-W. Lin, and Z.-H. Wei, “Wheatstone bridge giant-magnetoresistance based cell counter,” *Biosens. Bioelectron.*, vol. 57, pp. 48–53, Jul. 2014.

[98] M. F. Hansen and G. Rizzi, “Exchange-Biased AMR Bridges for Magnetic Field Sensing and Biosensing,” *IEEE Trans. Magn.*, vol. 53, no. 4, pp. 1–11, Apr. 2017.

[99] S. Adem, S. Jain, M. Sveiven, X. Zhou, A. J. O’Donoghue, and D. A. Hall, “Giant magnetoresistive biosensors for real-time quantitative detection of protease activity,” *Sci. Rep.*, vol. 10, no. 1, Art. no. 1, May 2020.

[100] C.-C. Huang, X. Zhou, D. Ying, and D. A. Hall, “A GMR-based magnetic flow cytometer using matched filtering,” in *2017 IEEE SENSORS*, Oct. 2017, pp. 1–3.

[101] C.-C. Huang, P. Ray, M. Chan, X. Zhou, and D. A. Hall, “An aptamer-based magnetic flow cytometer using matched filtering,” *Biosens. Bioelectron.*, p. 112362, Jun. 2020.

[102] O. Y. Galkin, O. B. Besarab, M. O. Pysmenna, Y. V. Gorshunov, and O. M. Dugan, “Modern magnetic immunoassay: Biophysical and biochemical aspects,” *Regul. Mech. Biosyst.*, vol. 9, no. 1, pp. 47–55, 2018.

[103] C. Reig, D. Ramírez, F. Silva, J. Bernardo, and P. Freitas, “Design, fabrication, and analysis of a spin-valve based current sensor,” *Sens. Actuators Phys.*, vol. 115, no. 2, pp. 259–266, Sep. 2004.

[104] H. Chandrakumar and D. Marković, “An 80-mVpp Linear-Input Range, 1.6-GΩ Input Impedance, Low-Power Chopper Amplifier for Closed-Loop Neural Recording That

Is Tolerant to 650-mVpp Common-Mode Interference," *IEEE J. Solid-State Circuits*, vol. 52, no. 11, pp. 2811–2828, Nov. 2017.

[105] S. Zhang, C. Gao, X. Zhou, and Q. Li, "23.7 A 130dB CMRR Instrumentation Amplifier with Common-Mode Replication," in *2020 IEEE International Solid- State Circuits Conference - (ISSCC)*, Feb. 2020, pp. 356–358.

[106] R. R. Harrison and C. Charles, "A low-power low-noise CMOS amplifier for neural recording applications," *IEEE J. Solid-State Circuits*, vol. 38, no. 6, pp. 958–965, Jun. 2003.

[107] V. Majidzadeh, A. Schmid, and Y. Leblebici, "Energy Efficient Low-Noise Neural Recording Amplifier With Enhanced Noise Efficiency Factor," *IEEE Trans. Biomed. Circuits Syst.*, vol. 5, no. 3, pp. 262–271, Jun. 2011.

[108] J. A. Kaehler, "Periodic-switching filter networks-a means of amplifying and varying transfer functions," *IEEE J. Solid-State Circuits*, vol. 4, no. 4, pp. 225–230, Aug. 1969.

[109] H. Chandrakumar and D. Marković, "A High Dynamic-Range Neural Recording Chopper Amplifier for Simultaneous Neural Recording and Stimulation," *IEEE J. Solid-State Circuits*, vol. 52, no. 3, pp. 645–656, Mar. 2017.

[110] J. Markus, J. Silva, and G. C. Temes, "Theory and applications of incremental ΔΣ converters," *IEEE Trans. Circuits Syst. Regul. Pap.*, vol. 51, no. 4, pp. 678–690, Apr. 2004.

[111] A. C. Sun, E. Alvarez-Fontecilla, A. G. Venkatesh, E. Aronoff-Spencer, and D. A. Hall, "High-Density Redox Amplified Coulostatic Discharge-Based Biosensor Array," *IEEE J. Solid-State Circuits*, vol. 53, no. 7, pp. 2054–2064, Jul. 2018.

[112] D. A. Armbruster and T. Pry, "Limit of Blank, Limit of Detection and Limit of Quantitation," *Clin. Biochem. Rev.*, vol. 29, no. Suppl 1, pp. S49–S52, Aug. 2008.

[113] W. F. Brown, "Thermal Fluctuations of a Single-Domain Particle," *Phys. Rev.*, vol. 130, no. 5, pp. 1677–1686, Jun. 1963.

[114] F. Ludwig, E. Heim, and M. Schilling, "Magnetorelaxometry of magnetic nanoparticles - a new method for the quantitative and specific analysis of biomolecules," in *4th IEEE Conference on Nanotechnology, 2004.*, Aug. 2004, pp. 245–248.

[115] L. Néel, "Théorie du traînage magnétique des substances massives dans le domaine de Rayleigh," *J. Phys. Radium*, vol. 11, no. 2, pp. 49–61, 1950.

[116] A. P. Astalan, F. Ahrentorp, C. Johansson, K. Larsson, and A. Krozer, "Biomolecular reactions studied using changes in Brownian rotation dynamics of magnetic particles," *Biosens. Bioelectron.*, vol. 19, no. 8, pp. 945–951, Mar. 2004.

[117] N. L. Adolphi, D. L. Huber, J. E. Jaetao, H. C. Bryant, D. M. Lovato, D. L. Fegan, E. L. Venturini, T. C. Monson, T. E. Tessier, H. J. Hathaway, C. Bergemann, R. S. Larson, and E. R. Flynn, "Characterization of magnetite nanoparticles for SQUID-relaxometry and magnetic needle biopsy," *J. Magn. Magn. Mater.*, vol. 321, no. 10, pp. 1459–1464, May 2009.

[118] H. C. Bryant, N. L. Adolphi, D. L. Huber, D. L. Fegan, T. C. Monson, T. E. Tessier, and E. R. Flynn, “Magnetic properties of nanoparticles useful for SQUID relaxometry in biomedical applications,” *J. Magn. Magn. Mater.*, vol. 323, no. 6, pp. 767–774, Mar. 2011.

[119] E. Romanus, M. Hückel, C. Groß, S. Prass, W. Weitschies, R. Bräuer, and P. Weber, “Magnetic nanoparticle relaxation measurement as a novel tool for in vivo diagnostics,” *J. Magn. Magn. Mater.*, vol. 252, pp. 387–389, Nov. 2002.

[120] R. W. Chantrell, S. R. Hoon, and B. K. Tanner, “Time-dependent magnetization in fine-particle ferromagnetic systems,” *J. Magn. Magn. Mater.*, vol. 38, no. 2, pp. 133–141, Sep. 1983.

[121] R. Kötitz, W. Weitschies, L. Trahms, and W. Semmler, “Investigation of Brownian and Néel relaxation in magnetic fluids,” *J. Magn. Magn. Mater.*, vol. 201, no. 1–3, pp. 102–104, Jul. 1999.

[122] C. Johnson, N. L. Adolphi, K. L. Butler, D. M. Lovato, R. Larson, P. D. D. Schwindt, and E. R. Flynn, “Magnetic relaxometry with an atomic magnetometer and SQUID sensors on targeted cancer cells,” *J. Magn. Magn. Mater.*, vol. 324, no. 17, pp. 2613–2619, Aug. 2012.

[123] N. L. Adolphi, D. L. Huber, J. E. Jaetao, H. C. Bryant, D. M. Lovato, D. L. Fegan, E. L. Venturini, T. C. Monson, T. E. Tessier, H. J. Hathaway, C. Bergemann, R. S. Larson, and E. R. Flynn, “Characterization of magnetite nanoparticles for SQUID-relaxometry and magnetic needle biopsy,” *J. Magn. Magn. Mater.*, vol. 321, no. 10, pp. 1459–1464, May 2009.

[124] R. Street and J. C. Woolley, “A Study of Magnetic Viscosity,” *Proc. Phys. Soc. Sect. A*, vol. 62, no. 9, p. 562, 1949.

[125] E. P. Wohlfarth, “The coefficient of magnetic viscosity,” *J. Phys. F Met. Phys.*, vol. 14, no. 8, p. L155, 1984.

[126] D. V. Berkov and R. Kötitz, “Irreversible relaxation behaviour of a general class of magnetic systems,” *J. Phys. Condens. Matter*, vol. 8, no. 9, p. 1257, 1996.

[127] C. R. Tamanaha, S. P. Mulvaney, J. C. Rife, and L. J. Whitman, “Magnetic labeling, detection, and system integration,” *Biosens. Bioelectron.*, vol. 24, no. 1, pp. 1–13, Sep. 2008.

[128] L. Li, K. Y. Mak, C. W. Leung, S. M. Ng, Z. Q. Lei, and P. W. T. Pong, “Detection of 10-nm Superparamagnetic Iron Oxide Nanoparticles Using Exchange-Biased GMR Sensors in Wheatstone Bridge,” *IEEE Trans. Magn.*, vol. 49, no. 7, pp. 4056–4059, Jul. 2013.

[129] J. Xu, Q. Li, X. Y. Gao, F. F. Leng, M. Lü, P. Z. Guo, G. X. Zhao, and S. D. Li, “Detection of the Concentration of MnFe2O4 Magnetic Microparticles Using Giant Magnetoresistance Sensors,” *IEEE Trans. Magn.*, vol. 52, no. 4, pp. 1–4, Apr. 2016.

[130] B. Bechen, A. Kemna, M. Gnade, T. v. d. Boom, and B. Hosticka, “Noise Considerations of Integrators for Current Readout Circuits,” *Adv Radio Sci*, vol. 3, pp. 331–336, May 2005.

[131] T. Korn, F. Müller, D. Grundler, and C. Schüller, “Characterization of Permalloy films on high-bandwidth striplines,” *J. Magn. Magn. Mater.*, vol. 272–276, Supplement, pp. E1341–E1342, May 2004.

[132] Ł. Pawliszak, M. Tekielak, and M. Zgirski, “Miniature coils for producing pulsed inplane magnetic fields for nanospintronics,” *Rev. Sci. Instrum.*, vol. 86, no. 3, p. 034711, Mar. 2015.

[133] K. Mackay, M. Bonfim, D. Givord, and A. Fontaine, “50 T pulsed magnetic fields in microcoils,” *J. Appl. Phys.*, vol. 87, no. 4, pp. 1996–2002, Feb. 2000.

[134] S. S. Jian Wang, “An improved Helmholtz coil and analysis of its magnetic field homogeneity,” *Rev. Sci. Instrum. - REV SCI INSTR*, vol. 73, no. 5, pp. 2175–2179, 2002.

[135] I. Sasada and Y. Nakashima, “Planar coil system consisting of three coil pairs for producing a uniform magnetic field,” *J. Appl. Phys.*, vol. 99, no. 8, p. 08D904, Apr. 2006.

[136] M. S. Crosser, S. Scott, A. Clark, and P. M. Wilt, “On the magnetic field near the center of Helmholtz coils,” *Rev. Sci. Instrum.*, vol. 81, no. 8, p. 084701, Aug. 2010.

[137] E. Mori, “Ultra fast and high efficiency inductive coil driver,” US6670796 B2, Dec. 30, 2003.

[138] G. Villar and E. Alarcon, “Inductor-current zero-crossing detection mixed-signal CMOS circuit for a DCM-operated 3-level switching power converter,” in *IEEE International Symposium on Circuits and Systems, 2008. ISCAS 2008*, May 2008, pp. 2606–2609.

[139] V. Michal, “Inductor Current Zero-Crossing Detector and CCM/DCM Boundary Detector for Integrated High-Current Switched-Mode DC-DC Converters,” *IEEE Trans. Power Electron.*, vol. 29, no. 10, pp. 5384–5391, Oct. 2014.

[140] D. J. B. Bechstein, J.-R. Lee, C. C. Ooi, A. W. Gani, K. Kim, R. J. Wilson, and S. X. Wang, “High performance wash-free magnetic bioassays through microfluidically enhanced particle specificity,” *Sci. Rep.*, vol. 5, p. 11693, Jun. 2015.

[141] J.-R. Lee, N. Sato, D. J. B. Bechstein, S. J. Osterfeld, J. Wang, A. W. Gani, D. A. Hall, and S. X. Wang, “Experimental and theoretical investigation of the precise transduction mechanism in giant magnetoresistive biosensors,” *Sci. Rep.*, vol. 6, p. 18692, Jan. 2016.

[142] G. Li, S. X. Wang, and S. Sun, “Model and experiment of detecting multiple magnetic nanoparticles as biomolecular labels by spin valve sensors,” *IEEE Trans. Magn.*, vol. 40, no. 4, pp. 3000–3002, Jul. 2004.

[143] G. Li, S. Sun, and S. X. Wang, “Spin valve biosensors: Signal dependence on nanoparticle position,” *J. Appl. Phys.*, vol. 99, no. 8, p. 08P107, Apr. 2006.

[144] R. De Palma, S. Peeters, M. J. Van Bael, H. Van den Rul, K. Bonroy, W. Laureyn, J. Mullens, G. Borghs, and G. Maes, “Silane Ligand Exchange to Make Hydrophobic Superparamagnetic Nanoparticles Water-Dispersible,” *Chem. Mater.*, vol. 19, no. 7, pp. 1821–1831, Apr. 2007.

[145] R. De Palma, C. Liu, F. Barbagini, G. Reekmans, K. Bonroy, W. Laureyn, G. Borghs, and G. Maes, “Magnetic Particles as Labels in Bioassays: Interactions between a Biotinylated Gold Substrate and Streptavidin Magnetic Particles,” *J. Phys. Chem. C*, vol. 111, no. 33, pp. 12227–12235, Aug. 2007.

[146] K.-M. Lenssen, A. Kuiper, J. Broek, R. Rijt, and A. Loon, “Sensor properties of a robust giant magnetoresistance material system at elevated temperatures,” *J. Appl. Phys.*, vol. 87, pp. 6665–6667, May 2000.

[147] S. Mondal and D. A. Hall, “An ECG chopper amplifier achieving 0.92 NEF and 0.85 PEF with AC-coupled inverter-stacking for noise efficiency enhancement,” in *2017 IEEE International Symposium on Circuits and Systems (ISCAS)*, May 2017, pp. 1–4.

[148] S. Mondal and D. A. Hall, “A 13.9-nA ECG Amplifier Achieving 0.86/0.99 NEF/PEF Using AC-Coupled OTA-Stacking,” *IEEE J. Solid-State Circuits*, vol. 55, no. 2, pp. 414–425, Feb. 2020.

[149] L. Shen, N. Lu, and N. Sun, “A 1V 0.25uW inverter-stacking amplifier with 1.07 noise efficiency factor,” in *2017 Symposium on VLSI Circuits*, Jun. 2017, pp. C140–C141.

[150] U. Ha, J. Lee, M. Kim, T. Roh, S. Choi, and H.-J. Yoo, “An EEG-NIRS Multimodal SoC for Accurate Anesthesia Depth Monitoring,” *IEEE J. Solid-State Circuits*, vol. 53, no. 6, pp. 1830–1843, Jun. 2018.

[151] C. Reig, D. Ramírez, F. Silva, J. Bernardo, and P. Freitas, “Design, fabrication, and analysis of a spin-valve based current sensor,” *Sens. Actuators Phys.*, vol. 115, no. 2, pp. 259–266, Sep. 2004.

[152] B. Y. T. Kamath, R. G. Meyer, and P. R. Gray, “Relationship between frequency response and settling time of operational amplifiers,” *IEEE J. Solid-State Circuits*, vol. 9, no. 6, pp. 347–352, Dec. 1974.

[153] Q. Fan, F. Sebastiano, J. H. Huijsing, and K. A. A. Makinwa, “A 1.8 μW 60 nV/√Hz Capacitively-Coupled Chopper Instrumentation Amplifier in 65 nm CMOS for Wireless Sensor Nodes,” *IEEE J. Solid-State Circuits*, vol. 46, no. 7, pp. 1534–1543, Jul. 2011.

[154] C. C. Enz and G. C. Temes, “Circuit techniques for reducing the effects of op-amp imperfections: autozeroing, correlated double sampling, and chopper stabilization,” *Proc. IEEE*, vol. 84, no. 11, pp. 1584–1614, Nov. 1996.

[155] Y. Chae, K. Souri, and K. A. A. Makinwa, “A 6.3 μW 20 bit Incremental Zoom-ADC with 6 ppm INL and 1 μV Offset,” *IEEE J. Solid-State Circuits*, vol. 48, no. 12, pp. 3019–3027, Dec. 2013.

[156] R. T. Baird and T. S. Fiez, “Linearity enhancement of multibit ΔΣ A/D and D/A converters using data weighted averaging,” *IEEE Trans. Circuits Syst. II Analog Digit. Signal Process.*, vol. 42, no. 12, pp. 753–762, Dec. 1995.

[157] B. Gönen, F. Sebastiano, R. Quan, R. van Veldhoven, and K. A. A. Makinwa, “A Dynamic Zoom ADC With 109-dB DR for Audio Applications,” *IEEE J. Solid-State Circuits*, vol. 52, no. 6, pp. 1542–1550, Jun. 2017.

[158] D. M. Horan and R. A. Guinee, “Correlation analysis of random number sequences based on pseudo random binary sequence generation,” in *IEEE Information Theory Workshop, 2005.*, Aug. 2005, pp. 82–85.

[159] J. Welz, I. Galton, and E. Fogleman, “Simplified logic for first-order and second-order mismatch-shaping digital-to-analog converters,” *IEEE Trans. Circuits Syst. II Analog Digit. Signal Process.*, vol. 48, no. 11, pp. 1014–1027, Nov. 2001.

[160] S. Mondal, C.-L. Hsu, R. Jafari, and D. Hall, “A dynamically reconfigurable ECG analog front-end with a 2.5 × data-dependent power reduction,” in *2017 IEEE Custom Integrated Circuits Conference (CICC)*, Apr. 2017, pp. 1–4.

[161] C. Zong, S. Mondal, D. A. Hall, and R. Jafari, “Digitally assisted analog front-end power management strategy via dynamic reconfigurability for robust heart rate monitoring,” *ACM SIGBED Rev.*, vol. 12, no. 3, pp. 36–39, Aug. 2015.

[162] A. C. Sun and D. A. Hall, “Point-of-Care Smartphone-based Electrochemical Biosensing,” *Electroanalysis*, vol. 31, no. 1, pp. 2–16, 2019.

[163] T. Matić, L. Šneler, and M. Herceg, “An Energy Efficient Multi-User Asynchronous Wireless Transmitter for Biomedical Signal Acquisition,” *IEEE Trans. Biomed. Circuits Syst.*, vol. 13, no. 4, pp. 619–630, Aug. 2019.

[164] X. Zhang, Z. Zhang, Y. Li, C. Liu, Y. X. Guo, and Y. Lian, “A 2.89 uW Dry-Electrode Enabled Clockless Wireless ECG SoC for Wearable Applications,” *IEEE J. Solid-State Circuits*, vol. 51, no. 10, pp. 2287–2298, Oct. 2016.

[165] S. Mondal and D. A. Hall, “A 107 µW MedRadio Injection-Locked Clock Multiplier with a CTAT-biased 126 ppm/°C Ring Oscillator,” in *2019 IEEE Custom Integrated Circuits Conference (CICC)*, Apr. 2019, pp. 1–4.

[166] S. Mondal and D. A. Hall, “A 67-µW Ultra-Low Power PVT-Robust MedRadio Transmitter,” presented at the 2020 IEEE Radio Frequency Integrated Circuits Symposium (RFIC), Aug. 2020.

[167] S. Maity, D. Yang, B. Chatterjee, and S. Sen, “A sub-nW Wake-up Receiver for Human Body Communication,” in *2018 IEEE Biomedical Circuits and Systems Conference (BioCAS)*, Oct. 2018, pp. 1–4.

[168] P.-H. P. Wang, H. Jiang, L. Gao, P. Sen, Y.-H. Kim, G. M. Rebeiz, P. P. Mercier, and D. A. Hall, “A Near-Zero-Power Wake-Up Receiver Achieving −69-dBm Sensitivity,” *IEEE J. Solid-State Circuits*, vol. 53, no. 6, pp. 1640–1652, Jun. 2018.

[169] H. Jiang, P.-H. P. Wang, L. Gao, C. Pochet, G. M. Rebeiz, D. A. Hall, and P. P. Mercier, “A 22.3-nW, 4.55 cm2 Temperature-Robust Wake-Up Receiver Achieving a Sensitivity of −69.5 dBm at 9 GHz,” *IEEE J. Solid-State Circuits*, vol. 55, no. 6, pp. 1530–1541, Jun. 2020.